Bent Laue Crystals in Biomedical X-ray Imaging Applications

A Dissertation Submitted to

the College of Graduate Studies and Research

in Partial Fulfillment of the Requirements

for the Degree of Doctor of Philosophy

in the

Division of Biomedical Engineering

College of Engineering

University of Saskatchewan

By

Zhu, Ying

Saskatoon, SK

Canada

Permission to Use

In presenting this dissertation in partial fulfilment of the requirements for a Degree of Doctor of Philosophy from the University of Saskatchewan, I agree that the Libraries of this University may make it available for inspection. I further agree that permission for copying of this dissertation in any manner, in whole or in part, for scholarly purposes may be granted by the professors who supervised this dissertation work or, in their absence, by the Head of the Division or the Dean of the College in which this dissertation work was done. It is understood that any copying or publication or use of this dissertation or parts thereof for financial gain shall not be allowed without the author's written permission. It is also understood that due recognition shall be given to me and to the University of Saskatchewan in any scholarly use which may be made of any material in this dissertation.

Requests for permission to copy or to make other use of the material in the dissertation in whole or in part should be addressed to:

Head of the Division of Biomedical Engineering

University of Saskatchewan

57 Campus Drive

Saskatoon, Saskatchewan

Canada, S7N 5A9

Abstract

This dissertation presents several synchrotron-based biomedical X-ray imaging projects involving bent Laue silicon (Si) crystals.

Log-spiral bent Laue analyzers (BLA) were made from 20 μm thick Si crystals to map manganese (Mn) fluorescence in the X-ray fluorescence (XRF) imaging of the human brain with Parkinson's disease (PD). The BLA improved Mn specificity in XRF imaging and achieved a Mn detection limit of 0.5 mM concentration and an energy resolution of 34.5 eV.

A novel method of three dimensional (3D) confocal XRF imaging of iodine was designed based on the one dimensional (1D) focusing ability of a log-spiral BLA made from 175 μm thick Si crystals. Combined with a pencil beam or a two dimensional (2D) focused beam, a 3D voxel of $100 \times 100 \times 124$ μm^3 could be used to probe the 3D elemental mapping of a sample.

A cylindrical bent Laue monochromator (BLM) was made from 600 μm thick Si crystals to simultaneously prepare three beams for the three-energy K-Edge Subtraction (KES) imaging and KES Computed Tomography (CT). A novel three-beam chopper was made as the first beam chopper for fast switching among the three beams. The three-energy KES imaging was successfully used to track uptake of injected iodine with time in a live mouse. The first simultaneous dual-energy KES imaging and the first KES CT imaging were successfully performed in Canada at the Biomedical Imaging and Therapy (BMIT) beamline.

A novel rat head restraint and its corresponding field flatteners were constructed using a rapid-prototyping machine for the KES project based on CT scan data of a rat. This type of animal restraint worked well to immobilize the animal and holds great promise in improving the

image quality and repeatability while reducing stress on experimental animals. The field flattener improved the signal-to-noise ratio (SNR) of the image at a cost of raised maximum exposure to some regions of the subject and reduced anatomical information in the images. In animal imaging applications, this method holds great promise to visualize low concentrations of contrast agents.

Another cylindrical BLM was made to perform the novel Near Edge Spectral Imaging (NESI) and NESI CT. It showed high sensitivity for iodine with a measured detection limit of 2 $\mu g/cm^2$ and a slightly better SNR performance than conventional KES imaging. The overwhelming impact of NESI is that it will bring together contrast imaging and elemental speciation imaging through X-ray Absorption Near Edge Structure (XANES) and Extended X-ray Absorption Fine Structure (EXAFS) analysis which have been totally different realms.

Acknowledgments

Special thanks go to my supervisor Dr. Dean Chapman who opens the door of X-ray imaging to me, inspires me with his sparkling ideas and great passion to explore any possibilities and guides me through the data analysis and dissertation writing. Deep thanks go to my co-supervisor Dr. Helen Nichol who helped me step into biology and metal metabolism and helped with my writing and presenting.

I would like to thank Valerie Verge, Bernhard Juurlink and Nicky Cox in Anatomy and Cell Biology for assistance with rats; Sheldon Wiebe, Helen Nichol and Richard McCrea for arranging medical CT for three rats; Troy Anderson and Lori Toews in Royal University Hospital for their expertise in medical CT; Claude Lapointe, Patrick Cadman and Deluan Tu in the Saskatoon Cancer Center for helping to determine the X-ray visibilities of rapid prototyping materials; Garth Wells at the Canadian Light Source (CLS) for providing the ultraviolet (UV) light source; Manouchehr Hashemi in Electrical and Computer Engineering, Arlene Drimmie and Hui Wang in Biochemistry for suggesting or providing tetrahydrofuran; Ian J. Burgess in Chemistry for crystal orientation; Sheila Boire and Jim Boire in RMD Engineering Inc. for crystal orientation and wafer cutting; Ike Oguocha in Mechanical Engineering for consultations about wafer cutting apparatus; Ramaswami Sammynaiken, Ken Thoms and Gabriele Schatte at the Saskatchewan Structural Sciences Centre (SSSC) for wafer etching, Helen Nichol, Banafsheh Moazed and Karen Yuen in Anatomy and Cell Biology for chemicals, lab apparatus, Mn and iron (Fe) foil standards and a UV light oven; Oana Marcu at National Advisory Committee on Aeronautics (NACA) Ames Research Center for providing and shipping *Drosophila* pupae; Juan

Ianowski in Physiology for help with *Drosophila* culture; Ali Rajput at Royal University Hospital for providing the human brain samples; Helen Nichol and Bogdan F. Gh. Popescu in Anatomy and Cell Biology for preparation of the human brain samples; Robert Wilson in Engineering Machine Shop for operation of the rapid-prototyper; Daniel Vessey in Engineering Machine Shop for precise computer numerical control (CNC) machining of the three-beam chopper; Zhouping Wei at the University of Saskatchewan (U of S) for CT reconstructions, Zhong Zhong at the National Synchrotron Light Source for the discussion of confocal XRF imaging; the CLS machine shop for providing parts materials and machining and the CLS engineering department for printing posters.

Great thanks go to my co-workers Honglin Zhang for inspiring discussions, Brian Bewer for constant help with instrumentations, Zhouping Wei, Sheila Boire, Ning Zhu, Bhallaje Kannan and Nazanin Samadi for discussions, help with the experiments and and many other academic activities.

I also wish to thank George Belev, Adam Webb, Huang Chun, Stephen Hanson and Tomasz Wysokinski at the BMIT bending magnet (BM) beamline, Chang-Yong Kim, Ruifeng Chen and Ning Chen at the Hard X-ray Microanalysis (HXMA) beamline at the CLS for their efforts in preparing and assisting in operating the beamlines. The experiments described in my dissertation were performed at the BMIT BM and HXMA beamlines at the CLS which is supported by NSERC, NRC, CIHR and U of S. My projects were funded by a NSERC Discovery grant (Dr. Dean Chapman), a U of S Graduate Scholarship, a CIHR THRUST Training Grant – Training in Health Research Using Synchrotron Techniques and two U of S student travel awards.

To my parents Shaoren and Shuping and brother Jeff

To my husband Yongxu

To my children born during my PhD, Bingxuan, Xueqi and Yikai

Contents

List of Tables

List of Figures

List of Abbreviations

1D	One-dimensional
2D	Two-dimensional
3D	Three-dimensional
4D	Four-dimensional
ACGIH	American Conference of Governmental Industrial Hygienists
ASTM	American Society for Testing and Materials
BLA	Bent Laue silicon analyzer of a logarithmic spiral shape
BLM	Bent Laue silicon monochromator of a cylinder shape
BM	Bending magnet beamline
BMIT	Biomedical Imaging and Therapy
$CaCl_2$	Calcium chloride
CLS	Canadian Light Source
CLSM	Confocal Laser Scanning Microscopy
CNC	Computer Numerical Control
CRL	Compound refractive lenses
CT	Computed Tomography
DICOM	Digital Imaging and Communications in Medicine
DV	Dorsal-ventral view
DXA / DEXA	Dual-Energy X-ray Absorptiometry
EXAFS	Extended X-ray Absorption Fine Structure
FOM	Figure of merit
FSI	Fluorescence Subtraction Imaging

FWHM	Full width at half maximum
HXMA	Hard X-ray Microanalysis
ID	Insertion device
I.D.	Inner diameter
IDL	Interactive Data Language
KB	Kirkpatrick-Baez
KES	K-Edge Subtraction
LSCM	Laser Scanning Confocal Microscopy
MECT	Multiple Energy Computed Tomography
MXA / MEXA	Multiple Energy X-ray Analysis / Absorptiometry
Mn	Manganese
Mn-SOD	Mn-containing superoxide dismutase
NaI	Sodium iodide
NESI	Near Edge Spectral Imaging
O.D.	Outer diameter
PD	Parkinson's disease
PVC	Polyvinyl chloride
RMS	Root-mean-square
Si	Silicon
SNR	Signal-to-noise ratio
SSSC	Saskatchewan Structural Sciences Centre
STL	Standard Tessellation Language
STXM	Scanning Transmission X-ray Microscope
TLV	Threshold limit value
TXM	Transmission X-ray Microscope

UCACS	University Committee on Animal Care and Supply
U of S	University of Saskatchewan
UV	Ultraviolet
XAFS	X-ray Absorption Fine Structure
XANES	X-ray Absorption Near Edge Structure
XAS	X-ray Absorption Spectroscopy
XRF	X-ray Fluorescence

List of Symbols

B	Bone material
BP	Bragg's plane
BS	$CaCl_2$ solution resembling the bone
C	Contrast material
C_E	Three-beam chopper rotation motion for energy iteration
cm	centimeter, a length unit
χ	Asymmetry angle
d	Spacing of the Bragg's planes
D	Dose
D_3	Determinant of the $\frac{\mu}{\rho}$ matrix in three-energy KES
D_{33}	Determinant of the $\frac{\mu}{\rho}$ product average matrix in three-component NESI
D_{DV}	Surface dose after a dorsal-ventral field flattener
D_{LAT}	Surface dose after a lateral field flattener
D_{mm}	Determinant of the $\frac{\mu}{\rho}$ product average matrix in m-component NESI
D_{noff}	Surface dose without a field flattener
DP	Diffraction Plane
ΔE	Energy resolution
$\Delta E/E$	Energy bandwidth
δE	Average energy difference from edge energy of an element
δE_{max}	Edge-to-center diffracted energy difference in a BLM
Δh	Transversal size along z axis of a BLA's detectable region
$\Delta\theta$	Crystal reflectivity width
$\Delta\theta_B$	Bragg angle difference between $K_{\alpha 1}$ and $K_{\alpha 2}$ fluorescence
$\Delta\theta_L$	Angular difference of lattice planes at the incident and exit of a single ray

Δs	Change of the source to BLA crystal distance
Δv	Vertical size along *y* axis of a BLA's detectable region
Δy	Vertical distance along *y* axis
º	Degree, an angle unit
eV	Electron volt, an energy unit
E	Energy
E_{3K}	Harmonic of the three times K-edge energy
E_{3KA}	Harmonic of the three times K-edge energy at the above beam
E_{3KB}	Harmonic of the three times K-edge energy at the below beam
E_A	Above K-edge energy
E_B	Below K-edge energy
E_{CT}	Equivalent photon energy of CT images
E_K	K-edge energy
E_{Ka}	Energy of the K_α fluorescence
f	Focal length or virtual focal length
f_1	Source to crystal distance of a BLM
f_2	Geometric focal length of a BLM
F	Focal point or virtual focal point
F_G	Geometrical focus of a BLM
F_S	Single ray focus of a BLM
Φ	Coronal opening angle of a bent crystal
g	Gram, a weight unit
GeV	Giga electron volt, an energy unit
γ	A scaling factor
h	Higher energy or above the edge energy
H	Plastic holder material
HU	Hounsfield Unit
I	BLA in the positive / upper incident of Si (111) diffraction
-I	BLA in the negative / lower incident of Si (111) diffraction
II	BLA in the positive / upper incident of Si (400) diffraction
-II	BLA in the negative / lower incident of Si (400) diffraction

k	Photoelectron's wave vector
keV	Kilo-electron volt, an energy unit
kV	Kilovolt, a voltage unit
kVp	Kilovolt peak, a voltage unit
l	Lower energy or below the edge energy
l	Active arc length of a bent Laue crystal
L	Single ray focus length of a BLM
λ	Wavelength
mA	milliampere, a current unit
mGy	milli-Gray, a dose unit
min	minute, a time unit
mm	millimeter, a length unit
mM	millimolar, a concentration unit
$mrad$	milliradian, an angle unit
msr	millisteradian, a solid angle unit
M	Matrix material
μ	Linear absorption coefficient
μm	micron, a length unit
μM	micromolar, a concentration unit
μrad	microradian, an angle unit
$\frac{\mu}{\rho}$	Mass absorption coefficient
N	Image pixel number or the number of photon or flux
O	The origin of the BLA logarithmic spiral curve
P	Field flattener material
θ_B	Bragg's angle
θ_{B1}	Bragg's angle of the $K_{\alpha 1}$ fluorescence
θ_{B2}	Bragg's angle of the $K_{\alpha 2}$ fluorescence
r	Crystal bending radius
R	Normal center point
R_{eq}	Equivalent crystal reflectivity

R_{ij}	An inverse matrix element of the $\frac{\mu}{\rho}$ product average matrix for NESI
RPM	Revolution per minute
ρ	Density
ρ_{ι}	Density of iodine
$\rho_{\iota 0}$	Prepared iodine concentration
$\rho_{\iota e}$	Estimated iodine density
ρ_{ω}	Density of water
s	Second, a time unit
s	Source-to-crystal distance
s_{CB}	Sensitivity coefficient of bone to the contrast image
s_{MB}	Sensitivity coefficient of bone to the matrix image
S	Source point
S_R	Sample stage rotation motion for CT imaging
S_V	Sample stage vertical scanning motion for CT imaging
SR	Surface reflection focus from a bent crystal
σ	Projected mass density
t	Thickness
t_m	Maximum thickness
T	Soft tissue material
T	Tesla, magnetic field unit
TOT	Total material
ν	Poisson's Ratio
V_B	Vertical size of the incident beam
V_{ij}	An inverse matrix element of the $\frac{\mu}{\rho}$ matrix for KES imaging
w	Transversal active width of a crystal
W	Water material
ω_D	Darwin width of the crystal diffraction
Ω	Solid angle
x	Horizontal axis along the BLA focal direction

x	Lateral direction of an animal
y	Vertical axis in the BLA diffraction plane
y	Dorsal-ventral direction of an animal
Ψ	Transversal opening angle
z	Transversal axis perpendicular to the BLA diffraction plane
z	Caudal direction along an animal

Chapter 1 Introduction

1.1 Overview

Bent Laue silicon (Si) crystals have been used as X-ray optics for a variety of applications at synchrotron facilities and laboratories worldwide. The major advantages of the bent Laue crystal include the high imaging flux due to the focusing and increased integrated reflectivity, large solid angle of diffraction due to bending, good system stability and tolerance in diffraction and alignment due to the flat top reflectivity within the widened reflectivity bandwidth. The most common use is as a focusing monochromator to provide high imaging flux of monochromatic beam for imaging purposes, such as a cylindrical bent Laue monochromator (BLM) for coronary angiography [Suo88, Suo93], a cylindrical BLM for Multiple Energy Computed Tomography (MECT) [Ren97] and a sagittal focussing BLM [Zho01]. Another application is the use as an X-ray fluorescence analyzer in the Cauchois geometry [Cau32], such as a log-spiral bent Laue analyzer (BLA) for the Extended X-ray Absorption Fine Structure (EXAFS) detection [Zho99] and a log-spiral BLA for X-ray Absorption Spectroscopy (XAS) [Kar00].

This dissertation presents several synchrotron-based biomedical X-ray imaging projects involving bent Laue Si crystals. Four log-spiral BLAs were made from 20 μm thick Si (111) and Si (400) crystals to map manganese (Mn) fluorescence in X-ray fluorescence (XRF) imaging of the human brain with Parkinson's disease (PD). Two log-spiral BLAs were made from175 μm thick Si (111) crystals for a novel three dimensional (3D) confocal XRF imaging of iodine. A

cylindrical BLM was made from a 600 μm thick Si (511) crystal to simultaneously prepare three beams for three-energy K-Edge Subtraction (KES) imaging and KES Computed Tomography (CT) of a small animal with injected iodine. A novel three-beam chopper was made as the first beam chopper for fast switching among the three beams for this project. A novel rat head restraint and its corresponding field flatteners were rapid-prototyped based on the CT scan of a rat for the KES project as well. Another cylindrical BLM was made from a 600 μm thick Si (511) crystal to perform the novel Near Edge Spectral Imaging (NESI) and NESI CT of a mouse with injected iodine.

These bent Laue Si crystals were applied in several biomedical X-ray imaging modalities, K-Edge Subtraction imaging, Near Edge Spectral Imaging, X-ray fluorescence imaging and confocal XRF imaging. These imaging modalities are introduced in the following sections with literature reviews and project motivations.

1.2 K-Edge Subtraction Imaging

1.2.1 Conventional KES Imaging

The conventional KES [Rub85], also called dichromography or dual-energy subtraction imaging, is an imaging method that uses the logarithmic subtraction of two images taken above and below a contrast's edge energy to sort out the projected density images of two components, the contrast and the matrix material. The image contrast of KES relies on a huge jump (about 5.5 times for Iodine) in the X-ray absorption coefficient $\frac{\mu}{\rho}$ of the contrast material over its edge energy compared with a small change in the $\frac{\mu}{\rho}$ of the matrix material (about 0.7% change for water). Conventional KES provides better image quality and lower dose than the clinical angiography which takes an image after contrast medium injection and the temporal subtraction

practice which subtracts two images taken before and after the contrast medium injection [Bal03].

Since the first proposal in 1953 [Jac53], the synchrotron application of dual-energy KES has been widely used in coronary angiography, cerebral angiography, neurovascular intravenous angiography, bronchography, lung imaging, mammography, lymphatic imaging, brain tumor imaging and KES-CT [Zha09]. Many implementation methods for the dual-energy KES emerged from a time sequence method to simultaneous methods using either an X-ray tube or a synchrotron source.

The typical time sequence method using an X-ray tube as the source took images with and without a filter and/or at different X-ray tube voltages [Kel77, Ume92]. The typical synchrotron-based time sequence method used a double crystal monochromator to prepare a parallel beam of above or below the edge energy, one at a time. The double crystal monochromator could be two perfect crystals [Zha08] or a perfect crystal combined with a bent crystal [Zho97]. For the time sequence method, any misalignment or motion from a live organism during the energy switch period would produce motional image blurring in the subtracted images.

A simultaneous KES for an X-ray tube source used a flat Bragg crystal monochromator and a double slits collimator to prepare two beams of the above and below edge energy at the same time [Bal02]. Synchrotron-based simultaneous KES used a variety of crystal monochromators to prepare two beams of the above and below the edge energy at the same time and focus or cross them at the sample position. The crystal monochromator used could be two separate perfect crystal monochromators [Tho89], two separate bent crystal monochromators [Suo88, Ill95] or a single bent crystal monochromator with a beam splitter [Suo93]. The

simultaneous KES avoids the motional image blurring especially for a living organism imaging system. The focusing monochromators gained greater photon flux within a smaller pixel size at a price of the cross-over artifact since the beam was not parallel through the sample.

1.2.2 Three-Energy KES Imaging

For the conventional dual-energy KES, one of the artifacts in the images comes from bone, which is discussed in detail in chapter 5.1.2. Bone produces negative pixel values in the contrast image, cuts down the amount of contrast material detected and thus impairs the ability to properly interpret the images. This is a severe artifact especially when the full body of an animal with thick bones is imaged. Another artifact for time sequenced KES is the motional image blurring arising from the movements of a live organism between the two images. Any misalignment will show up in the subtracted images and worsen the detectable limit of the contrast agent.

The problem with the dual-energy KES with the presence of bone is that the object was assumed to be composed of two materials, contrast and matrix material. To properly account for three components, a third imaging energy should be added to solve for contrast, matrix and bone material. There were several investigations of three-energy KES based on an X-ray tube source using three different tube voltages or three filters to take three images [Kel76, Rie81, Rie82]. Synchrotron-based three-energy KES was reported by R. H. Menk using a single crystal BLM, a beam splitter and a tin filter [Men97].

We developed a combined system of a BLM and a three-beam chopper to perform three-energy KES at the BMIT at the CLS. The BLM diffracts an energy band of 268 *eV* above and below the iodine K-edge and focuses the beam (a line focus) on the sample. Right after the monochromator, the chopper sequentially prepares three energies for three images rapidly taken at each pixel. This X-ray imaging system not only allows a contrast image free of both artifacts,

but also produces an additional image of bone which has potential application for anatomy or even visualization of calcifications.

1.2.3 Three Beam Chopper

Beam choppers or beam switchers were used in X-ray imaging to redefine the beams for different purposes. The majority of the applications were to produce monochromatic X-ray pulses for dose control, heat load control or image quality, such as a rotating tunnel chopper [Oku98], a slotted chopper [Gem07] or an adjustable assembly of blades [Ren05]. Comparison among tunnel choppers, edge choppers and slotted choppers for producing monochromatic X-ray pulses were reported [Cam09]. Several applications of fast switching between the two beams were reported for dual-energy KES, such as a rotating slit (tunnel chopper) [Zem84] and two-drum (edge choppers) beam-switcher [Zem86]. For fast switching among three beams in three-energy KES, none of the above beam choppers or beam switchers for manipulating one or two beams could be used.

A novel tunnel chopper for fast switching among three beams for three-energy KES was designed and built with tin bronze. During one revolution of the three-beam chopper, about 60° opening time was achieved for each of the three beams which were 120° apart. Since the chopper dimension was closely related to the three-beam heights after a BLM, a decision of three equal beam heights was made based on the optimization study of the three-beam heights and practical considerations. The design of the three-beam chopper, the material selection and the chopper assembly are presented in this dissertation.

1.2.4 Near Edge Spectral Imaging

Since the 1990s, X-ray spectromicroscopy became a popular chemical imaging technique essentially in the soft X-ray regime [Ade90, Kir09]. It is a combined technique to perform the X-ray Absorption Near Edge Structure (XANES) [Sto96] or EXAFS through either a transmission

X-ray microscope (TXM) or a scanning transmission X-ray microscope (STXM) [Rar88] using either an X-ray tube source or a synchrotron source. X-ray spectromicroscopy has the advantages of high spatial resolution (~50 *nm*) from the STXM, high spectral resolution (~0.05 *eV*) from the monochromator adjustment at a synchrotron source, adjustable energy step size and pixel dwell time at a cost of time-consuming raster scan and energy traversal. Typical image stacks of 50^2 ~ 256^2 pixels took 0.5 ~ 10 hours for 50~200 energy steps for each pixel and 1~60 *ms* pixel dwell time for each energy [Jac00]. Over the last decade, tomographic spectromicroscopy emerged to obtain 4 dimensional (4D) data sets of (x, y, E, θ) for 3D chemical imaging using the STXM-based "chemical tomography" [Hit03, Joh07]. Due to the time-consuming 3D scan, a small 3D volume was only imaged at two or a few energies which substantially limited the performance of XANES analysis. It is desirable that the chemical imaging and "chemical tomography" could be quickly and easily performed on large samples, for example animals.

Multiple-energy X-ray analysis / absorptiometry (MXA or MEXA) is a composition analysis technique derived from the well-established dual-energy X-ray absorptiometry (DXA or DEXA) which is routinely used in the clinical determination of bone mineral density and osteoporosis diagnosis. This technique shared the similar theory with the KES algorithm without specifically designated energies bracketing an absorption edge of an element. But the reported MXA measurements were taken at a few energies produced by synchrotron sources [Sch03], isotope sources [Jon88], X-ray tube sources with changing filters, tube voltages, target materials or a multichannel analyzer of an energy-dispersive detector [Koz99].

The NESI system (Figure 1.1) proposed in this dissertation would provide a new technique to perform two-dimensional (2D) and 3D chemical imaging of large samples in the hard X-ray regime, fast and easily through the use of a BLM. Instead of traversing hundreds of

energies at each pixel and raster scanning sub-micron pixel sizes using X-ray spectromicroscopy, NESI only requires one line-scan motion to get a raw data cube of (*x, y, E*) with hundreds of energies simultaneously acquired in one shot. Right now the NESI energy resolution is about 2.4 *eV* per pixel width which could be improved by increasing the sample-to-detector distance and/or switching to a high resolution imaging detector. The vertical spatial resolution is now 100 μm set by the beam size at focus and could be a few microns in the near future. Combined with 50 ~ 100 *mm* width of the beam and BLM, this spatial resolution is great for small animals.

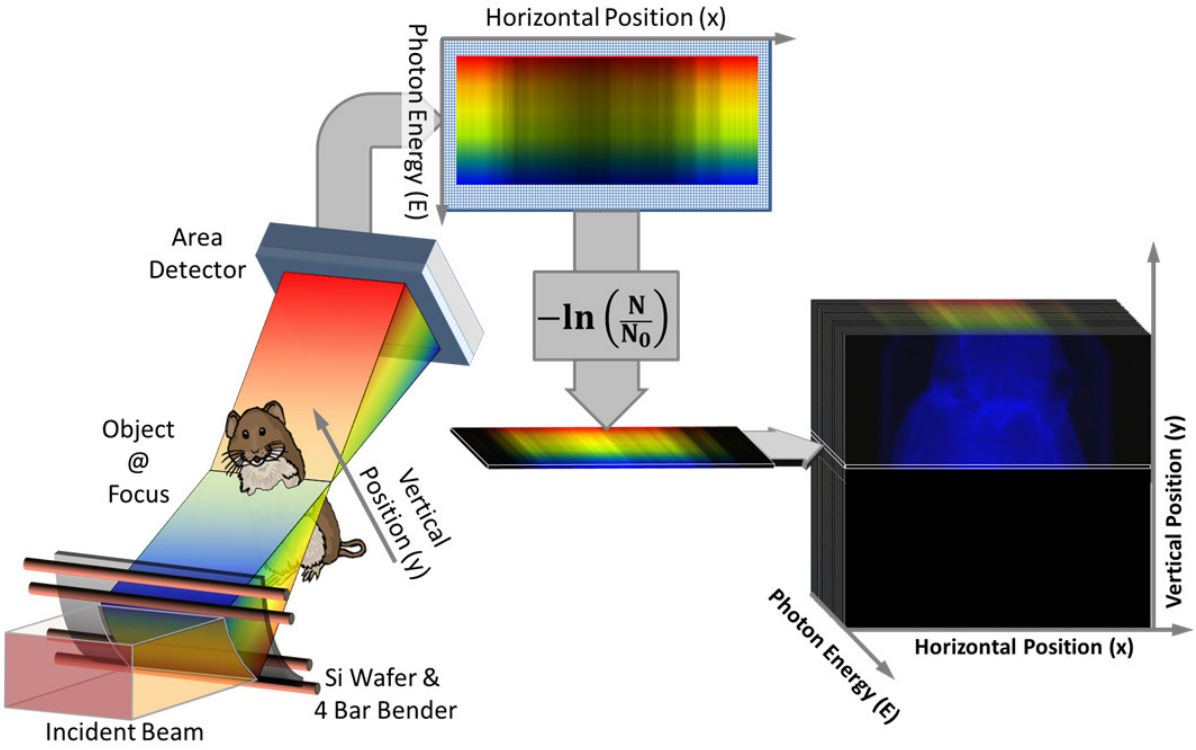

Figure 1.1 Schematic diagram of the NESI system (image courtesy of Dr. Dean Chapman)

The NESI system extends the conventional KES system to include a small focus BLM and an area detector beyond the focus instead of a line detector. This NESI system will have several advantages compared to the conventional KES system.

First, the NESI system could instantly provide a full near edge spectrum of the contrast material at every pixel width. With enough energy resolution to perform XANES analysis, the contrast species of various oxidation states could be spatially determined by this chemical imaging process if the various oxidation states are separated by a few eV.

Second, EXAFS could be performed to some extent using BLMs with shorter bending radius and larger energy bandwidth to investigate the local structure information.

Third, the XANES and EXAFS measurements at each pixel take just one shot which is quick enough to consider time resolved spectroscopy which is in great demand to investigate rapidly varying phenomena.

Fourth, the NESI system does not block the X-rays that are near or at the K-edge of the element. This allows much more imaging flux since the X-rays in the orbital plane of the synchrotron source would be fully used. This can easily increase the available flux by at least a factor of 5.

Fifth, the small line focus of the NESI system increases the flux and dose to the sample due to the focused beam. Combined with high flux from the orbital plane, this high resolution and high flux would open a door to applications such as cell level imaging and radiation therapy investigations.

Sixth, the simultaneously prepared energies eliminate motion artifacts in the image and allows for the imaging of living systems.

Seventh, since hundreds of imaging energies would determine hundreds of components in theory, several other interesting components in the sample, besides the contrast species, could also be determined by the NESI algorithm, as long as they have sufficient attenuation variations to obtain enough sensitivity. For example, including a component of bone in the NESI analysis

during the full body imaging of an animal would eliminate the image contamination due to the presence of bone and provide an extra image of bone.

Last, the NESI system could be used both in a projection setup to get a 3D data cube of (x, y, E) and in a CT implementation to obtain a 4D data set of (x, y, E, θ) which can be converted to a 4D data set of (x, y, z, E) though conventional reconstruction algorithms. And both implementations would perform fast enough for imaging larger samples such as a small animal.

1.3 X-ray Fluorescence Imaging

1.3.1 XRF Imaging of Manganese

Mn is the 12th most abundant element in the earth's crust, the 4th most widely used metal in the world, following Fe, Al and Cu. Mn is mostly used to make stainless steel, batteries and aluminum alloys such as beverage cans. Mn is also found in coins, gasoline additives, paints, glasses, pesticides, fungicides, fertilizers and animal feeds.

Mn is an essential nutrient for all known living organisms. There are many proteins and enzymes containing Mn or having Mn cofactors, such as Mn-containing superoxide dismutase (Mn-SOD). The healthy level of Mn maintained by the human body is 10 mg, which is mainly stored in the liver and kidneys.

Mn deficiency is rare in humans and animals. But excessive exposure to Mn is toxic and will cause neurological disorders. Manganism is a neurodegenerative disease caused by Mn poisoning, mostly from occupational exposure to Mn dusts among welders and miners. It was reported that welding trades were routinely exposed to Mn levels above the previously proposed American Conference of Governmental Industrial Hygienists (ACGIH) threshold limit value (TLV) of 0.03 mg/m^3, and has sufficiently high probabilities to exceed the current ACGIH TLV

of 0.2 mg/m^3 [Wel04]. Later stages of manganism have symptoms of bradykinesia and rigidity which are similar to PD, and excess Mn accumulation was found in brains of manganism patients. Interest in the similarity between the symptoms of manganism and PD led to investigations into the regional accumulation of Mn in the human brain [Ola04, Gui10].

XRF imaging is an excellent technique for simultaneous in situ localization of metals in whole tissues. However the presence of scattered radiation and fluorescence from the adjacent element, Fe, that is present in high abundance [Pop09], may interfere with and limit the ability to detect ultra-dilute Mn. Fe also limits the *k* (photoelectron's wave vector) range for Mn EXAFS making it difficult to determine how Mn is chemically coordinated.

Traditional methods of XRF detection include the use of an X-ray filter and Soller slits [Sol24, Lyt75] which provides a large solid angle of photon acceptance, is cheap and easy to use but without energy-discriminating ability. Any fluorescence or scattered photon with energy lower than the filter's K-edge energy penetrating through the filter and Soller slits will be picked up by the detector along with some of the fluorescence and scattering from the filter and slits themselves. The penetration through the filter makes it even harder to detect the fluorescence from the ultra-dilute Mn due to filter absorption. Use of a solid state detector achieves good energy resolution, but suffers from limited count rate, cooling requirements and cost [Kar00].

A BLA-based XRF detection system could improve elemental specificity in XRF imaging and make long-range Mn EXAFS possible [Zho99]. Briefly, XRF from the sample passes through a BLA to reach an area detector behind. Normally the area detector is put close to the BLA to achieve a larger solid angle of photon acceptance with Soller slits in between to block the transmitted beams (Figure 1.2). Combining a BLA with an energy discriminating detector should improve the energy resolution to several *eV*. With an energy resolution of this

caliber, highly specific imaging of ultra-dilute elements should be possible and in addition to extend the k-range for Mn EXAFS.

The enabling technology for this project is the use of a bent Laue fluorescence detection system which uses a bent Si crystal to diffract the fluorescence X-rays from the specimen into a detector. Thus this device selects the X-ray energy by diffraction as opposed to the use of a solid state detector which selects energy by the amount of charge released by the incoming X-ray photon.

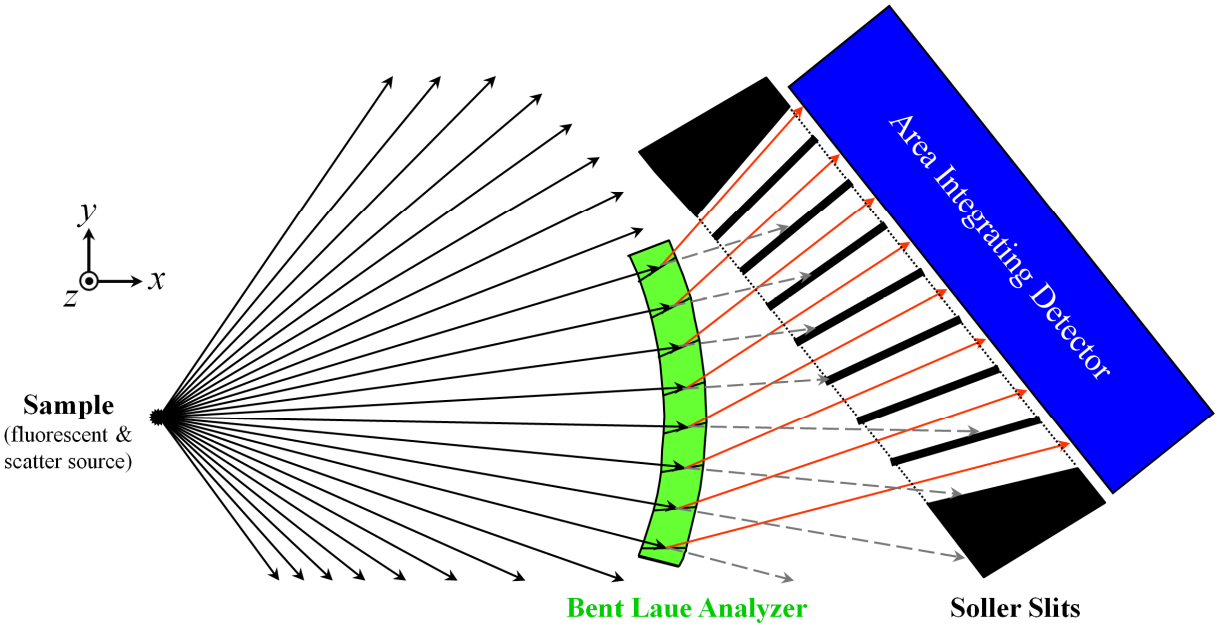

Figure 1.2 Schematic diagram of a bent Laue detector (image courtesy of Dr. Dean Chapman)

The advantage of this method of energy selection is that the energy resolution is quite good, typically from a few *eV* to 10s of *eV* depending on the design and energy. There is no pile-up or count rate limitation in the energy selection process. This is important in biological systems with dilute elements of interest at third generation synchrotron sources. It can significantly reject X-rays not coming from the focal region. The BLA could provide a large solid angle of photon acceptance into an area detector afterwards. And the cost is relatively low, around US$10,000 for

the total detection system. The disadvantages are that the system will only detect fluorescence of a single element or a short range of energy span, the system has to be carefully aligned, and it works most effectively when the beam size is small. For example, the XRF is accepted from a region of approximately 20 μm in the diffraction plane and approximate 3 mm in the transverse plane.

1.3.2 Confocal XRF Imaging

Confocal microscopy is a 3D imaging method originated from a patent of an optical microscope in 1957 [Min57]. Its optical sectioning is based on a point illumination through an objective lens and a pinhole before a detector to reject off-focus beams (Figure 1.3), which thus came the "confocal" term in its name. The illuminated point is actually a 3D volume with its depth proportional to the incident wavelength. Laser Scanning Confocal Microscopy (LSCM) or Confocal Laser Scanning Microscopy (CLSM) became a standard technique using a scanning laser for high resolution optical images since the late 1980s [Cre78, Paw06]. During the next decade, confocal fluorescence microscopy was developed for 3D detection of samples labeled with fluorescence markers using a confocal microscope combined with excitation and detection

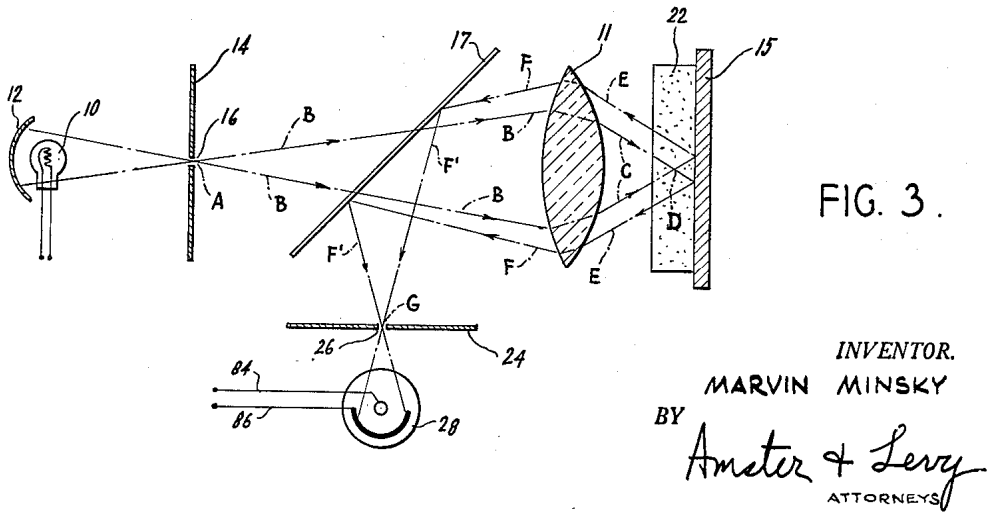

Figure 1.3 Principle of confocal microscopy (figure courtesy of Marvin Minsky [Min57])

filters to study the monochromatic fluorescence and phosphorescence [Spr08].

Switching gears from visible light and laser to the X-ray realm, confocal XRF spectroscopy is a 3D XRF imaging method using a confocal setup of X-ray focusing optics, normally one for the X-ray excitation of a sample, another for the X-ray detection before an area detector. The key point of this 3D XRF imaging is to form a 3D micro volume within the sample by superposition of foci among the X-ray focusing optics in both the excitation and detection channels. 3D raster scanning of the sample would simply produce 3D elemental mappings. Compared to XRF micro-tomography, confocal XRF imaging does not need a CT reconstruction algorithm and it provides direct investigation of the region of interest within the sample without the need to solve the whole sample as the first requirement. This particularly benefits the imaging of big animals without a wide enough beam to cover the full width of the sample to perform CT and it saves data storage as well. This imaging method was investigated in the past decade using either a tabletop X-ray tube or synchrotron radiation as its source and it provides a variety of applications in archaeology, materials science, environmental science and life science.

The common form of confocal XRF imaging uses two-dimensional (2D) focusing X-ray optics for both the excitation and detection channels, referred to here as “2D + 2D” focusing setup. The most popular confocal X-ray optic is a polycapillary lens [Russian patent Kum84] which is a bundle of hollow glass channels to bend grazing incident X-rays using total external reflection [Kum90]. As suggested by M.A. Kumakhov, this polychromatic X-ray focusing optic could be used in variety of combinations [Kum00]. Two polycapillary half or full lenses used in both the excitation and detection of a sample is the most common form of confocal setup (Figure 1.4A) for both the synchrotron source [Jan04, Zoe08] and the tabletop source [Lin08]. Even three polycapillary lenses were used to coincide with the foci to deliver double flux from two X-

ray tubes [Tsu07]. The polycapillary lens could also be used in the detection channel only while using other 2D X-ray focusing optics in the excitation channel for a variety of applications, such as monocapillary lens [Wol06], Kirkpatrick-Baez (KB) mirrors [Sun08] or compound refractive lenses (CRL) [Vin04]. Besides the polycapillary lens, what is also used in the detection channel is a polycapillary conic collimator (Poly-CCC) which is a conically shaped assembly of glass polycapillaries to direct X-rays emitted from a small region (Figure 1.4B) [Kan03].

Confocal full-field X-ray microscopy is another form of confocal XRF imaging by superposition of a sheet beam prepared by a one-dimensional (1D) focusing mirror and the object plane of a 2D X-ray focusing optics, such as a Fresnel zone plate [Tak10] or a Wolter mirror [Tak09], before an energy dispersive area detector (Figure 1.5). This form of confocal XRF imaging is referred to here as "1D + 2D" focusing setup. A Wolter mirror is a grazing incidence X-ray focusing optic based on total external reflection from the platinum-coated inner surface of a glass tube of axisymmetric hyperboloidal and ellipsoidal shape [Wol52].

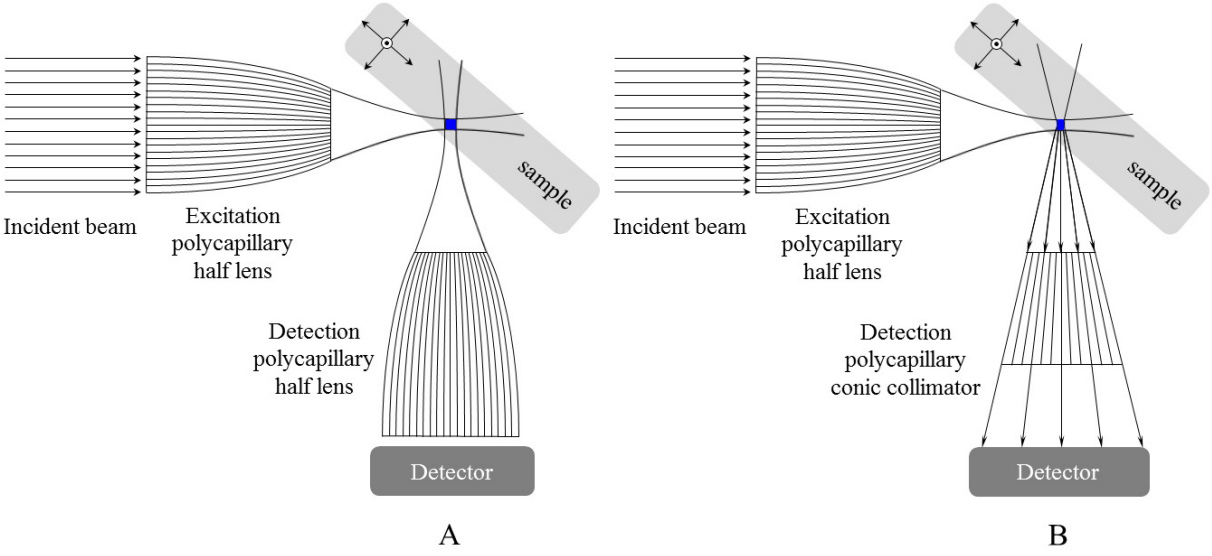

Figure 1.4 Principle of confocal XRF imaging in "2D + 2D" focusing setup. The sample could be excited and detected by two polycapillary half lenses (A) or excited by a polycapillary half lens while detected by a polycapillary conic collimator (B) (Adapted figure from [Mal05] under the reuse license in Appendix I.4). The blue region denotes the coincident micro-volume of the beam-excited double-cone region and the detectable double-cone region.

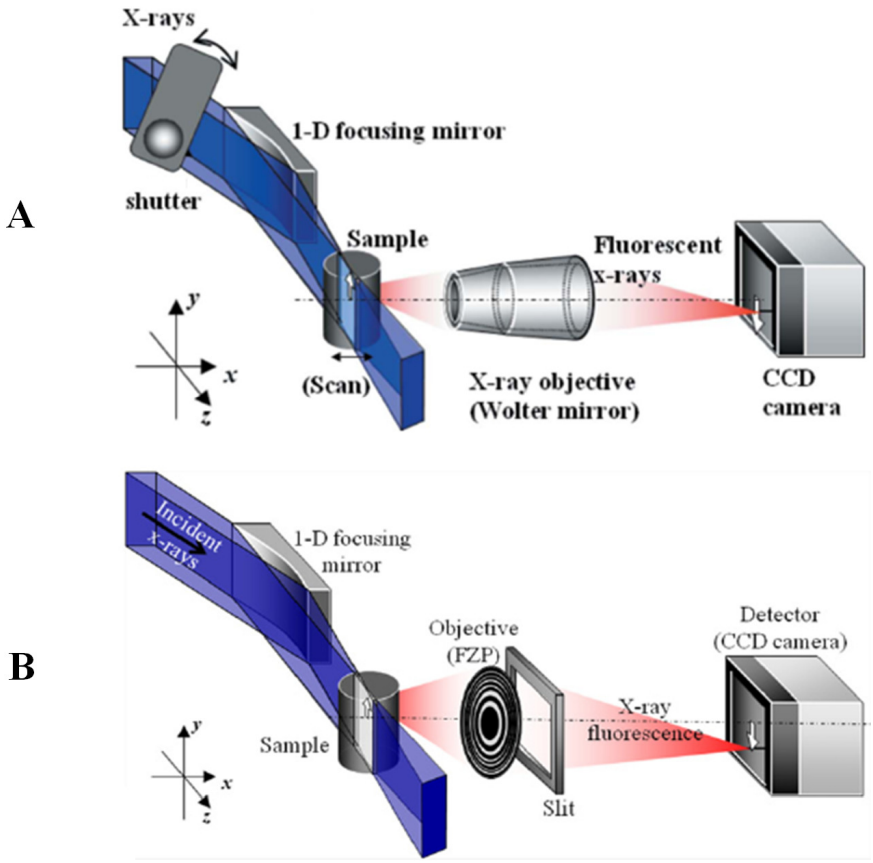

Figure 1.5 Principle of confocal full-field X-ray microscopy referred to here as "1D + 2D" focusing setup. The 2D focusing X-ray optics before the detector could be a Wolter mirror (A, figure courtesy of [Tak09] under the reuse license in Appendix I.5) or a Fresnel zone plate (B, figure courtesy of [Tak10] under the reuse license in Appendix I.7).

For the specific application of reaching a deeper region (tens of *mm*) within a soft material without thinking about self-absorption by the sample, two medical injection needles were used as collimators for both the excitation and detection channels of the confocal XRF setup for the study of Zn in oyster tissue [Tsu06]. This confocal XRF setup is limited to some invasive study of soft sample or hard surfaces in liquids.

1.3.3 BLA-based Confocal XRF Imaging

We propose a new method to perform 3D elemental mapping using a novel confocal XRF detection system (Figure 1.6). This detection system is based on the use of a BLA of a

logarithmic spiral shape which only diffracts photons of certain energy from a double-prism region with the center of the logarithmic spiral as its waist. Reversing the beam direction, the BLA could also be treated as a 1D focusing optic with its focusing axis along the vertical axis *y*. When the sample is irradiated by a 2D-focused beam or a pencil beam whose axis is coincident with the focusing axis of a BLA, only the signals from the 3D voxel within the sample could be captured by the detector. The 3D voxel, shown as a blue region in Figure 1.6, is the superposition of the irradiated cylinder (for pencil beam) or double-cone (for 2D focused beam) region and the BLA detectable double-prism region. This new BLA-based confocal XRF imaging is referred to here as the "2D + 1D" focusing setup to form a 3D voxel within a sample. This technique enables the X-ray sectioning and 3D mapping of XRF from a certain element within a sample by simple 3D raster scanning.

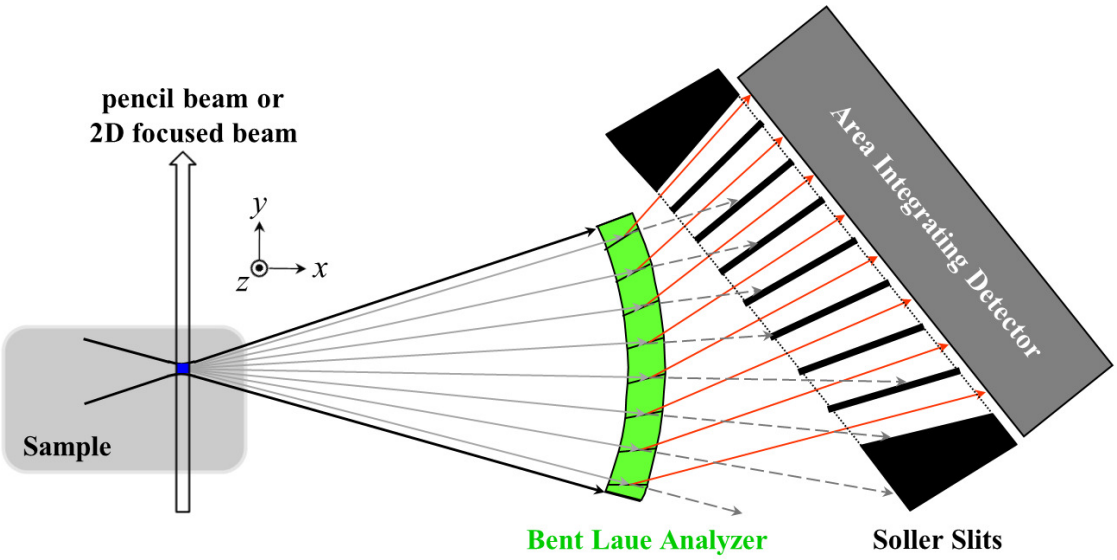

Figure 1.6 Principle of BLA-based confocal XRF imaging referred to here as "2D + 1D" focusing setup. The blue region denotes the coincident micro-volume of the beam-excited cylinder (for pencil beam) or double-cone (for 2D focused beam) region and the BLA-detectable double-prism region.

1.4 Animal Imaging Devices

Biomedical X-ray imaging applications sometime involve a live animal as the test object. These applications require considerable animal care, dose considerations and image quality improvements. Two types of animal imaging devices were designed for these purposes, small animal restraints for KES and XRF imaging and field flatteners for KES imaging applications.

1.4.1 Small Animal Restraints

Animal motion artifacts from movements are of primary concern in biomedical imaging and radiation therapy research. Animals under anesthesia continue to make breathing movements which are transmitted throughout the body. Thus a well-designed physical restraint for a live animal is of great importance to reduce image blur and improve image quality or the accuracy of radiation beam therapy.

Among the few reports describing animal head restraints, three types of immobilization methods are found: rigid mounting of the bone or skull through the skin [Wyr00], box or cylinder restraints that pin an animal by the auditory canal [Bid94, Bay77, Lah98] and plaster or resin molds taken directly from the animal [Fau75, How01]. These methods are either inhumane, introducing excessive stress on the animal, increasing morbidity and mortality, or complicated to follow and difficult to achieve an exact match between applications.

Rapid prototyping technology has been used previously to make radiotherapy facemasks for humans [San02] to replace traditional thermoplastic head immobilization devices [Pil95]. This technology provides a totally new method to fabricate small animal restraints which has not been found in previous publications.

1.4.2 Field Flatteners

Beamlines at synchrotron sources deliver huge photon fluxes that may overwhelm the capabilities of detectors to sense a weak signal in the presence of a tremendous background [Tho00, Lew03]. Signals of a few photons may represent important information and therefore the investigation of these weak features is one of the major goals of biomedical imaging. This is particularly true in KES imaging, where the photon flux received by the detector may come both through the object and around it without hitting anything. In KES imaging subtle differences in transmission through an object about the absorption edge of an element are used to create an image of the projected density of that element. This is done by a logarithmic subtraction of images acquired with energies above and below the absorption edge. Since the detector must register a broad dynamic range of transmitted intensity in a linear way for the logarithmic subtraction method to be successful, either the detector's dynamic range must be large or the range must be reduced to match available detectors. This need to limit dynamic range inspired the concept of a field flattener.

A field flattener is a device placed in the beam path that attenuates the input monochromatic beam before it passes through an object in order to equalize the flux across the field of view. It produces an image that contains a limited range of intensity variation, referred herein as a flattened image, with only those un-flattened features of interest left behind. The use of a field flattener reduces the dynamic range of flux received by the detector, allowing the user to employ the upper end of the detector linearity. Therefore the field flattener improves the SNR since X-ray exposures can be driven to or near detector overflow. This removes the need for a wide dynamic range linear detector and allows detectors with modest performance to be used successfully in KES applications. It helps to not only take full advantage of synchrotron fluxes and detector capacities, but also protect the detector in an easy way. However, a field flattener

removes anatomical information from each raw image (above or below K-edge image) that may provide useful landmarks.

In biomedical imaging, water is commonly used as a field flattener to simulate soft tissue, but it is a poor simulation for hard tissues and whole animals [Rig05]. Submerging a live anaesthetized animal in water creates practical and ethical problems. Not only must the animal be restrained while maintaining its air supply and body temperature but sensitive equipment must be protected from water leakage. The other concern is that the different path length of escaping fluorescence photons along various directions would impair the performance of fluorescence imaging when it was also performed at the same time with KES imaging. Rapid prototyping technology enables the manufacture of a field flattener that takes into account the X-ray absorption differences between soft tissue and bone, and in fact any tissue and their combinations found within an animal. Also, the field flattener fabricated by a rapid prototyper avoids the leakage and air bubble problems that may occur when water is used.

1.5 Innovations

Innovation sometimes happens while solving unexpected problems.

When the traditional KES imaging was performed on a live rat with injected iodine, we found a frequent artifact caused by small movements of the animal during the time taken to switch from an energy above to an energy below the iodine K-edge. To solve this problem, a humane rat head restraint was designed based on a CT scan of a rat and "printed" by a rapid prototyper. The second problem encountered was unwanted contrast arising from bone and other anatomy. To solve this problem the same CT scan data was used to design and "print" a brand new X-ray imaging product, a "field flattener", to use with the animal in the restraint to remove

the anatomy information while improving the sensitivity to iodine due to the "flattening" of the image intensity scale.

The third innovation was developed to solve a data analysis problem. During analysis for the BLA-based Mn XRF imaging, it was realized that the BLA is sensitive to the depth of the sample. A circular image pattern showed up for the concave surface of the gelatin sample which was prepared flat but melted a bit in the hot experimental hutch. A 3D confocal XRF imaging method was then conceived using a BLA.

The fourth innovation was the design of a three-beam chopper to fast switch among three beams for the three-energy KES imaging project. This project led to the first simultaneous iodine KES imaging and KES CT in Canada.

Interestingly, the final innovation was the spectrum-based NESI imaging method which abandoned the three-beam chopper but would not have happened without it. In theory this NESI is a general form of KES imaging and furthermore, it brings together contrast imaging and elemental speciation imaging through XANES and EXAFS analysis which have been totally different realms.

1.6 Outline and Contributions

This dissertation includes six Chapters and nine Appendixes. Following this introductory chapter, chapter two covers some X-ray diffraction basics and definitions as well as equations involved in the log-spiral bending and cylindrical bending of a Laue crystal.

Chapter three involves two parts, rat head restraints and field flatteners for the KES imaging projects which are published as;

Zhu, Y.; Zhang, H.; McCrea, R.; Bewer, B.; Wiebe, S.; Nichol, H.; Ryan, C.; Wysokinski, T.; Chapman, D., Fabrication of a small animal restraint for synchrotron biomedical imaging using a rapid prototyper, Nuclear Instruments and Methods in Physics Research, Section A: Accelerators, Spectrometers, Detectors and Associated Equipment, 582 (1) (2007) 229-32.

Zhu, Y.; Zhang, H.; Bewer, B.; Popescu, B.F.; Nichol, H.; Chapman, D., Field flatteners fabricated with a rapid prototyper for K-edge subtraction imaging of small animals, Nuclear Instruments and Methods in Physics Research, Section A: Accelerators, Spectrometers, Detectors and Associated Equipment, 588 (3) (2008) 442-7.

Chapter four includes the detailed description of two projects using a log-spiral BLA for XRF imaging, from Mn to iodine. The first experimental result of the Mn BLA project is published as;

Zhu, Y.; Bewer, B.; Zhang, H.; Nichol, H.; Thomlinson, B.; Chapman, D., Bent Laue X-ray Fluorescence Imaging of Manganese in Biological Tissues – Preliminary Results, 10th International Conference on Radiation Instrumentation (SRI 2009), Melbourne, Australia, American Institute of Physics Conference Proceedings, 1234 (2010) 457-60.

Chapter five introduces the traditional KES imaging and its image artifacts due to motion and the presence of bone that were the motivations for the three-energy KES imaging project. This chapter presents the theoretical equations for the projected density images and the signal-to-noise ratio (SNR), the optimization of the third imaging energy selection and, the BLM design, crystal preparations, experimental results and conclusions. The three-beam chopper design and three-beam height optimization process are presented as a section within this project. Chapter five ends with the NESI project that is an extension from the conventional KES and three-energy

KES. The NESI theory from two to three to an arbitrary number of components are presented with detailed derivations in Appendices A-H.

Chapter six concludes the dissertation and outlines further research for each project. Re-use licenses for the three published papers and four published figures are listed in Table I.1 and attached in Appendix I as required.

The cylindrical bending equations in Chapter 2.3 and the BLM design in Chapter 5.2.2.2 were based on the thesis work of a previous student Honglin Zhang with full credit [Zha09].

Chapter 2 X-Ray Diffraction by Bent Laue Crystals

2.1 X-ray Diffraction Basics

X-ray diffraction follows either kinematical diffraction theory or dynamical diffraction theory [Zac45, Als01]. The kinematical diffraction theory studies the scattering from imperfect crystals such as a mosaic of small perfect crystals, quasicrystals or incommensurated crystals (depending on whether they have averaged periodicity or not) and neglects the multiple scattering effects. The kinematical diffraction intensity increases with the crystal volume until the beam reaches the limit of the extinction depth and enters the dynamical diffraction domain. The dynamical diffraction theory studies the X-ray diffraction from the perfect crystals which have long range periodic order at the atomic level and takes into account the refraction and multiple scattering effects. The bent Si crystals described in the dissertation are essentially free of defects and dislocations and fall into the dynamical diffraction theory, whereas the diffraction by a strongly bent crystal may behave according to the kinematical diffraction theory.

X-ray diffraction from a crystal may occur either in a reflection mode (Bragg case) or a transmission mode (Laue case) both of which follow the Bragg's law of

$$\lambda = 2d \sin\theta \tag{2.1}$$

where λ is the wavelength of incident beam, d is the spacing of Bragg planes and θ is the incident angle to the Bragg planes. The term "Darwin width" in the dissertation refers to the angular width of the crystal's reflectivity curve. While the Bragg diffraction has a flat top of total

reflection and wide Darwin width [Als01], the Laue diffraction has a sharp reflectivity peak and narrow Darwin width [Ren97].

Symmetric diffraction occurs when the Bragg plane is parallel (Bragg case) or perpendicular (Laue case) to the surface plane. In the asymmetric diffraction cases, an asymmetry angle χ is defined as the angle between the Bragg plane and surface plane (Bragg case) or surface normal (Laue case). While the Darwin width is normally in μrad and energy bandwidth in 10^{-5} for flat crystal diffraction, bent crystal diffraction would achieve a *mrad* reflectivity bandwidth, big solid angle of detection, 10^{-3} energy bandwidth and an order of magnitude higher integrated reflectivity. Besides the widening effect, the bent crystal diffraction acquires a flat top reflectivity curve which is a great benefit to system stability and alignment [Ren97].

The reflectivity of a bent crystal is estimated based on the lamellae model [Ero90, Boe78] first developed by White [Whi50] leading to a computer model, REFLECT program [Ete89]. The lamellae model assumes a bent crystal as a stack of flat perfect lamellae with gradually changing tilt angle to account for the curvature of the crystal. The lamellae thickness is set such that the tilt angle between successive lamellae is equal to a Darwin width of the reflection. Since the strong reflection only happens within the angular range of a Darwin width, only a few lamellae are involved in diffraction with a parallel incident monochromatic beam (plane wave). The diffracting lamellae sweep through the crystal thickness as the incident beam direction changes in relation to the crystal. Based on dynamical diffraction theory, the reflection and transmission are calculated for each lamella and summed for the total reflectivity. The reflectivity width of a bent crystal is set by the acceptance angle which is the Bragg angle change as the beam goes through the bent crystal [Ero90, Suo93],

$$\Delta\theta = \frac{t}{r}[(\tan(\chi \pm \theta_B) + \frac{(1+\upsilon)}{2}\sin 2\chi \mp \tan\theta_B(\cos^2\chi - \upsilon\sin^2\chi)] \qquad (2.2)$$

where t is the crystal thickness, r is the bending radius, θ_B is the Bragg angle and ν is the Poisson ratio [Bra73]. It is found that $\Delta\theta = 0$ for a symmetric bent crystal when setting $\chi = 0$ in equation (2.2). This indicates that the bent symmetric crystal behaves like a flat crystal and the broadening of the Darwin width occurs only when an asymmetric crystal is bent [Ren97]. The X-ray diffraction described in the dissertation is through the use of asymmetric bent Laue crystals. The differential version of the Bragg's Law in equation (2.1) is used to estimate the energy bandwidth of an asymmetric bent Laue crystal as

$$\frac{\Delta E}{E} = \frac{\Delta\theta}{\tan\theta_B} = \frac{1}{\tan\theta_B}\frac{t}{r}[(\tan(\chi \pm \theta_B) + \frac{(1+\upsilon)}{2}\sin 2\chi \mp \tan\theta_B(\cos^2\chi - \upsilon\sin^2\chi)] \qquad (2.3)$$

There are two bending geometries of a Laue crystal from a point source. In the Cauchois geometry [Cau32] (Figure 2.1A), the point source is located at the concave side of a bent Laue

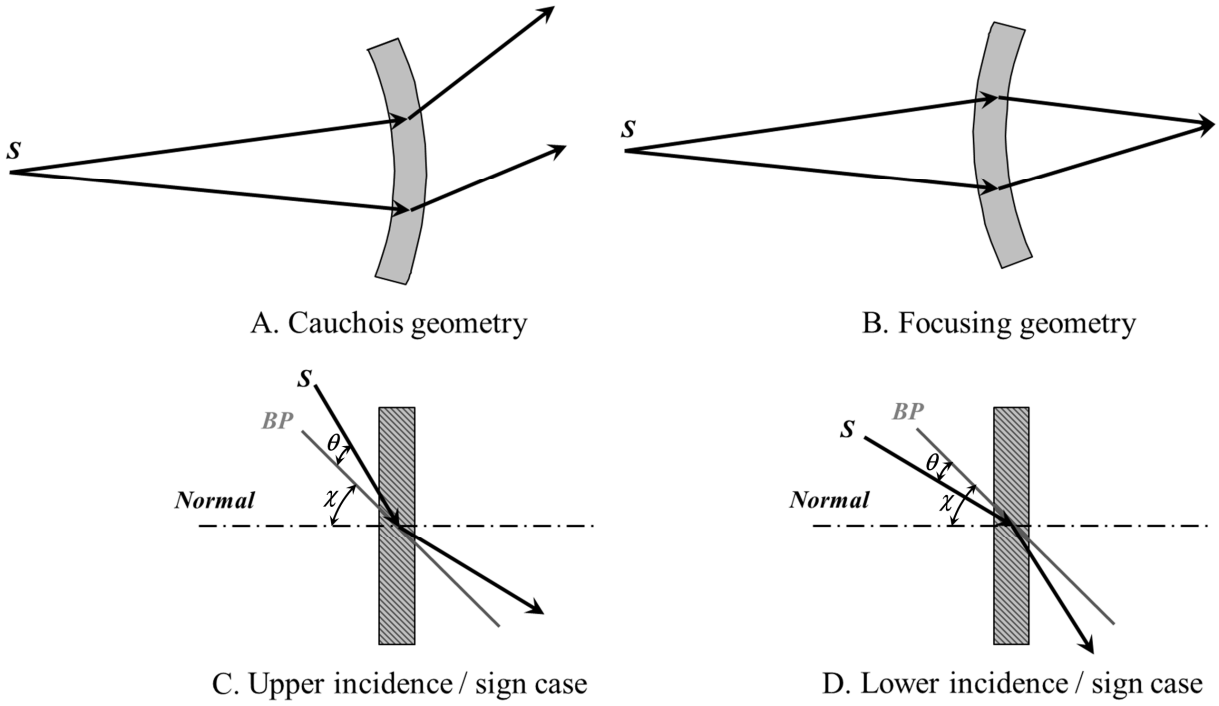

Figure 2.1 Definition of bent Laue Geometries

crystal while it is at the convex side in the focusing geometry (Figure 2.1B). There are two incident geometries in the Laue case which contribute to the upper and lower signs in the equations within this chapter including the equations (2.2) and (2.3). The incident beam direction locates between the Bragg planes *BP* and surface normal in the lower incidence / sign case (Figure 2.1D) while it locates outside of the *BP* and surface normal in the upper incidence / sign case (Figure 2.1C).

Two types of asymmetric bent Laue crystals were prepared for totally different applications. One is a log-spirally bent crystal in the Cauchois geometry as a BLA for XRF detection and confocal XRF imaging. Both the upper and lower incidences were designed for this application. Another is a cylindrically bent crystal in the focusing geometry as a BLM for the KES and NESI imaging with only the upper incidence designed.

2.2 Log-Spiral Bending of a Laue Crystal

The Bragg's law in equation (2.1) tells us that for a monochromatic energy to be diffracted, the polychromatic beam has to be incident onto the crystal at the same Bragg angle. For a parallel incident beam, a flat crystal at a correct tilt angle would satisfy the Bragg condition everywhere. For a monochromatic beam from a point source to satisfy the Bragg condition, that is to be incident onto a crystal at the same Bragg angle everywhere, the crystal has to be bent along a logarithmic spiral shape [DeB14, Sak82].

As shown in Figure 2.2, the Rowland circle has a diameter of r and centers at the mid-point of r [Row83]. The source point S, the virtual focal point F and the center of bending radius R always land on a Rowland circle with the source-to-crystal distance s, focal length f and bending radius r having the Rowland conditions of

$$s = r\cos(\chi \pm \theta_B)$$
$$f = r\cos(\chi \mp \theta_B) \tag{2.4}$$

Detailed derivations of the sign case in the above equation are shown in Figure 2.3.

For a $\Delta\phi$ increase of coronal opening angle in Figure 2.3, the Δs increase of the source-to-crystal distance s_0 has the relation of

$$\Delta s = s_0 \Delta\phi \tan(\chi \pm \theta_B) \tag{2.5}$$

Integration of the equation (2.5) would derive the required shape of the bent crystal as

$$s(\phi) = s_0 e^{tg(\chi \pm \theta_B)\phi} \tag{2.6}$$

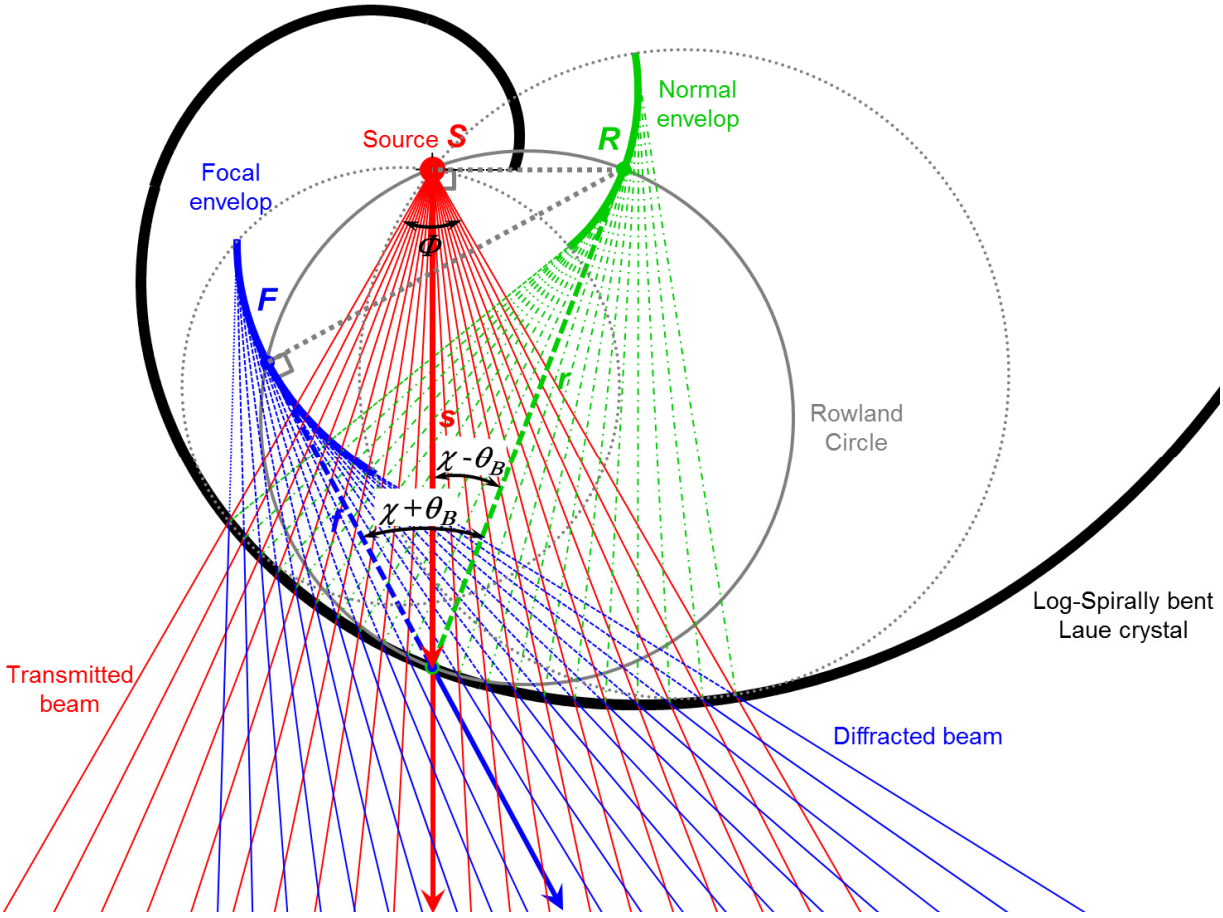

Figure 2.2 Geometry of a log-spirally bent Laue crystal (black) in lower case with relationship to the incident (red), transmitted (red) and diffracted (blue) beams. The source *S* (red), virtual focal point *F* (blue) and bending radius center *R* (green) all land on a Rowland circle (grey).

that is apparently a logarithmic spiral shape expressed in polar coordinates (s, ϕ). Combining with equation (2.4), the envelops of the bending radius center R and the virtual focal point F are also a similar segment of logarithmic spiral curve as shown in Figure 2.2,

$$r(\phi) = r_0 e^{tg(\chi \pm \theta_B)\phi}$$
$$f(\phi) = f_0 e^{tg(\chi \pm \theta_B)\phi} \tag{2.7}$$

Similarly, from $\Delta s = \Delta l \sin(\chi \pm \theta_B)$ the active arc length of the bent Laue crystal is calculated by

$$l = \frac{s}{\sin(\chi \pm \theta_B)} = \frac{s_0}{\sin(\chi \pm \theta_B)} e^{tg(\chi \pm \theta_B)\phi}\Big|_{-\phi}^{\phi} \tag{2.8}$$

As the incident angle can vary by an acceptance angle $\Delta\theta$ that is defined in Equation (2.2), this leads to a transversal opening angle Ψ and transversal active width of the crystal w that are calculated (Figure 2.4A) as

$$\Psi = 2\cos^{-1}\left(\cos\Delta\theta - ctg\,\theta_B \sin\Delta\theta\right) \approx 2\sqrt{2ctg\,\theta_B \Delta\theta} = 2\sqrt{2\frac{\Delta E}{E}}$$
$$w = s\Psi \approx 2s\sqrt{2\frac{\Delta E}{E}} \tag{2.9}$$

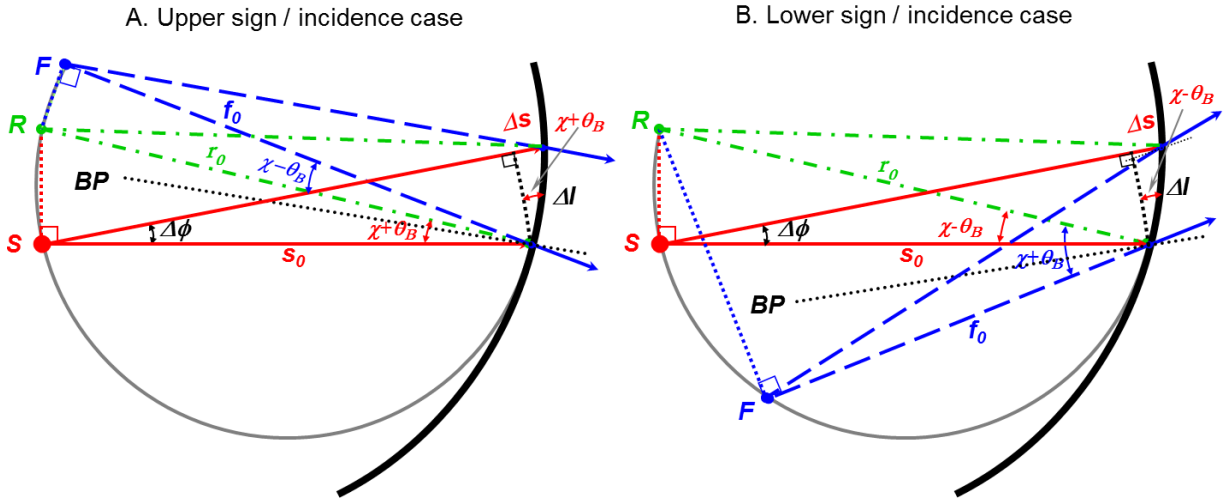

Figure 2.3 The upper (A) and lower (B) sign / incidence cases for a BLA (black curve). Source S, focal point F, normal center R, Bragg planes BP, source to crystal distance s, virtual focal length f, bending radius r, Bragg angle θ_B, asymmetry angle χ and crystal active arc length l.

So both the transversal opening angle Ψ and the transversal active width w are proportional to the square root of the energy bandwidth. As seen from the Figure 2.4B and C, both the vertical size Δv and transversal size Δh of the detectable region of the source S are determined by the acceptance angle $\Delta\theta$ as

$$\Delta v = s\Delta\theta$$
$$\Delta h = w \approx 2s\sqrt{2\frac{\Delta E}{E}} \tag{2.10}$$

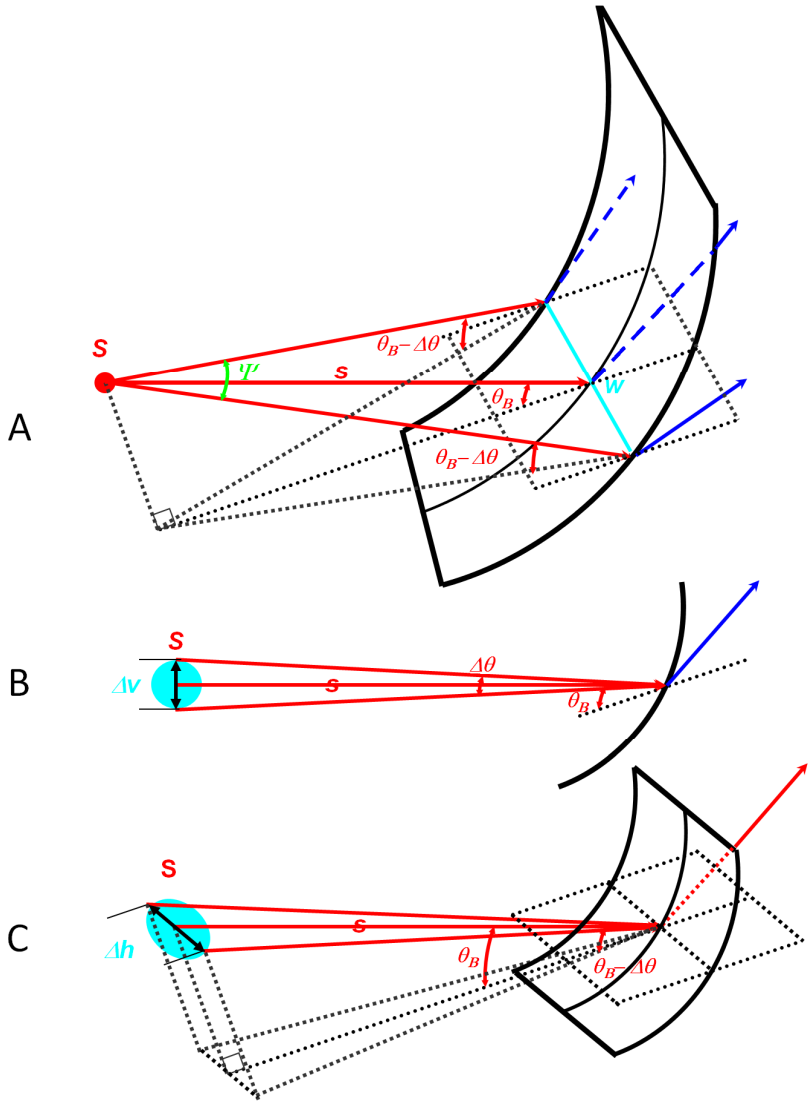

Figure 2.4 The derivation geometries for the transversal opening angle Ψ (A), vertical size Δv (B) and transversal size Δh (C) of the detectable region in the source S.

Because of the one-dimensional (1D) focusing geometry, the typical vertical size of the detectable region is in microns and the typical transversal size of the detectable region is in millimeters.

The solid angle of a bent crystal with coronal opening angle Φ and transversal opening angle Ψ can be approximated as

$$\Omega = 4\sin^{-1}(\sin\frac{\Phi}{2}\sin\frac{\Psi}{2}) \tag{2.11}$$

2.3 Cylindrical Bending of a Laue Crystal

In the focusing geometry (Figure 2.5A), a cylindrically bent Laue crystal with a certain bending radius r could achieve a geometrical focus F_G at the geometrical focal length f_2 that has a relation with the source-to-crystal distance f_1 as [Suo93]

$$\frac{\cos(\chi \mp \theta_B)}{f_2} - \frac{\cos(\chi \pm \theta_B)}{f_1} = \frac{2}{r} \tag{2.12}$$

A single polychromatic ray incident to a Laue crystal will experience a spatial broadening of the reflected beam due to the reflection from each layer along the incident beam direction within the crystal. When the Laue crystal is bent (Figure 2.5B), this single ray broadening will have a real focus F_S in the upper incident geometry with the single ray focal length L calculated as [Zha09]

$$L = \frac{t\sin 2\theta_B}{2\Delta\theta_L \cos(\chi \pm \theta_B)} \tag{2.13}$$

where t is the crystal thickness, $\Delta\theta_L$ is the angular difference of the lattice planes at the incident and exit point of one single ray with calculations referred to Honglin Zhang's dissertation [Zha09]. While there are other similar approaches to achieve source size limited focusing [Suo93, Sch97], the approach by Zhang was used in this dissertation.

As shown in Figure 2.5C, sub-micron focus size could be achieved when the "magic" condition of $f_2 = L$ is met and the geometrical focus F_G is coincident with the single ray focus F_S. Please refer to Honglin Zhang's dissertation [Zha09] for further information.

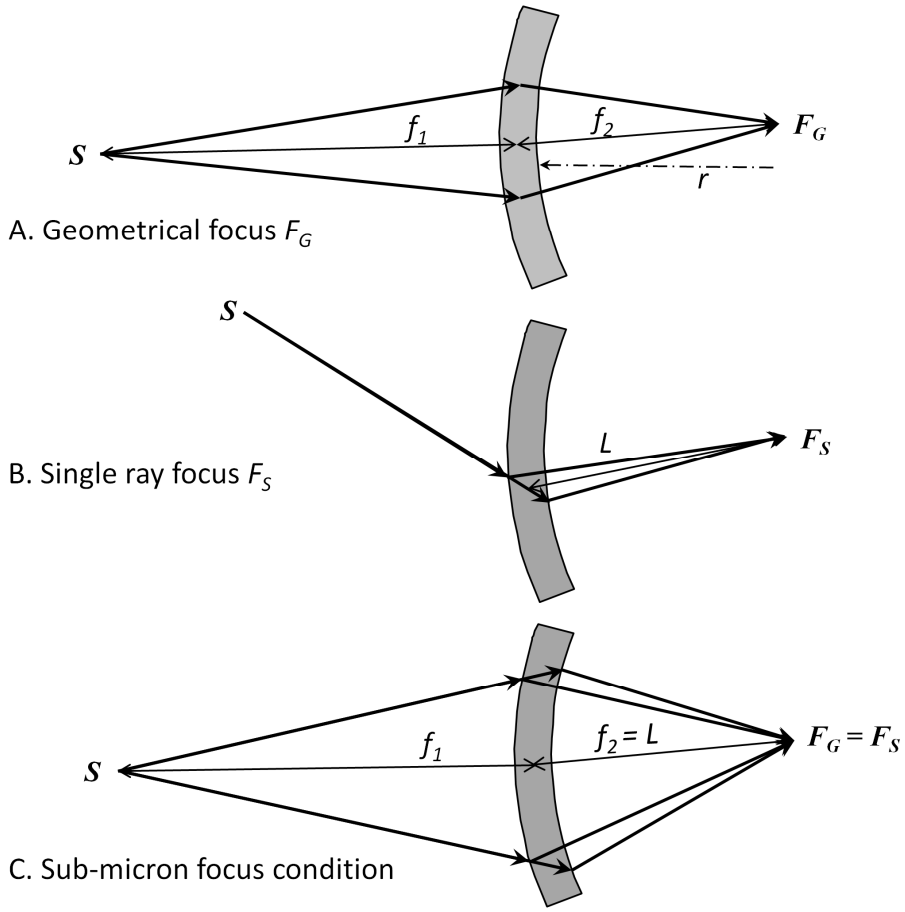

Figure 2.5 The geometrical focus F_G (A), single ray focus F_S (B) and the sub-micron focus condition (C) for a BLM with bending radius r, source-to-crystal distance f_1, geometrical focal length f_2 and single ray focal length L.

Chapter 3 Animal Imaging Devices

For biomedical X-ray imaging applications involving live animals, two types of animal imaging devices are designed considering animal care, dose reduction and image quality improvements. With the widespread use of rapid prototyping technology, many biomedical models [Tie06, Irs06] which were difficult to manufacture can now be finely fabricated to any customized sophisticated shape. This chapter describes novel small animal restraints and field flatteners for KES imaging applications fabricated by this simple, fast and cost effective rapid prototyping technology. The use of such systems holds great promise for improving the quality and repeatability of X-ray images of live animals.

3.1 Rat Head Restraints for Biomedical Applications

Biomedical research at synchrotron facilities may involve imaging or radiation therapy of live animals. The live animals are required to remain motionless for extended periods of time to obtain quality images or expected therapy results. Even breathing movements reduce image quality or therapy accuracy. But on the other hand excessive restraint of animals increases morbidity and mortality. This chapter describes humane animal restraints designed to eliminate head movements while promoting animal survival.

3.1.1 Materials and Methods

3.1.1.1 Medical CT

Two euthanized rats of 420 *g* and 486 *g* were imaged in a standard medical CT (GE LightSpeed Ultra 8slice) at the Royal University Hospital in Saskatoon. The rats were spirally

scanned from head to tail with an X-ray tube voltage of 120 *kVp*, a current of 100 *mA* for the first rat and 130 *mA* for the second rat, an axial slice thickness of 0.625 *mm*, a transverse plane pixel spacing of 0.467 *mm* for the first rat and 0.352 *mm* for the second rat. The CT image data was in the Digital Imaging and Communications in Medicine (DICOM) format (Figure 3.1). A total of 102 slices from the nose to the near shoulder of each rat were chosen to form the head restraint.

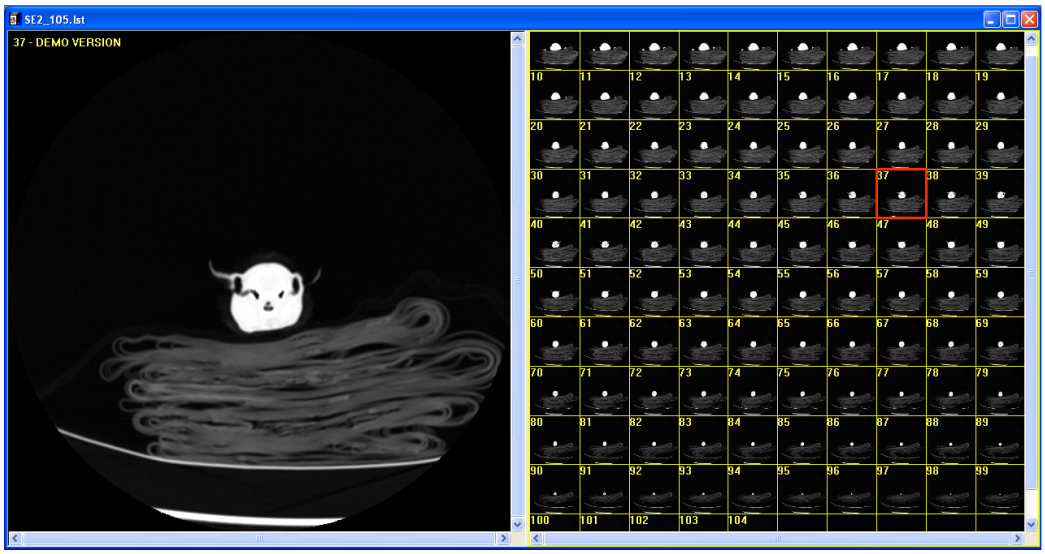

Figure 3.1 DICOM images of the first rat on a CT bench with cloth padding

3.1.1.2 Image Editing

The Interactive Data Language (IDL) (from ITT Visual Information Solutions, Boulder, Colorado, USA) DICOM Toolkit was used to provide full access to DICOM images. A common polygonal region of interest for all slices was selected to remove unwanted structures in the images such as cloth padding and the support table. Surface contours were defined using an appropriate gray-scale threshold that reflects the radio-opacity level of the skin instead of fur. The contour representing the outer skin, which is always the largest contour in the region of interest, was selected to form the inner shell of the restraint. Small contours inside and outside this main contour were discarded to eliminate unwanted features. A convolution function was

used to expand the solid image within this contour by 3 *mm*. The original solid image was subtracted from the expanded one to make a shell that conforms to the shape of the rat's head.

Other simple attachments, such as a support frame and labels, were designed in the images. An appropriate rotation and reposition of the image corresponding to the support frame were applied to all the DICOM slices (Figure 3.2). The images for the second rat restraint were edited to enlarge its nose hole for better respiration and its ear holes for easier loading an animal into the restraint and stretching its ears out.

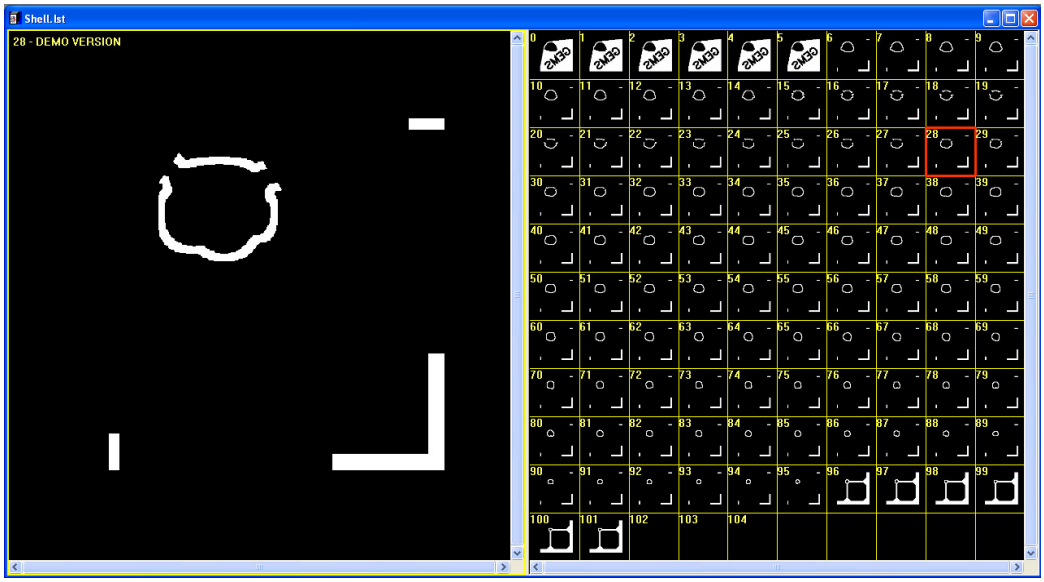

Figure 3.2 DICOM images of the head restraint for the second rat

3.1.1.3 Conversion and Fabrication

DICOM images of the two restraints were converted into Standard Tessellation Language (STL) format with either "accurate" or "smooth" setting using the freeware JuliusLight (from Julius Software Framework, Research Center, Caesar, Bonn, Germany). For comparison, both settings were tried out. The smooth setting was used in the head restraint for the first rat and the accurate setting was used in that for the second rat.

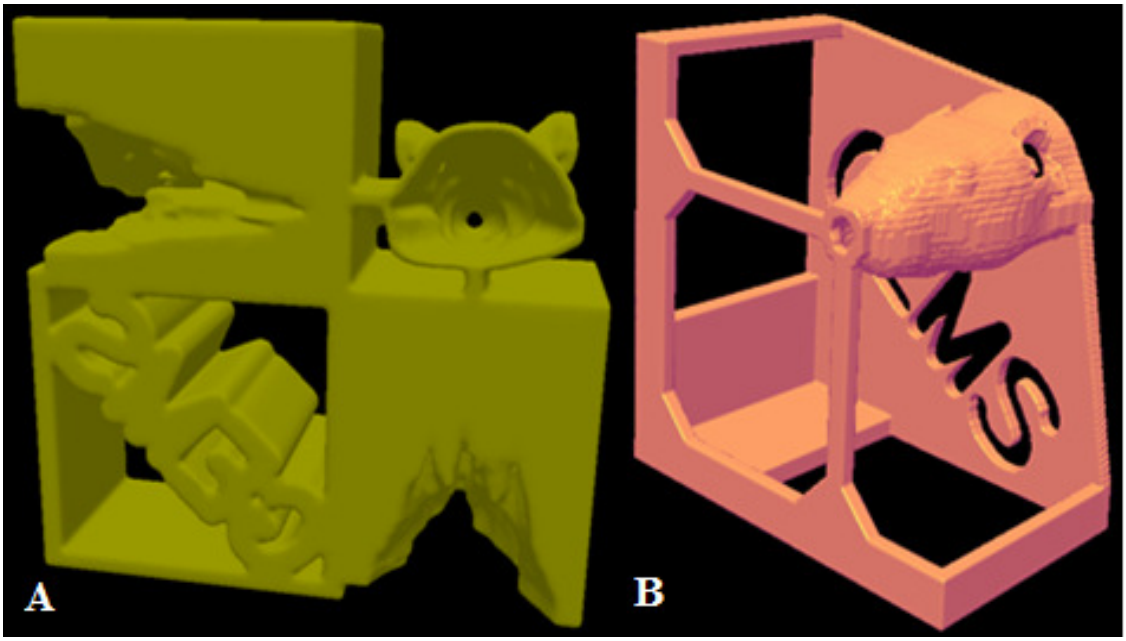

Figure 3.3 STL files of the head restraints for the first rat (A) and the second rat (B)

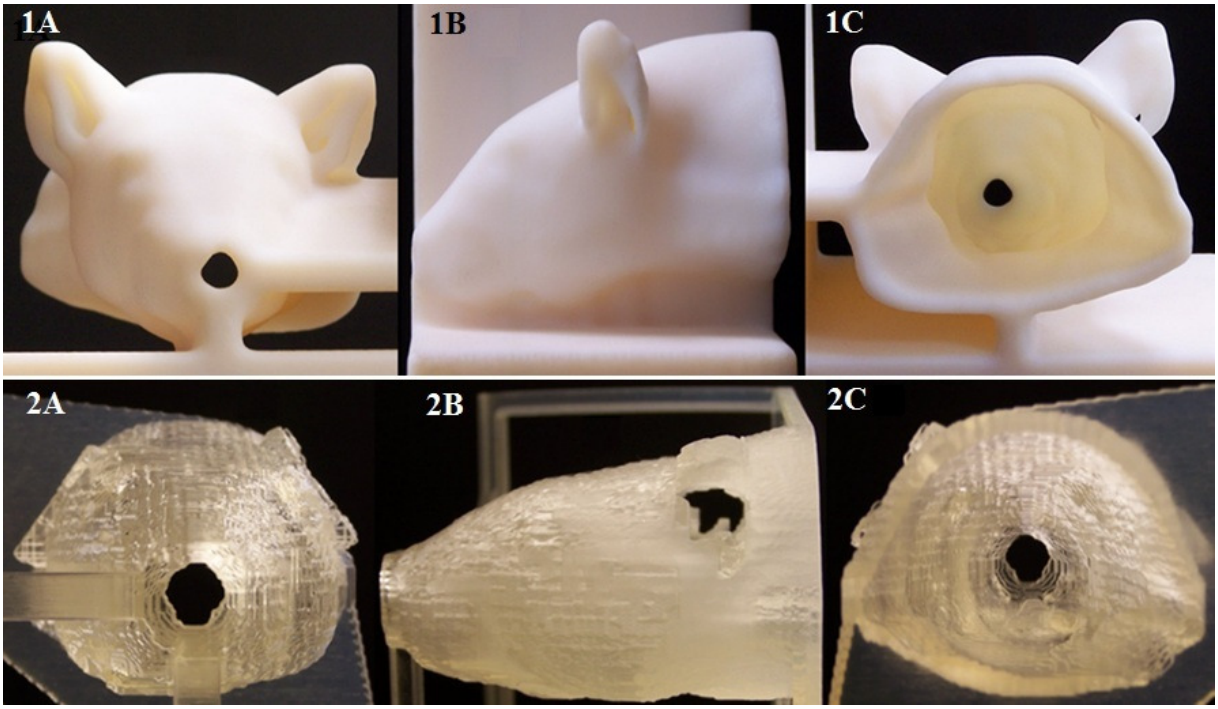

Figure 3.4 Two head restraints: one for the first rat (420 *g*) using smooth setting and VeroWhite® material viewed from front (1A), side (1B) and back (1C) respectively, another for the second rat (486 *g*) with enlarged nose hole and chopped ear holes using accurate setting and FullCure®720 material viewed from front (2A), side (2B) and back (2C) respectively.

The STL files which describe the triangular surface geometry of 3D objects were directly imported into a rapid prototyper to fabricate 3D models (Figure 3.3). The Eden500V™ (Objet Geometries Ltd., Billerica, Massachusetts, USA) at the Engineering Machine Shop of the U of S was used to fabricate the two restraints with a print resolution of 42 μm in the *X* and *Y* axis and 16 μm in the *Z* axis. VeroWhite® is an acrylic-based photopolymer material of opaque white used for the fabrication of the first restraint (Figure 3.4 1A-1C) and FullCure®720 is a transparent one used for the second restraint (Figure 3.4 2A-2C).

3.1.2 Experiments

A separate body bed was constructed from Lucite and lined with padding to keep the animal warm (Figure 3.5). Velcro straps prevented the body from sliding backwards. Both the head restraint and the body bed snapped into a fitted tray. The anesthetized rat was lowered head first into the head restraint to ensure that its nose was unobstructed and then the body was

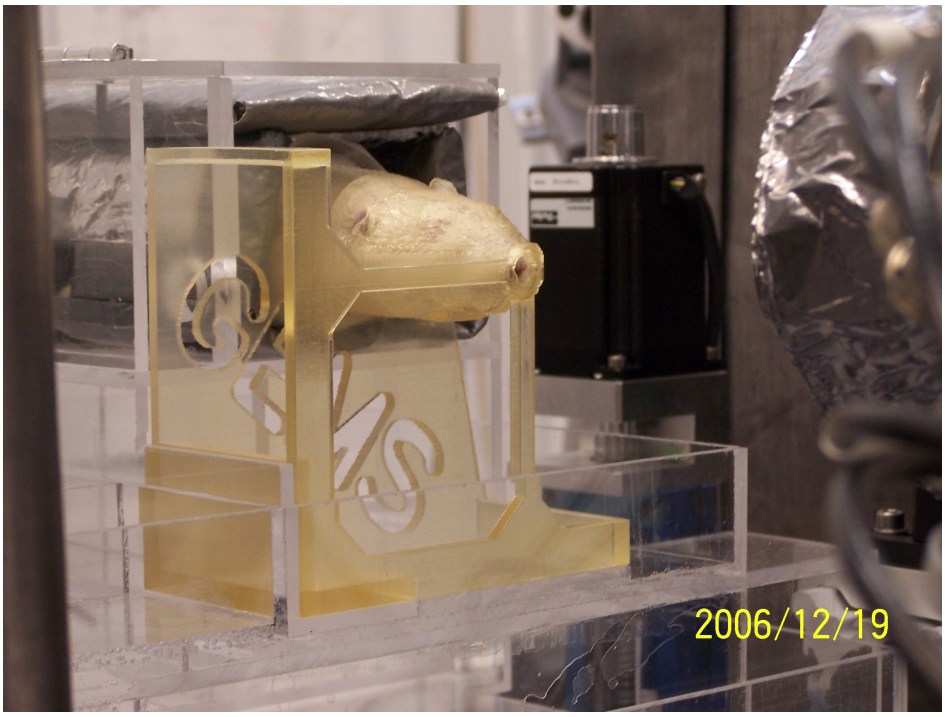

Figure 3.5 The head restraint for the second rat with padded body bed was used in the KES experiment at HXMA beamline at CLS

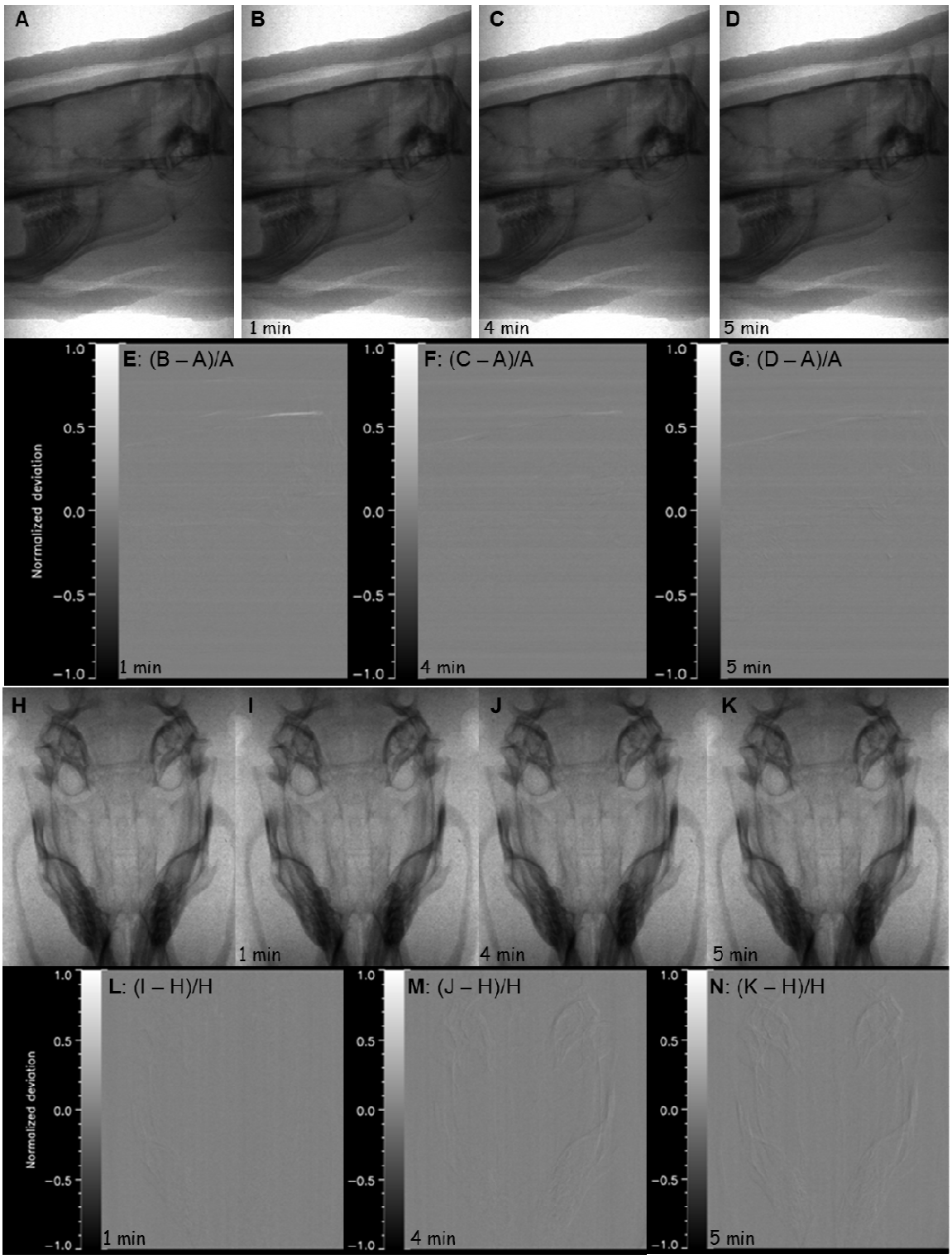

Figure 3.6 Motion artifacts of a rat in the restraint. Top row are images in lateral view taken at above iodine K-edge, the third row is DV view at below iodine K-edge. Subsequent images B-D or I-K were taken at 1, 4 and 5 min after the initial image A or H, respectively. The second and the bottom rows are normalized subtracted images E-G and L-N for 1, 4 and 5 min respectively.

secured into the bed. The two head restraints could be turned 90° standing on the tray, providing images of a rat in both a lateral view and dorsal-ventral (DV) view.

The restraints were first used during KES imaging experiments at the HXMA beamline at the CLS in Dec 2006 (Figure. 3.5). The energy of the monochromatic beam was sequentially switched between 100 *eV* above and below the iodine K-edge energy at 33.17 *keV* by a double crystal monochromator. The beam size was 0.25 *mm* vertical height by 28 *mm* horizontal width. KES images were taken with an X-ray camera (Photonic Science X-ray FDI VHR 90 *mm*, Photonic Science Ltd., UK, 18.7 μm^2 pixel size, 10 *ms* exposure) in line scan mode at 2 *mm/s* vertical scan velocity.

To test for motion artifact, image sets of an anesthetized rat in the second restraint were taken in lateral or DV views with energy above or below the iodine K-edge. The initial images were subtracted from the subsequent images taken at 1, 4 and 5 minutes later respectively to check for motion artifact (Figure 3.6). While blurring of the baseline images were visually estimated as the motion artifact during image acquisition, the subtracted images were evaluated for the motion artifact between image samplings.

3.1.3 Results

There was no obvious indication of motion artifacts during each image acquisition (about 1 minute) (Figure 3.6A-D, H-K). There was little fluctuation of signal intensity indicating little movement between the sampling periods (Figure 3.6E-G, L-N). Average deviations in the normalized subtracted images shown in the Figure 3.6 were listed in the Table 3.1. Average deviations in all the data collected were in the range of 2.6% - 3.5% for various experimental settings including above and below the iodine K-edge in both lateral and DV views.

Table 3.1 Average deviations in the normalized subtracted images in Figure 3.6

average deviation	*1 min later*	*4 min later*	*5 min later*
lateral view images	2.7%	2.7%	2.8%
DV view images	2.9%	3.0%	3.1%

3.1.4 Conclusions and Discussions

For the KES imaging experiments, the rats were treated under Animal Care protocol #20040125 approved by University Committee on Animal Care and Supply (UCACS). The fabrication and the usage of the animal restraints require neither incision by operation nor trauma from auditory pins compared with the conventional animal restraints mentioned before. Throughout the experiment neither death nor signs of respiratory distress or any other discomfort has been found in animals in these restraints.

Rapid prototyping is a simple, fast and relatively inexpensive method to fabricate humane, custom animal restraints. This type of animal restraint worked well to immobilize the animal and holds great promise for improving the quality and repeatability of images while reducing stress on experimental animals. Besides KES, the thin shell restraint with uniform thickness also worked well in XRF imaging measurements [Zha08].

One drawback is that the restraint should roughly match the size of the animal to be imaged. Immobilization may be compromised if the animal is too large or small for the restraint. The “smooth” conversion from DICOM to STL, averaging slightly displaced DICOM images to get a blurred density image, or using elastic rapid-prototyping material to print would help to make restraints more generic, but this needs further investigation.

It should be mentioned that all the data presented here were based on the use of the second restraint. The reason is that the second restraint was a standalone restraint while the first one was attached with its matching field flatteners [Zhu08] and was not designed for measurements of motion artifacts.

3.2 Field Flatteners for K-Edge Subtraction Imaging

One of the difficulties in X-ray imaging is the need to record a wide dynamic range of intensities on the detector. For example, some rays may miss the object being imaged entirely while others may suffer many orders of magnitude attenuation in passing through. The range of intensities which may strike the detector has inspired the concept of a field flattener. A field flattener is a device placed upstream of an object that reduce the average dose onto the object, equalize the flux across the field of view and improve the image quality. Using rapid prototyping technology, two sets of field flatteners were fabricated and used in a KES imaging experiment.

3.2.1 Materials and Methods

Projected density images were used to determine a field flattener's thickness for a specific projection of an animal. First, a test object or phantom was CT imaged to determine the equivalent photon energy and scaling factor of the CT system which allowed CT images of an animal to be converted into projected density images. Second, the animal images were segmented into bone and soft tissue components. Third, using tabulated attenuation coefficients for bone, soft tissue and plastic, a spatial distribution of the equivalent plastic thickness for each slice was calculated at the mean energy of KES imaging and finally imported into a rapid prototyper to build the field flatteners.

3.2.1.1 Medical CT

Two euthanized rats were imaged in a standard medical CT as described in chapter 3.1.1.1. The same 102 slices for the first head restraint were used to form its matching field flatteners, while 90 slices in the imaging field of view were used to form the matching field flatteners for the second set [Zhu07].

3.2.1.2 CT Calibration

A phantom was imaged in the X-ray CT along with a rat to determine the equivalent photon energy, E_{CT}, of CT images as well as a scaling factor, γ, between image values and the actual absorption of the phantom. The phantom was composed of plastic and water to simulate soft tissue and a calcium chloride ($CaCl_2$) solution to simulate bone (Figure 3.7).

CT images provide a series of planar images of the scaled X-ray absorption which are proportional to the density of the tissue being imaged. Specifically, the CT number in the CT image of the water, N_W (W for water), determines the scaling factor $\gamma$by

Figure 3.7 An image of a phantom scanned at the same time with the first rat for CT image calibration. The phantom is made of a plastic tube of distilled water placed in another plastic tube of calcium chloride ($CaCl_2$) solution.

$$N_W = \gamma \frac{\mu}{\rho}_W (E_{CT}) \rho_W t_W \tag{3.1}$$

where N_W is the Hounsfield number plus 1000, so that a value of zero corresponds to air. $\frac{\mu}{\rho}(E_{CT})$ is the mass absorption coefficient at the equivalent photon energy E_{CT}, ρ is the density and t is its thickness in the image. Accordingly, the CT number in the CT image of the $CaCl_2$ solution, N_{BS} (*BS* for $CaCl_2$ solution resembling the bone), is

$$N_{BS} = \gamma \frac{\mu}{\rho_{BS}} (E_{CT}) \rho_{BS} t_{BS} \tag{3.2}$$

where N_{BS} is the Hounsfield number plus 1000. Combining the equations (3.1) and (3.2) leads to a ratio which uniquely determines the equivalent photon energy E_{CT} using

$$\frac{\frac{\mu}{\rho}_{BS} (E_{CT})}{\frac{\mu}{\rho}_W (E_{CT})} = \frac{N_{BS} \rho_W t_W}{N_W \rho_{BS} t_{BS}} \tag{3.3}$$

The equivalent photon energy of 69.13 *KeV* and the scaling factors for the CT of two rats were determined using IDL DICOM Toolkit.

3.2.1.3 Segmentation and Projection

After CT image calibration, animal images were analyzed. The rat head was assumed to be composed of soft tissue and bone. Since field flatteners compensate X-ray absorption along the path, both the rat head and its plastic holder [Zhu07] were taken into account. The KES experiment recorded projection images in both lateral and DV views, in which *x* denoted the lateral direction, *y* denoted the DV direction, and *z* denoted the caudal direction along the animal. The projected absorption of the rat head and its holder were expressed as coming from three components, plastic holder (*H*), soft tissue (*T*), and bone (*B*), with the total (*TOT*). (In the following, the *N* refers to the Hounsfield number plus 1000, so that a value of zero corresponds to zero attenuation or the attenuation of air.)

$$N_H(E_{CT},x,y)=\gamma\tfrac{\mu}{\rho}_H(E_{CT})\int_{t_H(x,y)}\rho_H(x,y,z)dz=\gamma\tfrac{\mu}{\rho}_H(E_{CT})\bar{\sigma}_H(x,y)$$

$$N_T(E_{CT},x,y)=\gamma\tfrac{\mu}{\rho}_T(E_{CT})\int_{t_T(x,y)}\rho_T(x,y,z)dz=\gamma\tfrac{\mu}{\rho}_T(E_{CT})\bar{\sigma}_T(x,y) \quad (3.4)$$

$$N_B(E_{CT},x,y)=\gamma\tfrac{\mu}{\rho}_B(E_{CT})\int_{t_B(x,y)}\rho_B(x,y,z)dz=\gamma\tfrac{\mu}{\rho}_B(E_{CT})\bar{\sigma}_B(x,y)$$

$$N_{TOT}(E_{CT},x,y)=\gamma[\tfrac{\mu}{\rho}_H(E_{CT})\bar{\sigma}_H(x,y)+\tfrac{\mu}{\rho}_T(E_{CT})\bar{\sigma}_T(x,y)+\tfrac{\mu}{\rho}_B(E_{CT})\bar{\sigma}_B(x,y)]$$

In the CT images, the soft tissue and bone regions were segmented to isolate each independently using the contour procedure in IDL. Then the projected mass density σ along a projection path for each component was found from the measured *N* from the segmented image using E_{CT} and γ which were previously determined:

$$\bar{\sigma}_H(x,y)=\frac{N_H(E_{CT},x,y)}{\gamma\tfrac{\mu}{\rho}_H(E_{CT})}=\rho_H t_H(x,y)$$

$$\bar{\sigma}_T(x,y)=\frac{N_T(E_{CT},x,y)}{\gamma\tfrac{\mu}{\rho}_T(E_{CT})} \quad (3.5)$$

$$\bar{\sigma}_B(x,y)=\frac{N_B(E_{CT},x,y)}{\gamma\tfrac{\mu}{\rho}_B(E_{CT})}$$

The projected equivalent absorption length of the field flattener (*P*) at the KES experimental energy E_K, which is 33.17 *keV* for the iodine K-edge, was thus determined by

$$\tfrac{\mu}{\rho}_P(E_K)\rho_P t_P(x,y)=\tfrac{\mu}{\rho}_H(E_K)\bar{\sigma}_H(x,y)+\tfrac{\mu}{\rho}_T(E_K)\bar{\sigma}_T(x,y)+\tfrac{\mu}{\rho}_B(E_K)\bar{\sigma}_B(x,y) \quad (3.6)$$

The rat head holder (*H*) and its matching field flatteners (*P*) were fabricated from the same plastic by a 3D printer, i.e. $\tfrac{\mu}{\rho}_H=\tfrac{\mu}{\rho}_P$ and $\rho_H=\rho_P$,

$$t_P(x,y)=t_H(x,y)+\frac{\tfrac{\mu}{\rho}_T(E_K)\bar{\sigma}_T(x,y)}{\tfrac{\mu}{\rho}_P(E_K)\rho_P}+\frac{\tfrac{\mu}{\rho}_B(E_K)\bar{\sigma}_B(x,y)}{\tfrac{\mu}{\rho}_P(E_K)\rho_P} \quad (3.7)$$

Substituting back with $\bar{\sigma}_T(x,y)$ and $\bar{\sigma}_B(x,y)$ leads to

$$t_P(x,y) = t_H(x,y) + \left[\frac{\frac{\mu}{\rho_T}(E_K)}{\frac{\mu}{\rho_T}(E_{CT})} N_T(E_{CT},x,y) + \frac{\frac{\mu}{\rho_B}(E_K)}{\frac{\mu}{\rho_B}(E_{CT})} N_B(E_{CT},x,y) \right] \frac{1}{\gamma \frac{\mu}{\rho_P}(E_K)\rho_P} \quad (3.8)$$

$t_P(x,y)$ in Equation (3.8) is the equivalent thickness of the field flattener material that has the same absorption as the animal's bone, soft tissue and plastic holder at 33.17 *keV*. The field flatteners were created by drawing a planar curve of *t* for each slice,

$$t = t_m - t_P(x,y) \qquad \text{(where } t_m > t_P(x,y)\text{)} \quad (3.9)$$

where t_m is the maximum thickness of the field flattener. Other simple attachments, such as a support frame and labels, were also added to the DICOM images (Figure 3.8).

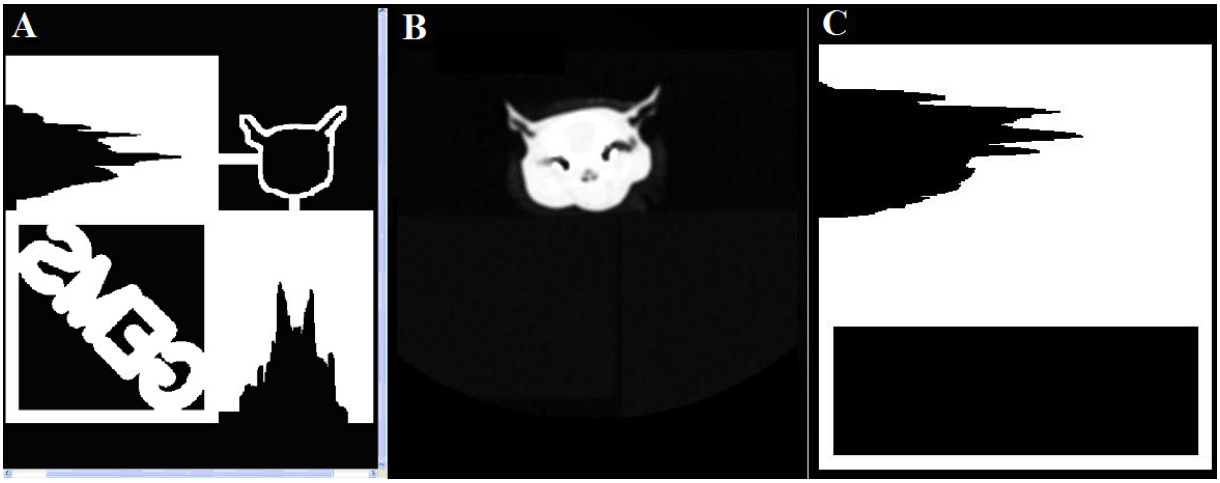

Figure 3.8 DICOM image slices of the first rat head holder and its corresponding field flatteners in lateral and DV views (A), the second rat head (B) and its matching lateral field flattener (C).

3.2.1.4 Conversion and Fabrication

The DICOM images of the field flatteners were converted into STL format with "accurate" or "smooth" setting using the freeware JuliusLight [Jul]. For comparison, "smooth" setting was used for the first set of field flatteners and "accurate" setting was used for the second set. STL files were imported into a rapid prototyper (Eden500V™ from Objet Geometries Inc.) to fabricate the field flatteners (Figure 3.9). Two sets of field flatteners were fabricated using

opaque (VeroWhite®) or transparent (FullCure®720) acrylic-based photopolymer materials (Figure 3.10).

The selection of the materials was based on their similarities in X-ray visibility compared with Lucite which is the material used in the field flattener calculation for both field flatteners (*p*) and the rat head holder (*h*). The CT experiment to compare the X-ray visibilities of Lucite and VeroWhite® was done at Saskatoon Cancer Center in Nov. 2006. The result showed a very similar Hounsfield Unit (*HU*) number, that is, 116.0 *HU* for Lucite and 111.8 *HU* for VeroWhite® material at an X-ray Voltage of 120 *kVp*. Even though FullCure®720 is the second closest material to Lucite in X-ray visibility after VeroWhite® (from Objet Geometries Ltd., Billerica, Massachusetts, USA), it was chosen because of its preferred transparent property.

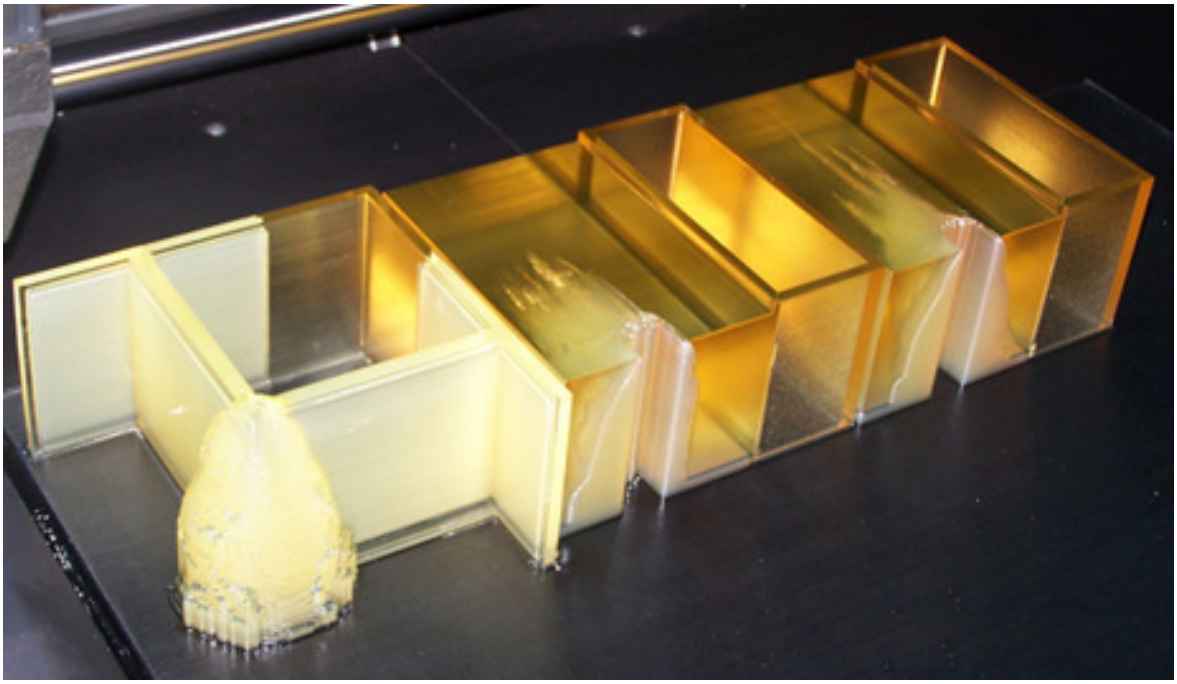

Figure 3.9 The second rat head holder and its two corresponding lateral and DV field flatteners were freshly finished the prototyping on the working platform of the Eden500V™, with ivory material still supporting the prototypes.

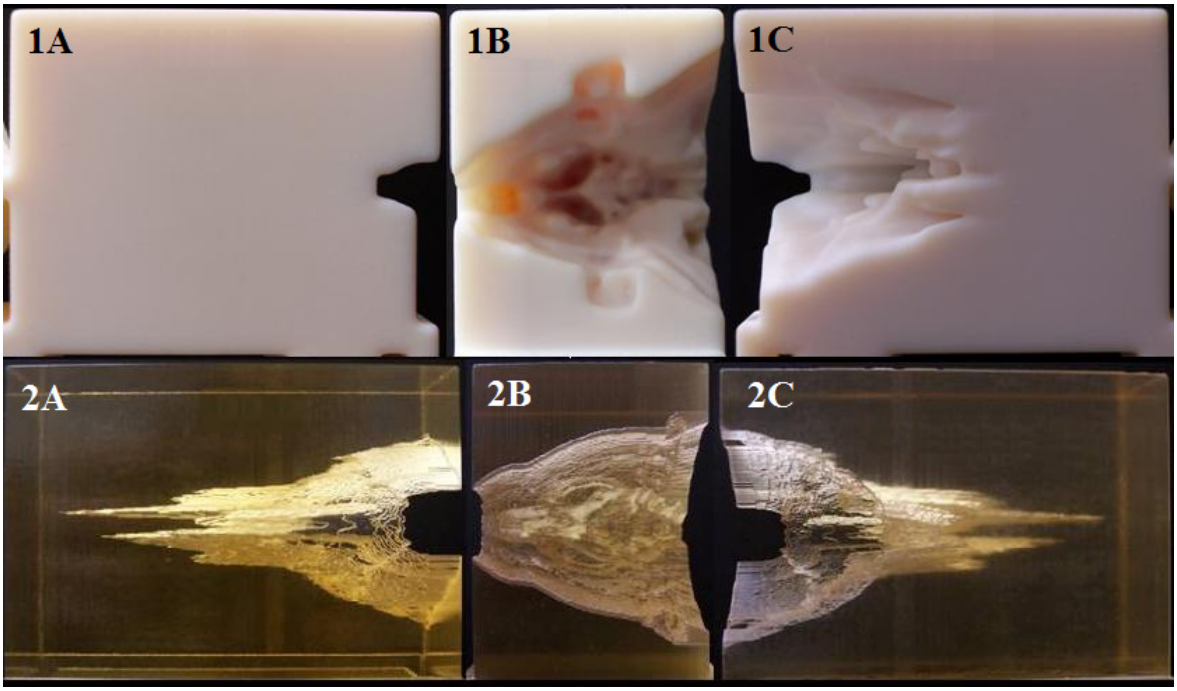

Figure 3.10 Two DV view field flatteners in opaque VeroWhite® for the first rat (1) and in transparent FullCure®720 for the second rat (2), in front (A), side (B) and back (C) views, respectively.

3.2.2 Experiments

Both sets of the field flatteners were used in KES imaging experiments at the HXMA beamline at the CLS in Dec. 2006 (Figure 3.11). KES images were taken with an X-ray camera from Photonic Science (18.7 μm square pixel size, 10 *ms* exposure) in line scan mode at 2 *mm/s* vertical scan velocity. The beam size was 0.25 *mm* vertical height by 28 *mm* horizontal width. The energy of the monochromatic beam was manually switched between 100 *eV* above and below the iodine K-edge at 33.17 *keV* by a double crystal monochromator. Two micropipettes containing 50 *mM* and 10 *mM* concentration of iodine solutions were implanted in the head of a 410 *g* euthanized rat. The rat was KES imaged by vertical scanning four sweeps for both up and down directions with and without a field flattener in lateral and DV views.

While the first set of field flatteners was closely attached to its rat head holder nicely

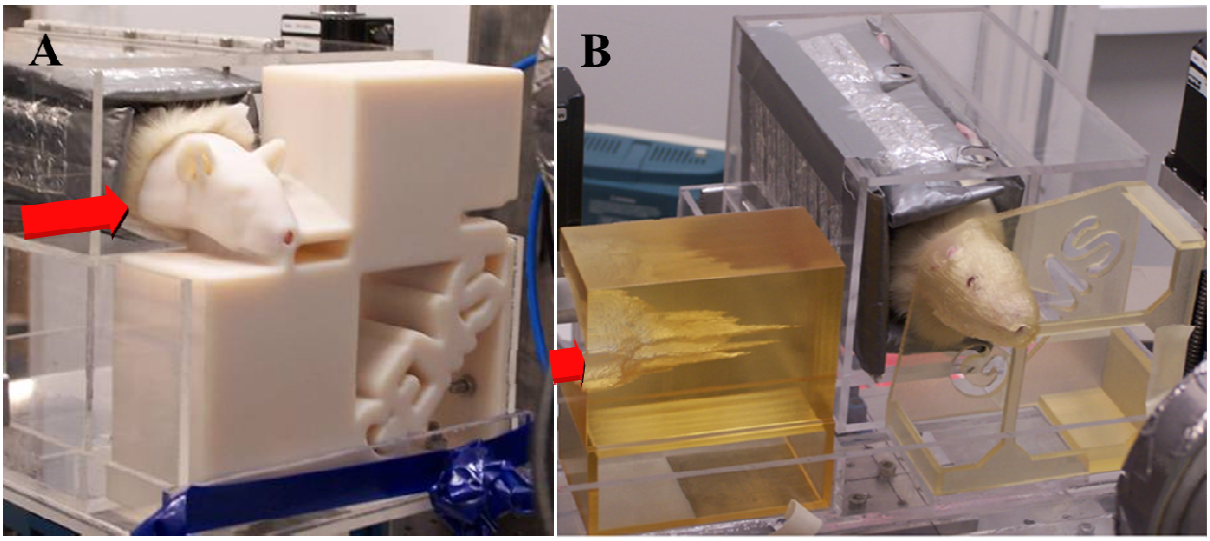

Figure 3.11 Field flatteners used in the KES experiments at the HXMA beamline at the CLS. While the lateral field flattener in the first set was used in the downstream of a rat (A), the DV field flattener in the second set was used in the upstream of a rat (B). The solid red arrows indicate the incident beam direction.

showing the direction of the projection, the second set was separated from its holder to enable comparison of images taken with and without the field flatteners (Figure 3.11). Besides, a separate field flattener could always be put upstream of the animal to reduce the dose and away from the animal to reduce the secondary scattering into the fluorescence detector nearby.

3.2.3 Results and Discussions

From the projected density images of iodine in lateral view, the two micropipettes of iodine solution were easily discerned side by side in the rat head, while the iodine images in DV view only showed one micropipette of iodine due to the vertical overlapping positions of the two micropipettes (Figure 3.12 1-4C). As expected the projected density images of iodine show less anatomical information of the rat with field flatteners than without (Figure 3.12 2C vs. 1C, 4C vs. 3C). Some skeletal features remain due to vibrations introduced from the vertical scan motion which causes mismatches between raw images. In practice, faint anatomic structures help with

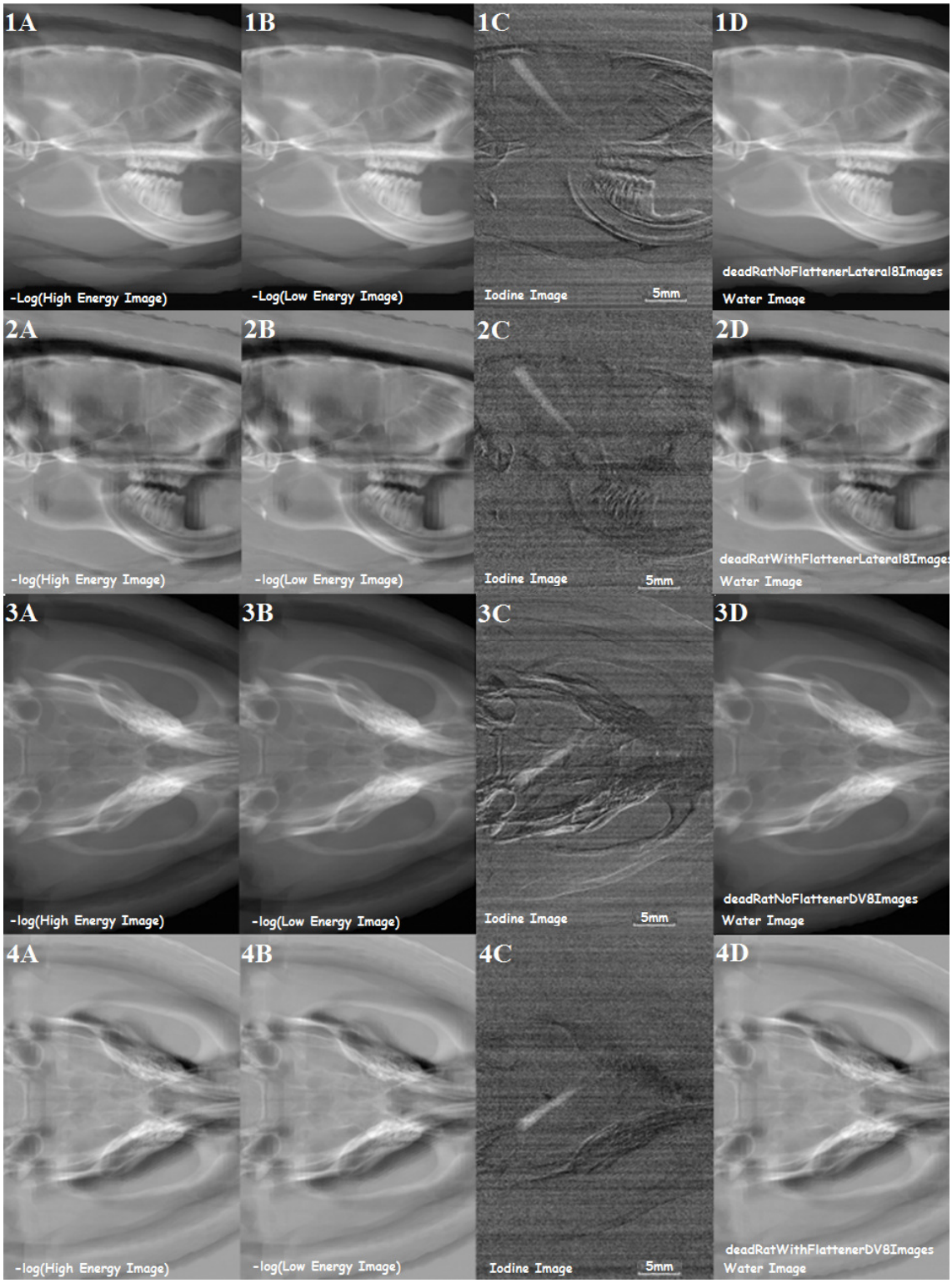

Figure 3.12 Images of a euthanized rat without (1) and with (2) a lateral field flattener, without (3) and with (4) a DV field flattener. Each row contains negative logarithms of images taken at above (A) and below (B) the iodine K-edge, the projected density images of iodine (C) and water/tissue (D). Each image was the average of a data set of eight images.

the localization of iodine in the animal. Analysis of the images with field flatteners and their histogram distributions (Figure 3.13) discovered that the high flux on the long tail of the histogram curves corresponded with the darkest area in the images, for example, in the muscle layer that covers the skull and between the superior and inferior molars in the lateral view (Figure 3.12 2A, 2B and 2D) and in the area bordered by the zygomatic arch and the maxillary bone in the DV view (Figure 3.12 4A, 4B and 4D). These were the result of improper compensation of X-ray absorption by field flatteners due to several factors. The experimental rat of 410 *g* had some size differences compared with the medical CT rat of 486 *g*, on which the rat head holder and field flatteners were based. There was the possibility of positional misalignment between the rat head and the field flatteners since they are totally separate. And the voxel element in the medical CT image that was used to create the field flatteners was big enough to create steps in the thickness of field flatteners. The smooth conversion from DICOM to STL, or

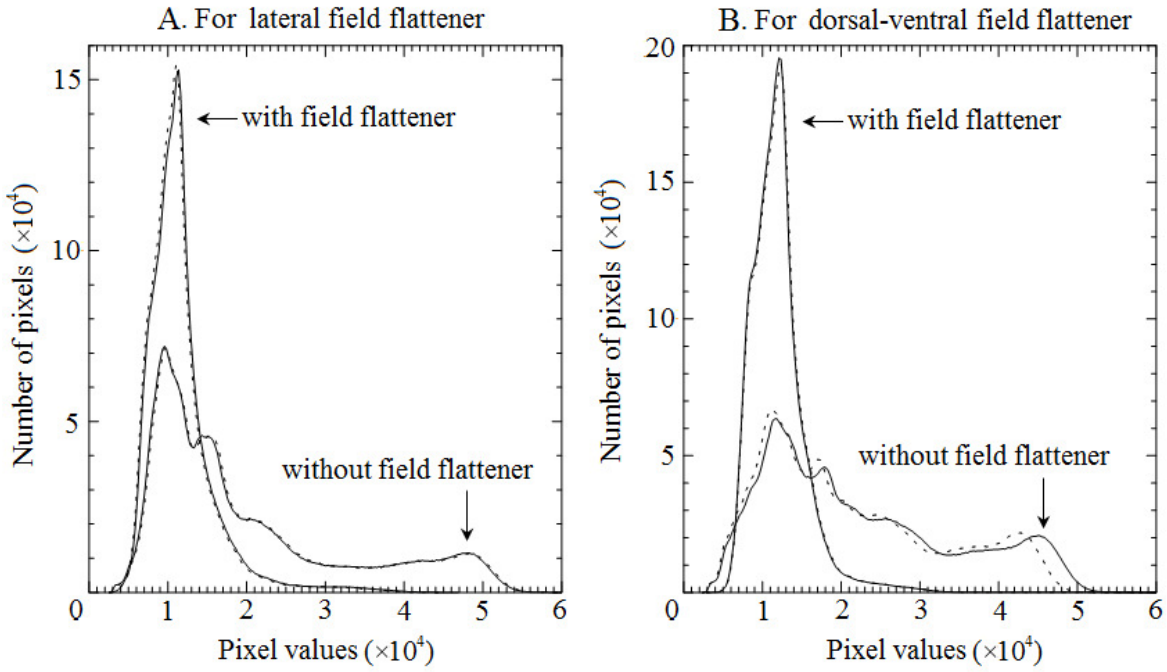

Figure 3.13 Histograms of raw images taken with and without field flatteners in lateral view (A) and DV view (B). The solid lines indicate the histograms of the images taken at above K-edge energy and the dashed lines indicate those at below K-edge energy.

averaging slightly displaced DICOM images to get a blurred density image should make the field flatteners suitable for "generic" rats but this needs further investigation.

The field flatteners improved the SNR of both the raw images and the iodine images (Table 3.2). The maximum surface dose to the animal was increased by a factor of 1.72 in lateral view and 4.37 in dorsal view from the non-flattened case despite the reduced average surface exposure to the animal (Table 3.3). A "perfect" field flattener will create a constant exit dose from the subject, thus increasing the entrance or surface dose to some regions of the subject while maintaining lower average exposure to the subject. The increase in SNR arises in part from the regionally increased maximal exposure and in part from removal of anatomical noise. For KES, the latter may not be important and may be advantageous in some applications. While not implemented in this experiment, the further way to improve SNR is to raise the compressed pixel

Table 3.2 SNR of the images with and without a field flattener

SNR of images	*images in lateral view*			*images in DV view*		
	above edge	*below edge*	*iodine image*	*above edge*	*below edge*	*iodine image*
without a field flattener	1.61	1.60	3.02	1.87	1.86	2.29
with a field flattener	2.67	2.65	3.63	3.34	3.34	3.97
SNR improvement	+65.4 %	+65.6 %	+20.3%	+78.2%	+79.9%	+73.3%

Table 3.3 Surface dose ratio of the animal with a lateral (D_{LAT}) or DV (D_{DV}) field flattener compared with the non-flattened case (D_{noff})

Dose ratio to non-flattened case	*maximum*	*minimum*	*average*
D_{LAT} / D_{noff}	1.72	0.13	0.43
D_{DV} / D_{noff}	4.37	0.18	0.52

value range to the upper end of the detector linearity (Figure 3.13). This could further double the SNR if the mismatch problem is well controlled since the SNR is proportional to the square root of the incident flux. But it will come at the cost of elevated average dose to the animal. In principal the improved SNR of KES with field flatteners could make it possible to visualize contrast agents at dilutions that would not be visible using standard medical CT.

It should be emphasized that the field flattener described here is used with live animal subjects for research. The increased SNR is due to an increase in exposure to the subject while limiting the need for a wide dynamic range, linear response digital detector. Though it could be applied clinically, the KES method is best applied at a synchrotron source and thus the applications are typically only for research purposes. A field flattener could be used in clinical applications where an increase in patient exposure can be tolerated to improve the visualization of a contrast material. The field flattener allows this possibility while limiting the exposure to the detector. However, one serious impediment is that a field flattener is made for a specific projection and object. For research with specific size animals and specific views, the field flattener is a feasible solution to obtain high sensitivity images. For general radiography, with differing views, subject size, and anatomical variations, a field flattener would not be feasible.

3.2.4 Conclusions

A field flattener fabricated by a rapid prototyper improved the SNR of KES images at a cost of raised maximum exposure to some regions of the subject and reduced anatomical information in the images. In research applications with animal systems, this method holds great promise to visualize low concentrations of contrast agents. Further improvements should standardize the field flatteners for “generic” rats and raise the compressed range of incident photon flux to the high end of the detector linearity to further improve the SNR. Clinical applications of field flatteners need further investigations.

Chapter 4 Bent Laue Analyzers for X-ray Fluorescence Imaging

For biomedical X-ray imaging applications, chapter 3 presents two types of animal imaging devices, animal restraints for both KES and XRF imaging and field flatteners for KES imaging. This chapter introduces the bent Laue crystals used for XRF imaging projects.

A BLA is a Si crystal bent to a logarithmic spiral shape and placed upstream of an area detector for specific XRF detection [Zho99]. The BLA-based XRF detection system can achieve excellent energy resolution and large solid angle of photon acceptance with nearly no count rate limitation, but at a price of limited applicable energy range. Two groups of BLAs were made for the XRF detection from manganese (Chapter 4.1) and iodine (Chapter 4.2) respectively, while the latter was designed to demonstrate the novel idea of 3D confocal XRF imaging.

4.1 Bent Laue XRF Imaging of Manganese in Biological Tissues

Mn is not abundant in human brain tissue, but it is recognized as a neurotoxin. Since the symptoms of manganese intoxication are similar to Parkinson's disease (PD), the investigation of the link between environmental, occupational or dietary Mn exposure and PD in humans is a hot research topic in the recent decade [Ola04, Gui10]. A BLA-based Mn fluorescence detection system was built to improve elemental specificity in XRF imaging. Chapter 4.1 describes the optimal design and fabrication of a group of BLAs and its synchrotron application to Mn fluorescence detection in biological samples.

4.1.1 Bent Laue Analyzer Design

Four sets of BLAs (denoted as *I, -I, II, -II*) were designed with both positive and negative beam incident geometry onto the {111} Bragg planes *BP* (Figure 4.1) of two Si wafers, Si (111) (*I*) and Si (400) (*II*), respectively. As shown in Figure 4.1, the horizontal focal direction is defined as axis *x*, the vertical direction in the diffraction plane (paper plane) is defined as axis *y* and the transversal direction perpendicular to and pointing out of the diffraction plane is defined as axis *z* in the Chapter 4.

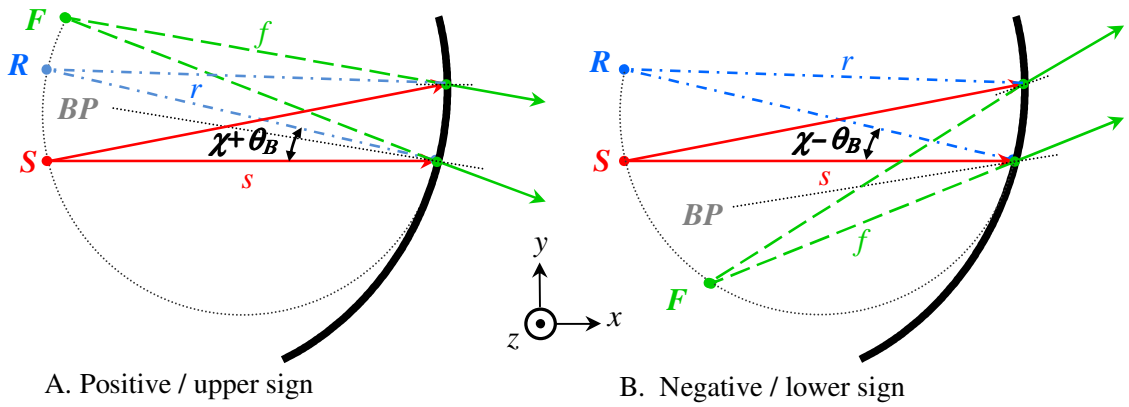

A. Positive / upper sign B. Negative / lower sign

Figure 4.1 The positive / upper (A) and negative / lower (B) sign cases for a BLA (bold curve). Source *S*, focal point *F*, normal center *R*, Bragg planes *BP*, source to crystal distance *s*, virtual focal length *f*, bending radius *r*, Bragg angle θ_B and asymmetry angle χ

4.1.1.1 Methods

Based on a lamella model [Ero90, Boe78] and the REFLECT program [Ete89], the reflectivity, reflectivity width and lamella layers of BLAs were calculated as a function of thicknesses and bending radii of the Si crystal as shown in Figure 4.2 and 4.3. The colors represent the reflectivity with the corresponding pseudo-color bar on the right side indicating the mapping between the pseudo-color and the reflectivity value. Iso-reflectivity is shown as white solid lines with the reflectivity value labeled. Considering the collection of both Mn $K_{\alpha 1}$ and $K_{\alpha 2}$

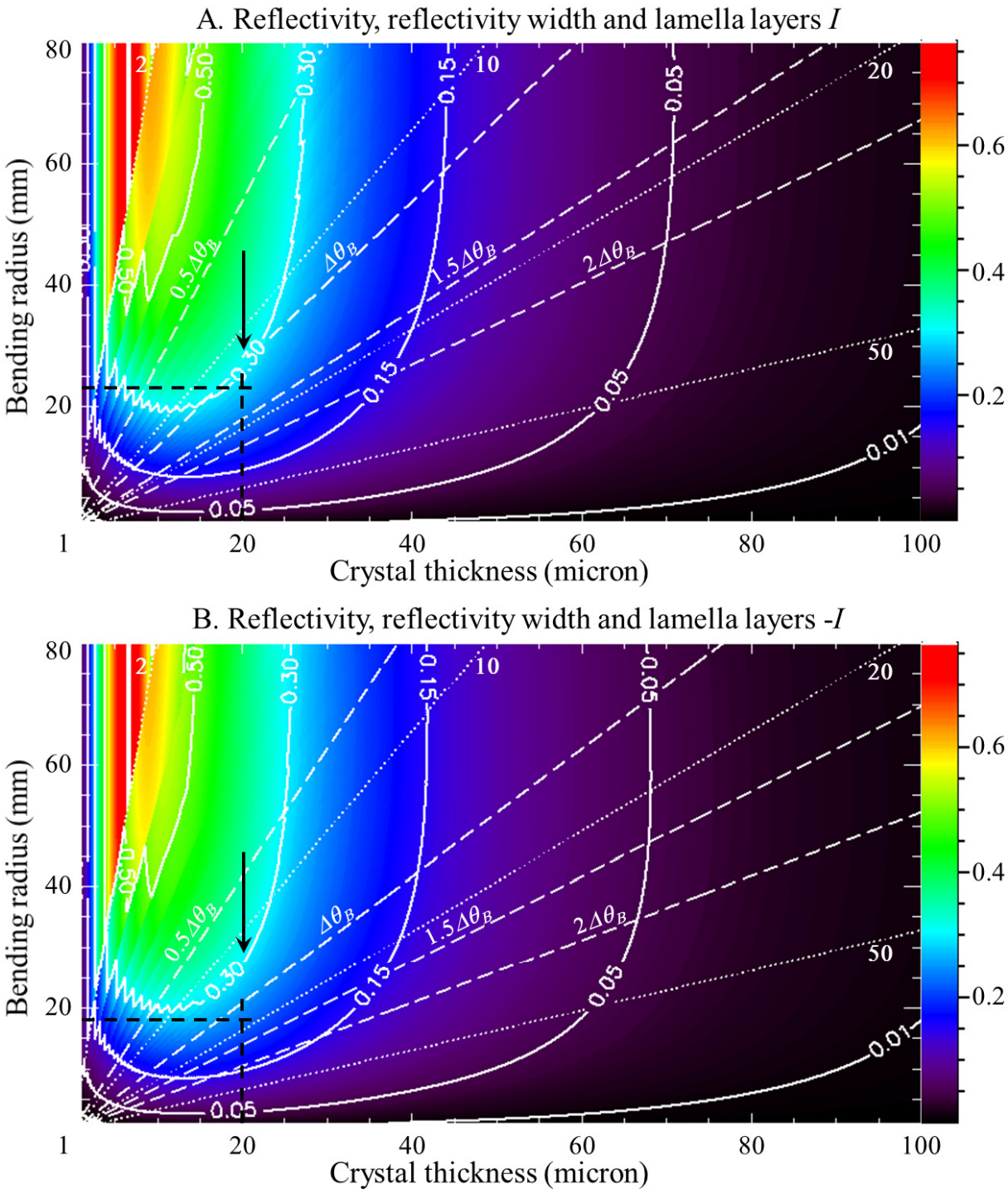

Figure 4.2 The reflectivity (pseudo-color mapping and white solid isolines), reflectivity width (white dashed isolines in the unit of $\Delta\theta_B$) and lamella layers (white dotted isolines) of BLAs using Si (111) (A for *I* and B for -*I*) for Mn K_α fluorescence vs. crystal thickness and bending radius. The black arrows note the suggested crystal thickness. The black dashed crosses indicate the final parameters of the crystal thickness and bending radius.

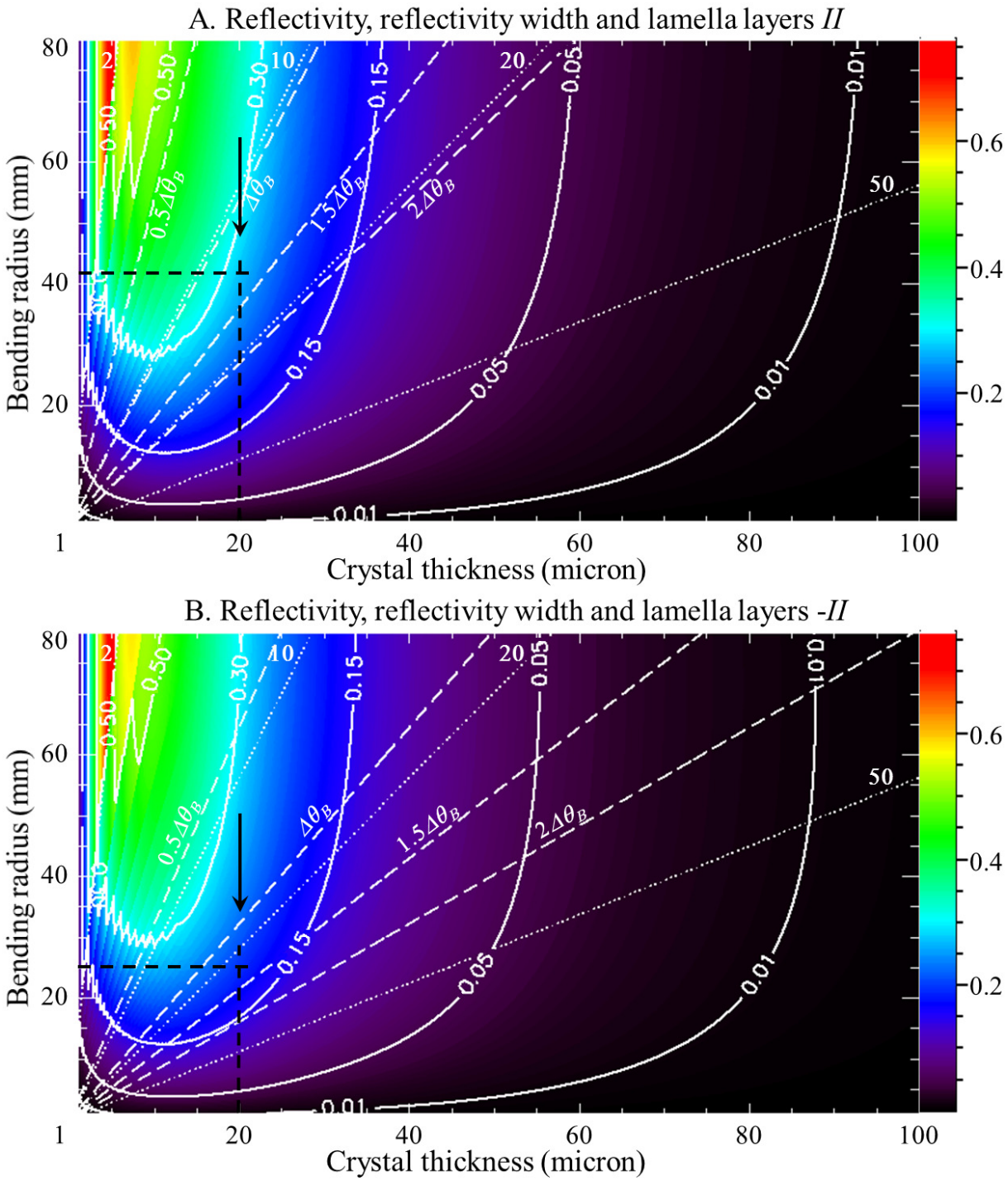

Figure 4.3 The reflectivity (pseudo-color mapping and white solid isolines), reflectivity width (white dashed isolines in the unit of $\Delta\theta_B$) and lamella layers (white dotted isolines) of BLAs using Si (400) (A for *II* and B for *-II*) for Mn K_α fluorescence vs. crystal thickness and bending radius. The black arrows note the suggested crystal thickness. The black dashed crosses indicate the final parameters of the crystal thicknesses and bending radii.

fluorescence at the same time, the reflectivity width should be larger than the Bragg angle difference $\Delta\theta_B$ between Mn $K_{\alpha 1}$ and $K_{\alpha 2}$ which is 0.67 *mrad*. In Figure 4.2 and 4.3 iso-width of reflectivity is shown in white dashed lines denoted in the unit(s) of $\Delta\theta_B$ and lamella iso-layers are shown in white dotted lines with the number of lamella layers labeled. Comparisons within Figure 4.2 and 4.3 indicate that the lamella layers are the same between the upper and lower incidences while the reflectivity and reflectivity width of upper incidence are bigger than those of lower incidence as expected due to larger region of interaction between the beam and crystal. A limitation of the lamella model is that the smaller the lamella layer number, the more intermittent the estimated reflectivity appears which is obvious in Figure 4.2 and 4.3 when the lamella layers are less than 10. A Si crystal thickness of 20 μm was roughly determined based on the maximal reflectivity along the isolines of reflectivity width of $\Delta\theta_B$ in all four cases.

Groups of rocking curves (reflectivity vs. incident angle) were drawn with a crystal thickness of 20 μm and a reflectivity width ranging from $0.5\Delta\theta_B$ ~ $2.5\Delta\theta_B$, showing the merging process of the Mn $K_{\alpha 1}$ and $K_{\alpha 2}$ fluorescence peaks. By selecting the just merging point of the two peaks, a reflectivity width of $1.2\Delta\theta_B$ and $1.3\Delta\theta_B$ were roughly determined for Si (111) (*I* and *–I*) and Si (400) (*II* and *–II*) crystals, respectively. This step aims at the highest energy resolution for collecting both of the Mn $K_{\alpha 1}$ and $K_{\alpha 2}$ fluorescence peaks at the same time. From the reflectivity curves at the desired reflectivity width of $1.2\Delta\theta_B$ and $1.3\Delta\theta_B$ (Figure 4.4), a crystal thickness of 20 μm was again confirmed by the reflectivity peaks in all four cases. Even though a crystal thickness of 15 μm is an optimal choice for Si (400), it is not commercially available.

With the crystal thickness (20 μm) and reflectivity width ($1.2\Delta\theta_B$ for *I* and *–I*, $1.3\Delta\theta_B$ for *II* and *-II*) being set, the BLA parameters were all calculated. For practical reasons the source to crystal center distance *s* was rounded to integer numbers of 18 *mm* (*I* and *–I*) or 24 *mm* (*II* and

–*II*), and the reflectivity width was thus adjusted to 1.160$\Delta\theta_B$ (0.778 *mrad* for *I* and –*I*) or 1.294$\Delta\theta_B$ (0.868 *mrad* for *II* and -*II*). The equivalent reflectivity was estimated as a square peak with its width equal to the reflectivity width based on the rocking curves from Mn $K_{\alpha 1}$ and $K_{\alpha 2}$ fluorescence (Figure 4.5).

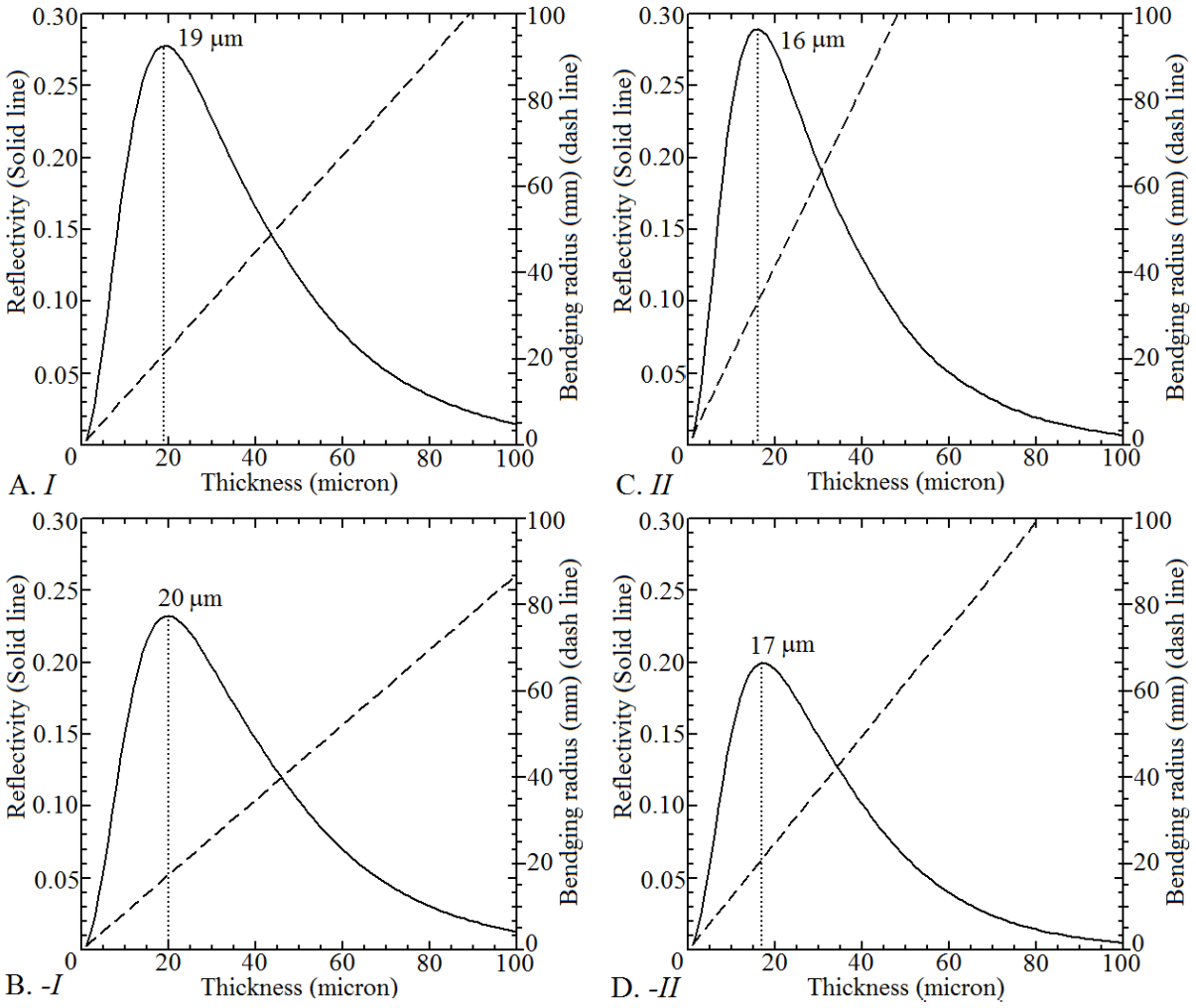

Figure 4.4 The reflectivity (solid line) and bending radius (dashed line) at a constant reflectivity width of 1.2$\Delta\theta_B$ (A and B) and 1.3$\Delta\theta_B$ (C and D) vs. crystal thickness of BLAs. The vertical dotted lines indicate the crystal thickness reaching the maximal reflectivity.

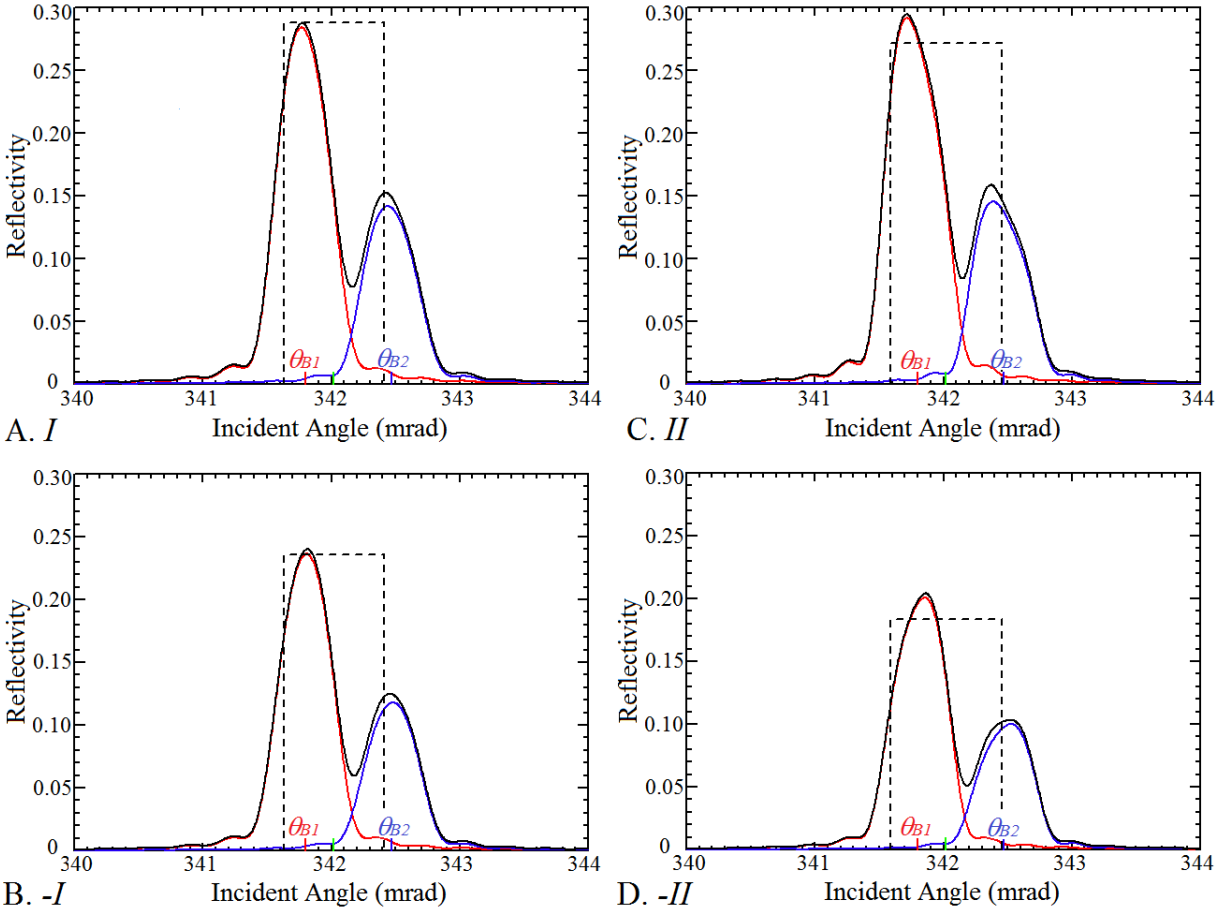

Figure 4.5 The calculated rocking curves from Mn $K_{\alpha 1}$ (red lines) and $K_{\alpha 2}$ (blue lines) fluorescence and the sum of the two (black lines). The equivalent reflectivity was estimated as a square peak (dashed lines) with its width equal to the reflectivity width. The θ_{B1} and θ_{B2} refer to the Bragg angles of the Mn $K_{\alpha 1}$ and $K_{\alpha 2}$ fluorescence, respectively.

4.1.1.2 Specifications

With all the parameters determined at this point, BLAs were designed with geometric dimensions drawn in Figure 4.6 and primary parameters listed in Table 4.1. In the experimental setup, two Amptek detectors (XR-100T CdTe with 25 mm^2 detection area and XR-100CR Si with 13 mm^2 detection area from Amptek Inc., Bedford, MA, U.S.) were vertically placed with a fixed $2\theta_B$ angle (39.2°) apart accepting both the transmitted and diffracted beams from the BLA at the same time.

We define the figure of merit (FOM) of a BLA as the product of the reflectivity and the solid angle subtended by the crystal effective diffraction area of 2 *mm* by 8 *mm*. The FOM is drawn as a function of crystal thicknesses and bending radii in Figure 4.7 and 4.8. The colors

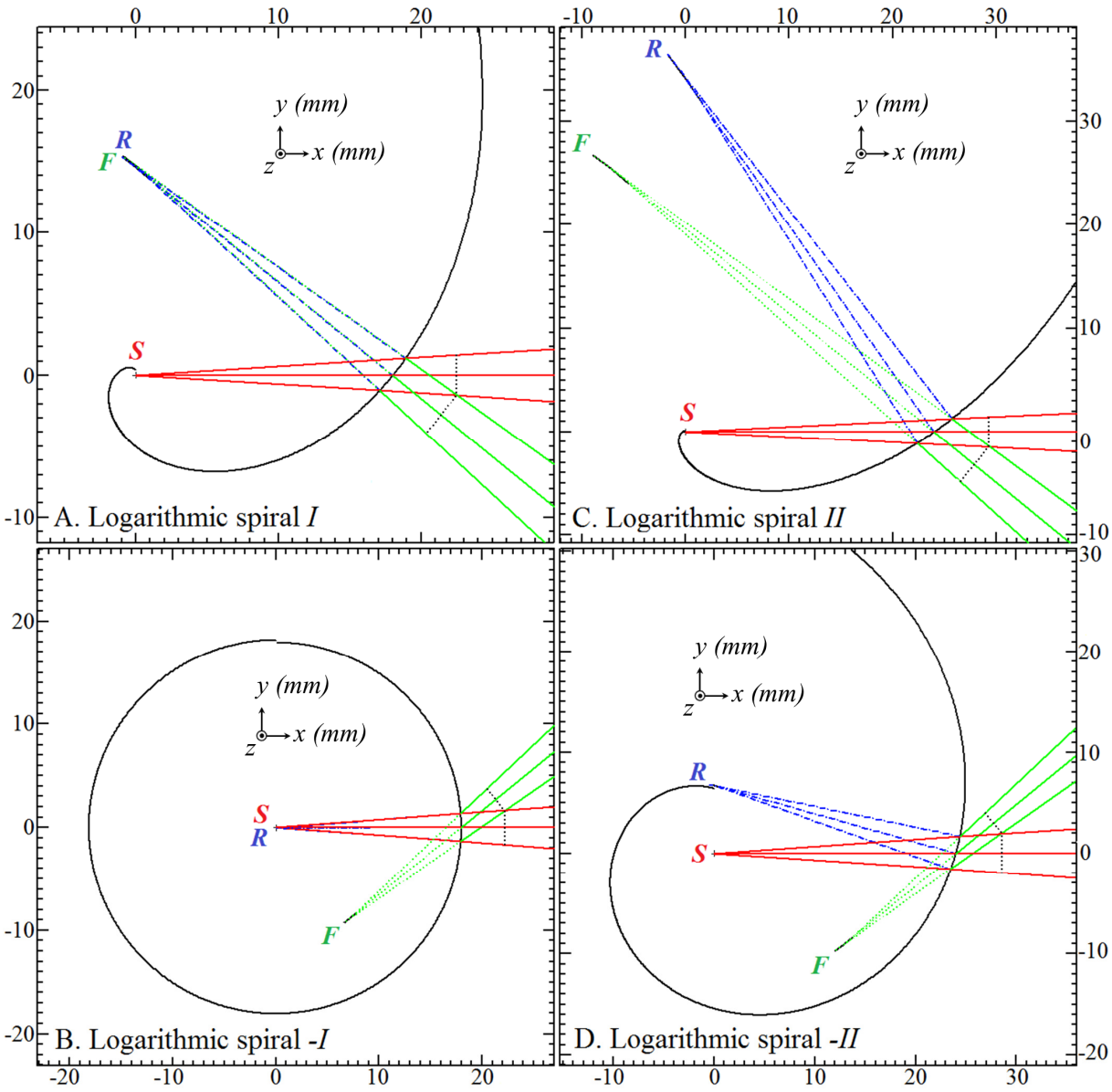

Figure 4.6 The logarithmic spirals (black) of the BLAs with respect to the positions of source *S*, focal point *F* and normal center *R*. The horizontal axes denote the dimension (*mm*) along the focal direction *x* and the vertical axes denote the dimension (*mm*) along *y* axis in the diffraction plane. The transmission lines (red), diffraction path (green) and the crystal surface normal (blue) are plotted according to the given active area of the two Amptek detectors.

Table 4.1 Design parameters of the BLAs for Mn fluorescence detection combined with the two Amptek detectors.

Design parameters	*I*	*-I*	*II*	*-II*
Si wafer	Si (111)		Si (400)	
Diffraction Plane DP	{111}			
Asymmetry angle χ (°)	19.5		35.3	
Poisson ratio	0.262 [Bra73]			
Polarization	No			
Mn K_α energy E_{Ka} (keV)	5.895			
Bragg angle θ_B (°)	19.6			
Darwin width ω_D (μrad)	42.5			
Crystal thickness t (μm)	20			
Crystal central bending radius r (mm)	23.2	18.0	41.7	24.9
Crystal active width (transversal) (mm)	2			
Crystal active length (coronal) (mm)	2.9	2.7	4.1	3.4
Source to crystal center distance s (mm)	18		24	
Central focal length f (mm)	23.2	14.0	40.1	14.3
Coronal opening angle (°)	7.1	8.5	5.6	7.9
Transversal opening angle (°)	6.4		4.8	
Solid angle Ω (msr)	13.8	16.4	8.1	11.5
Equivalent reflectivity R_{eq} (%)	28.8	23.6	27.1	18.4
FOM (msr)	4.0	3.9	2.2	2.1
Lamella layers	14	18	13	22
Reflectivity width $\Delta\theta$ (μrad)	778 (1.160$\Delta\theta_B$)		868 (1.294$\Delta\theta_B$)	
Energy resolution ΔE (eV)	12.9		14.4	
Energy bandwidth ΔE/E (%)	0.22		0.24	
Detectable region vertical size Δv (μm)	14		21	
Detectable region transversal size Δh (mm)	2.4		3.4	

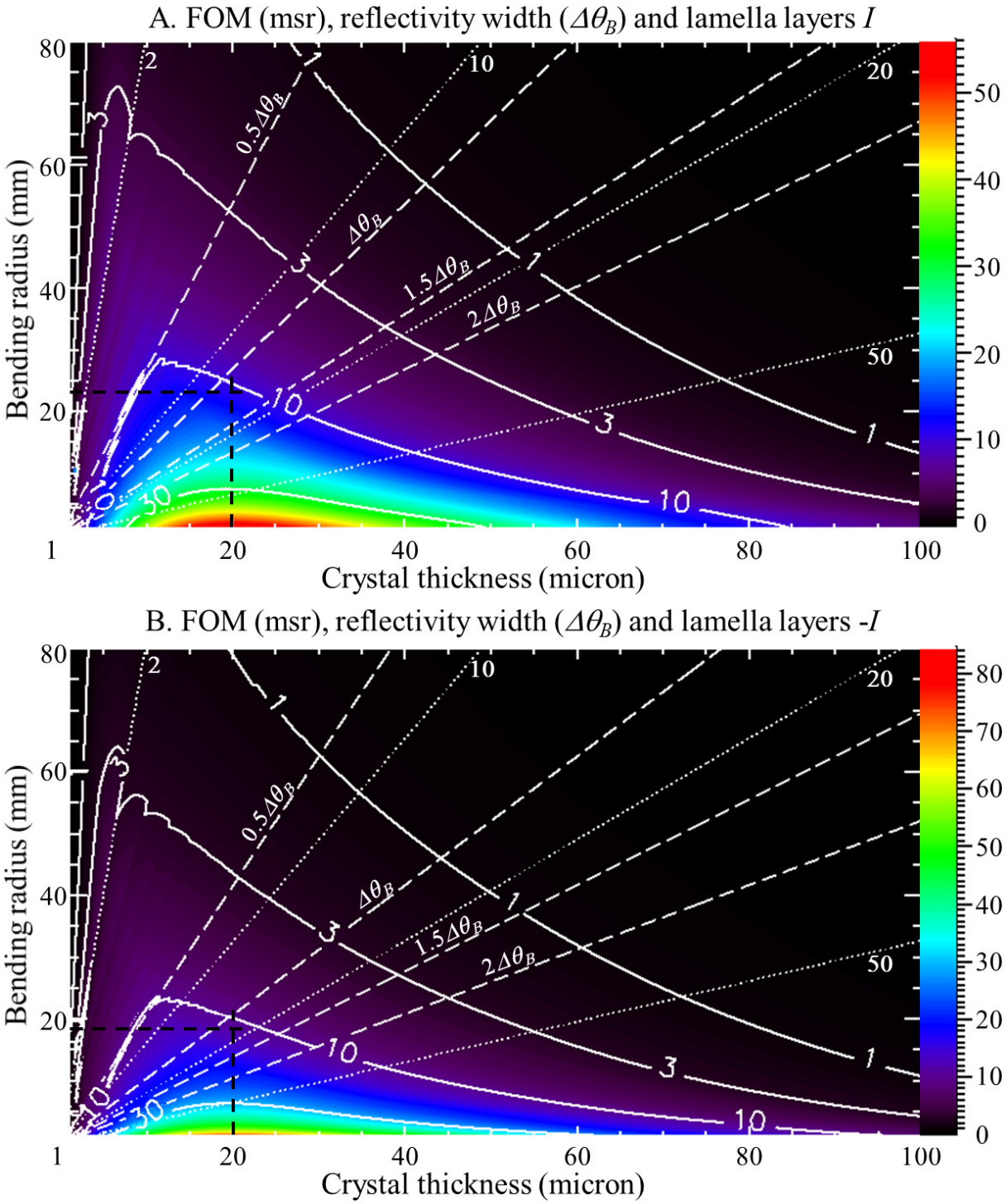

Figure 4.7 The FOM (pseudo-color mapping and white solid isolines in the unit of *msr*), reflectivity width (white dashed isolines in the unit of $\Delta\theta_B$) and lamella layers (white dotted isolines) of BLAs using Si (111) (A for I and B for $-I$) for Mn K_α fluorescence vs. crystal thickness and bending radius at a given active crystal area of 2 *mm* by 8 *mm*. The black dashed crosses indicate the final parameters of the crystal thickness and bending radius.

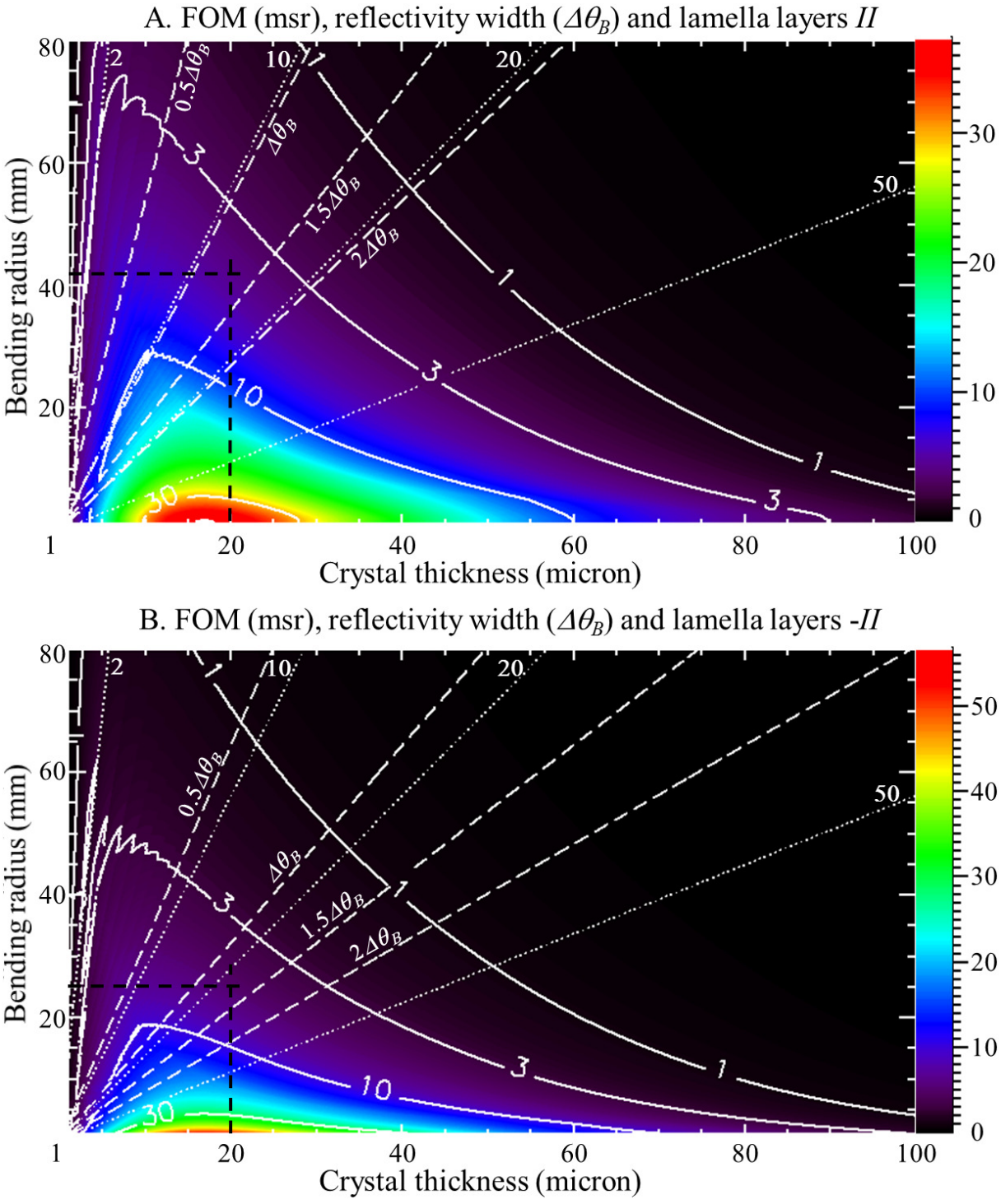

Figure 4.8 The FOM (pseudo-color mapping and white solid isolines in the unit of *msr*), reflectivity width (white dashed isolines in the unit of $\Delta\theta_B$) and lamella layers (white dotted isolines) of BLAs using Si (400) (A for *II* and B for *-II*) for Mn K_α fluorescence vs. crystal thickness and bending radius at a given active crystal area of 2 *mm* by 8 *mm*. The black dashed crosses indicate the final parameters of the crystal thickness and bending radius.

represent the FOM with the corresponding pseudo-color bar on the right side. Iso-FOM is shown in white solid lines with the FOM value labeled. Again, the iso-width of reflectivity is shown in white dashed lines denoted in the unit(s) of $\Delta\theta_B$ and lamella iso-layers are shown in white dotted lines with the number of lamella layers labeled. Figure 4.7 and 4.8 show that the chosen parameters noted by the black crosses are nearly optimal under a condition that 20 μm is the minimum crystal thickness commercially available.

4.1.2 Bender Design

Four sets of BLA benders were designed using Solidworks software (Solidworks Corp., Concord, Massachusetts, USA.) along with source pointers for proper alignment (Figure 4.9) and a positioning holder for two Amptek detectors (Figure 4.10). The logarithmic spiral curves were specifically imported from IDL using functions defined by a macro and evaluated smoothly

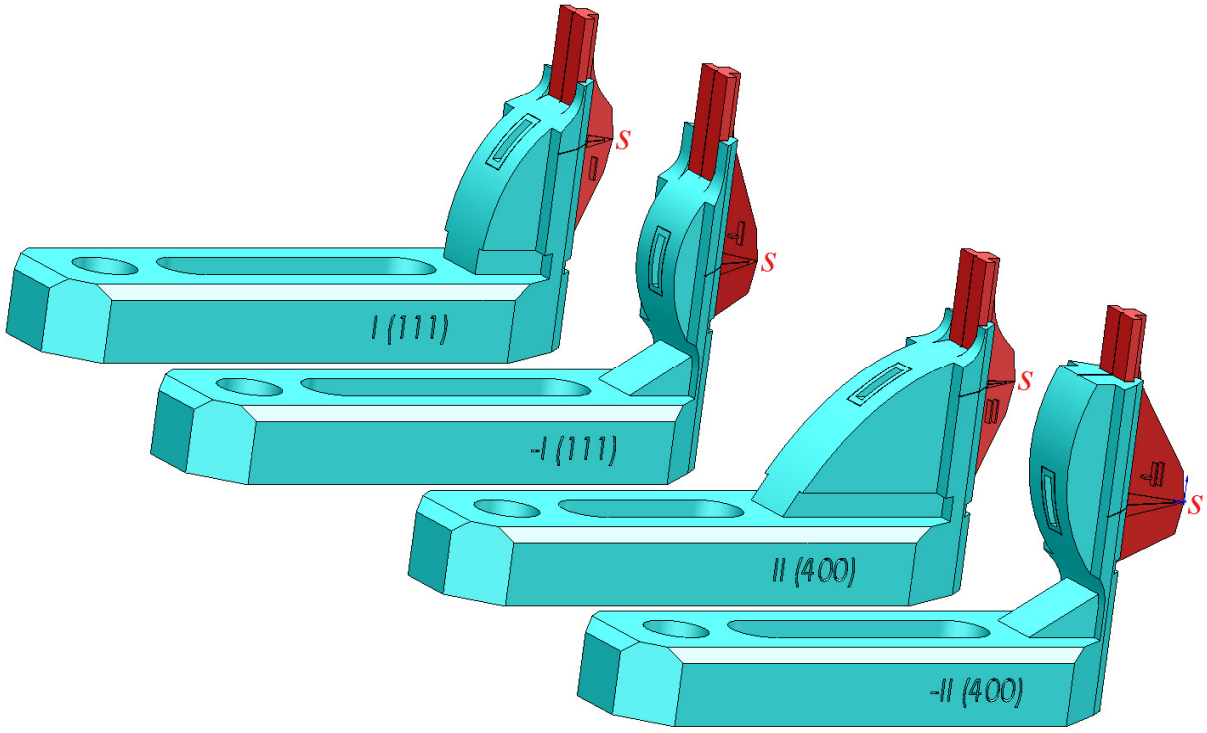

Figure 4.9 Four sets of BLA benders (cyan) along with their source pointers (red). The outside rectangles on the curved surfaces of logarithmic spiral shape define a crystal size of 4 *mm* by 10 *mm* and the inside rectangles of 2 *mm* by 8 *mm* designate the apertures for the beam path. The removable source pointers (red) point at the fluorescence and scattering center *S*.

using “Curvature” functions in Solidworks. The source pointer was removed from the top after proper alignment and a copper plate with a predefined aperture was inserted in the same place during the experiment to define the beam size onto the detectors.

The BLA benders, source pointers and the detector holder were fabricated using a Rapid Prototyper Eden500V^{TM} (Objet Geometries Ltd., Billerica, Massachusetts, USA) at the Engineering Machine Shop of the U of S.

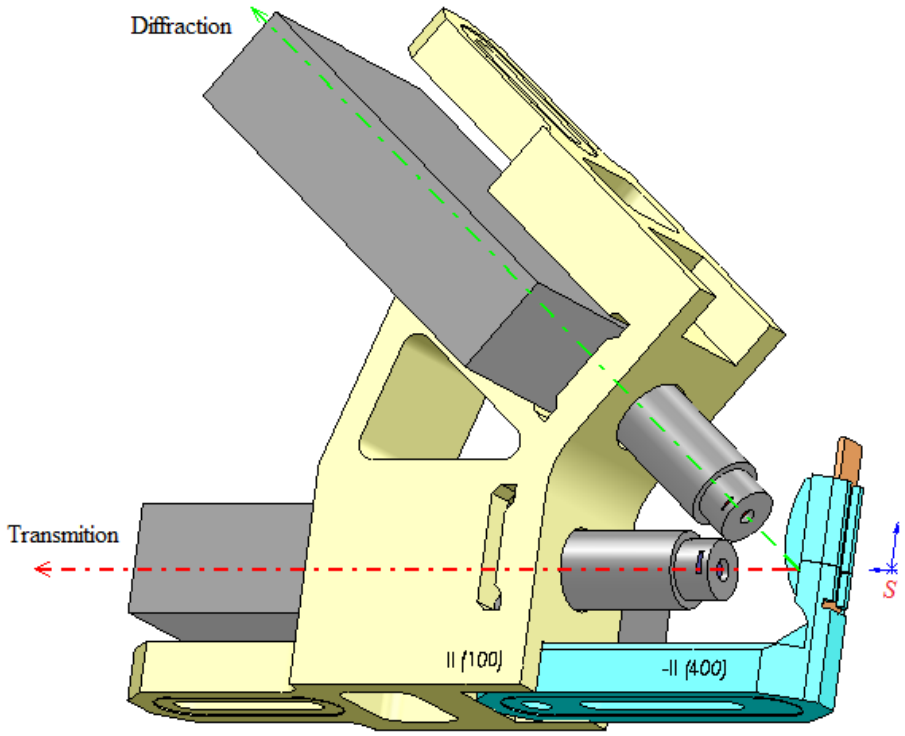

Figure 4.10 A detector holder (yellow) defines a $2\theta_B$ angle of 39.2° between the two Amptek detectors (grey). A BLA bender (cyan) could be docked into the either side of the detector holder for an easy switch of the two detectors. A rectangle copper plate (brown) was slide into the slot instead of its source pointer during the experiment. A predefined aperture was drilled in the middle of the copper plate to define the beam size.

4.1.3 Crystal Preparations

4.1.3.1 Releasing, Cutting and Bending

Si wafer (111) and (400) of 150 *mm* diameter and 20 μm thickness were ordered from Addison Engineering Inc. (San Jose, California, USA). The Si wafers of 20 μm thickness were so fragile that both had cracks throughout the wafers right out of the delivery box (Figure 4.11). The Si wafers on the original packing were strongly adhered to a polyvinyl chloride (PVC) film of 80 μm thickness by a layer of acrylic adhesive of 15 μm thickness. The standard way to release a wafer from the PVC film is to go through a specific ultraviolet (UV) exposure, that is, UV irradiation at 200 ~ 400 *nm* wavelength in high intensity (minimum 15 mW/cm^2) but at low dose (around 300 mJ/cm^2). Since such a dedicated UV curing system was not locally available, the Si wafer (400) was exposed under several other types of UV sources locally accessible. It was overexposed by longer irradiation of low intensity UV light before the above UV curing requirements were obtained from the UV tape manufacturer (Ultron Systems Inc., Moorpark, California, USA).

Both the unexposed Si (111) and overexposed Si (400) wafers were still adhered to the

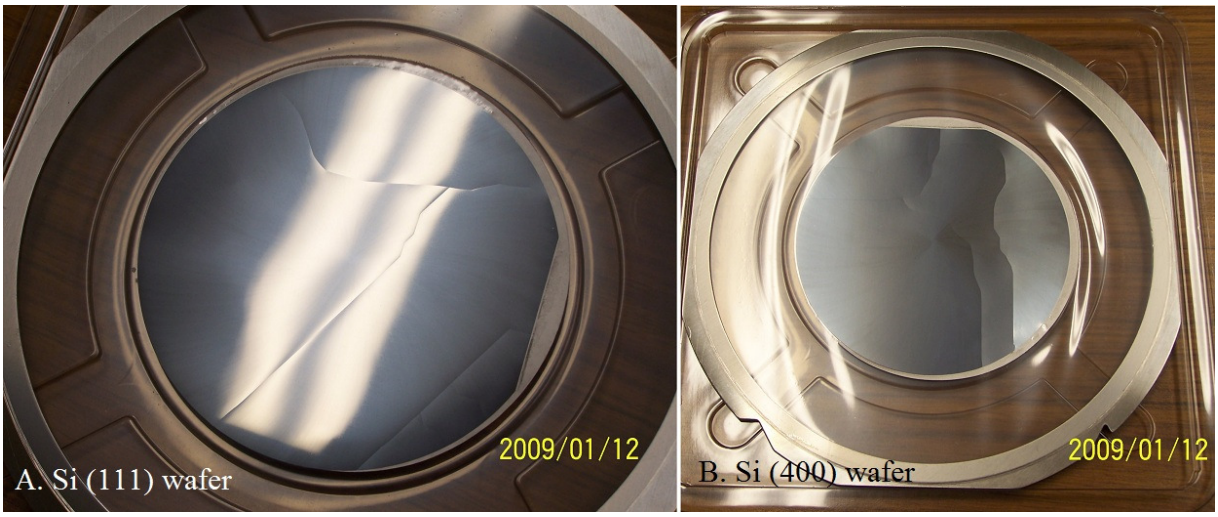

Figure 4.11 Si wafers out of box with 150 *mm* diameter and 20 μm thickness.

PVC tape tightly. As indicated by the UV tape manufacturer that nothing can be done to an overexposed UV curable tape, dissolving the PVC tape by an appropriate solvent appeared to be the only solution. The later experiences of crystal bending showed that the PVC film made the tightly taped crystal too stressed to be successfully bent without cracks. Releasing the crystal from the PVC tape allowed it to be freely bent and provided the maximum probability to survive the bending process. Several solvents were tried out to dissolve the PVC tape. Tetrahydrofuran (from EMD Chemicals at Gibbstown, New Jersey, USA) was a successful solvent as suggested by Dr. Manouchehr Hashemi.

The Si wafer taped on the backing PVC film was first scratched into many 4 *mm* by 10 *mm* rectangles by a diamond scriber based on the direction of the {220} flat edge on the wafer. The orientation was marked on each rectangle. Then the Si wafer was cut into bigger pieces which were dipped into the tetrahydrofuran solution one by one until partially dissolved. Small crystals released from the PVC tape were picked up by a tweezer and cleaned by acetone to remove any residue. Finally these small crystals were dried by themselves, sandwiched between weighing papers and stored in a cardboard box. Attention was paid to try to preserve the orientation of each small piece during the whole process of dissolving, cleaning and relocation as the original orientation markings were cleaned off in the solution. The dissolving process was observed to effectively grow and fully extend any invisible damage from the edges of the crystal pieces. Attempts to dissolve the whole wafer all at once would easily get too many pieces to keep track of each orientation. Cutting the Si (111) wafer was an even greater challenge resulting many pieces of irregular shape obtained due to its tri-fold symmetry (Figure 4.14).

The final step of crystal preparation was to bend and mount the crystal pieces onto the BLA benders. Small pieces of Kapton film were rubbed with fur to make them electrostatic

enough to pick up the crystals automatically and hold them firmly. One end of a Kapton film was first fixed on the BLA bender by Kapton tape. After a crystal was finely positioned on the inner side of the Kapton film, the Kapton film was firmly rolled over using a finger from the outside against the logarithmic spiral surface of the BLA bender. Then the other end of the Kapton film was tightly taped on the bender with the crystal bent and sandwiched between the Kapton film and bender surface without touching any tape (Figure 4.12).

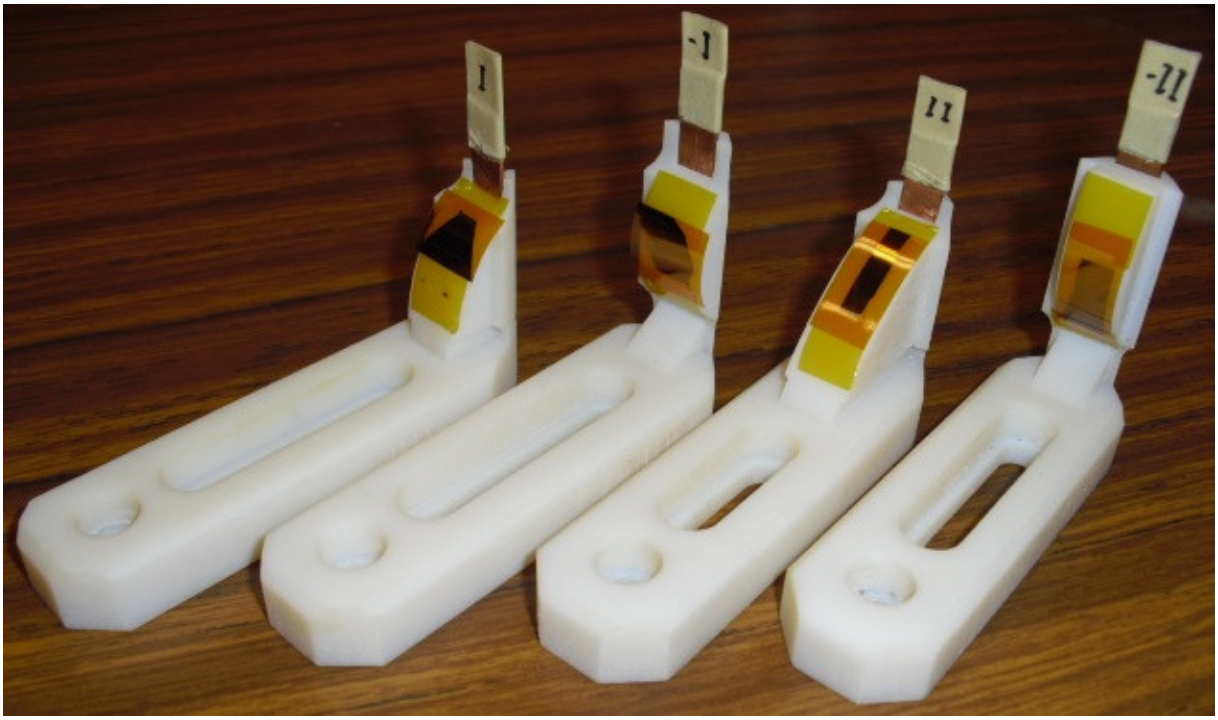

Figure 4.12 BLAs with crystals mounted and copper plates with apertures inserted (from left to right is *I, -I, II, -II*)

4.1.3.2 Crystal Orientation

Before mounting the crystals, the Si (111) crystal was orientated by X-rays to ensure the proper positioning on the BLA benders. The Si (400) did not go through this step because its orientation would not be wrong due to its four-fold symmetry as shown in its stereographic projection [Cul56] (Figure 4.13) as long as it was cut along the {220} flat edge of the original

wafer. Using a Cu target X-ray tube as a photon source, the back-reflection Laue photographs [Cul56] of the Si (111) crystals were taken at Prof. Ian J. Burgess's lab (department of Chemistry, U of S). The back-reflection Laue photographs (Figure 4.15B and C) confidently defined the orientation of the Si (111) crystals (Figure 4.14) as compared to the simulated result (Figure 4.15A).

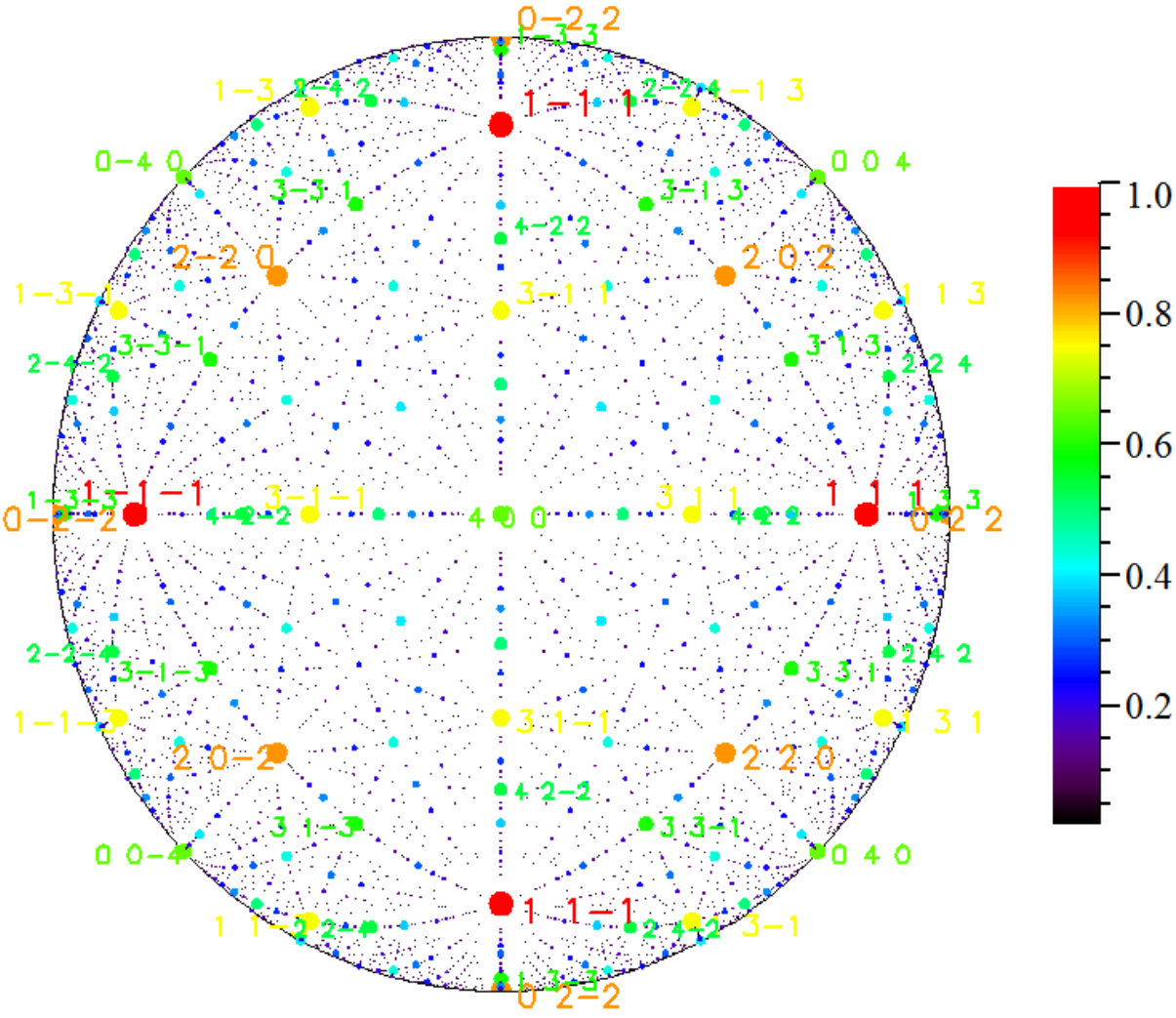

Figure 4.13 Stereographic projection of Si (400) where the relative reflectivity of each plane was mapped by the pseudo-color and the size of the dot and its Miller index label.

To prepare for the second experiment, the original crystals on the BLAs were all replaced by new crystals and freshly mounted to ensure tight bending along the logarithmic spiral contours on the BLA frames. Before mounting the crystals, the Si crystals were orientated at the BMIT beamline at the CLS. The transmission Laue photographs [Cul56] (Figure 4.16B and C) confirmed the orientation of the Si (111) crystals (Figure 4.14) compared with the simulated results (Figure 4.16A).

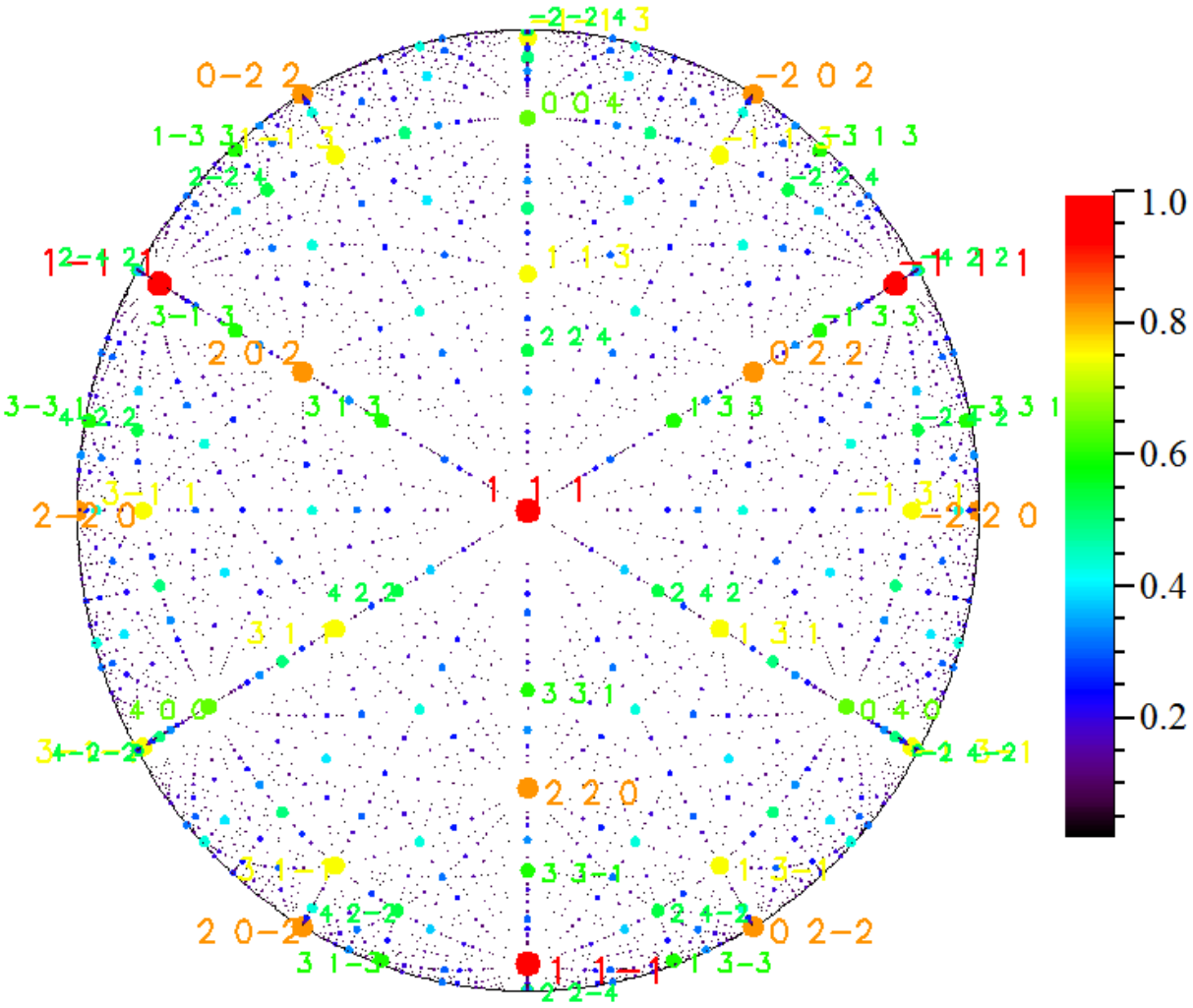

Figure 4.14 Stereographic projection of Si (111) where the relative reflectivity of each plane was mapped by the pseudo-color and the size of the dot and its Miller index label.

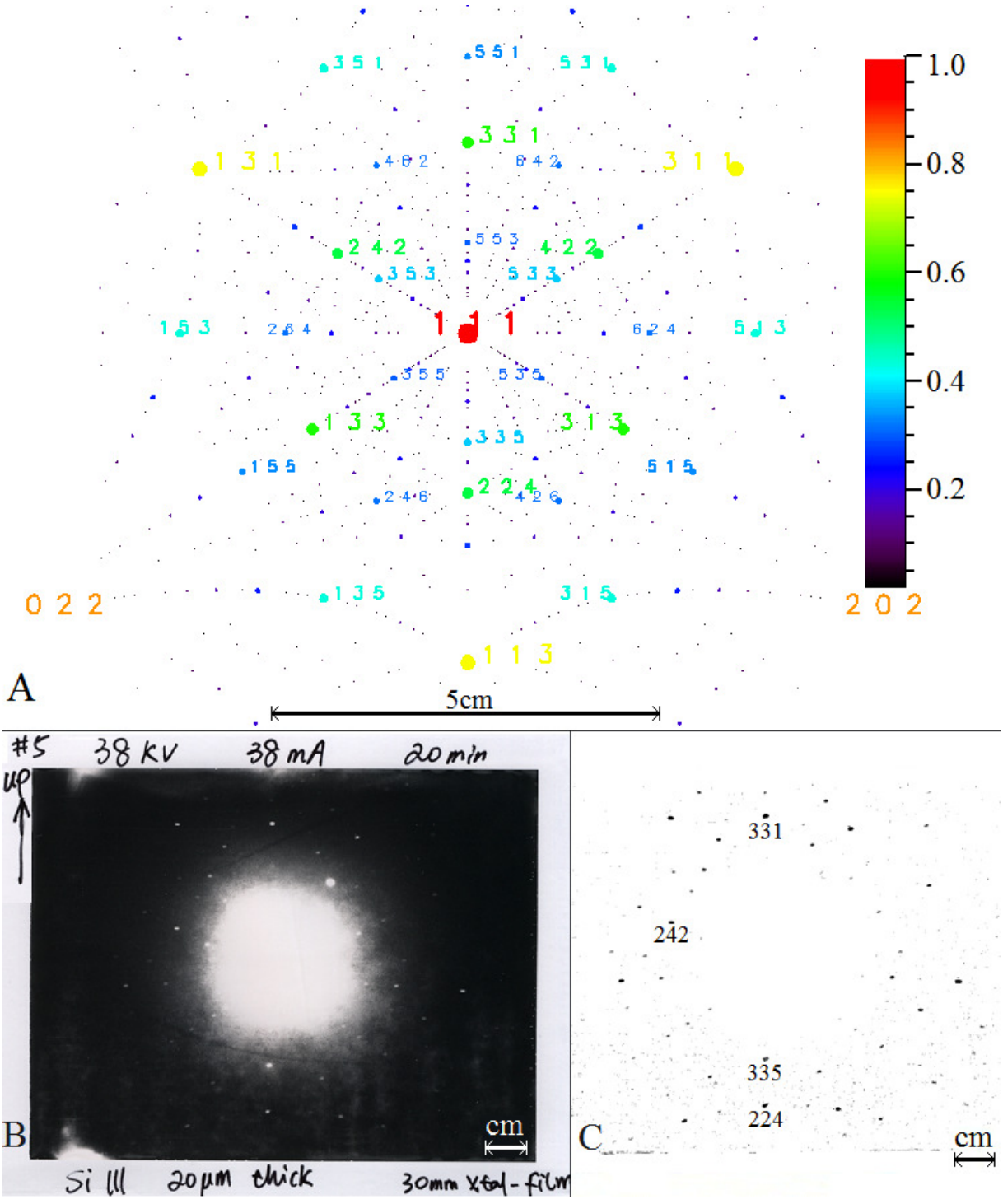

Figure 4.15 Back-reflection Laue photograph of Si (111) of 20 μm thickness was taken by a Cu target X-ray tube at 38 kV tube voltage, 38 mA tube current, 20 minutes exposure time and 30 mm crystal-to-film distance. The simulated result (A) is corresponding to the stereographic projection in Figure 4.14. The original exposure on the film (B) was image processed to the Laue diffraction pattern (C) with some recognized diffraction spots noted.

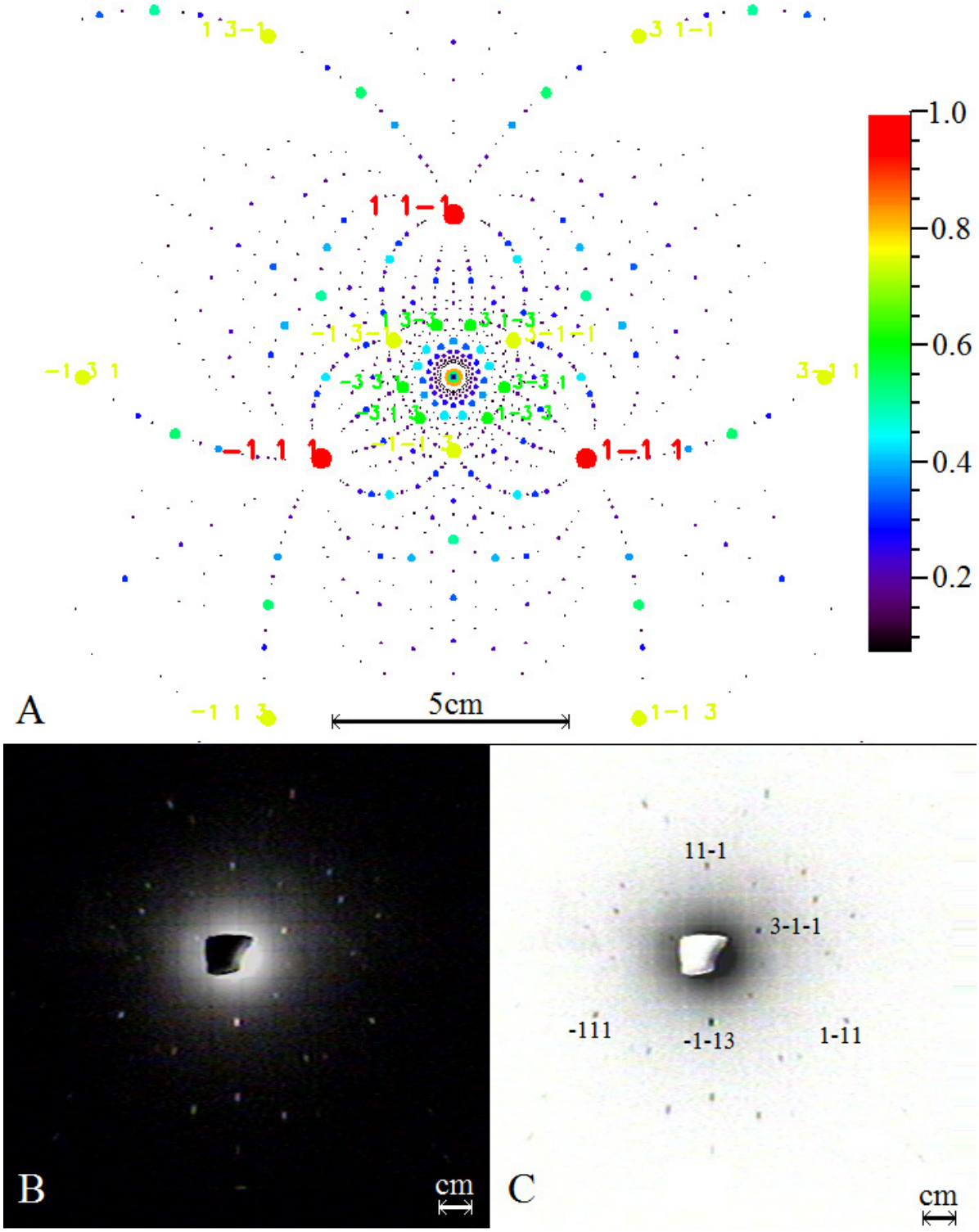

Figure 4.16 Transmission Laue photograph of Si (111) of 20 μm thickness at 50 *mm* crystal-to-film distance obtained at BMIT beamline. The fluorescence screen was taped with a lead beam stop and gridding of 1 *cm* spacing. The simulated result (A) is corresponding to the stereographic projection in Figure 4.14. The original capture (B) was inverted (C) with some spots noted.

4.1.4 Implementation

4.1.4.1 Experimental Setup

The detection system based on the BLA (*-II*) was set up and validated by biological samples at the HXMA beamline at the CLS. As shown in the experimental setup (Figure 4.17), the BLA and two Amptek detectors (XR-100T CdTe with 25 mm^2 detection area and XR-100CR Si with 13 mm^2 detection area from Amptek Inc., Bedford, MA, U.S.) were mounted on a XYZ stage 90° to the incident beam direction in the horizontal plane to minimize the elastic and Compton scattering. Samples were mounted on a XY stage 45° to the incident beam. Two air filled ion chambers were used to measure the beam intensity, a micro ion chamber of 10 *mm* length (from Advanced Design Consulting Inc., U.S.) upstream of the sample and an ion chamber of 15 *cm* plate length downstream of the sample. Our system (Figure 4.17A) was built

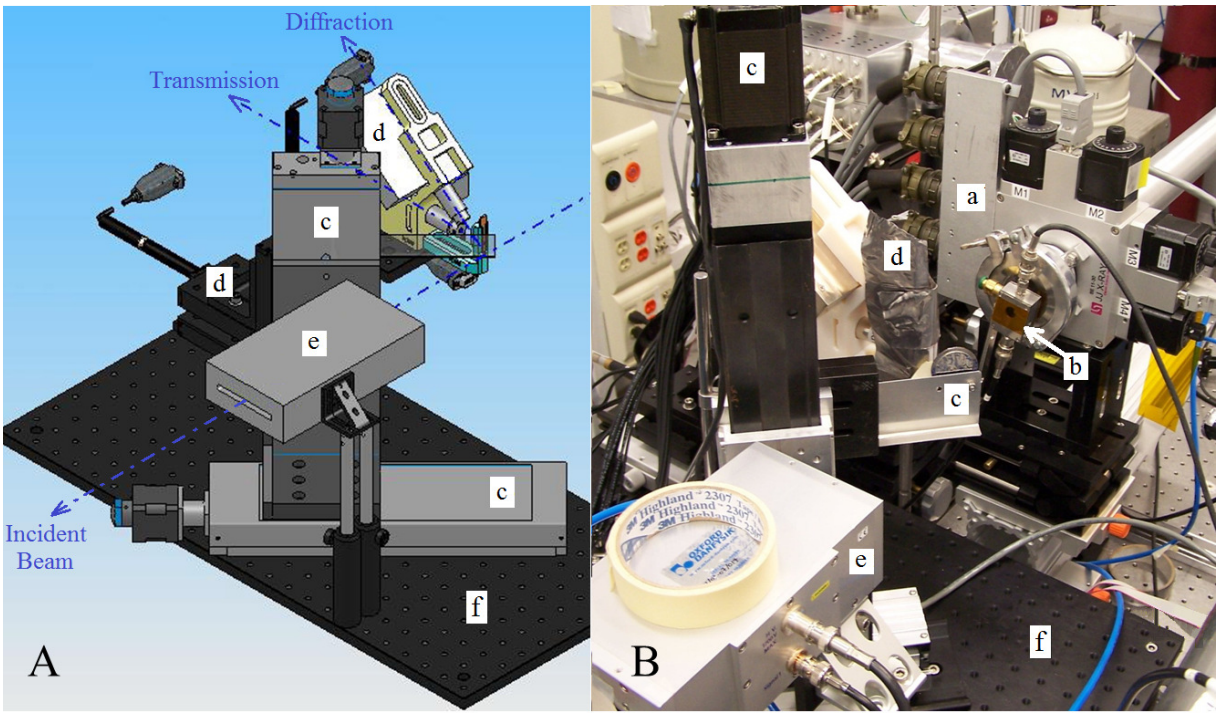

Figure 4.17 The experimental setup at the HXMA beamline (B) showing the JJ X-ray slits (a) and the micro ion chamber (b), and a Solidworks assembly (A) of our system including BLA detection system on a XYZ stage (d), a XY stage for the sample holder (c) and a downstream ion chamber (e) on a black breadboard (f).

on a breadboard (from Thorlabs) for easy carry in during the experiment. The monochromatic energy of the incident beam was set to 6.639 *keV* or 7.212 *keV* which is 100 *eV* above the Mn or Fe K-edge, respectively. Due to the limited space in the microprobe endstation at HXMA beamline, our BLA-based detection system was set up at the X-ray Absorption Fine Structure (XAFS) endstation and used non-focused incident beam as the source. The beam size was limited to 1 *mm* wide by 33 μm high by continuously adjusting the slits (from JJ X-Ray A/S, Denmark) in one direction to avoid backlash effects.

4.1.4.2 Vertical Beam Size Measurement

The JJ X-Ray slits were used to set the vertical beam size. However, the sample was located downstream (~100 *mm*) of the slits and since the beam was divergent a measurement of the vertical beam size was necessary. A tungsten blade was mounted on the sample stage and vertically scanned across the beam to measure the vertical beam size after the slits. A scanning speed of 4.167 $\mu m/s$ and a pulse time of 100 *ms* made a step size of 0.4167 μm between the successive measurement points. To find the minimum vertical beam size after the slits, several vertical slit gaps were set and the photon counts after the scanning blade were recorded by the downstream ion chamber (Figure 4.18). The blade scanning results were smoothed by averaging and the first derivatives were taken based on the smoothed data to get the full width at half maximum (FWHM) of the derivative peak. From the FWHMs of the first derivative at different vertical gap settings of the slits (Figure 4.18C), a minimum of 25 μm of the FWHM was achieved at 90 μm gap setting of the vertical slit. Full beam intensity without the blade was recorded when the vertical gap of the slit was increased from 50 μm where no intensity was observed until 90 μm where the minimum FWHM was achieved in the previous test. Back projection along the data line in Figure 4.18D easily estimated a vertical beam size of 33 μm

at 90 μm gap setting of the vertical slit.

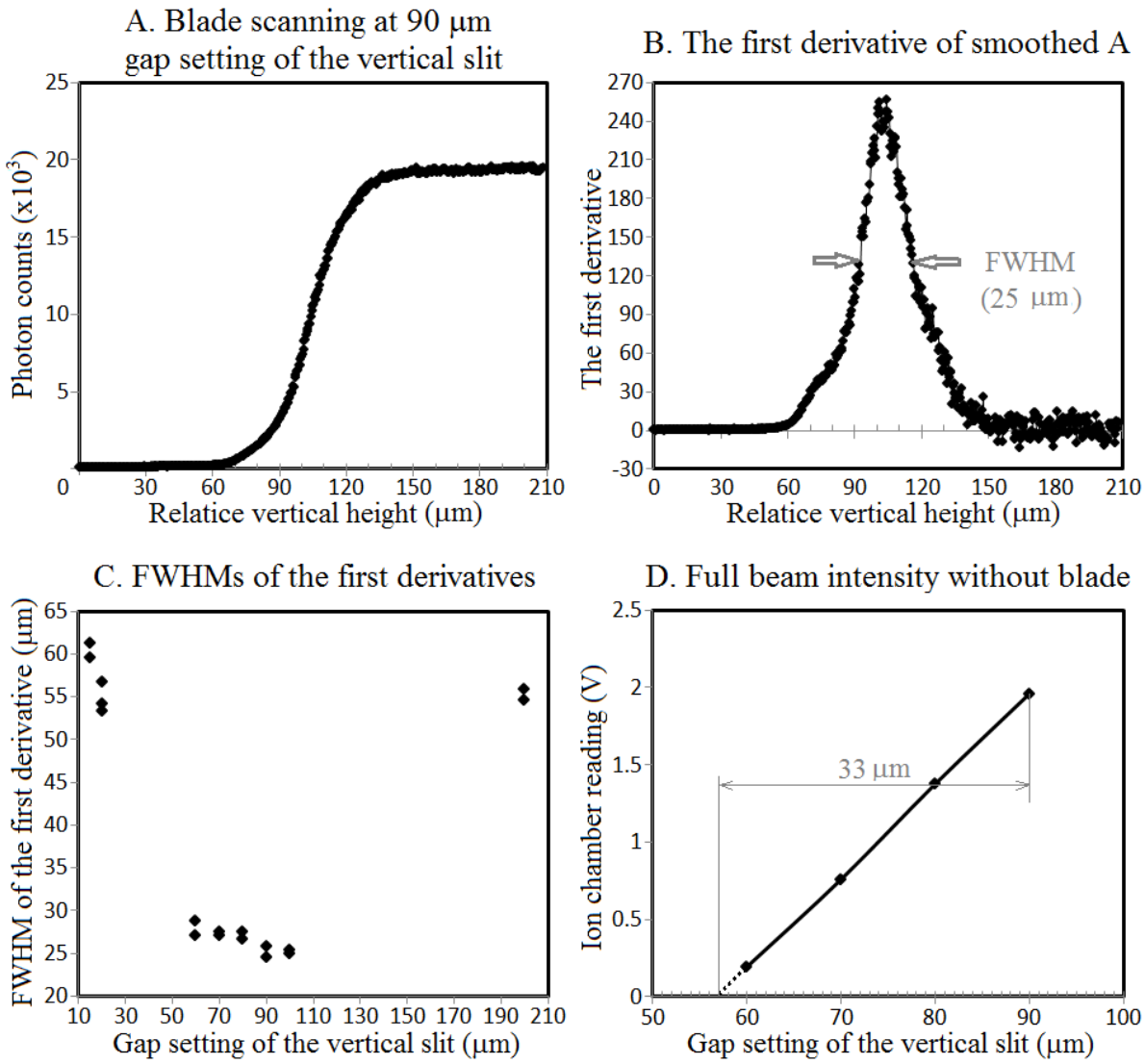

Figure 4.18 Vertical beam size measurement results. Setting the vertical gap of the JJ X-Ray slits as 90 μm, photon counts after the vertically scanning blade was recorded (A) and its first derivative (B) was calculated from the smoothed A. The FWHM of the first derivative was measured at different vertical gap settings of the slits (C). The full beam intensity measurement (D) estimated the vertical beam size of 33 μm at the 90 μm of the slits gap setting.

4.1.4.3 Combined Resolution Measurement

A Mn foil sample (44.8 $\mu g/cm^2$ of Mn on Mylar of 2.5 μm thick, from Micromatters Inc.) was irradiated by an incident beam of 6.639 keV. The Mn K_α fluorescence was recorded by the

Amptek Si detector in both the transmission and diffraction directions while the whole detection system was in vertical (Bragg angle) scanning motion (Figure 4.19). It should be noted that moving the BLA in the vertical direction effectively changes the Bragg angle when the source of fluorescence is fixed. There is a slight coupling of Bragg angle with the source to crystal distance s. Since the range of vertical motion Δy is small, the change of source to crystal distance Δs (s'-s) is small. It could be easily derived that

$$\Delta s = \frac{1}{2}\frac{s'}{s^2}(\Delta y)^2 \approx \frac{1}{2s}(\Delta y)^2 \tag{4.1}$$

Despite the different dwell time in the data collections (0.1 s for the transmission measurement and 25 s for the diffraction measurement), a strong peak of the diffracted Mn fluorescence was observed to correspond to the dip in the transmitted Mn fluorescence at the

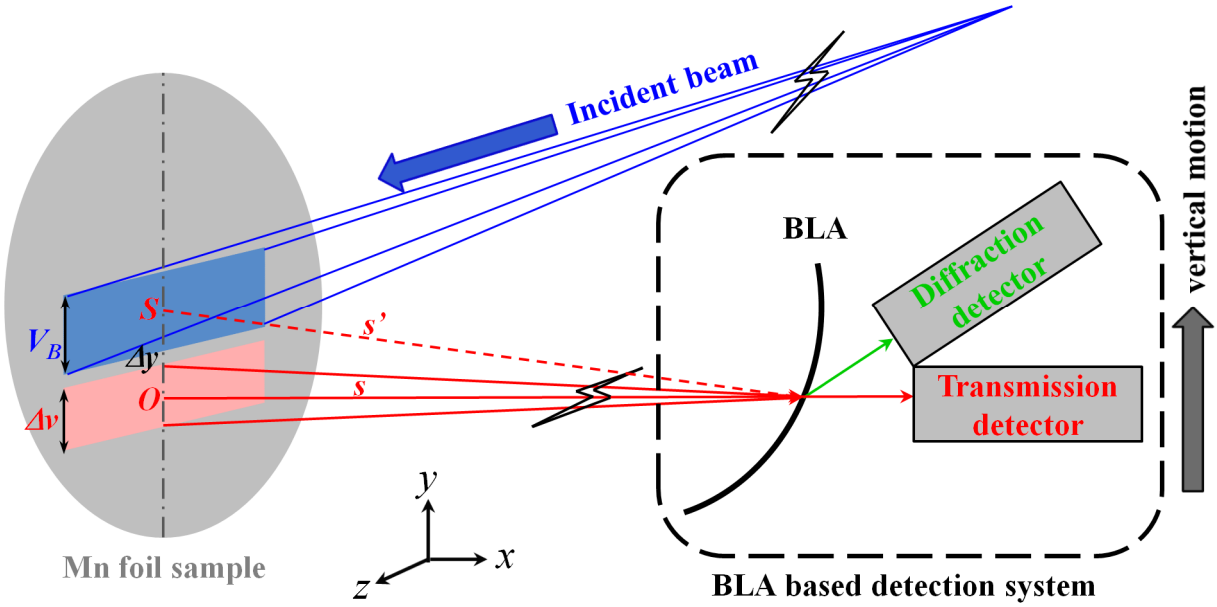

Figure 4.19 Combined resolution measurement setup. The BLA-based detection system (dashed rectangle) was vertically scanning the Mn foil sample (grey oval) which was irradiated by an incident beam of 6.639 *keV*. *O* is the origin of the BLA logarithmic spiral, *S* is the source of fluorescence, s is the source to crystal (BLA) distance, Δy is the vertical motion distance *OS*. V_B is the vertical size of the incident beam (blue parallelogram), Δv is the vertical size of the detectable region of the BLA (pink parallelogram).

exactly same 11.35 *mm* relative vertical height (Figure 4.20). The measured FWHM of about 60 μm in both peaks should be a convoluted result from the real vertical size of the detectable region (Δv) and the vertical beam size of 33 μm (V_B) which was measured in section 4.1.4.2. The sharp peak and the sharp dip indicated that the real vertical size of the detectable region Δv was close to the vertical beam size V_B. A flat top in the peak or a flat bottom in the dip would show up if the real vertical size of the detectable region Δv was quite different from the vertical beam size V_B in either side (bigger or smaller). Assuming both Δv and V_B comply with normal (or Gaussian) distribution, the FWHM of the convoluted peak is,

$$FWHM = \sqrt{(V_B)^2 + (\Delta v)^2} \tag{4.2}$$

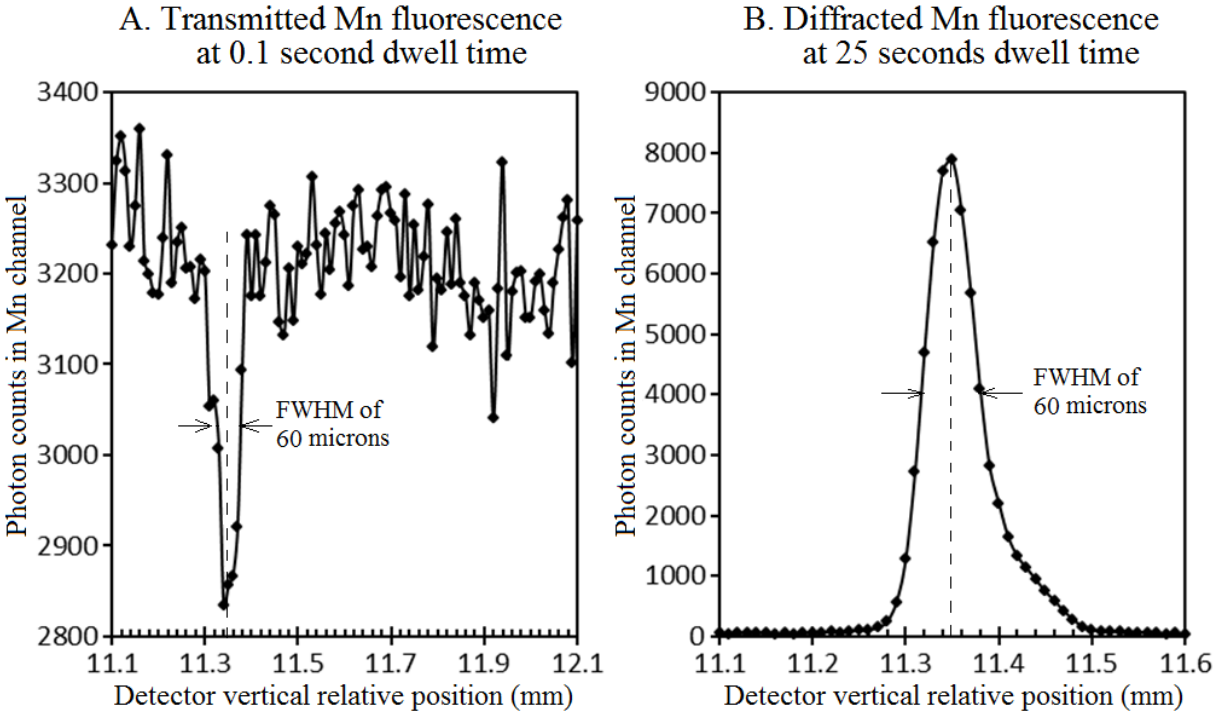

Figure 4.20 The transmitted (A) and diffracted (B) Mn K_α fluorescence from the Mn foil at 6.639 *keV* incident energy were collected by the Amptek Si detector while the whole detection system was in vertical scanning motion. The dashed lines indicate that both the dip (A) and the peak (B) occurred at the same relative height of 11.35 *mm* with FWHM of about 60 μm.

Then the real vertical size of the detectable region (Δv) was calculated as 50 μm and the energy resolution ΔE was calculated as 34.5 eV according to energy bandwidth equation

$$\frac{\Delta E}{E} = \frac{\Delta \theta}{tg\theta_B} = \frac{\Delta v}{s \cdot tg\theta_B} \tag{4.3}$$

Where the E is detected Mn K_α fluorescence energy, θ_B is the Bragg angle of the Mn K_α fluorescence incident on {111} plane of Si and s is the source to crystal distance (Table 4.1, 24 mm for the BLA -*II*). Both results were sufficiently close to the theoretical values (Table 4.1, 21 μm for the vertical size of detectable region Δv and 14.4 eV for the energy resolution ΔE).

4.1.5 The First Experiments

This detection system was first validated by collecting Mn fluorescence from Mn and Fe foils, imaging gelatin calibration samples and adult *Drosophila* in March 2009.

4.1.5.1 Spectra from Mn and Fe Foils

The XRF spectra of the Mn foil and an Fe foil (46.0 $\mu g/cm^2$ of Fe on Mylar of 2.5 μm thick, from Micromatters Inc.) which were overlapped back to back were collected for 5 minutes by the Amptek Si detector at 7.212 keV incident energy (Figure 4.21). The Mn K_α fluorescence (5.895 keV) was the only strong peak in the diffracted spectrum (Figure 4.21B), whereas it was a much smaller peak in the transmitted spectrum (Figure 4.21A). But the count rate of the Mn K_α fluorescence in the diffracted spectrum reduced to nearly 1/3 of that in the transmitted one. Mn K_β fluorescence (6.490 keV) was estimated to overlap with the Fe K_α fluorescence (6.400 keV). Fe K_β fluorescence (7.058 keV) was estimated on top of the Compton scattering (7.112 keV) and elastic scattering.

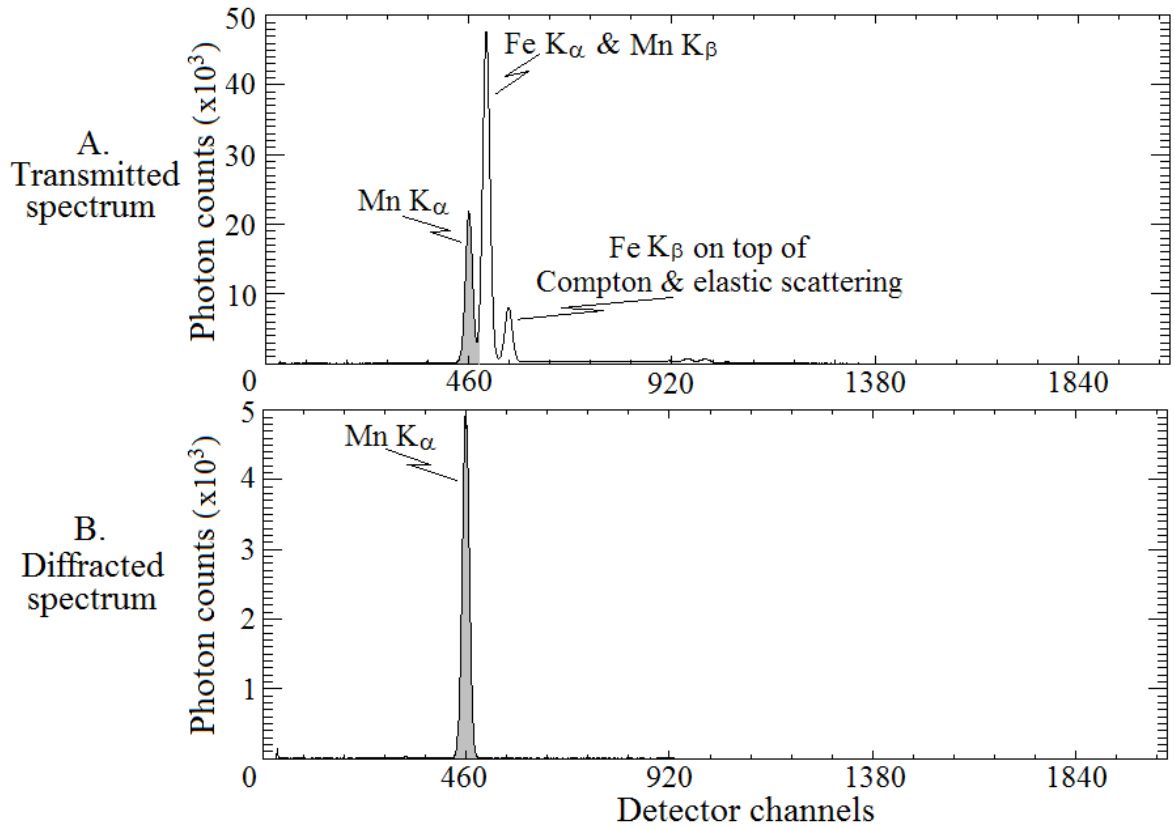

Figure 4.21 The transmitted (A) and diffracted (B) spectra of the overlapped Mn and Fe foils were collected for 5 minutes by the Amptek Si detector with 2048 channels at 7.212 *keV* incident energy. The Mn fluorescence (grey shadow) peaked at channel 460.

4.1.5.2 XRF Imaging of Gelatin

Manganese chloride was dissolved in 10% gelatin to give final concentrations ranging from 500 *mM* down to 0.05 μM. The warm Mn-gelatin solutions were transferred into a multi-well plastic plate and allowed to harden (Figure 4.22). This gelatin calibration sample was raster scanned by the BLA (*-II*) detection system at a speed of 1 *mm/s*, 1 *mm* step size and 1 *s* dwell time at 6.639 *keV* incident energy. The images from the Amptek Si detector in the diffraction direction showed that the diffracted Mn fluorescence (Figure 4.23B) nearly occupied the entire diffracted spectra (Figure 4.23A) whereas it was not the case in the images from the Amptek CdTe detector in the transmission direction (Figure 4.24). This means that the BLA efficiently

diffracted the signals of Mn fluorescence while greatly limited the elastic scattering, Compton scattering and other noise. The Figure 4.23C showed that the Mn concentration of 12.5 *mM* can be easily detected. The circular patterns in the images suggested that the BLA detection system was sensitive to depth because the surface of the gelatin sample was not flat, but concave in each well.

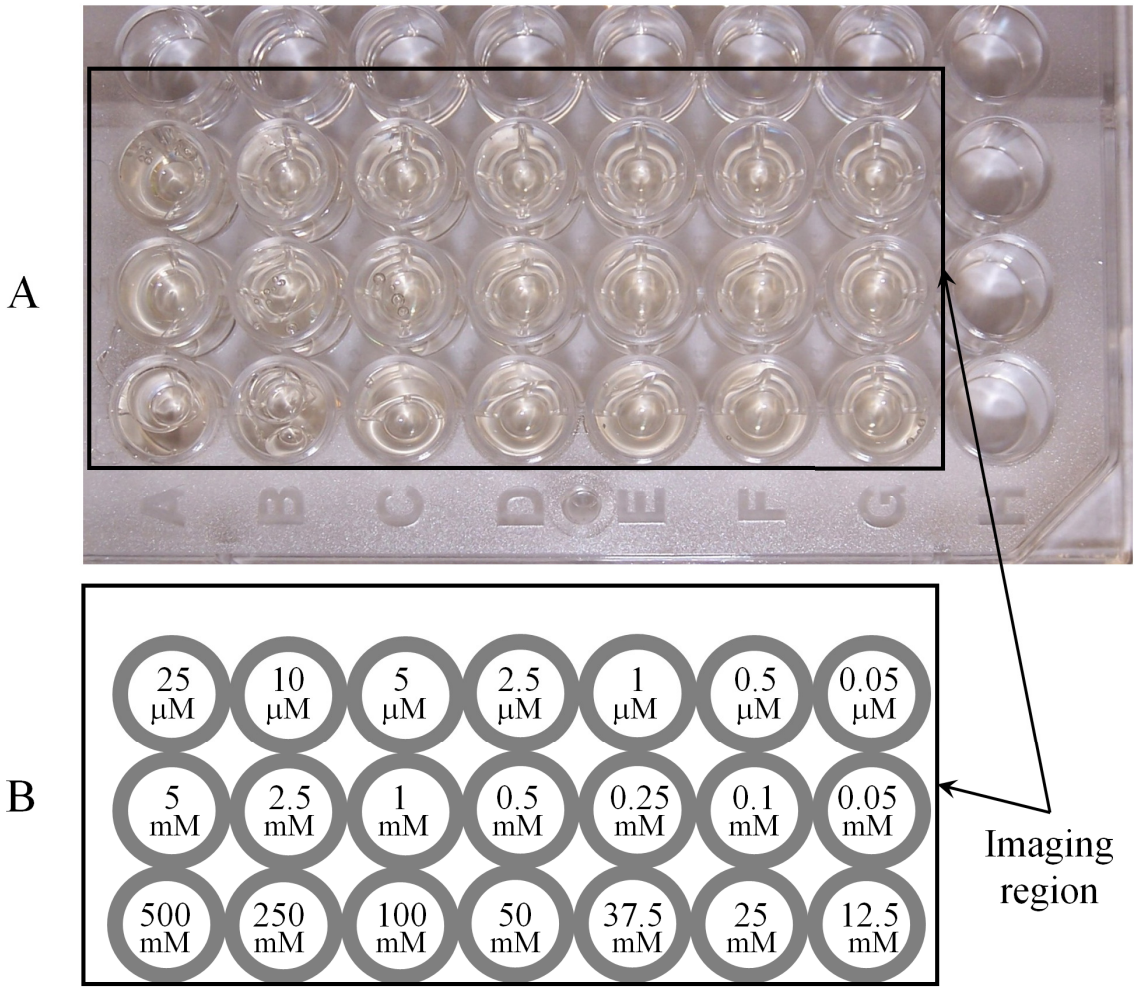

Figure 4.22 Gelatin calibration sample (A) and the pattern of the Mn concentrations within the multi-well (B) both with the imaging region noted by the black rectangle.

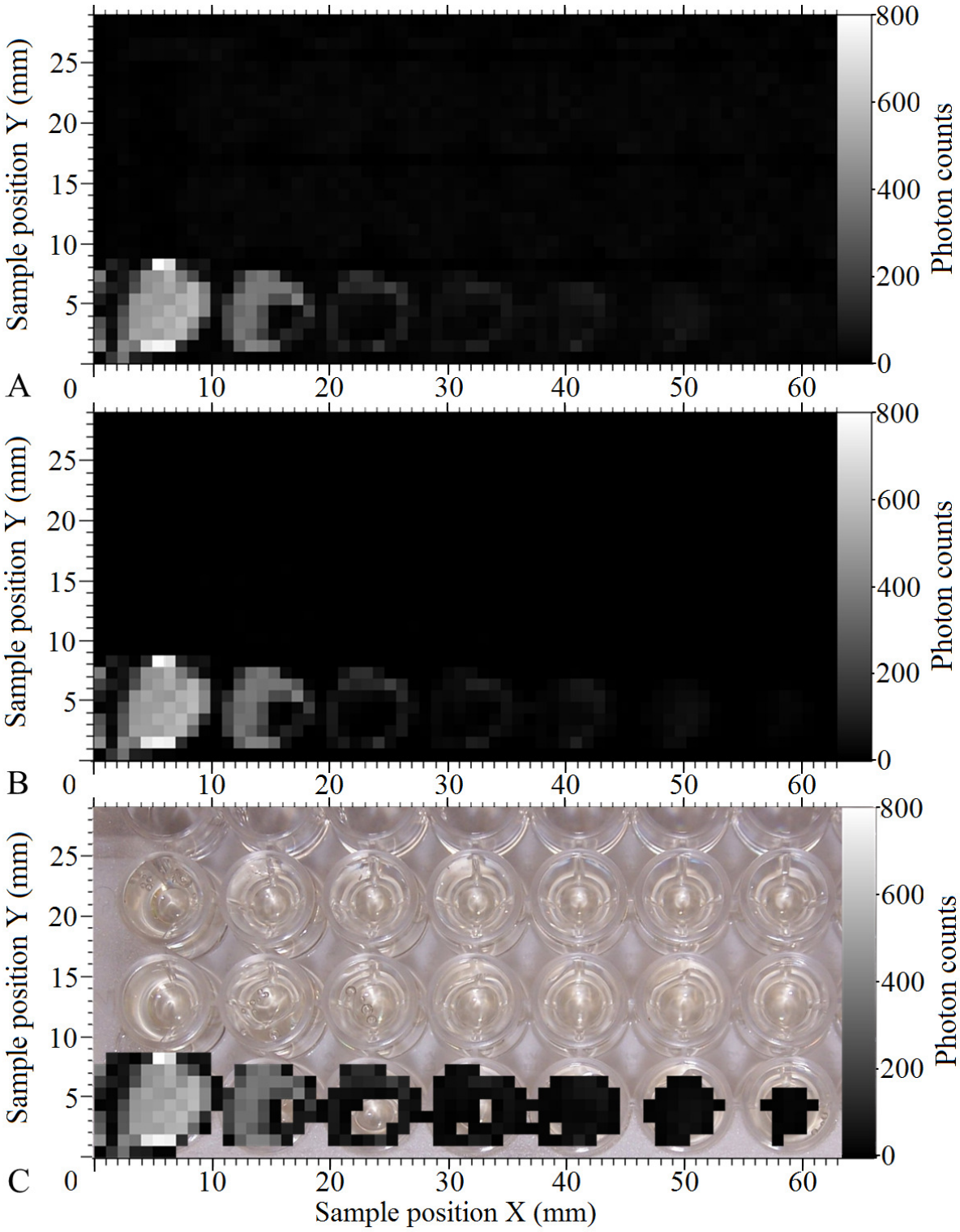

Figure 4.23 All spectra image (A) and the Mn fluorescence image (B) of the gelatin sample diffracted to the Amptek Si detector. Setting 0-count-pixels as transparent, the Mn fluorescence image (B) was overlapped on top of the gelatin sample photo to make the composite image (C).

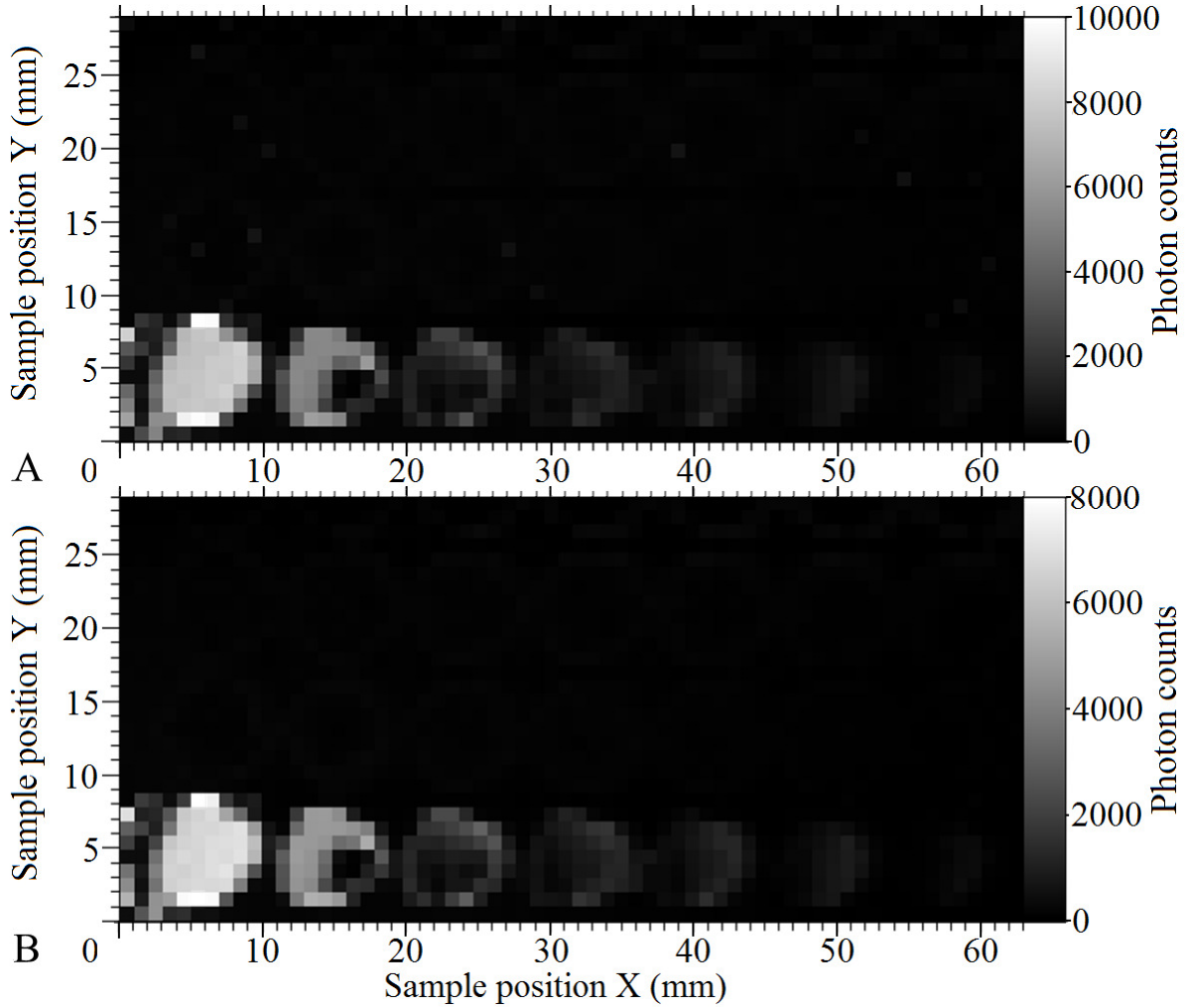

Figure 4.24 All spectra image (A) and the Mn fluorescence and elastic scattering image (B) of the gelatin sample transmitted to the Amptek CdTe detector.

4.1.5.3 XRF Imaging of Drosophila

Drosophila were fed on standard yeast/cornmeal *Drosophila* diet supplemented with Mn ranging from 0.5-100 *mM* concentrations (Table 4.2) and packed on a Lucite plate by metal-free Mylar tape (Matrix Technology Ltd.) in 6 groups (Figure 4.25). The *Drosophila* sample was raster scanned by the BLA (*-II*) detection system at a speed of 1 *mm/s*, 0.5 *mm* step size and 0.5 *s* dwell time at 6.639 *keV* incident energy. The diffracted Mn fluorescence (Figure 4.26B) occupied the most part of the diffracted spectra (Figure 4.26A) whereas the transmitted Mn

Table 4.2 Concentrations of $MnCl_2.4H_2O$ in the *Drosophila* diet

Drosophila group number	*#1*	*#2*	*#3*	*#4*	*#5*	*#6*
Mn concentration (*mM*)	100	75	50	25	1	0.5

Figure 4.25 *Drosophila* sample in the imaging setup (A) and the *Drosophila* sample photo (B) noted with the imaging region (black rectangle) and the *Drosophila* packing groups (while lines) with group numbers (1 - 6).

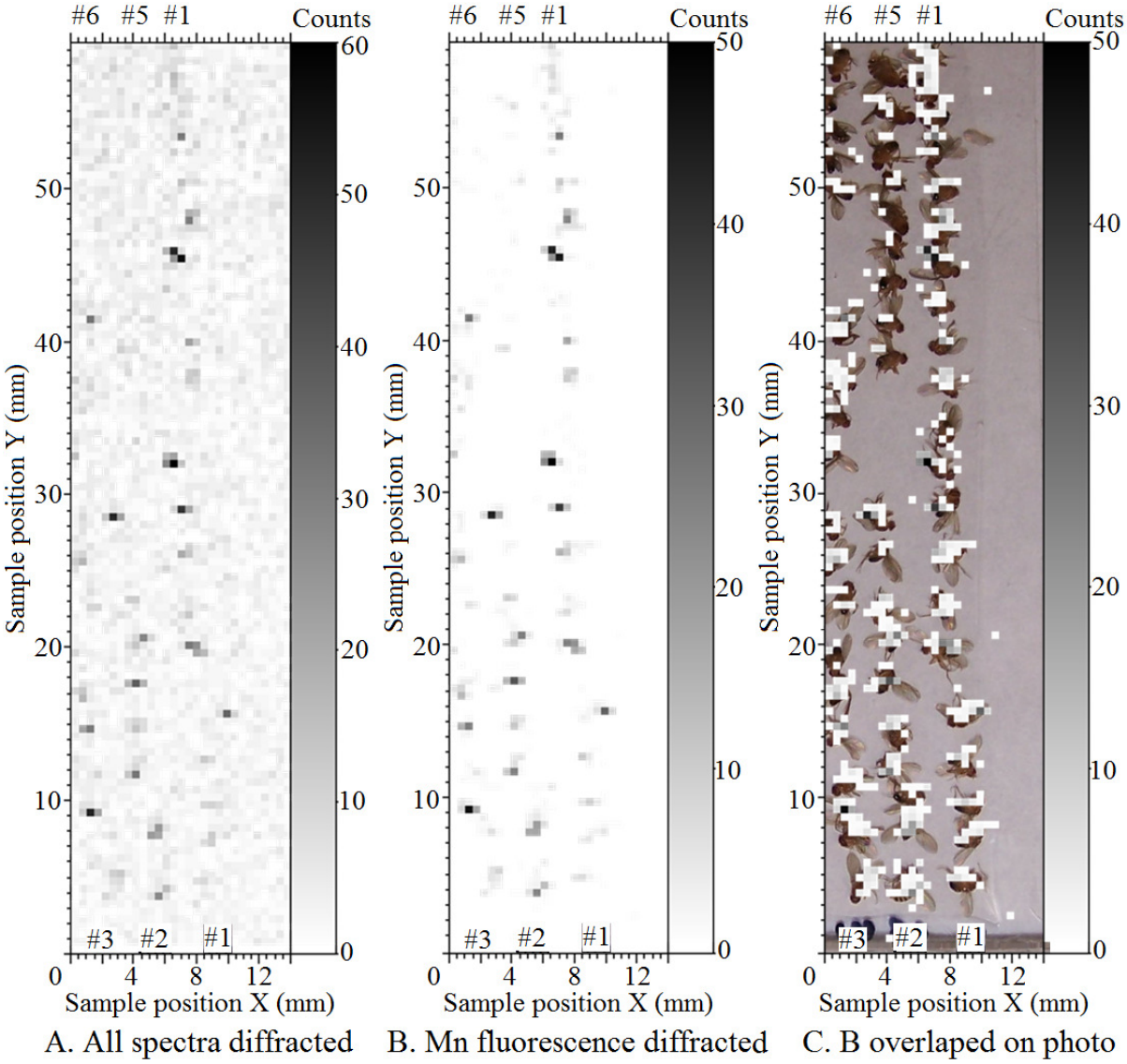

Figure 4.26 All spectra image (A) and the Mn fluorescence image (B) of the *Drosophila* sample diffracted to the Amptek Si detector. Setting 0-count-pixels as transparent, the Mn fluorescence image (B) was overlapped on top of the *Drosophila* sample photo to make the composite image (C).

fluorescence (Figure 4.27B) was less prominent in the transmitted spectra (Figure 4.27A). Excellent correlations were observed between the Mn fluorescence signals and the *Drosophila* positions in both of the diffracted and transmitted Mn fluorescence images (Figure 4.26C, Figure 4.27C). This correlation was stronger among the *Drosophila* groups fed on higher Mn

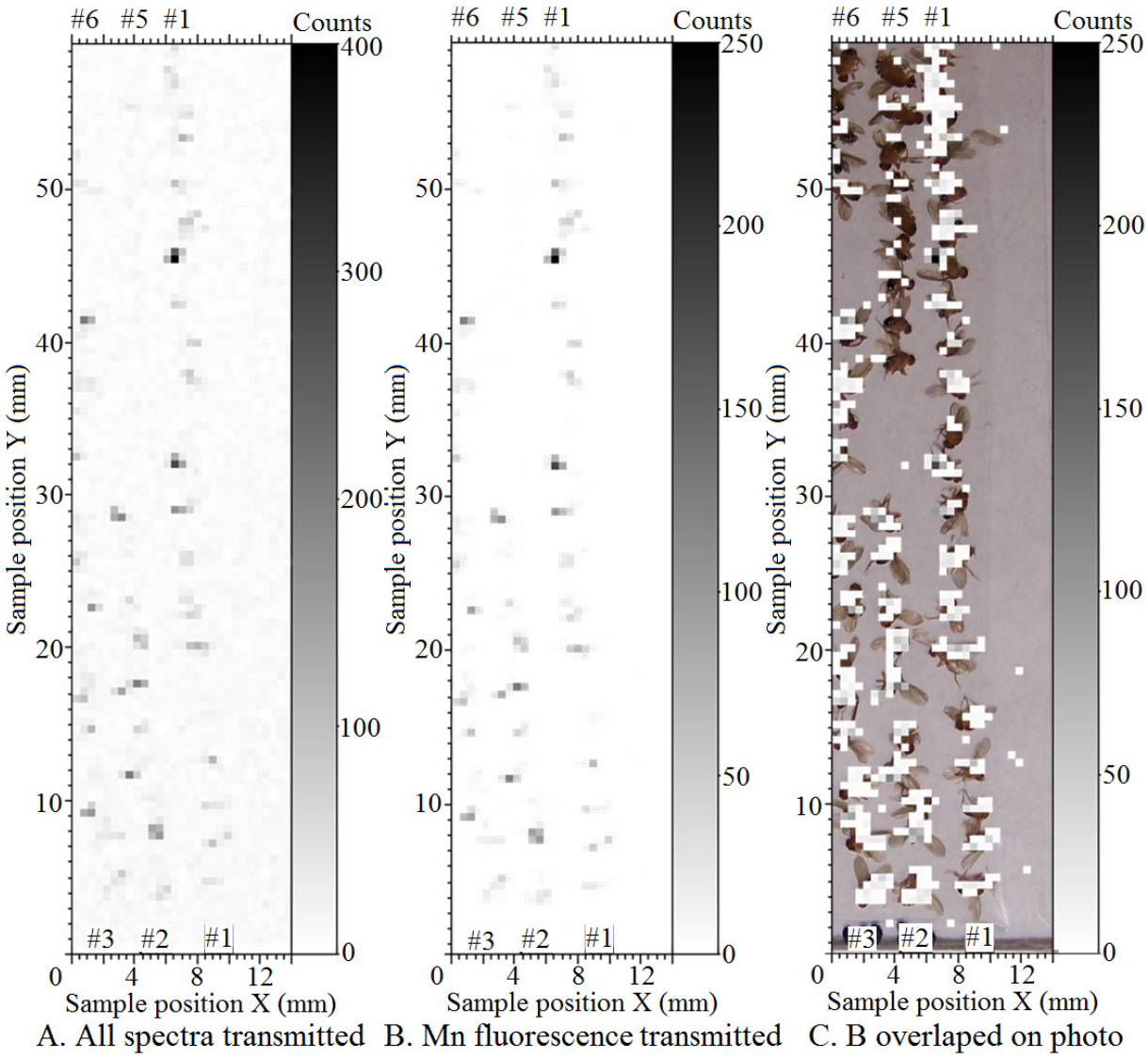

Figure 4.27 All spectra image (A) and the Mn fluorescence image (B) of the *Drosophila* sample transmitted to the Amptek Si detector. Setting 0-count-pixels as transparent, the Mn fluorescence image (B) was overlapped on top of the *Drosophila* sample photo to make the composite image (C).

concentrations (#1-3), but weaker among groups on lower Mn concentrations (#5-6) as expected. The correlation of Mn signals with the *Drosophila* group #6 indicated that the detection limit of 0.5 *mM* can be achieved by the BLA (*-II*) detection system.

4.1.6 The Second Experiment

The same detection system based on the BLA (-*II*) mounted with a new crystal was set up at the HXMA beamline at the CLS in May 2010. The beam size was limited to 100 μm wide and 100 μm high for most tests by continuously adjusting the slits (from JJ X-Ray A/S, Denmark) in one direction to avoid backlash effects. This detection system was tested by XRF imaging of Mn and Fe solutions in tubing and human brain slices.

4.1.6.1 XRF Imaging of Mn and Fe Solutions

A series of solutions with different combinations of Mn and Fe concentration were prepared from $MnCl_2.4H_2O$ and $FeCl_3.6H_2O$ crystals (Table 4.3). The solutions were injected into 31 pieces of polyethylene tubing (Intramedic^{TM} PE160, 1.14 *mm* I.D., 1.57 *mm* O.D.) and packed on a Lucite plate in sequence (from #1 tubing on the top to #31 on the bottom). The tubing sample was raster scanned at a speed of 2 *mm/s* by the BLA detection system. Both the Amptek CdTe detector in the transmission direction and the Amptek Si detector in the diffraction direction were set up with channels for Mn K_α and Fe K_β fluorescence photons. Setting the incident energy at 6.639 *keV* (100 *eV* above Mn K-edge) only excited the Mn and thus obtained "Fe off" images (Figure 4.28). Setting the incident energy at 7.212 *keV* (100 *eV* above Fe K-

Table 4.3 Concentrations of $MnCl_2.4H_2O$ and $FeCl_3.6H_2O$ in the tubing sample

Tubing number (from top to bottom)	*$MnCl_2.4H_2O$ Concentration (mM)*	*$FeCl_3.6H_2O$ concentration (mM)*
#1	100	0
#2	75	0.001
#3	50	0.01
#4	25	0.0125
#5	10	0.025

#6	8.75	0.0375
#7	7.5	0.05
#8	6.25	0.0625
#9	5	0.075
#10	3.75	0.0875
#11	2.5	0.1
#12	1.25	0.125
#13	1	0.25
#14	0.875	0.375
#15	0.75	0.5
#16	0.625	0.625
#17	0.5	0.75
#18	0.375	0.875
#19	0.25	1
#20	0.125	1.25
#21	0.1	2.5
#22	0.0875	3.75
#23	0.075	5
#24	0.0625	6.25
#25	0.05	7.5
#26	0.0375	8.75
#27	0.025	10
#28	0.0125	25
#29	0.01	50
#30	0.001	75
#31	0	100

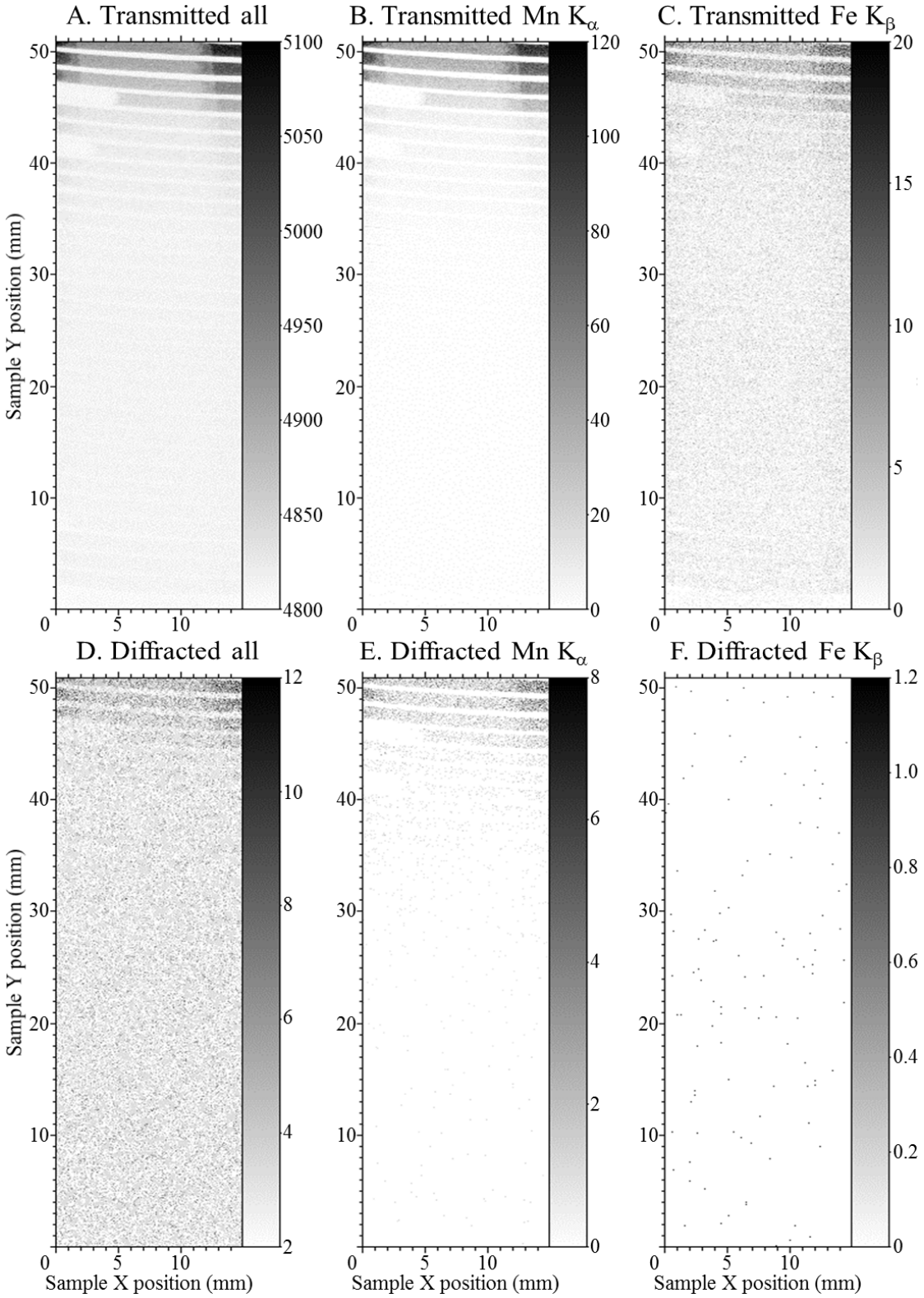

Figure 4.28 "Fe off" images of the tubing sample of Mn and Fe solutions. The intensity bars on the right side of images denote the normalized photon counts.

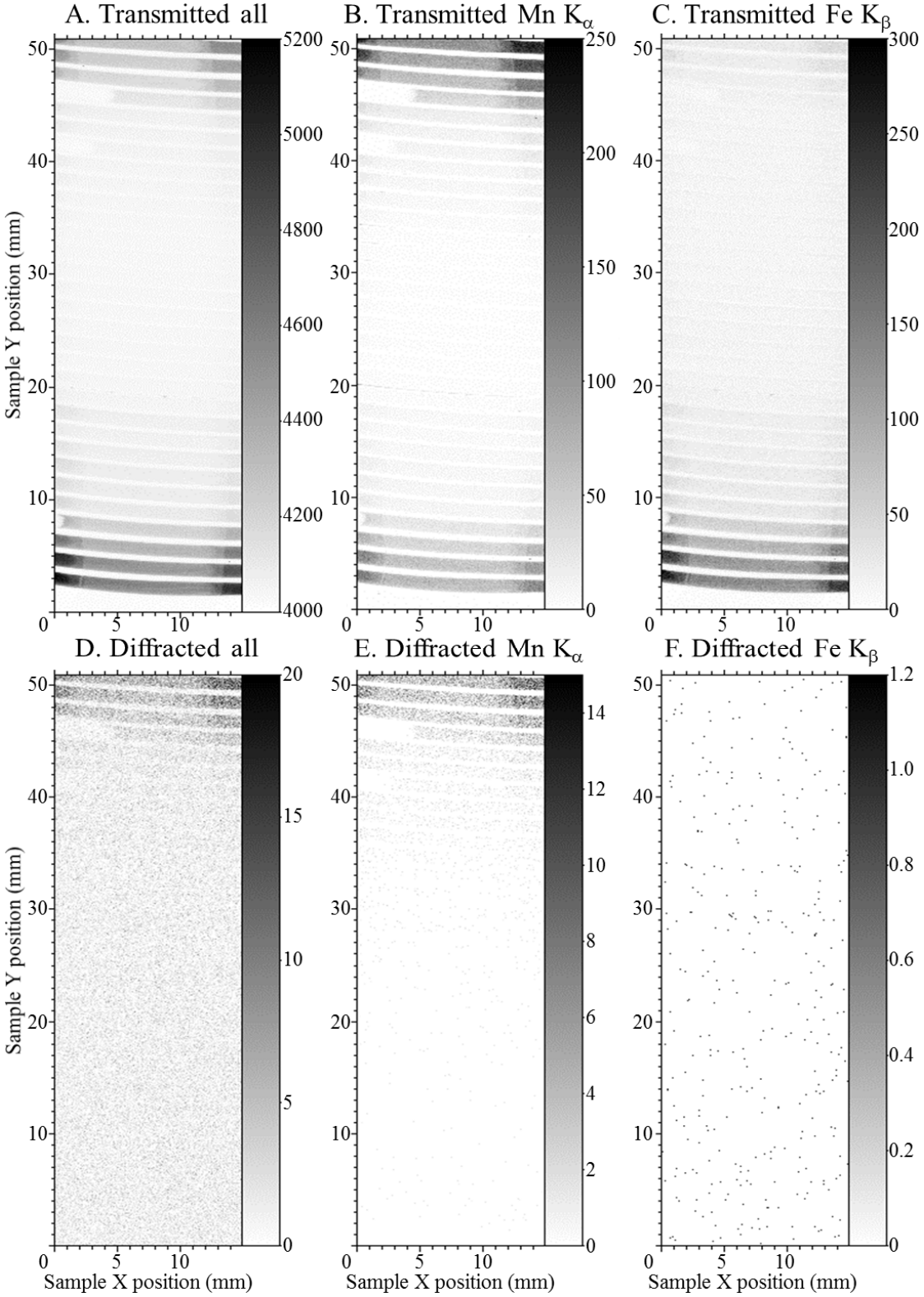

Figure 4.29 "Fe on" images of the tubing sample of Mn and Fe solutions. The intensity bars on the right side of images denote the normalized photon counts.

edge) excited both the Mn and Fe and hence resulted "Fe on" images (Figure 4.29). In the images from Figure 4.28 and Figure 4.29, missing signals on one side of several tubes corresponded to air in the tubes, and the stronger signals on both ends resulted from the tape on the center region.

From the detector report, the FWHM of the Amptek Si detector at 5.9 *keV* is 209 *eV* and the FWHM of the Amptek CdTe detector at 59.5 *keV* is 694 *eV*. The coarse energy resolution of the Amptek detectors explained the mutual invasion between the Mn and Fe fluorescence channels. For example, a little Mn K_β fluorescence invaded into the Fe K_β channel (C in Figure 4.28-29), a lot of Fe K_α intruded into the Mn K_α channel (Figure 4.29B). This phenomenon did not happen in the diffracted images due to the use of the BLA, that is, no Fe fluorescence was detected in the Mn channels (Figure 4.29E) and no Mn fluorescence in the Fe channels (F in Figure 4.28-29). Actually no signal was detected in the Fe channels even in the "Fe on" image (Figure 4.29F). This provided convincing evidence that the BLA was properly designed and made for the detection of Mn K_α fluorescence, not the Fe fluorescence.

However it was noticed that the diffracted Mn K_α fluorescence was only a small fraction of the transmitted Mn K_α fluorescence (E vs. B in Figure 4.28-29). It would not be accurate to interpret the detection limit of Mn fluorescence based on these weak diffracted images.

4.1.6.2 XRF Imaging of Human Brains

Five pieces of human brain of the substantia nigra region were selected from a collection of Dr. Ali Rajput (U of S). The brain tissues were formalin fixed with gelatin, sliced to about 1 *mm* thick, heat sealed by metal-free polyproplene film (from Goodfellow Cambridge Ltd., 30 μm thick) and taped onto a metal-free Lucite plate for raster scanning for fluorescence imaging. Four pieces of brain slice (Figure 4.30) were imaged during the second beamtime at the HXMA

beamline, three of which were from PD patients and one was a control who died from head injury. The human brain samples were treated under protocol #06-250 approved by the U of S Biomedical Research Ethics Board (Bio-REB).

The incident energy was set to 7.212 *keV* to excite both the Mn and Fe. The brain samples were raster scanned by the same BLA detection system. Both the Amptek CdTe detector in the transmission direction and the Amptek Si detector in the diffraction direction were set up with channels for Mn K_α and Fe K_β fluorescence photons. The same distribution pattern was

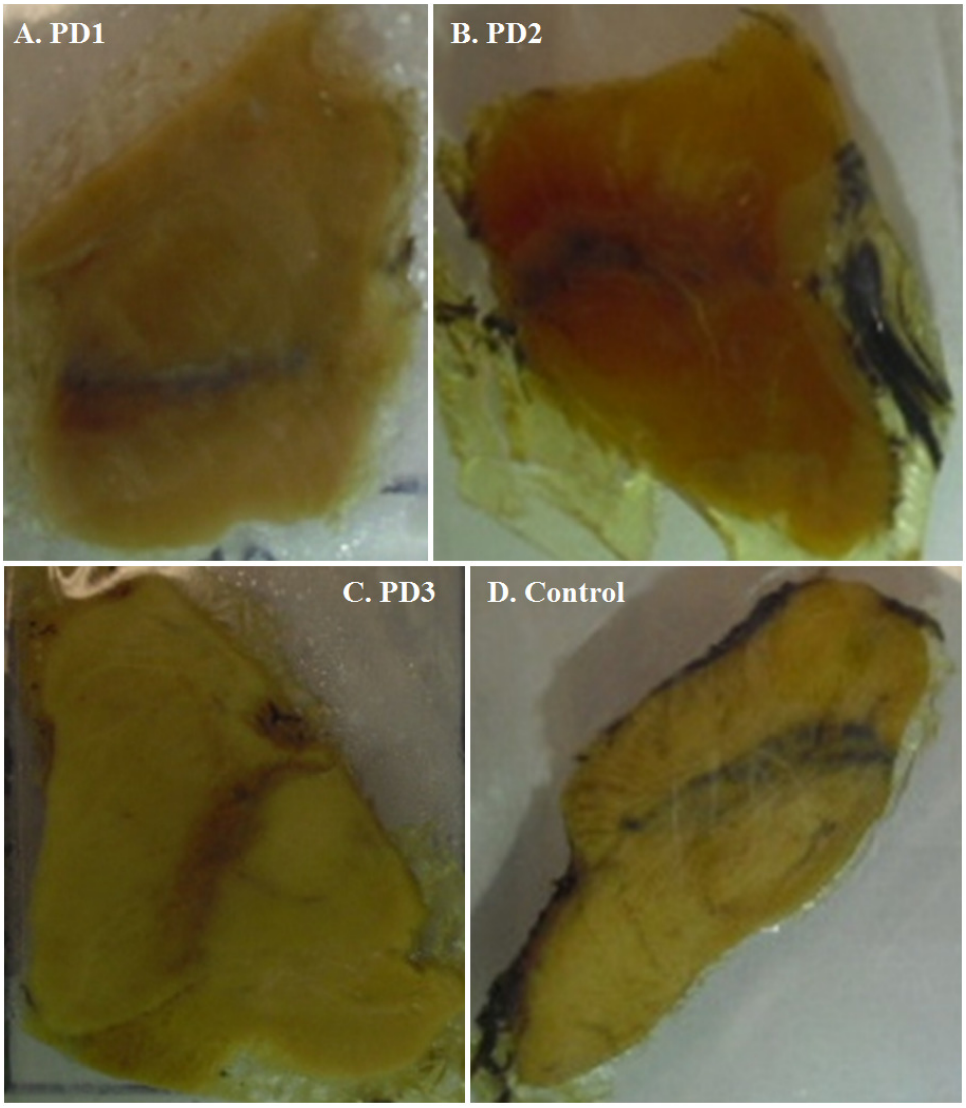

Figure 4.30 Human brain slices from PD patients (A-C) and a control (D).

found between images of transmitted Mn K_α and Fe K_β due to the mutual invasion between the Mn and Fe fluorescence channels in the Amptek CdTe detector (B vs. C in Figure 4.31-4.34). Despite of the weak diffraction from the brain samples, a different distribution pattern was discernible in the diffracted Mn K_α and Fe K_β images which provided evidence that no Fe fluorescence invaded into the Mn channels (E vs. F in Figure 4.31-4.34). Actually no signal was detected in the diffracted Fe channels (F in Figure 4.31-4.34). This again showed that the BLA was successfully made to specifically detect Mn K_α fluorescence, not the Fe fluorescence.

Unfortunately it was noticed that the diffracted Mn K_α fluorescence was only a small fraction of the transmitted Mn K_α fluorescence (E vs. B in Figure 4.31-34). Even if no noticeable difference was observed between the Mn distributions in the PD brains and the control brain (E in Figure 4.31-34), it is hard to draw a firm conclusion based on these weak diffracted images.

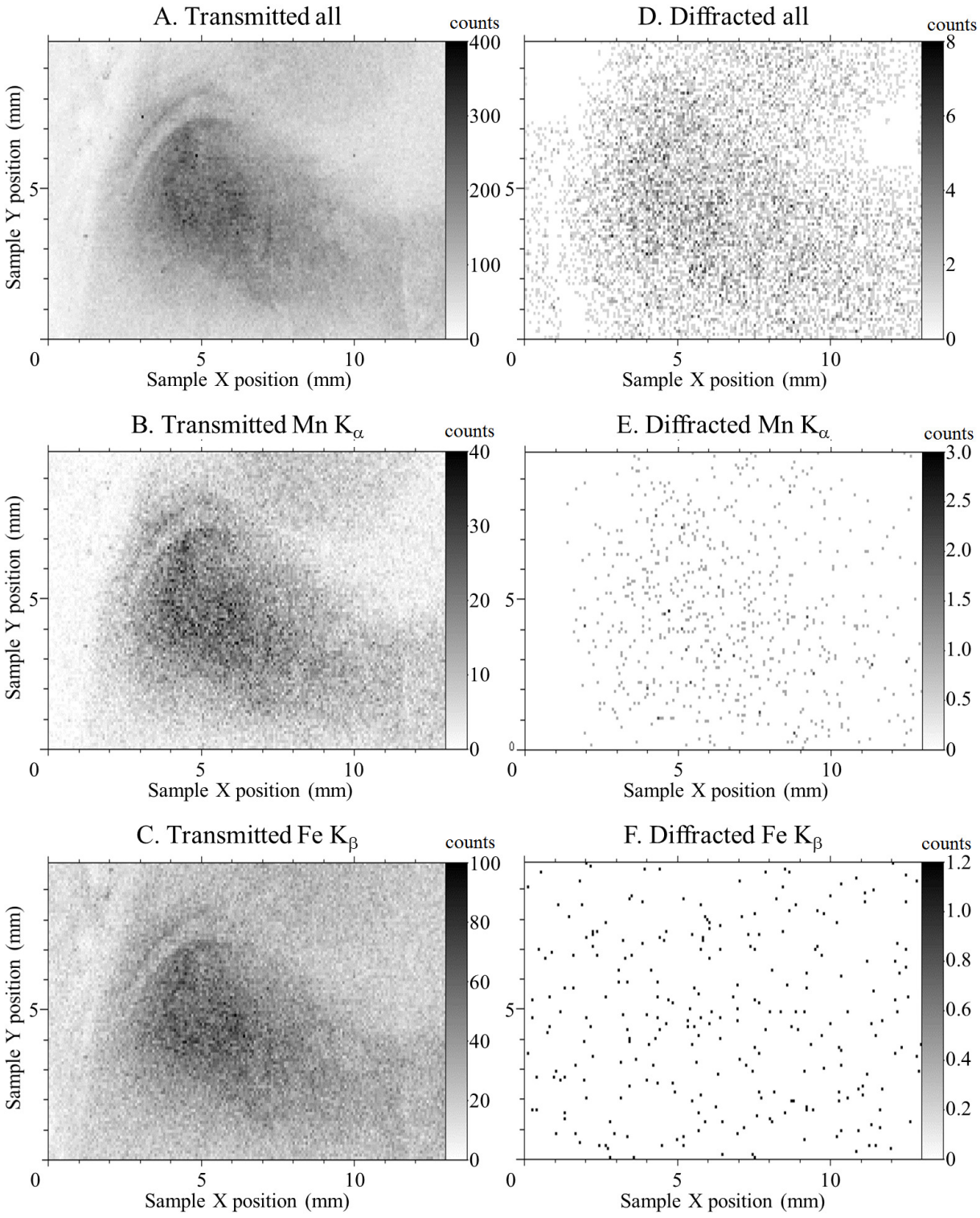

Figure 4.31 XRF images of the PD1 brain sample at 50 μm by 50 μm beam size and 200 ms dwell time. The intensity bars on the right side of images denote the normalized photon counts.

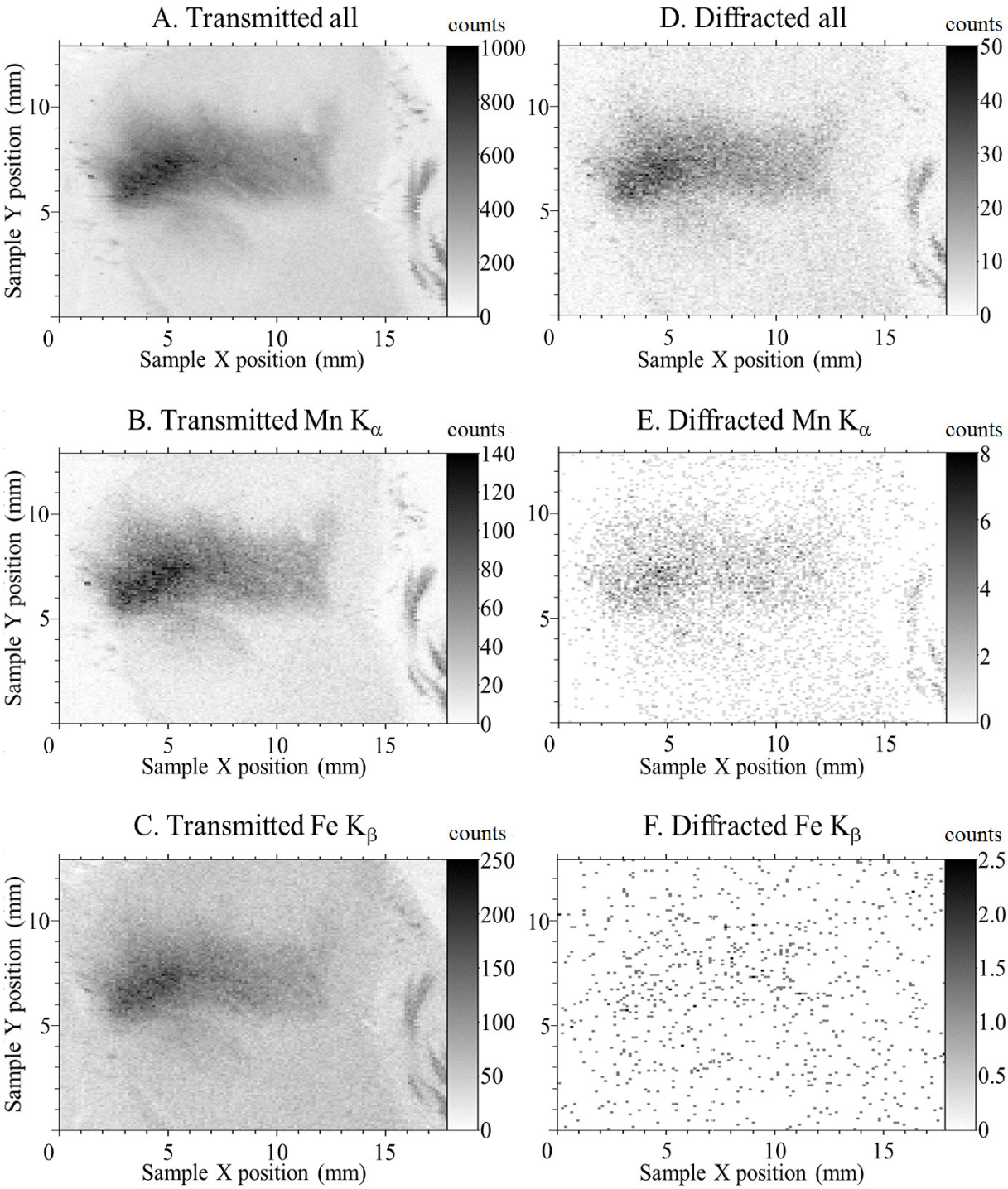

Figure 4.32 XRF images of the PD2 brain sample at 100 μm by 100 μm beam size and 50 *ms* dwell time. The intensity bars on the right side of images denote the normalized photon counts.

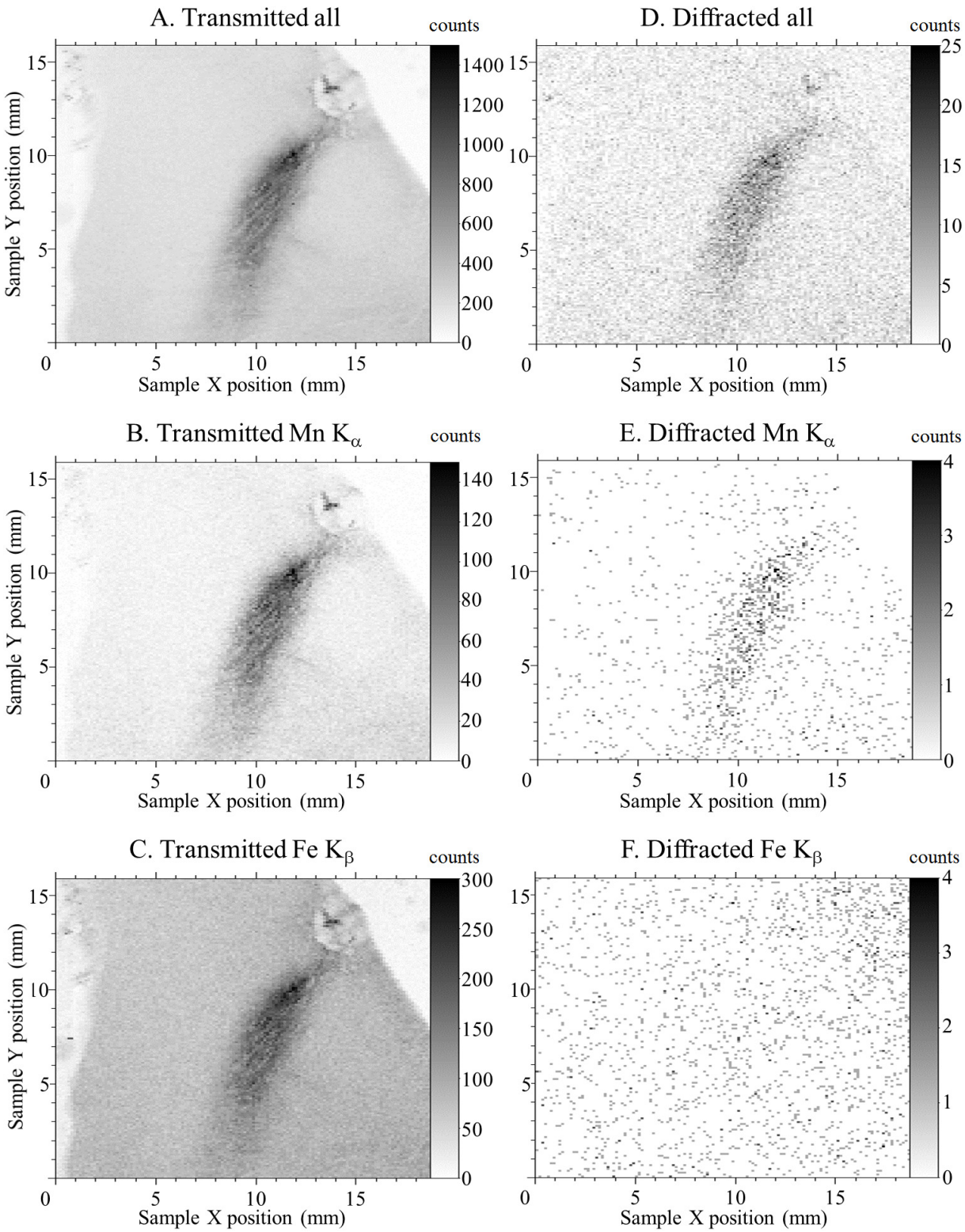

Figure 4.33 XRF images of the PD3 brain at 100 μm by 100 μm beam size and 250 *ms* dwell time. The intensity bars on the right side of images denote the normalized photon counts.

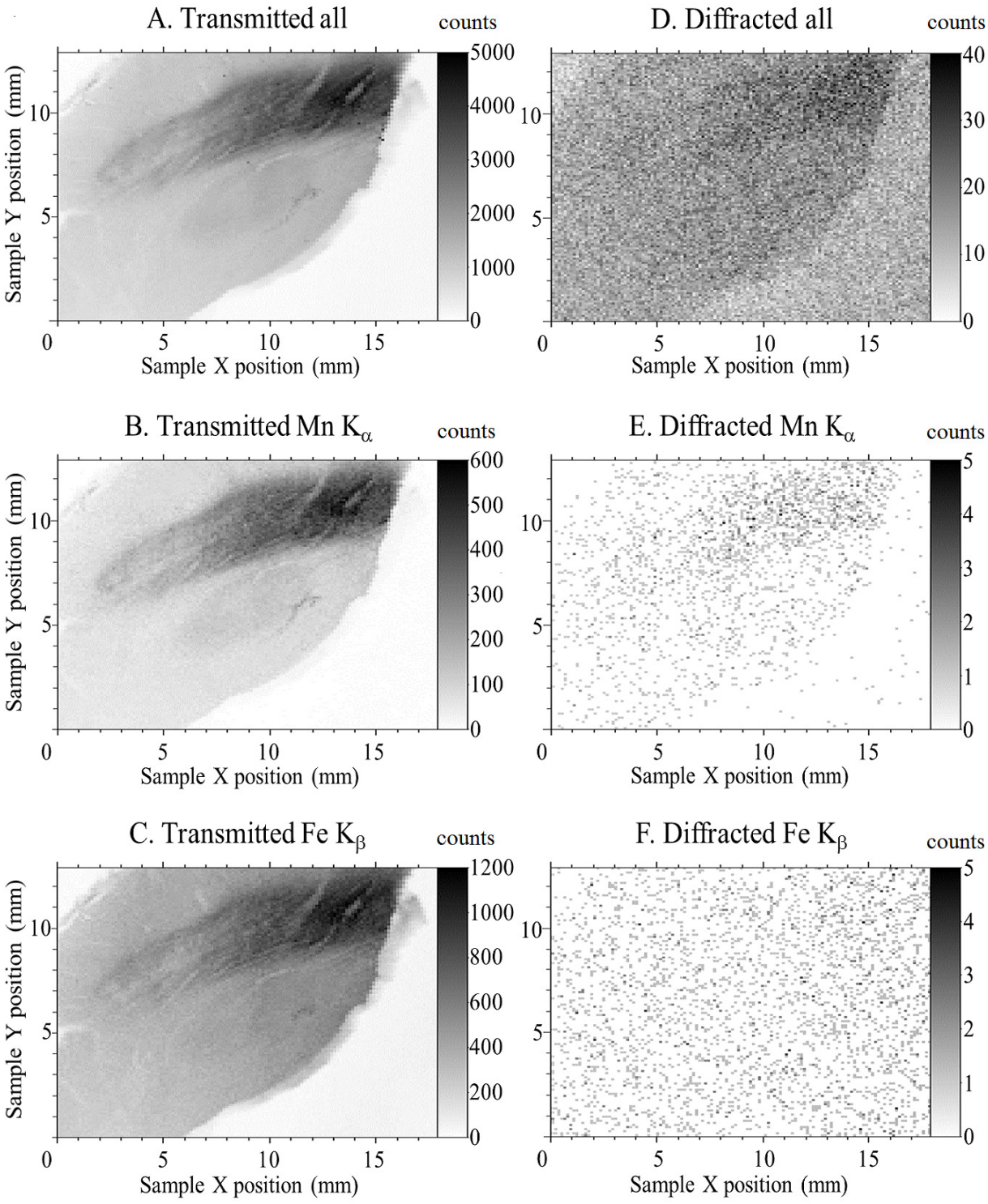

Figure 4.34 XRF images of the control brain sample at 100 μm by 100 μm beam size and 250 ms dwell time. The intensity bars on the right side of images denote the normalized photon counts.

4.1.7 Discussions and Future Works

This project optimized the BLA design specific for Mn K_α fluorescence detection, with a theoretical reflectivity of 28.8%, 23.6%, 27.1% or 18.4%, a theoretical FOM of 4.0 *msr*, 3.9 *msr*, 2.2 *msr* or 2.1 *msr* for BLA *I, -I, II* or *-II* respectively through proper bending of 20 μm thick Si crystals. Using two Amptek detectors enabled the measurements of the transmitted and diffracted spectra at the same time with a short sample-to-detector distance, 39.4 *mm* (for *I* and *-I*) or 45.4 *mm* (for *II* and *–II*). The designed energy resolution was 12.9 *eV* (for *I* and *-I*) or 14.4 *eV* (for *II* and *–II*) since the BLAs were designed to diffract the both Mn $K_{\alpha 1}$ and $K_{\alpha 2}$ (11.1 *eV* apart) fluorescence. The rapid prototyping of BLA frames provides a new method of fabrication with great precision (42 μm for X and Y, 16 μm for Z). The preliminary experiments on the BLA *-II* validated its efficacy to improve Mn specificity in XAS imaging. A Mn detection limit of 0.5 *mM* can be achieved by this detection system. Reasonable vertical size of detectable region of 50 μm and an energy resolution of 34.5 *eV* were achieved compared to the theoretical value of 21 μm and 14.4 *eV*. The differences were easily accounted for as due to mechanical vibration during the scan or a not perfectly aligned BLA detector. Both would lead to a bigger FWHM in the combined resolution measurement.

However, from the image scale comparison between the diffracted and transmitted Mn fluorescence images from the two experiments, we found that the second experiment did not get the same strong diffraction signals as the first experiment using the same BLA (*-II*). The reason might come from either a not precisely focused BLA after the alignment or not perfect bending and mounting of the crystal on the BLA frame for the second experiment. This would result in that only a portion of the crystal area contributed to the expected diffraction process.

Due to the limited space in the microprobe endstation at the HXMA beamline, our BLA detection system was set up at the XAFS endstation and used non-focused slits-defined small beam as the source which definitely sacrificed the incident flux. The preferred 100×100 μm^2 beam size in the second experiment limited the incident flux down to around 5.6 x 10^7 *photon/s* which was less than the incident flux of 8.8 x 10^7 *photon/s* provided by the 1 *mm* × 33 μm beam size in the first experiment. Without Soller slits, bigger vertical beam size than required by the BLA design (21 μm for BLA *-II*) would introduce more noise into the diffraction detector.

It should be mentioned that the alignment of the BLA detection system was a tricky process even with the help of the source pointer to set the initial position of the detection system. Among the three axes of motion in the BLA detection system, focusing along the vertical axis is most sensitive compared with the other two (inboard - outboard and upstream - downstream). Given the beam size in micron scale, it usually takes several scanning of all three axes before it came to a "focused" spot where maximum diffraction signal was observed.

Since two Amptek detectors were set up to receive both the transmitted and diffracted beam at the same time, no Soller slits were used to direct the desired diffracted beam and to block the transmitted beam and undesired diffracted beam such as Fe fluorescence. The BLA was thus observed to diffract a short span of energies at different vertical height. For example, during the second experiment the BLA *–II* was found to diffract Mn K_α fluorescence at 13.7 *mm* relative vertical height, Fe K_α fluorescence at 14.3 *mm* and Fe K_β fluorescence at 15.0 *mm* relative vertical height. In theory, the vertical height difference for BLA *–II* between the Mn K_α diffraction spot and Fe K_α diffraction spot is 0.67 *mm*, and the difference between the Fe K_α spot and Fe K_β spot is 0.72 *mm*. Both theoretical values were very close to the measured relative vertical height differences. It should be mentioned that even if the BLA at the Fe K_α spot (or

height) could diffract Fe K_α fluorescence, the logarithmic spiral shape was not optimized to do so and thus only a part of the crystal in the logarithmic spiral shape contributed to this diffraction. And the same is true for Fe K_β diffraction at the Fe K_β spot. Our BLA detection system was built on an aluminum breadboard which was supported by bolts surrounded with aluminum sheet rolls. The support was later found not stable enough to hold exactly the same vertical height in all circumstances which is critical to diffract the desired fluorescence signals.

Due to the limited beamtime at the HXMA beamline, the other three BLAs (*I, -I* and *II*) have not been used to perform the spectra and imaging tests. More tests are needed in the future including EXAFS measurements and a thorough study of human brain tissues using strong diffraction from the BLA detection system.

4.2 Novel Design of BLA-based Confocal XRF Imaging of Iodine

Inspired by the circular pattern in the Mn fluorescence images of the gelatin calibration sample, a new imaging method of 3D confocal XRF imaging was conceived by using a BLA (Figure 1.6). This technique enables the X-ray sectioning and 3D mapping of XRF from a certain element within a sample by simple 3D raster scanning. A BLA-based confocal XRF detection system was firstly designed and fabricated for imaging of iodine fluorescence which has an attenuation length of 2.67 *cm* in human tissue equivalent (ICRU4), 62.2 times longer than that of the Mn fluorescence. This much deeper penetration allows a much longer scanning depth appropriate for small animals such as mice and rats. Optimization of the design parameters, fabrication procedures and experimental plans are presented.

4.2.1 Bent Laue Analyzer Design

Two sets of BLAs (denoted as *I* and *–I*, respectively) were designed with beam incident onto both sides of the {111} Bragg planes of a Si (111) wafer. Similar design procedures for the confocal iodine BLAs were followed as the Mn BLAs described in chapter 4.1.1 with an extra effort on the design of the associated Soller slits.

4.2.1.1 Methods

Based on a lamella model and the REFLECT program, the reflectivity, reflectivity width and lamella layers of BLAs were calculated as a function of thicknesses and bending radii of the Si crystal as shown in Figure 4.35. The colors represent the reflectivity with the corresponding pseudo-color bar on the right side indicating the mapping between the pseudo-color and the reflectivity value. Iso-reflectivity is shown as white solid lines with the reflectivity value labeled. Considering the collection of both iodine $K_{\alpha 1}$ and $K_{\alpha 2}$ fluorescence at the same time, the reflectivity width should be larger than the Bragg angle difference $\Delta\theta_B$ between iodine $K_{\alpha 1}$ and $K_{\alpha 2}$ which is 0.721 *mrad*. In Figure 4.35 iso-width of reflectivity is shown in white dashed lines denoted in the unit(s) of $\Delta\theta_B$ and lamella iso-layers are shown in white dotted lines with the number of lamella layers labeled. Since choosing the optimal parameter is not straight forward from considering the reflectivity alone, the FOM defined as the product of the reflectivity and the solid angle subtended by the crystal effective diffraction area of 20 *mm* by 22.36 *mm* is drawn as a function of crystal thicknesses and bending radii (Figure 4.36). The colors represent the FOM with the corresponding pseudo-color bar on the right side. Iso-FOM is shown in white solid lines with the FOM value labeled. Again, the iso-width of reflectivity is shown in white dashed lines denoted in the unit(s) of $\Delta\theta_B$ and lamella iso-layers are shown in white dotted lines with the number of lamella layers labeled. The FOM figures (Figure 4.36) indicate an optimal Si crystal

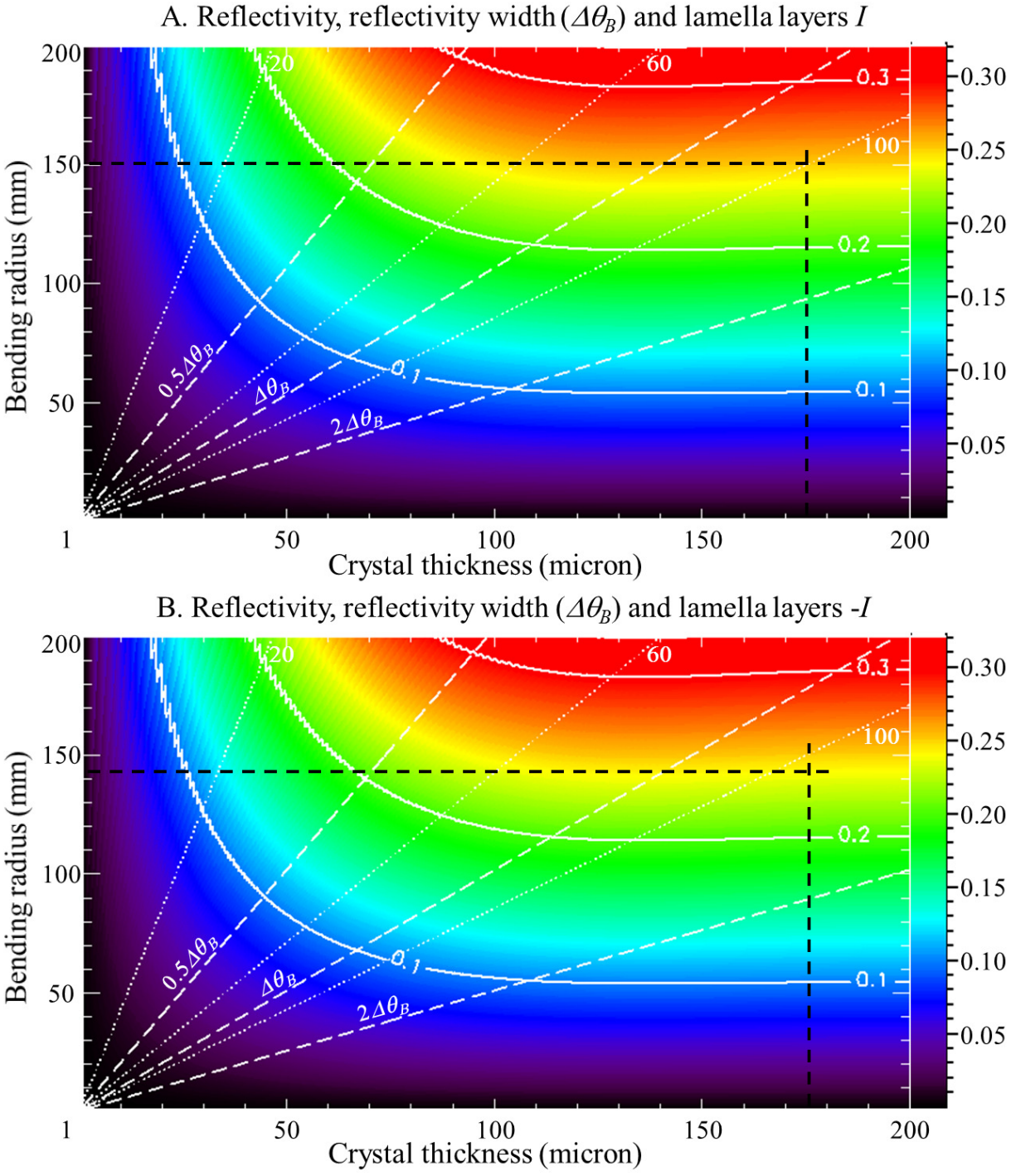

Figure 4.35 The reflectivity (pseudo-color mapping and white solid isolines), reflectivity width (white dashed isolines in the unit of $\Delta\theta_B$) and lamella layers (white dotted isolines) of BLAs using Si (111) (A for I and B for -I) for iodine K_α fluorescence vs. crystal thickness and bending radius. The black dashed crosses indicate the final parameters of the crystal thickness and bending radius.

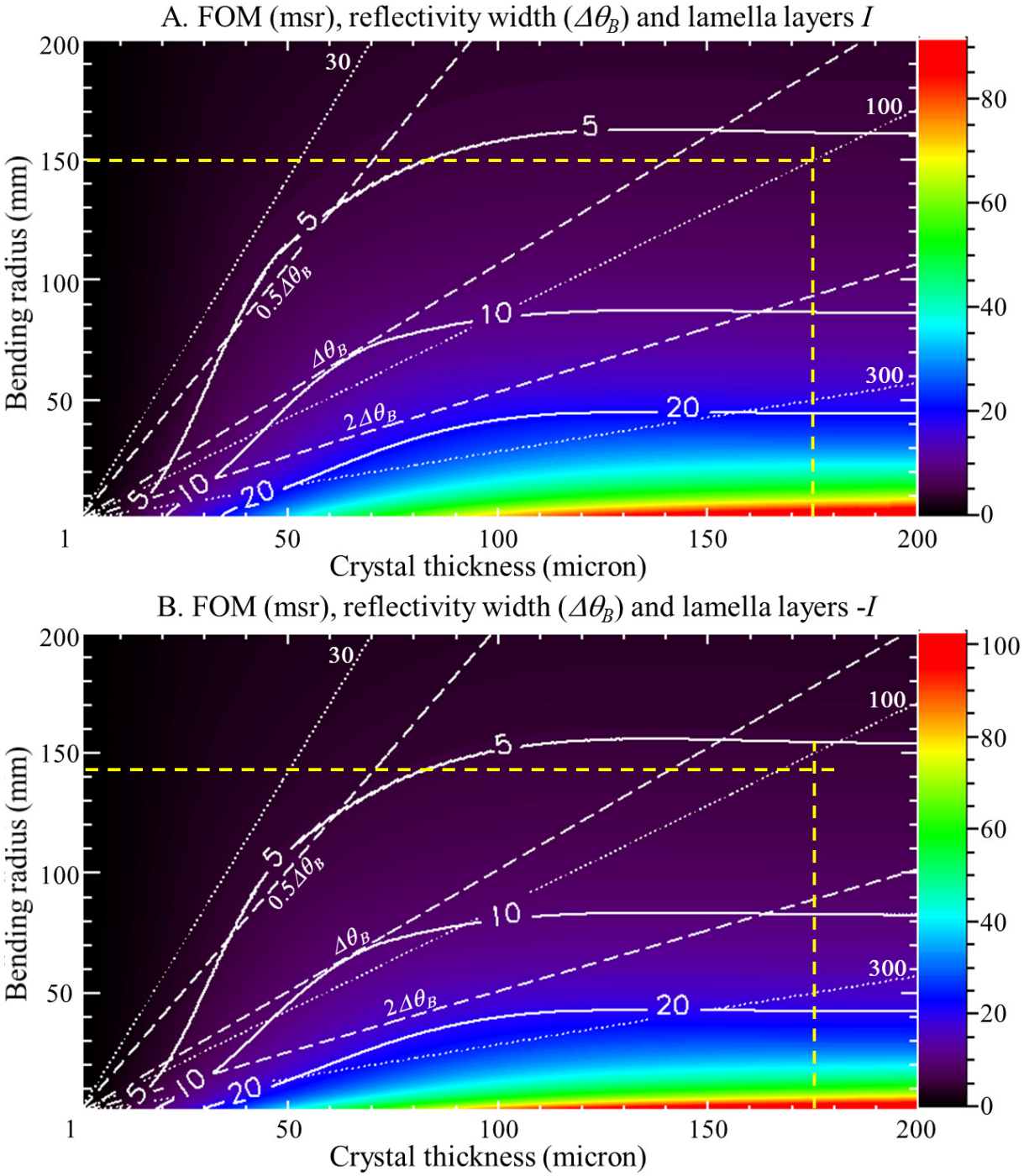

Figure 4.36 The FOM (pseudo-color mapping and white solid isolines in the unit of *msr*), reflectivity width (white dashed isolines in the unit of $\Delta\theta_B$) and lamella layers (white dotted isolines) of BLAs using Si (111) (A for I and B for $-I$) for iodine K_α fluorescence vs. crystal thickness and bending radius at a given active crystal area of 20 *mm* by 22.4 *mm*. The yellow dashed crosses indicate the final parameters of the crystal thickness and bending radius.

thickness of around 65 μm based on the maximal FOM along the isolines of reflectivity width of $\Delta\theta_B$ in both cases. However, its reflectivity is below 10% as suggested in the reflectivity figures (Figure 4.35). Since we had Si (111) wafers with 175 μm thickness and 2 inch diameter, 175 μm is set as the crystal thickness and its reflectivity along the isoline of reflectivity width of $\Delta\theta_B$ is much higher in both cases.

Groups of rocking curves (reflectivity vs. incident angle) were drawn with a crystal thickness of 175 μm and a reflectivity width ranging from $0.5\Delta\theta_B$ ~ $2.5\Delta\theta_B$, showing the merging process of the iodine $K_{\alpha 1}$ and $K_{\alpha 2}$ fluorescence peaks. By selecting the just merging point of the two peaks, a reflectivity width of $1.25\Delta\theta_B$ was roughly determined for both cases (*I*

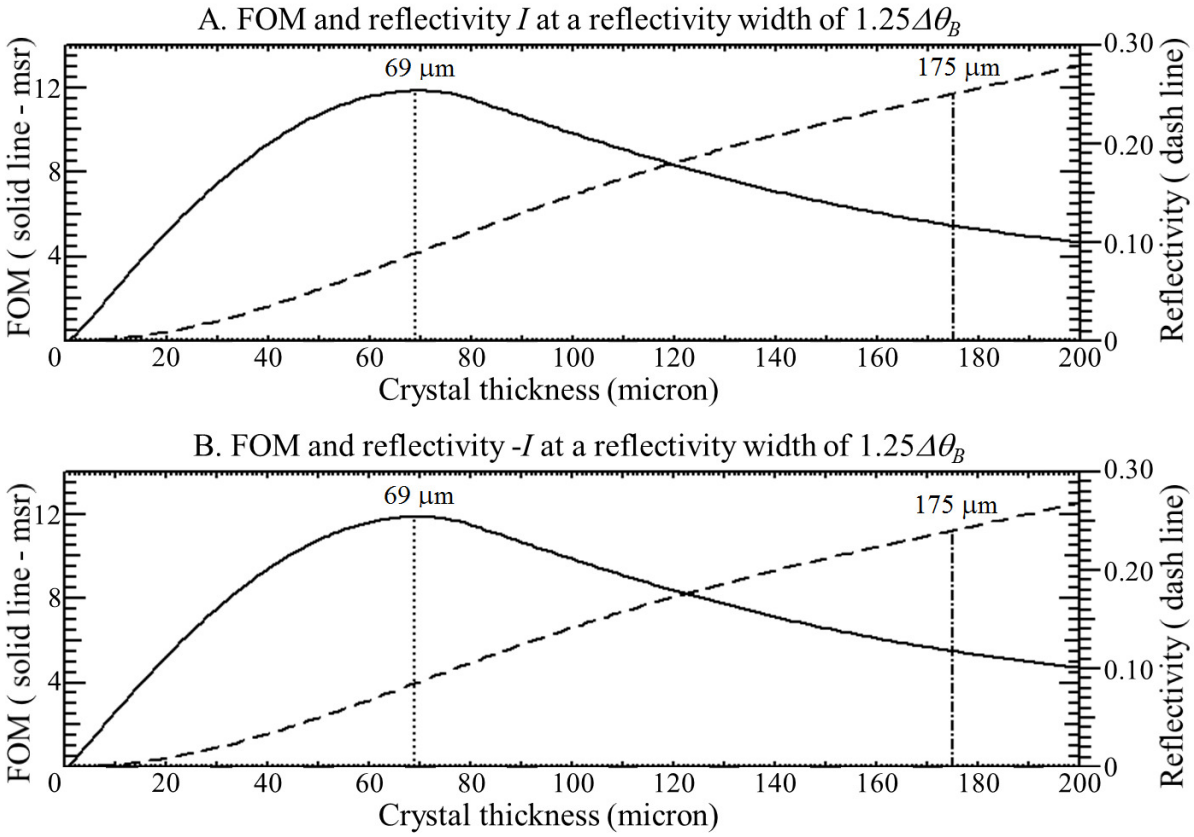

Figure 4.37 The FOM (solid line) and reflectivity (dashed line) at a constant reflectivity width of $1.25\Delta\theta_B$ vs. crystal thickness of BLAs. The vertical dotted lines indicate the crystal thickness reaching the maximal FOM. The vertical dash-dotted lines indicate the picked crystal thickness.

and $-I$). This step aims at the highest energy resolution for collecting both of the iodine $K_{\alpha 1}$ and $K_{\alpha 2}$ fluorescence peaks at the same time. From the FOM and reflectivity curves at the desired reflectivity width of $1.25\Delta\theta_B$ (Figure 4.37), the picked crystal thickness of 175 μm was confirmed as a good choice in both cases, even though a crystal thickness of 69 μm could reach the maximal FOM with a moderate reflectivity.

With the crystal thickness (175 μm) and reflectivity width ($1.25\Delta\theta_B$) for both cases being set, the BLA parameters were all calculated. For practical reasons the source to crystal center distance s was rounded to an integer number of 138 mm, and the reflectivity width was thus adjusted to $1.245\Delta\theta_B$ (0.896 $mrad$). The equivalent reflectivity was estimated as a square peak with its width equal to the reflectivity width based on the rocking curves from iodine K_α fluorescence (Figure 4.38).

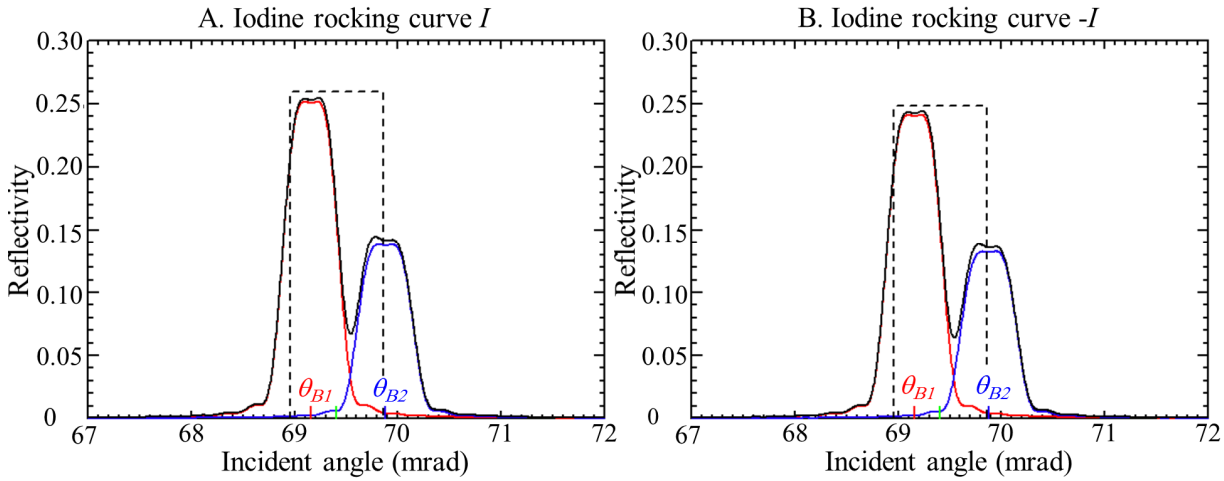

Figure 4.38 The calculated rocking curves from iodine $K_{\alpha 1}$ (red lines) and $K_{\alpha 2}$ (blue lines) fluorescence and the sum of the two (black lines). The equivalent reflectivity was estimated as a square peak (dashed lines) with its width equal to the reflectivity width. The θ_{B1} and θ_{B2} refer to the Bragg angles of the iodine $K_{\alpha 1}$ and $K_{\alpha 2}$ fluorescence, respectively.

4.2.1.2 Soller Slits Design

In the experimental setup, a NaI scintillation detector (C48NAXXB from FMB OXFORD Inc., Oxford, UK) with a detection area of 804 mm^2 (32 *mm* diameter) was placed after the BLA and tilted up at a fixed $2\theta_B$ angle (8.0°). To accept only the diffracted beams from the BLA, the detector should be placed either far enough away (0.27 *m*) to avoid the transmitted beam or after a set of Soller slits which lets through the diffracted beam but absorbs the transmitted one. To achieve larger solid angle (4 times bigger) for the detection of the diffracted beam, Soller slits were designed for each BLA. The Soller slits were made from lead sheet of 0.4 *mm* thick. The number of slits and the active length of the crystal that would provide the largest solid angle for the diffraction detector after the Soller slits then needs to be determined. Figure 4.39 was calculated where the colors represent the solid angle with the corresponding pseudo-color bar on the right side indicating the mapping between the pseudo-colors and the solid angle values. Iso-curves are shown as black solid lines with the solid angle values labeled. Based on the optimal selection in Figure 4.39, 14 pieces of 0.4 *mm* thick lead sheets with a minimal length of 20 *mm* were made as the Soller slits and the 27 *mm* of the crystal active length would provide a solid angle of 20.9 *msr* (*I* case) or 23.8 *msr* (*–I* case) for the diffraction detector after the Soller slits.

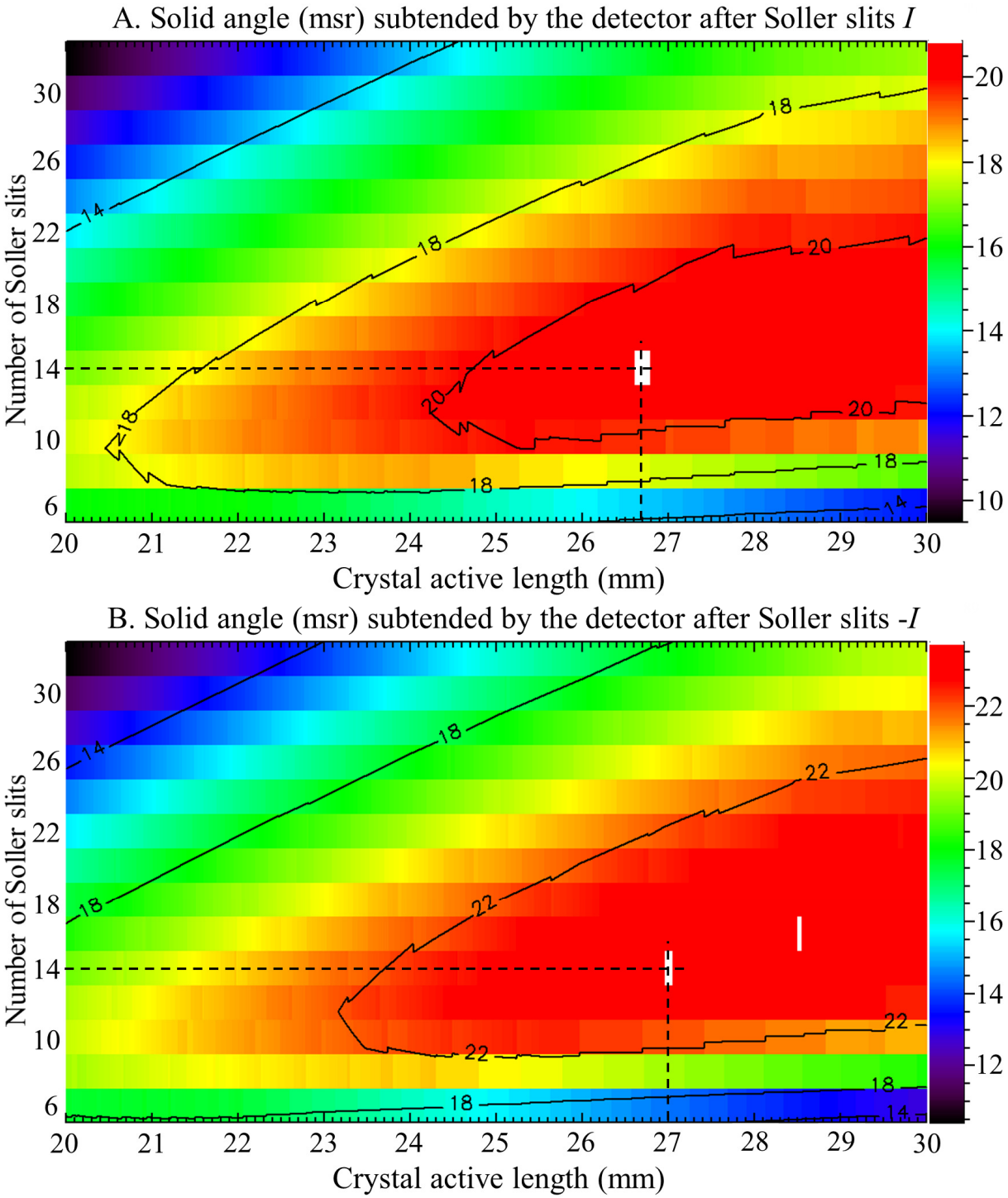

Figure 4.39 The solid angle (pseudo-color mapping and black solid isolines) subtended by the detector after Soller slits (A for *I* and B for *-I*) vs. the active diffraction length of the Si crystal and the number of Soller slits. The black dashed crosses indicate the optimal selection of the crystal active length and the number of the Soller slits.

4.2.1.3 Specifications

The detectable region of the BLAs is a double prism shape with its waist calculated as 124 μm (Figure 4.40). The vertical size of the detectable region is adjustable by changing the source-to-crystal distance s and/or the crystal reflectivity width $\Delta\theta$ which is influenced by the diffraction plane DP, crystal thickness t and bending radius r. The colors represent the probability of the signals originated from a specific point within a sample to be diffracted by the BLA without considering the self-absorption by the sample. The corresponding pseudo-color bars on the left side indicate the mapping between the colors and the diffraction. With all the parameters determined, BLAs were designed (Figure 4.41) with parameters listed (Table 4.4).

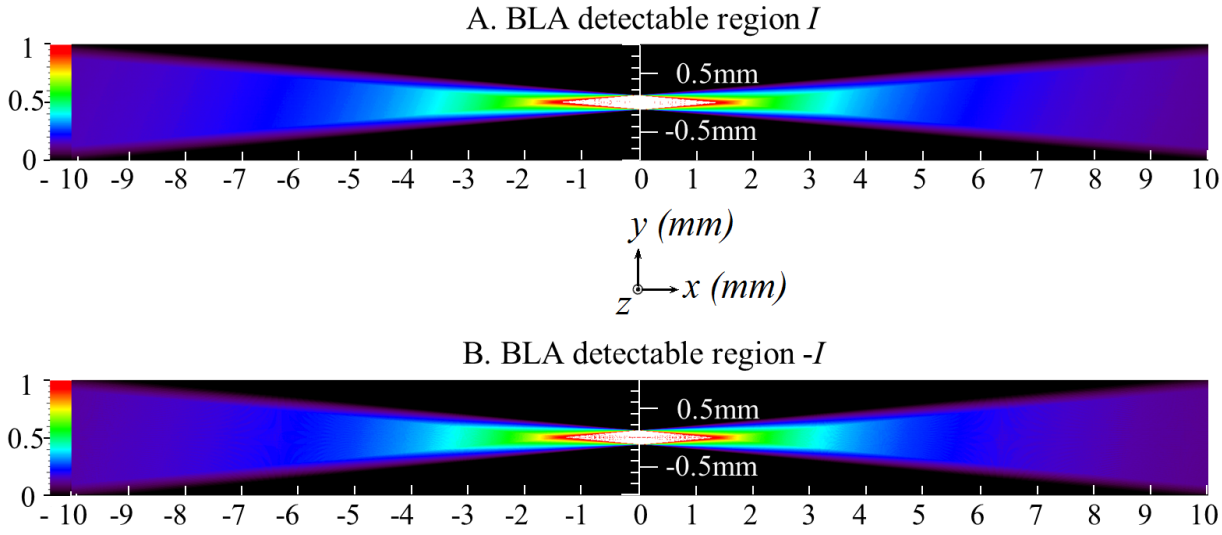

Figure 4.40 Calculated detectable region of BLAs. The colors represent the diffraction probability by the BLAs with a pseudo-color bar on the left side of each figure. The horizontal axes denote the dimension (*mm*) along the focal direction x and the vertical axes in the center denote the dimension (*mm*) along y axis in the diffraction plane.

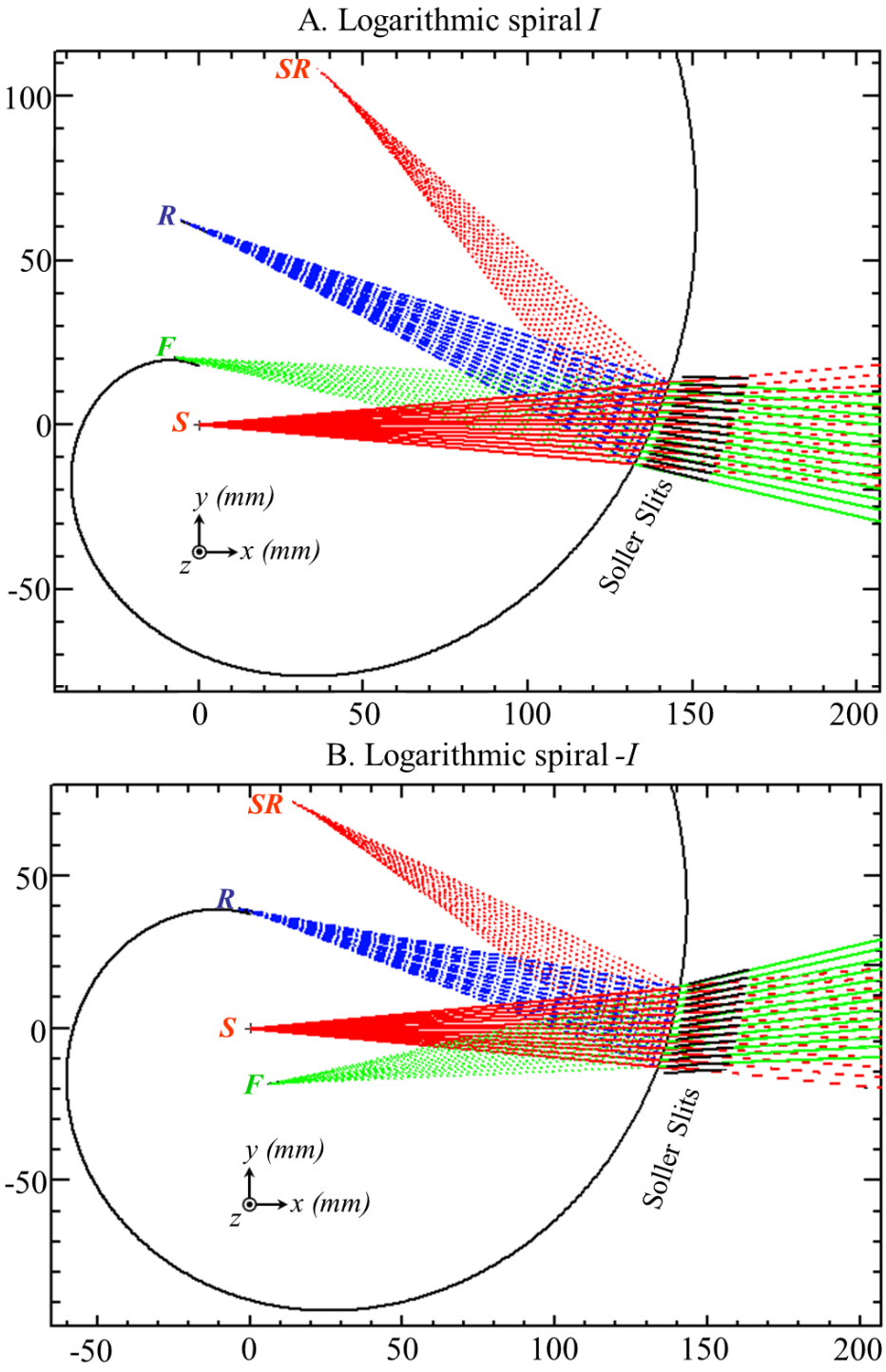

Figure 4.41 The logarithmic spirals (black curve) of the BLAs with respect to the positions of source *S*, focal point *F*, normal center *R*, surface reflection focus *SR* and the Soller slits (black lines). The horizontal axes denote the dimension (*mm*) along the focal direction *x* and the vertical axes denote the dimension (*mm*) along *y* axis in the diffraction plane. The transmission lines (red), diffraction path (green), crystal surface normal (blue) and the Soller slits (black) are plotted according to the given crystal active length.

Table 4.4 Design parameters of the BLAs for iodine fluorescence detection using NaI detector

Design parameters	*I*	*-I*
Si wafer	Si (111)	
Diffraction Plane DP	{111}	
Asymmetry angle χ (°)	19.5	
Poisson ratio	0.262 [Bra73]	
Iodine K_α energy E_{Ka} (keV)	28.509	
Bragg angle θ_B (°)	4.0	
Crystal thickness t (μm)	175	
Crystal central bending radius r (mm)	150.4	143.2
Surface reflection focus SR_x relative to S (mm)	43.7	19.7
Surface reflection focus SR_y relative to S (mm)	100.8	71.1
Crystal active width (transversal) (mm)	20	
Crystal active length (coronal) (mm)	26.8	27.0
Source to crystal center distance s (mm)	138	
Central focal length f (mm)	145.0	131.4
Coronal opening angle (°)	10.2	10.8
Transversal opening angle (°)	8.3	
Solid angle Ω (msr)	20.9	23.8
Equivalent reflectivity R_{eq} (%)	26.0	24.9
FOM (msr)	5.4	5.9
Lamella layers	99	104
Reflectivity width $\Delta\theta$ (μrad)	896 ($1.245\Delta\theta_B$)	
Energy resolution ΔE (eV)	368	
Energy bandwidth $\Delta E/E$ (%)	1.3	
Detectable region vertical size Δv (μm)	124	
Detectable region transversal size Δh (mm)	44.8	

4.2.2 Bender Design

Two sets of BLA benders were designed using Solidworks software along with source pointers for proper alignment (Figure 4.42). The logarithmic spiral curves were imported from IDL using a macro-defined function to Solidworks. The source pointer was removed from the top after proper alignment and a lead plate with a predefined aperture was inserted in the same place during the experiment to define the size of the beam onto the crystals. The Soller slits were inserted into the slots which were designed to attach the BLA bender and to keep the Soller slits from touching the crystals. The source pointers and the BLA benders with the Soller slits slots were fabricated using a Rapid Prototyper Eden500V^{TM} (Objet Geometries Ltd., Billerica, Massachusetts, USA) at the Engineering Machine Shop of the U of S.

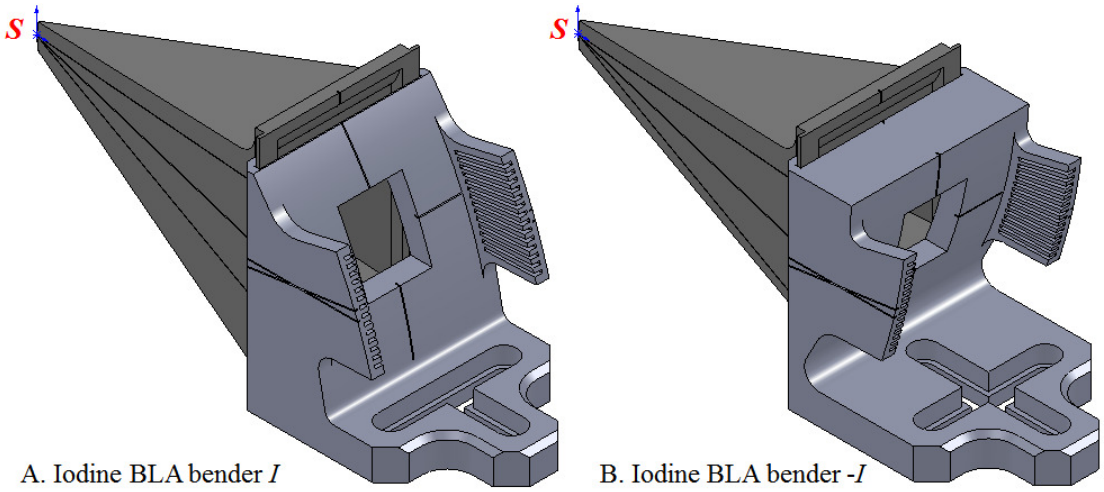

Figure 4.42 Two sets of BLA benders along with their source pointers (dark grey) and slots for the Soller slits. The rectangles on the curved surfaces of logarithmic spiral shape define the crystal mounting position. The removable source pointers point at the fluorescence and scattering center *S*.

4.2.3 Crystal Preparations

Two pieces of Si (111) wafer of 175 μm thickness and 50 *mm* diameter were oriented by transmission Laue diffraction using white beam at the BMIT BM beamline at the CLS, a similar

process as described in Figure 4.16. Since these round Si (111) wafers did not have flat edges as an orientation reference, the crystal orientation was not as simple as picking one direction from two possibilities. Effort was put on the arbitrary angle measurement of the wafer setup from the transmission Laue photographs and precise angle adjustment using rotational stages, line laser source and a weight on a string at the BMIT BM beamline.

The crystals were then cut into rectangles of 40 *mm* wide by 50 *mm* high along the preferred <111> direction by hand using a diamond scriber. To better survive the bending process, the four cut sides of the crystals were etched for strain relief with a HF (48%) : HNO_3 (69%) : distilled H_2O solution at a 3:6:6~10 volume ratio, a modified CP4A etchant [All57], at the Saskatchewan Structural Sciences Centre (SSSC, Saskatoon, SK, Canada) until orange peel-like features were observed on the surface.

The crystal was then bent along the logarithmic spiral surface of the BLA bender. This was done by hand by pressing a piece of Kapton film over the crystal which was then fixed on the BLA bender by Kapton tape (Figure 4.43). Setting a line laser source at the source point *S* in

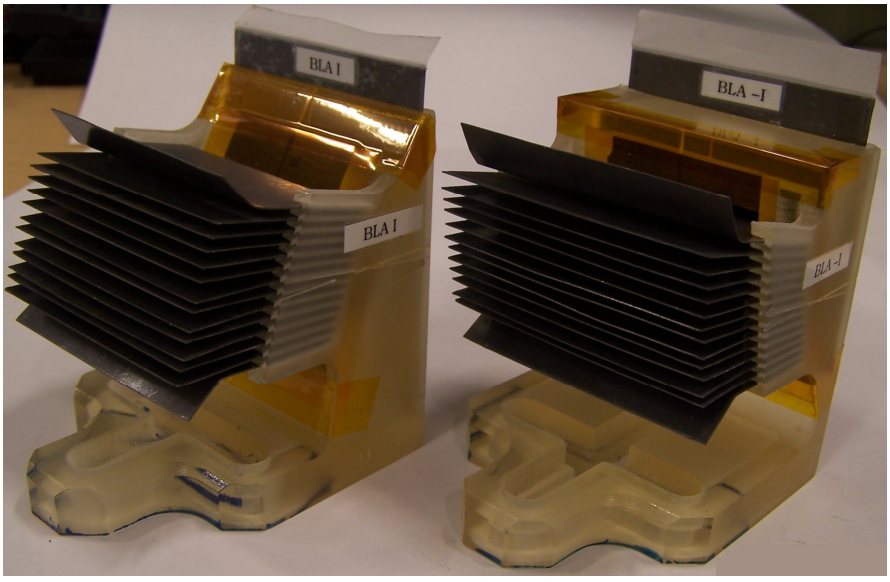

Figure 4.43 Two sets of BLAs with the crystals mounted, Soller slits packed and lead plates with apertures inserted.

a dark room, the crystal bending radius and bending uniformity was checked by measuring the position and shape of the surface reflection focus (*SR* in Figure 4.41) from the bent crystal (Figure 4.44).

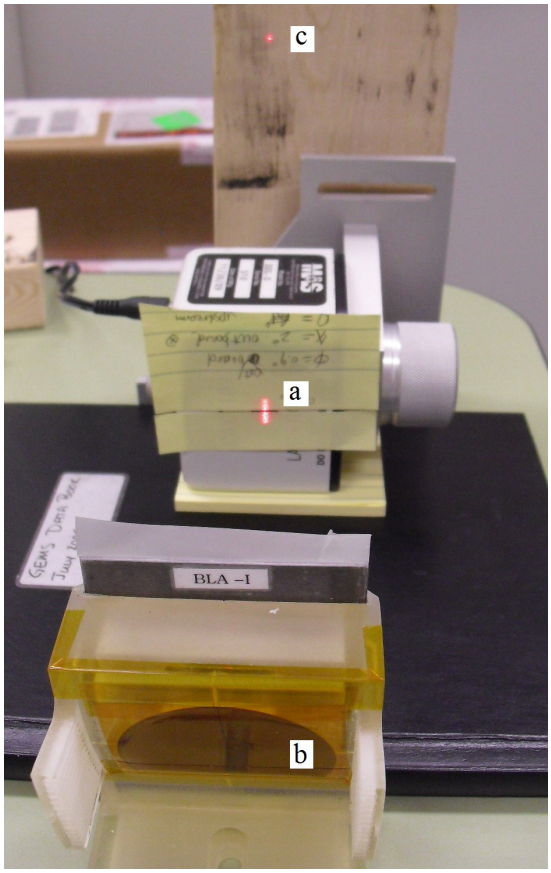

Figure 4.44 Checking the BLA bending through measurement of the reflection focus (c) from the crystal surface (b) using a line laser source (a).

4.2.4 Experiment

The experiments with the confocal XRF imaging system were planned on a dual-energy KES setup for iodine detection using a BLM (Figure 4.45). The two beams with energies bracketing the iodine K-edge could be separated by either a beam splitter before the BLM or a three-beam chopper which switched among the beams through rotation. The BLM diffracted the two beams upward at a 13.1° angle and focused them down to around 100 μm (a line focus) at

1.5 meters away. The detailed KES setup is described in Chapter 5 with the design of the BLM and the three-beam chopper. The bent Laue detector was set up on an XYZ stage 90º to the diffracted beam direction which was collinear with the *y* axis of the BLA (vertical axis in the diffraction plane). The 124 μm of slice thickness would be achieved by the X-ray sectioning of the BLA. The 3D voxel probing a sample would be 100 μm (along the *z* axis defined by the BLM) by 100 μm (along the *x* axis defined by horizontal slits) by 124 μm (along the *y* axis defined by the BLA). After the bent Laue detection system was aligned, XYZ scanning of a sample with the contrast agent (iodine) would produce a 3D XRF imaging of iodine. A precisely aligned BLA with a Si crystal perfectly bent along the logarithmic spiral curve would only diffract iodine fluorescence photons while the elastic and Compton scattering and other fluorescence photons would be rejected. This confocal XRF imaging combined with the KES setup would provide another opportunity to perform Fluorescence Subtraction Imaging (FSI) which is the subtraction of the two fluorescence images taken above and below the iodine K-edge energies [Zha08].

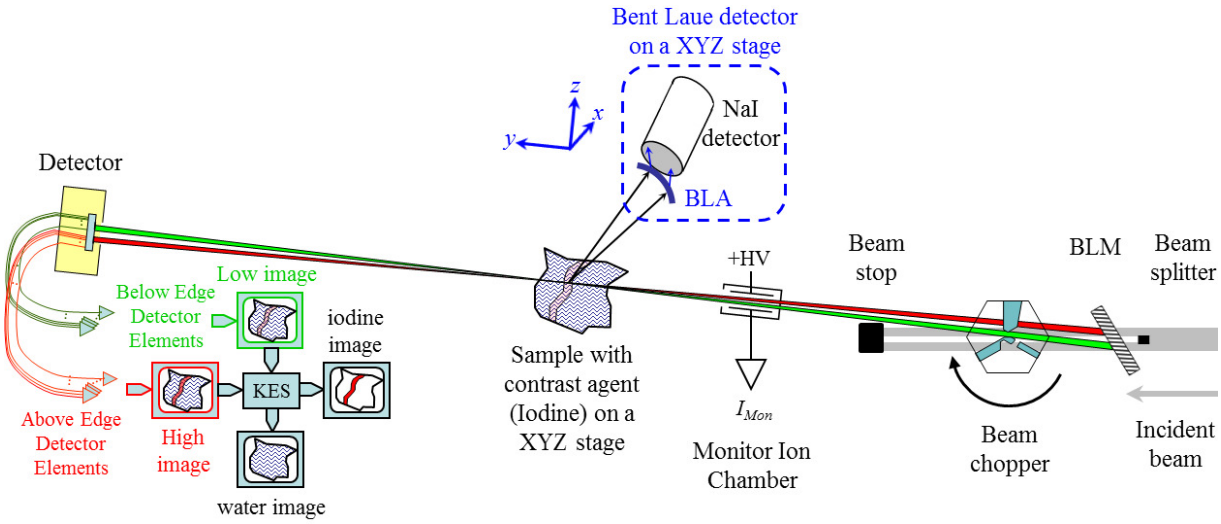

Figure 4.45 Diagram of the BLA-based confocal XRF imaging combined with the dual-energy KES setup (adapted figure from Dr. Dean Chapman)

The BLA-based confocal XRF imaging system (Figure 4.46) was set up at the BMIT bend magnet (BM) beamline at the CLS in July and Aug 2010. The experiment used a three-beam chopper to switch between the beams with average energies of 179 *eV* above and below the iodine K-edge (33.17 *keV*). The test object was a "physics rat" head which was printed by a rapid prototyper using the techniques described in Chapter 3.1. The rat head restraint was sealed with water and a cuvette of iodine solution (30 *mg/ml* concentration) within which a printed step wedge was inserted [Zha09]. The confocal XRF detection system containing the BLA and a NaI

Figure 4.46 Experimental setup of the confocal XRF imaging based on the KES arrangement at the BMIT BM beamline, showing the BLM (a), the three-beam chopper (b), a transmission beam stop (c), a diffraction ion chamber (d), a "physics rat" head with iodine solution (e) as the sample, the confocal BLA with NaI detector (f) with lead shielding, a Budker line detector (g) for KES imaging and a pivoted rail (h) which hold the equipment d-g and provided all of them a tilt angle of 13.1° upwards.

detector was set up 90° to the diffracted beam direction. The system alignment and preliminary tests were attempted, but due to beamtime scheduling and prerequisite focus on the BLM-based KES imaging, the system validation and detailed study of the BLA-based confocal XRF imaging still needs further investigation.

4.2.5 Discussions and Future works

In chapter 4.2, a novel method of confocal XRF imaging is proposed based on the 1D focusing ability of BLAs. This project optimized the BLA design specific for iodine K_α fluorescence detection, with a theoretical reflectivity of 26.0% (for *I* case) or 24.9% (for *-I* case) through proper bending of 175 μm thick Si crystals. Using the optimized Soller slits, the NaI detector after the BLA would achieve a solid angle of 20.9 *msr* (for *I* case) or 23.8 *msr* (for *-I* case) for the detection of the diffracted iodine K_α fluorescence. This design would achieve a theoretical FOM of 5.4 *msr* or 5.9 *msr* for BLA *I* or *-I* respectively. The designed energy resolution was 368 *eV* since the BLAs were designed to diffract both the iodine $K_{\alpha1}$ and $K_{\alpha2}$ fluorescence (295 *eV* apart). The vertical size of the detectable region was designed as 124 μm which could be adjusted by changing the source to crystal distance *s*, the crystal thickness *t*, the crystal bending radius *r* or a different diffraction plane *DP*. Combined with a pencil beam or a 2D focused beam, a 3D voxel with volume of 100 μm by 100 μm by 124 μm could be used to probe the 3D elemental (iodine) mapping of a sample. One limitation is that the detection depth (number of slices) depends on the fluorescence energy and the attenuation by the sample. Even though the experimental validation of the confocal XRF imaging system still needs further investigation, the proposed method shows great promise to perform a 3D elemental (iodine) mapping of a small animal such as a mouse. This method does not require a CT reconstruction algorithm for a 3D image and it could directly investigate a small region of interest within a

sample without the need to image the whole sample as a prerequisite. This method provides an alternative to perform the confocal XRF imaging and opens up a new application for bent Laue detectors.

Chapter 5 K-Edge Subtraction and Near Edge Spectral Imaging

Chapter 4 presents several Laue crystals bent in log-spiral shapes which were used in the Cauchois geometry as X-ray fluorescence analyzers. These BLAs either improves the Mn specificity in the XRF imaging or enables the novel design of a BLA-based confocal XRF imaging.

This chapter presents a cylindrically bent Laue crystal which is used in a focusing geometry as a beam monochromator. This BLM enables the simultaneous KES imaging and three-energy KES. When the single ray and geometric foci are matched, this BLM enables the Near Edge Spectral Imaging (NESI) that utilizes the full near edge spectrum for imaging of contrast species. This chapter starts from the conventional dual-energy KES, to three-energy KES with a three-beam chopper, to a novel generalized version - NESI.

5.1 Conventional KES

5.1.1 Rationale

KES is an imaging method that is used to image dilute contrast agents such as iodine in living organisms. The conventional KES assumes a sample as a two-component system, a contrast material (*C*) and a matrix material (*M*). The number of photons (*N*) arriving at the detector in the beam of higher energy (*h,* above the edge energy) and lower energy (*l,* below the edge energy) would be

$$N_l = N_{0l} e^{-\frac{\mu}{\rho}_{Ml} \rho_M t_M} e^{-\frac{\mu}{\rho}_{Cl} \rho_C t_C}$$
$$N_h = N_{0h} e^{-\frac{\mu}{\rho}_{Mh} \rho_M t_M} e^{-\frac{\mu}{\rho}_{Ch} \rho_C t_C} \quad (5.1)$$

where N_0 is the incident number of photons, $\frac{\mu}{\rho}$ is the mass absorption coefficient, ρ is the density and t is the thickness of a component. If we define r_h and r_l as the negative logarithm of the normalized images from the beam of high and low energy respectively,

$$r_l = -\ln\left(\frac{N_l}{N_{0l}}\right) = \frac{\mu}{\rho}_{Ml} \rho_M t_M + \frac{\mu}{\rho}_{Cl} \rho_C t_C$$
$$r_h = -\ln\left(\frac{N_h}{N_{0h}}\right) = \frac{\mu}{\rho}_{Mh} \rho_M t_M + \frac{\mu}{\rho}_{Ch} \rho_C t_C \quad (5.2)$$

the projected density images of the two components are derived as

$$\rho_M t_M = \frac{\frac{\mu}{\rho}_{Ch} r_l - \frac{\mu}{\rho}_{Cl} r_h}{\frac{\mu}{\rho}_{Ml} \frac{\mu}{\rho}_{Ch} - \frac{\mu}{\rho}_{Mh} \frac{\mu}{\rho}_{Cl}}$$
$$\rho_C t_C = \frac{\frac{\mu}{\rho}_{Ml} r_h - \frac{\mu}{\rho}_{Mh} r_l}{\frac{\mu}{\rho}_{Ml} \frac{\mu}{\rho}_{Ch} - \frac{\mu}{\rho}_{Mh} \frac{\mu}{\rho}_{Cl}} \quad (5.3)$$

These are the line integrals of the densities along the beam path within the object and typically bear the unit of g/cm^2 for $\rho_M t_M$ and mg/cm^2 for $\rho_C t_C$ when the contrast content is dilute. The matrix material is typically chosen to be water thus giving a "water equivalent image". As shown in equation (5.3), if the above and below K-edge attenuation for the matrix materials is the same ($\frac{\mu}{\rho}_{Ml} = \frac{\mu}{\rho}_{Mh}$), then $\rho_C t_C$ is proportional to the difference between the negative logarithm of the normalized high and low images, hence the term K-edge subtraction to describe the imaging process.

For KES CT images, the projection images at a serial of angles are first rearranged to sinograms for each slice. A sinogram is then CT reconstructed into a slice image. Since the normalization step is done either in the projection images or in the sinograms and the CT

reconstruction automatically performs the negative logarithm step, the reconstructed slices of the above and below edge energy are the r_h and r_l signals, respectively. Substituting the above and below slice images into the equation (5.3) will determine the projected density images along a pixel depth (t_0), that is $t_M = t_C = t_0$. The density image slices of the contrast material and equivalent water are finally obtained by dividing the pixel size t_0 and they typically bear the unit of g/cm^3 for ρ_M and mg/cm^3 for ρ_C when the contrast content is dilute.

Under the assumptions of Poisson counting statistics for the detected signals, the SNR of the projected density images are derived as,

$$\begin{aligned} SNR_C &= \frac{\frac{\mu}{\rho}_{Ml}\frac{\mu}{\rho}_{Ch} - \frac{\mu}{\rho}_{Mh}\frac{\mu}{\rho}_{Cl}}{\sqrt{\frac{\mu}{\rho}_{Ml}^2\left(\frac{1}{N_h}+\frac{1}{N_{0h}}\right)+\frac{\mu}{\rho}_{Mh}^2\left(\frac{1}{N_l}+\frac{1}{N_{0l}}\right)}}\rho_C t_C \\ SNR_M &= \frac{\frac{\mu}{\rho}_{Ml}\frac{\mu}{\rho}_{Ch} - \frac{\mu}{\rho}_{Mh}\frac{\mu}{\rho}_{Cl}}{\sqrt{\frac{\mu}{\rho}_{Cl}^2\left(\frac{1}{N_h}+\frac{1}{N_{0h}}\right)+\frac{\mu}{\rho}_{Ch}^2\left(\frac{1}{N_l}+\frac{1}{N_{0l}}\right)}}\rho_M t_M \end{aligned} \tag{5.4}$$

Assuming equal incident flux for two beams and dilute contrast material, SNR are simplified as,

$$\begin{aligned} SNR_C &\approx \sqrt{\frac{N_0}{1+e^{\mu t}}}\frac{\Delta\frac{\mu}{\rho}_C}{\sqrt{2}}\rho_C t_C \\ SNR_M &\approx \sqrt{\frac{N_0}{1+e^{\mu t}}}\frac{\Delta\frac{\mu}{\rho}_C}{\sqrt{\frac{\mu}{\rho}_{Ch}^2+\frac{\mu}{\rho}_{Cl}^2}}\frac{\mu}{\rho}_M\ \rho_M t_M \end{aligned} \tag{5.5}$$

where $\Delta\frac{\mu}{\rho}_C = \frac{\mu}{\rho}_{Ch} - \frac{\mu}{\rho}_{Cl}$, $\frac{\mu}{\rho}_M = \frac{\mu}{\rho}_{Mh} \approx \frac{\mu}{\rho}_{Ml}$, $N_0 = N_{0h} \approx N_{0l}$, $\mu = \frac{\mu}{\rho}_M\ \rho_M$ and $t = t_M + t_C$. The equation (5.5) points out that the SNR of the contrast image is proportional to the thickness, density and the absorption jump of the contrast material, as well as to the square root of the incident flux. It also is decreased with the thickness, density and attenuation coefficient of the matrix material.

5.1.2 Problem with Bone Present

In some cases the presence of bone is inevitable especially in the whole body imaging of an animal or human. As a hard tissue, bone has quite noticeable absorption change over the iodine edge energy compared with water which is considered equivalent to tissue (Figure 5.1).

When bone (B) is present, the dual-energy KES equation (5.1) for such a three-component system would be,

$$\begin{aligned} N_l^{'} &= N_{0l} e^{-\frac{\mu}{\rho}_{Ml} \rho_M t_M} e^{-\frac{\mu}{\rho}_{Cl} \rho_C t_C} e^{-\frac{\mu}{\rho}_{Bl} \rho_B t_B} \\ N_h^{'} &= N_{0h} e^{-\frac{\mu}{\rho}_{Mh} \rho_M t_M} e^{-\frac{\mu}{\rho}_{Ch} \rho_C t_C} e^{-\frac{\mu}{\rho}_{Bh} \rho_B t_B} \end{aligned} \tag{5.6}$$

And taking the negative logarithm of the normalized images results in,

$$\begin{aligned} r_l^{'} &= -\ln\left(\frac{N_l^{'}}{N_{0l}}\right) = \frac{\mu}{\rho}_{Ml} \rho_M t_M + \frac{\mu}{\rho}_{Cl} \rho_C t_C + \frac{\mu}{\rho}_{Bl} \rho_B t_B \\ r_h^{'} &= -\ln\left(\frac{N_h^{'}}{N_{0h}}\right) = \frac{\mu}{\rho}_{Mh} \rho_M t_M + \frac{\mu}{\rho}_{Ch} \rho_C t_C + \frac{\mu}{\rho}_{Bh} \rho_B t_B \end{aligned} \tag{5.7}$$

If equation (5.7) is used in equation (5.3), the resulting solutions for the projected contrast and matrix material are altered. Each picks up an additional term proportional to the projected

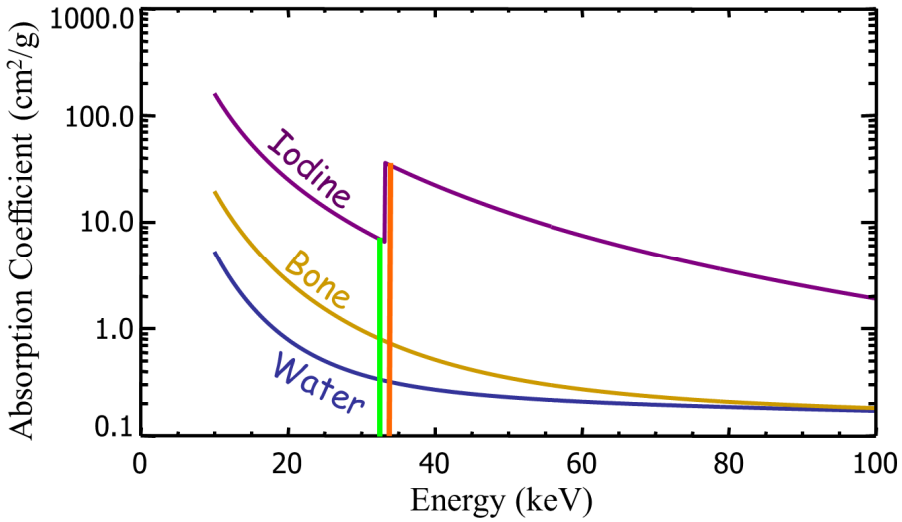

Figure 5.1 The absorption coefficients of the iodine (purple), bone (brown) and water (blue) compared at the high (orange) and low (green) side of the iodine K-edge energy.

density of bone material with a sensitivity coefficient of s_{CB} or s_{MB}, respectively.

$$\begin{aligned} (\rho_C t_C)' &= \rho_C t_C + s_{CB}\rho_B t_B \qquad \text{where} \quad s_{CB} = \frac{\frac{\mu}{\rho}_{Ml}\frac{\mu}{\rho}_{Bh} - \frac{\mu}{\rho}_{Mh}\frac{\mu}{\rho}_{Bl}}{\frac{\mu}{\rho}_{Ml}\frac{\mu}{\rho}_{Ch} - \frac{\mu}{\rho}_{Mh}\frac{\mu}{\rho}_{Cl}} < 0 \\ (\rho_M t_M)' &= \rho_M t_M + s_{MB}\rho_B t_B \qquad \text{where} \quad s_{MB} = \frac{\frac{\mu}{\rho}_{Bl}\frac{\mu}{\rho}_{Ch} - \frac{\mu}{\rho}_{Bh}\frac{\mu}{\rho}_{Cl}}{\frac{\mu}{\rho}_{Ml}\frac{\mu}{\rho}_{Ch} - \frac{\mu}{\rho}_{Mh}\frac{\mu}{\rho}_{Cl}} > 1 \end{aligned} \tag{5.8}$$

The values of $\rho_C t_C$ and $\rho_M t_M$ in equation (5.8) (after the equal sign) represent the true values of the projected contrast and matrix material, respectively. The parenthetical values of $(\rho_C t_C)$ and $(\rho_M t_M)$ before the equal sign represent the changed values of projected contrast and matrix material due to the presence of bone, respectively. The signs of the sensitivity coefficients indicate that the presence of bone could decrease or even cancel out the content of the contrast material in the contrast image while it greatly increases the content of the matrix material in the matrix image. The sensitivity coefficient is energy dependent as expected from the Equation (5.8). Figure 5.2 indicates that the both sensitivity coefficients s_{CB} and s_{MB} increase with bigger

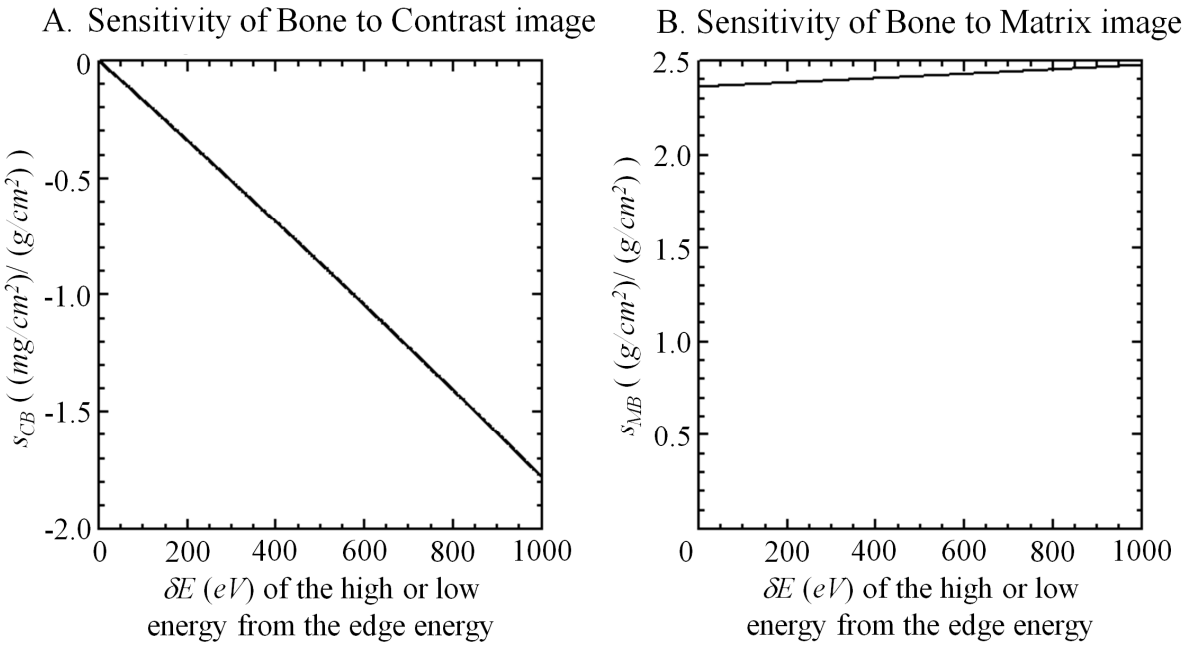

Figure 5.2 The sensitivity of bone to the contrast image (A) and matrix image (B) in relation with the energy difference of the high or low energy from the edge energy of Iodine.

δE which is the energy difference between the high or low imaging energy and the edge energy. So the bigger energy difference δE, the worse the influence from the bone. That s_{MB} starts from a positive number is due to a fixed ratio of the absorption change of bone over that of the matrix material when just crossing the edge energy. That s_{CB} starts from 0 is because of a huge contrast absorption change just around the edge energy instead of the linear absorption change of bone. For 150 *eV* above and below the iodine K-edge, the typical value of s_{MB} is 2.38 $(g/cm^2)/(g/cm^2)$ which means that 1 g/cm^2 of the projected density of bone will add 2.38 g/cm^2 of equivalent projected density for the matrix material, and the typical value of s_{CB} is -0.25 $(mg/cm^2)/(g/cm^2)$ which means that 1 g/cm^2 of the projected density of bone will cancel out 0.25 mg/cm^2 of the projected density of contrast material. Given a detection limit of 17.5 *mM.cm* (2.22 mg/cm^2 of iodine) in a detection system [Zha09] and imaging energies of 150 *eV* above and below the iodine K-edge, the presence of 4.75 *cm* length of bone would totally cancel out the least detectable amount of iodine in the contrast image. Thus the presence of bone induces a serious artifact in the conventional KES imaging.

5.2 Three-Energy KES using a Three-Beam Chopper

To overcome the image blurring due to the presence of bone, three-energy KES imaging is introduced. Combined with a BLM and a three-beam chopper, this method achieves simultaneous three-energy KES imaging and KES CT of live animals without motion artifact. This X-ray imaging system not only allows a contrast image free of both artifacts, but also produces an additional image of bone which has potential application for anatomy or even visualization of calcifications.

5.2.1 Rationale

For a three-component system (contrast material *C*, soft tissue *T* and bone *B*), the number of photon (*N*) arriving at the detector in the beam below the edge energy (*1*), above the edge energy (*2*) and a third imaging energy (*3*) would be,

$$\begin{aligned} N_1 &= N_{01} e^{-\frac{\mu}{\rho_{T1}}\rho_T t_T} e^{-\frac{\mu}{\rho_{B1}}\rho_B t_B} e^{-\frac{\mu}{\rho_{C1}}\rho_C t_C} \\ N_2 &= N_{02} e^{-\frac{\mu}{\rho_{T2}}\rho_T t_T} e^{-\frac{\mu}{\rho_{B2}}\rho_B t_B} e^{-\frac{\mu}{\rho_{C2}}\rho_C t_C} \\ N_3 &= N_{03} e^{-\frac{\mu}{\rho_{T3}}\rho_T t_T} e^{-\frac{\mu}{\rho_{B3}}\rho_B t_B} e^{-\frac{\mu}{\rho_{C3}}\rho_C t_C} \end{aligned} \tag{5.9}$$

If we define $r_i\ (1 \le i \le 3)$ as the negative logarithm of the normalized images from the beam *i*,

$$\begin{aligned} r_1 &= -\ln\frac{N_1}{N_{01}} = \tfrac{\mu}{\rho_{T1}}\rho_T t_T + \tfrac{\mu}{\rho_{B1}}\rho_B t_B + \tfrac{\mu}{\rho_{C1}}\rho_C t_C \\ r_2 &= -\ln\frac{N_2}{N_{02}} = \tfrac{\mu}{\rho_{T2}}\rho_T t_T + \tfrac{\mu}{\rho_{B2}}\rho_B t_B + \tfrac{\mu}{\rho_{C2}}\rho_C t_C \\ r_3 &= -\ln\frac{N_3}{N_{03}} = \tfrac{\mu}{\rho_{T3}}\rho_T t_T + \tfrac{\mu}{\rho_{B3}}\rho_B t_B + \tfrac{\mu}{\rho_{C3}}\rho_C t_C \end{aligned} \tag{5.10}$$

using 3×3 matrix operations the projected density images of the three components are easily derived as,

$$\begin{aligned} \rho_T t_T &= \frac{(\frac{\mu}{\rho_{B2}}\frac{\mu}{\rho_{C3}} - \frac{\mu}{\rho_{B3}}\frac{\mu}{\rho_{C2}})r_1 + (\frac{\mu}{\rho_{B3}}\frac{\mu}{\rho_{C1}} - \frac{\mu}{\rho_{B1}}\frac{\mu}{\rho_{C3}})r_2 + (\frac{\mu}{\rho_{B1}}\frac{\mu}{\rho_{C2}} - \frac{\mu}{\rho_{B2}}\frac{\mu}{\rho_{C1}})r_3}{\frac{\mu}{\rho_{T1}}(\frac{\mu}{\rho_{B2}}\frac{\mu}{\rho_{C3}} - \frac{\mu}{\rho_{B3}}\frac{\mu}{\rho_{C2}}) + \frac{\mu}{\rho_{B1}}(\frac{\mu}{\rho_{C2}}\frac{\mu}{\rho_{T3}} - \frac{\mu}{\rho_{C3}}\frac{\mu}{\rho_{T2}}) + \frac{\mu}{\rho_{C1}}(\frac{\mu}{\rho_{T2}}\frac{\mu}{\rho_{B3}} - \frac{\mu}{\rho_{T3}}\frac{\mu}{\rho_{B2}})} \\ \rho_B t_B &= \frac{(\frac{\mu}{\rho_{C2}}\frac{\mu}{\rho_{T3}} - \frac{\mu}{\rho_{C3}}\frac{\mu}{\rho_{T2}})r_1 + (\frac{\mu}{\rho_{T1}}\frac{\mu}{\rho_{C3}} - \frac{\mu}{\rho_{T3}}\frac{\mu}{\rho_{C1}})r_2 + (\frac{\mu}{\rho_{C1}}\frac{\mu}{\rho_{T2}} - \frac{\mu}{\rho_{C2}}\frac{\mu}{\rho_{T1}})r_3}{\frac{\mu}{\rho_{T1}}(\frac{\mu}{\rho_{B2}}\frac{\mu}{\rho_{C3}} - \frac{\mu}{\rho_{B3}}\frac{\mu}{\rho_{C2}}) + \frac{\mu}{\rho_{B1}}(\frac{\mu}{\rho_{C2}}\frac{\mu}{\rho_{T3}} - \frac{\mu}{\rho_{C3}}\frac{\mu}{\rho_{T2}}) + \frac{\mu}{\rho_{C1}}(\frac{\mu}{\rho_{T2}}\frac{\mu}{\rho_{B3}} - \frac{\mu}{\rho_{T3}}\frac{\mu}{\rho_{B2}})} \\ \rho_C t_C &= \frac{(\frac{\mu}{\rho_{T2}}\frac{\mu}{\rho_{B3}} - \frac{\mu}{\rho_{T3}}\frac{\mu}{\rho_{B2}})r_1 + (\frac{\mu}{\rho_{T3}}\frac{\mu}{\rho_{B1}} - \frac{\mu}{\rho_{T1}}\frac{\mu}{\rho_{B3}})r_2 + (\frac{\mu}{\rho_{T1}}\frac{\mu}{\rho_{B2}} - \frac{\mu}{\rho_{T2}}\frac{\mu}{\rho_{B1}})r_3}{\frac{\mu}{\rho_{T1}}(\frac{\mu}{\rho_{B2}}\frac{\mu}{\rho_{C3}} - \frac{\mu}{\rho_{B3}}\frac{\mu}{\rho_{C2}}) + \frac{\mu}{\rho_{B1}}(\frac{\mu}{\rho_{C2}}\frac{\mu}{\rho_{T3}} - \frac{\mu}{\rho_{C3}}\frac{\mu}{\rho_{T2}}) + \frac{\mu}{\rho_{C1}}(\frac{\mu}{\rho_{T2}}\frac{\mu}{\rho_{B3}} - \frac{\mu}{\rho_{T3}}\frac{\mu}{\rho_{B2}})} \end{aligned} \tag{5.11}$$

Or

$$\begin{aligned} \rho_T t_T &= \frac{1}{D_3}(V_{T1}r_1 + V_{T2}r_2 + V_{T3}r_3) \\ \rho_B t_B &= \frac{1}{D_3}(V_{B1}r_1 + V_{B2}r_2 + V_{B3}r_3) \\ \rho_C t_C &= \frac{1}{D_3}(V_{C1}r_1 + V_{C2}r_2 + V_{C3}r_3) \end{aligned} \quad where \begin{bmatrix} \frac{\mu}{\rho_{T1}} & \frac{\mu}{\rho_{B1}} & \frac{\mu}{\rho_{C1}} \\ \frac{\mu}{\rho_{T2}} & \frac{\mu}{\rho_{B2}} & \frac{\mu}{\rho_{C2}} \\ \frac{\mu}{\rho_{T3}} & \frac{\mu}{\rho_{B3}} & \frac{\mu}{\rho_{C3}} \end{bmatrix}^{-1} = \frac{1}{D_3}\begin{bmatrix} V_{T1} & V_{T2} & V_{T3} \\ V_{B1} & V_{B2} & V_{B3} \\ V_{C1} & V_{C2} & V_{C3} \end{bmatrix} \tag{5.12}$$

Under the assumptions of Poisson counting statistics for the detected signals, the SNR of the projected density images are derived as,

$$SNR_T = \frac{D_3}{\sqrt{V_{T1}^2\left(\frac{1}{N_1}+\frac{1}{N_{01}}\right)+V_{T2}^2\left(\frac{1}{N_2}+\frac{1}{N_{02}}\right)+V_{T3}^2\left(\frac{1}{N_3}+\frac{1}{N_{03}}\right)}}\rho_T t_T$$

$$SNR_B = \frac{D_3}{\sqrt{V_{B1}^2\left(\frac{1}{N_1}+\frac{1}{N_{01}}\right)+V_{B2}^2\left(\frac{1}{N_2}+\frac{1}{N_{02}}\right)+V_{B3}^2\left(\frac{1}{N_3}+\frac{1}{N_{03}}\right)}}\rho_B t_B \qquad (5.13)$$

$$SNR_C = \frac{D_3}{\sqrt{V_{C1}^2\left(\frac{1}{N_1}+\frac{1}{N_{01}}\right)+V_{C2}^2\left(\frac{1}{N_2}+\frac{1}{N_{02}}\right)+V_{C3}^2\left(\frac{1}{N_3}+\frac{1}{N_{03}}\right)}}\rho_C t_C$$

Assuming dilute contrast material in the object, equal incident and transmitted flux for the three beams, the SNR equation are simplified as,

$$SNR_T \approx \sqrt{\frac{N_0}{1+e^{\mu t}}}\frac{\frac{\mu}{\rho_{T1}}V_{T1}+\frac{\mu}{\rho_{T2}}V_{T2}+\frac{\mu}{\rho_{T3}}V_{T3}}{\sqrt{V_{T1}^2+V_{T2}^2+V_{T3}^2}}\rho_T t_T$$

$$SNR_B \approx \sqrt{\frac{N_0}{1+e^{\mu t}}}\frac{\frac{\mu}{\rho_{B1}}V_{B1}+\frac{\mu}{\rho_{B2}}V_{B2}+\frac{\mu}{\rho_{B3}}V_{B3}}{\sqrt{V_{B1}^2+V_{B2}^2+V_{B3}^2}}\rho_B t_B \qquad (5.14)$$

$$SNR_C \approx \sqrt{\frac{N_0}{1+e^{\mu t}}}\frac{\frac{\mu}{\rho_{C1}}V_{C1}+\frac{\mu}{\rho_{C2}}V_{C2}+\frac{\mu}{\rho_{C3}}V_{C3}}{\sqrt{V_{C1}^2+V_{C2}^2+V_{C3}^2}}\rho_C t_C$$

where $N_0 = N_{01} \approx N_{02} \approx N_{03}$, $\mu = \frac{\mu}{\rho_T}\rho_T$, $t = t_T + t_C + t_B$ and $N = N_1 \approx N_2 \approx N_3 = N_0 e^{\mu t}$

Similar to the SNR of the dual-energy KES, the three-energy SNR of the contrast image is proportional to the thickness and density of the contrast material, is proportional to the square root of the incident flux, and still has an opposite relation to the thickness, density and attenuation coefficient of the tissue material.

5.2.2 Materials and Methods

5.2.2.1 The Third Energy Optimization

Using the equations in Chapter 5.2.1 for the three-energy KES, an optimization of the third imaging energy was surveyed in an energy range from 35 *keV* to 150 *keV* (Figure 5.3). The other two imaging energies were set as 100 *eV* above and below the iodine K-edge energy (33.17 *keV*). Two parameters were optimized at the same time in the calculation. One is the third imaging energy and the other is the fraction of dose allocated to each of the three imaging energies. The calculation assumed a total dose of 10 *mGy* for the three energies incident on a sample of 5 *cm* thick water or tissue equivalent, 0.5 *cm* thick bone and a projected iodine density of 1 mg/cm^2. For each third imaging energy, the SNR of the iodine image was calculated for each of the possible dose allotments among the three energies and the maximal SNR of iodine was recorded. As noted by the dashed line in Figure 5.3, the optimal third imaging energy was found to be 92 *keV*. Since the beams were prepared by {311} diffraction in our experiments, the second

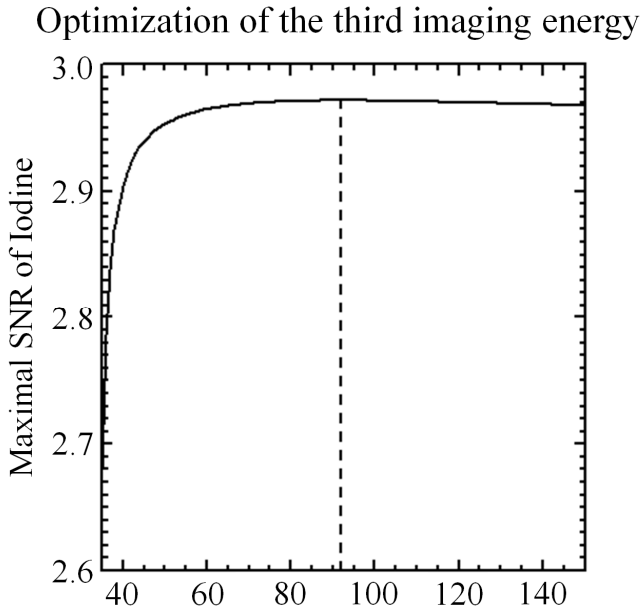

Figure 5.3 The maximal SNR of iodine image achievable at different third imaging energies when the above and below the edge energy are set as 33.27 *keV* and 33.07 *keV,* respectively. The optimal third imaging energy is 92 *keV* as denoted in the dashed line.

harmonic of the diffracted central energy which is 99.51 *keV* and closest to the optimum was chosen as the third imaging energy. As listed in Table 5.1, a projected iodine density of 1 mg/cm^2 should achieve the maximal SNR of 2.97 in the iodine image when the dose of the above and below energies (100 *eV* from the edge energy) are on average 99.5 times higher than that of the 99.51 *keV,* or the incident fluxes of the above and below energies are on average 73.6 times higher than that of the 99.51 *keV,* when the detector response is not considered. In other words, if the detection limit is set when the SNR is slightly bigger than 1, the above incident fluxes or dose requirements among the three energies would achieve an iodine detection limit lower than 1 mg/cm^2.

Table 5.1 The maximal SNR of the iodine image could be achieved for the third imaging energy of 99.51 *keV* and the corresponding dose and flux requirements, when the detector response is not considered.

	Below edge beam	*Above edge beam*	*Third imaging beam*
Beam energies (keV)	33.07	33.27	99.51
Total dose (mGy)		10	
Dose allotments (mGy)	4.925	5.025	0.05
Dose ratios	98.5	100.5	1
Incident flux (photon/cm^2)	9.3×10^9	9.6×10^9	1.3×10^8
Incident flux ratios	72.5	74.8	1
Maximal SNR of iodine image		2.97	

5.2.2.2 Bent Laue Monochromator Design

The designs and calculations of the BLM were based on the thesis work of a previous student Dr. Honglin Zhang. For a BLM diffracting the iodine K-edge energy (33.17keV) for BMIT at the CLS, the {311} diffraction from a Si (511) wafer would provide a “magic”

asymmetry angle which meets with the sub-micron focus size condition [Zha09]. Two BLMs were designed for both the BM and insertion device (ID) beamline for BMIT at the CLS.

The BLM design procedures started from the determination of the Si crystal's bending radius. Since the crystal thickness has no relation with the geometric focus length f_2 and very little effect on the single ray focus length L [Zha09], a 600 μm thick Si (511) wafer was used since it was already available in our lab. Given the {311} diffraction of 33.17 keV from a 600 μm thick Si (511) wafer at a source-to-crystal distance of the BMIT BM or ID beamline, the geometric focus length f_2 and the single ray focus length L were calculated for a range of crystal bending radii. The optimal crystal bending radius was chosen at the cross point of the f_2 and L curves.

Diffraction from a bent crystal normally has a broader energy bandwidth (about 10^{-3}) than the diffraction from a perfect crystal (about 10^{-5}). The diffracted energies within the bandwidth are spatially separated since the incident angles of the incident white beam are gradually changing along the cylindrically bent crystal. For a beam chopper after the BLM to separate the beams of different energies, the beams should have well-defined sizes or beam heights. The chopper-accepted beam height is closely related to the incident beam height which was defined as 5 mm for the BMIT ID beamline. The edge-to-edge energy span ($2\delta E_{max}$) that is diffracted from a 5 mm high incident beam was determined based on the above given parameters and the crystal bending radius.

The BLMs were then fully determined for the BMIT BM and ID beamlines with the geometric scheme shown in Figure 5.4 and design parameters listed in Table 5.2. As shown in Figure 5.4, the cylindrically bent BLM was tilted 9.9º ($\chi + \theta_B$) from the vertical to diffract the horizontal incident beam 13.1º ($2\theta_B$) upward. The geometric focus length f_2 was designed to be

equal to the single ray focus length L to reach the sub-micron focus size. 100 *mm* after the BLM, the chopper separated the three beams with a total beam height of 4.779 *mm*. The 100 *mm* distance between centers of the BLM and the chopper is the closest spacing allowed for physical setup while maintaining a reasonable beam height at the chopper position for easier machining of the chopper. For the same chopper to be used for both the BMIT BM and BMIT ID beamline at the CLS, the incident beam height of the BLM for BMIT BM beamline was adjusted to 5.056 *mm* to keep the same chopper beam height of 4.779 *mm*. The edge-to-edge diffracted energies were designed to be 268 *eV* or 223 *eV* above and below 33.17 *keV* for the BMIT BM or BMIT ID beamline, respectively. The BLM focus is a line focus. The focus width depends on the incident beam width and the BLM width. The theoretical focus sizes in Table 5.2 are the vertical height of the foci which were theoretically calculated assuming a perfect point source. The real source has a certain size, for example 118 μm height by 379 μm width for the BMIT BM source

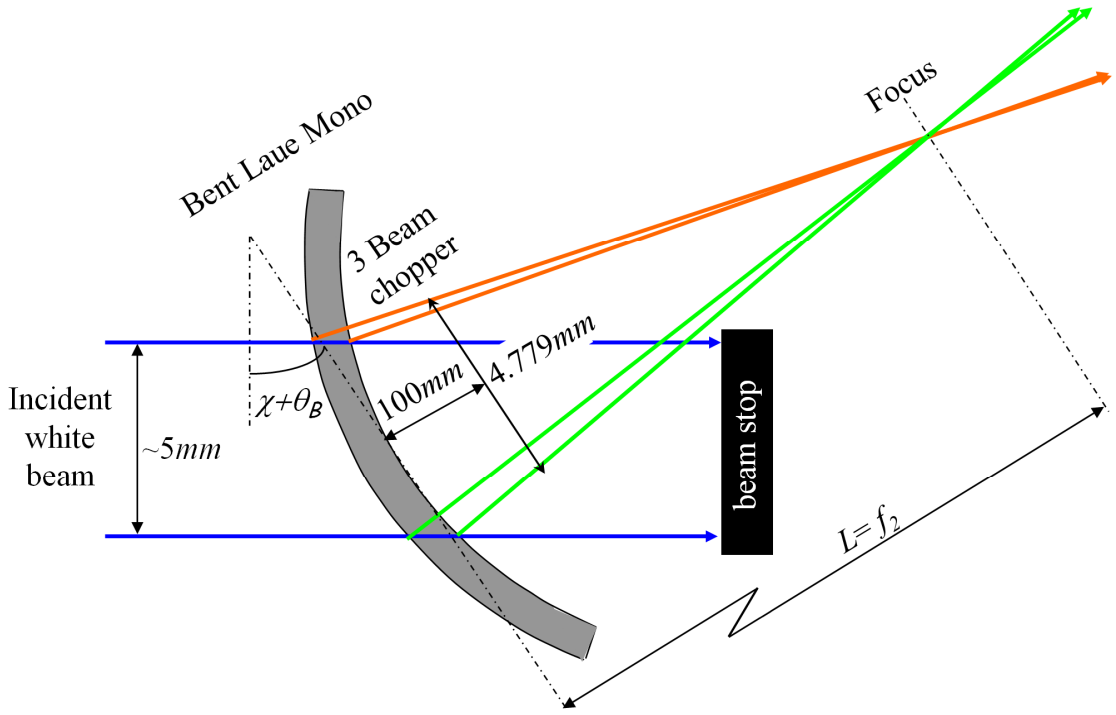

Figure 5.4 The BLM reaching the sub-micron focus size condition that the geometric focus length f_2 is equal to the single ray focus length L (Adapted figure from [Zha09]).

Table 5.2 Design parameters of the BLMs for iodine KES at the BMIT BM and ID beamlines

Design parameters	*BMIT BM beamline*	*BMIT ID beamline*
Si wafer	Si (511)	
Crystal thickness t (μm)	600	
Diffraction Plane DP	{311}	
Asymmetry angle χ (°)	3.3	
Poisson ratio	0.28 [Bra73]	
Central ray energy (keV)	33.17	
Bragg angle θ_B (°)	6.55	
Darwin width ω_D (μrad)	3.03	
Energy resolution of perfect crystal (eV)	0.87	
Source-to-crystal distance f_1 (m)	20.59	24.50
Crystal bending radius r (m)	3.13	3.72
Geometric focus length f_2 (m)	1.45	1.73
Single ray focus length L (m)		
Incident beam height (mm)	5.056	4.997
Chopper beam height (mm)	4.779	
Theoretical focus size (μm)	0.021	0.081
Practical limit of focus size (μm)	8.3	2.8
Edge-to-center energy difference δE_{max} (eV)	268	223
Diffracted beam divergence (mrad)	3.5	2.9
Intrinsic energy resolution (eV)	0.95	0.80
Intrinsic energy resolution considering Darwin width (eV)	1.29	1.18

and 39μm height by 1038μm width for the BMIT ID source. Considering the source-to-crystal distance f_1 and crystal-to-focus distance f_2, the practical limit of the focus sizes at the sample position would be 8.3 μm and 2.8 μm for BMIT BM and ID beamline, respectively. Since the

real focus size would not be smaller than its practical limit and the measured focus size of the present study is about 100 μm (Chapter 5.2.3.3), the calculation of the diffracted beam divergence is based on the 100 μm focus size, the incident beam height projected on the BLM and the distance between the two (f_2 or L). The intrinsic energy resolution in Table 5.2 is a property of the BLM and independent of the pixel size and distance of the detector in use. We could see that under the magic condition of $f_2 = L$, the intrinsic energy resolution of the BLM is close to the energy resolution of a perfect crystal. Considering the Darwin width of the crystal, the intrinsic energy resolution of the BLM is estimated as 1.29 eV and 1.18 eV for the BMIT BM and ID beamline, respectively.

5.2.2.3 Crystal Preparations

The Si (511) wafers were oriented by transmission Laue diffraction using white beam at the BMIT BM beamline at the CLS. The two fold symmetry was obvious in the transmission Laue photograph (Figure 5.5). Because the asymmetry angle is critical to achieve a sub-micron focus size for a BLM [Zha09], the error of asymmetry angle was measured for each wafer at RMD Engineering Inc. (Saskatoon, SK, Canada). Si wafers normally have an off-cut which is the angle between the actual surface plane and the desired atomic plane at the surface. Since the error of the {311} asymmetry angle is closely related to the off-cut of the (511) wafer and the error of the {220} flat edge which is always perpendicular to the (511) plane, the error of the {220} flat edge was measured instead. The off-cut angle was determined with a pencil beam (mainly K_α fluorescence at 8.04 keV) from a copper-target X-ray tube incident on the {220} flat edge at its Bragg angle (23.7º). A detector on the diffractometer was positioned to find the diffracted beam (Figure 5.6). The same {220} diffraction measurement was repeated with the (511) wafer flipped on the stage. The angle difference between the two measurements estimated

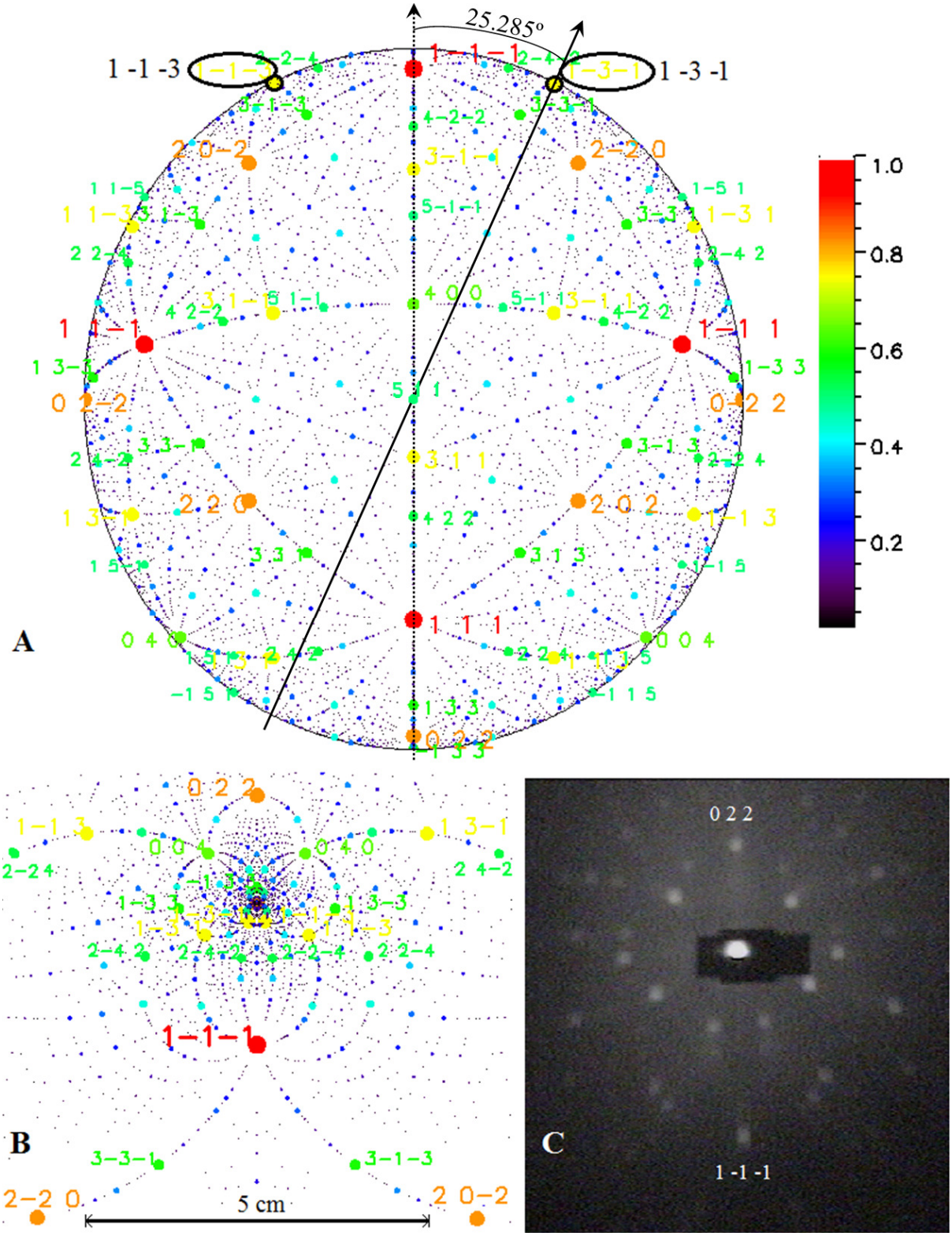

Figure 5.5 Stereographic projection of Si (511) (A), the transmission Laue simulation (B) at 30 *mm* crystal-to-film distance and the real photograph taken at the BMIT BM beamline (C). The relative reflectivity of each plane was mapped by color and size of the dot and its Miller index.

the error of the {220} flat edge which turned out to be in the range of 0.01° ~ 0.41° for the 10 tested wafers. Three wafers with the least error or off-cut (0.01°, 0.03° and 0.07°) were chosen as the BLM candidates.

Several Si (511) wafers of 5 inch diameter and 600 μm thickness were cut into rectangles of 70 *mm* wide by 103.5 *mm* high or 100 *mm* wide by 75 *mm* high along the desired [1,-3,-1] direction which is 25.285° away from the [1,-1,-1] direction. The cut sides of the wafers went through the same etching process as described in chapter 4.2.5 at the SSSC in Saskatoon.

The surface flatness of the Si wafers were checked for uniform bending by an optical flat (0.1λ accuracy on single surface, Edmund Optics Inc., Barrington NJ USA), a first surface mirror (Edmund Optics Inc., Barrington NJ USA) and a monochromatic light source (0.546 μm wavelength, Sequal UniLamp UL-12, Universal Photonics Inc., Hicksville NY USA) (Figure 5.7). The interference patterns showed the surface unevenness of about 10 μm.

The rectangular Si (511) wafer was then mounted in a four-bar bender [Zho97-2] to be bent cylindrically along the <311> direction. The bending radius was measured by focusing a fan laser beam (line laser source) in a dark room. The crystal bending uniformity was checked and

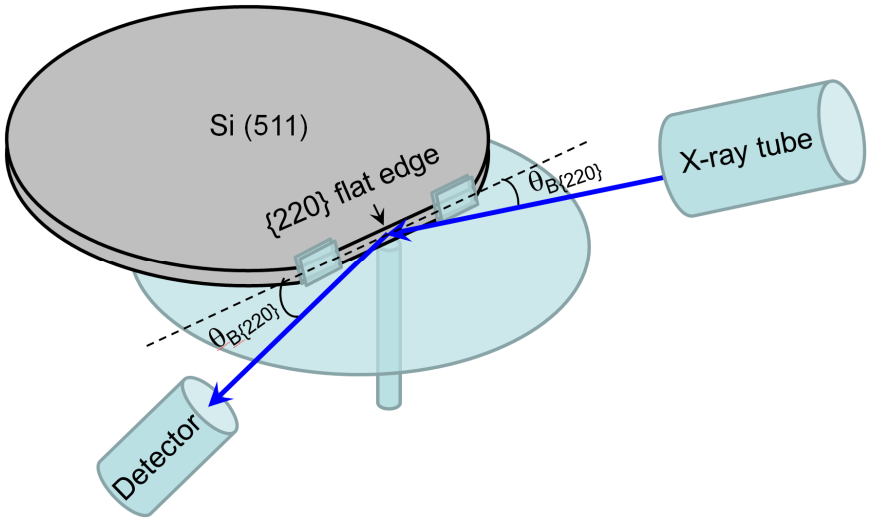

Figure 5.6 Sketch of off-cut measurement for Si (511) wafer

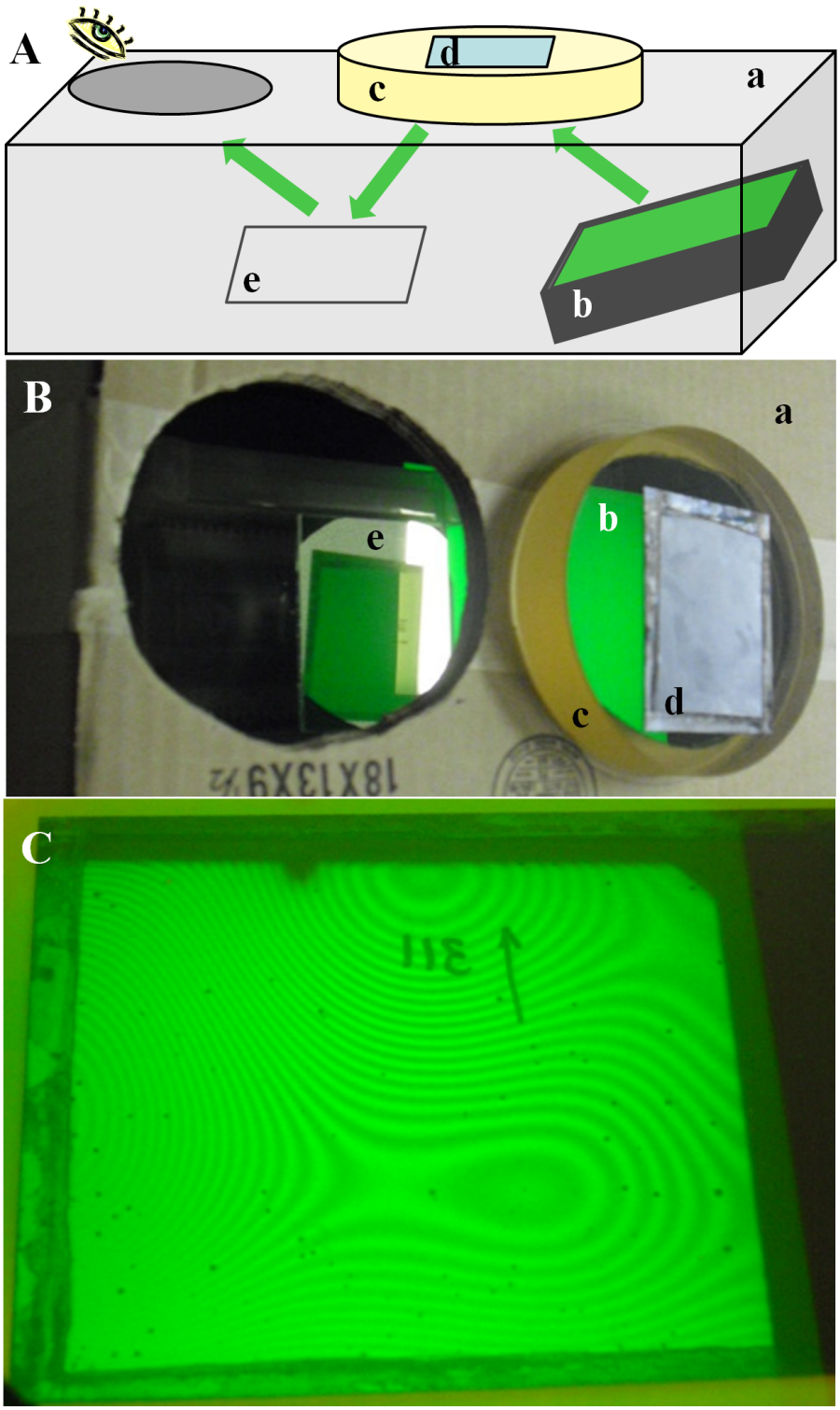

Figure 5.7 The sketch (A) and photo (B) of checking the flatness of the crystal surface. A green light box (b) and a first surface mirror (e) were put into a dark box (a) with two holes, one of which was covered by an optical flat (c) and a Si wafer (d). Counting the fringes in the interference pattern (C) indicated the unevenness of the crystal surface.

adjusted all across the wafer to make the focus on a viewing screen the same size and position (Figure 5.8).

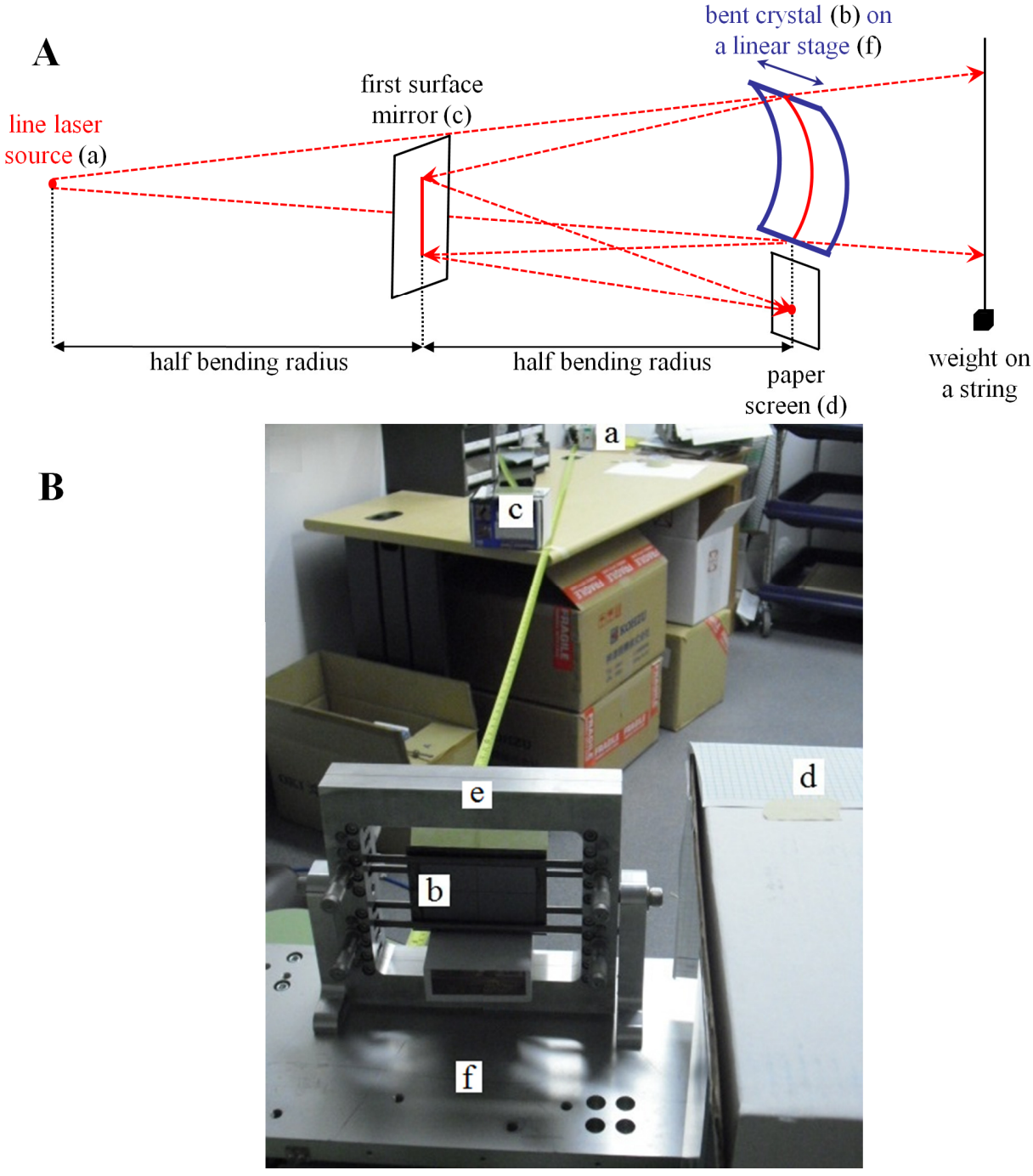

Figure 5.8 The sketch (A) and photo (B) for bending radius measurement and bending uniformity check while the bent crystal (b) in a four-bar bender (e) was moving from side to side on a linear stage (f). The weight on a string was a vertical reference for the line laser source.

5.2.2.4 Three-Beam Heights Optimization

Optimization of the three-beam heights was based on the flux requirement of the three beams to achieve the best SNR in the contrast image. The calculation considered the geometry and fluxes from both the BMIT BM (1.354 Tesla of magnetic field) and BMIT ID (Wiggler of 25 full and 2 half poles at 4.3 Tesla of magnetic field) beamlines at the CLS, and also considered the detecting efficiency of both the available detectors, the Budker line detector (40 *cm* equivalent thickness Xenon gas filled, 100 μm pixel size, from Budker Institute of Nuclear Physics, Russia) and the Photonic Science area detector (FDI VHR 90 *mm*, 100 μm thick or 7.5 mg/cm^2 projected density Gd_2O_2S, 18.7 μm pixel size, from Photonic Science Ltd., UK).

Similar to the simulation in chapter 5.2.2.1, the calculation assumed a total dose of 10 *mGy* for three energies incident on a sample of 5 *cm* thick water or tissue equivalent, 0.5 *cm* thick bone and a projected iodine density of 1 mg/cm^2. Detailed calculation of the flux requirement of the three beams to achieve the best SNR in the contrast image would consider the detector efficiency to respond to different energies and accurate energy difference δE of the above or below edge energy away from the iodine K-edge energy.

To determine the energy difference δE corresponding to the best SNR in the contrast image, several loops of iteration procedures were followed to refine the energy difference δE. The δE iteration started from δE_{max}, the edge-to-center energy difference of the diffracted beam, which is 268 *eV* or 223 *eV* for the BMIT BM or ID beamline as shown in Table 5.2, respectively. Knowing the exact above and below edge energies and the third energy as 99.51 *keV*, the flux requirement of the three energies to achieve the best SNR in the iodine image was calculated for both the Budker and the Photonic Science detectors. Considering the flux and energy distributions and filters in the BMIT BM or ID beamline as well as the {311} BLM reflectivity,

this flux requirement of the three energies was used to determine the three-beam heights after the BLM which directly defined the average energies of above and below beam. A new δE was then produced and used to adjust the above and below energies in the next iteration until no change of δE was observed. The final δE, three-beam heights ratio, the dose and flux requirements to achieve the best SNR in the iodine image are listed in Table 5.3.

The maximal SNRs of the iodine image in Table 5.3 show that the Budker detector responds better than the Photonic Science detector which is reasonable since the Budker detector has more photon stopping power throughout the energy range than the Photonic Science detector. The three-beam height ratios in Table 5.3 indicate that the BMIT ID beamline has more flux of 99.51 keV than the BMIT BM beamline which is predictable since the critical energy of the BMIT ID beamline is 24.05 keV while it is 7.57 keV for the BMIT BM beamline. But all the three-beam height ratios for the optimal SNR in Table 5.3 are not practical to machine a three-beam chopper. For practical reasons, the three-beam height ratios of 1:2:1 and 1:1:1 were suggested. The flux ratios and the SNR that would be achieved were calculated and listed in Table 5.3 as well. The designated three-beam height ratio of 1:2:1 and 1:1:1 achieved acceptable SNR at the BMIT ID beamline and only little SNR differences between the two.

These four choices of three-beam heights were also marked in Figure 5.9 which plots the change of the three-beam fluxes while enlarging the central beam heights at the BMIT BM and ID beamline. The flux of below edge beams (green lines) are barely seen since they are overlapped by the above edge beams (red lines).

Considering the impracticality of the optimal SNR and little SNR differences between the three-beam height ratios of 1:2:1 and 1:1:1, the choice of three equal beam heights is a good decision both theoretically and practically. With three beams of equal height, a projected iodine

Table 5.3 Parameters for the three-beam height optimization. The "Optimal SNR" listed the three-beam heights reaching the flux and dose requirements of the best SNR of the iodine image. The "Designated three-beam height ratio" listed the fluxes and SNR achieved using different detectors. The symbol *D* is for dose, *N* for flux and *h* for beam height. The subscript 1 is for above edge beam, 2 for below edge beam and 3 for 99.51 *keV* beam.

Beam line		*Optimal SNR*		*Three-beam height ratio (h_1:h_3:h_2)*			
				1:2:1		*1:1:1*	
	Detector	*Photonic Science*	*Budker*	*Photonic Science*	*Budker*	*Photonic Science*	*Budker*
BMIT	*Energy difference δE (eV)*	269	268	201		179	
	Three-beam heights ratio	1:4461:1	1:2568:1	1:2:1		1:1:1	
BM	*Dose ratio ($(D_1+D_2)/2D_3$)*	16	28	-		-	
	Flux ratio ($(N_1+N_2)/2N_3$)	12	21	69,253		153,522	
	SNR of iodine image	0.28	3.97	0.03	0.66	0.02	0.50
	SNR ratio (SNR/SNR_{max})	100%	100%	10%	17%	8%	13%
BMIT	*Energy difference δE (eV)*	220	217	167		149	
	Three-beam heights ratio	1:66:1	1:39:1	1:2:1		1:1:1	
ID	*Dose ratio ($(D_1+D_2)/2D_3$)*	20	33	-		-	
	Flux ratio ($(N_1+N_2)/2N_3$)	14	24	429		839	
	SNR of iodine image	0.28	3.98	0.24	3.75	0.22	3.62
	SNR ratio (SNR/SNR_{max})	100%	100%	85%	94%	79%	90%

density of 1 *mg/cm*^{2} should achieve the a SNR of 3.62 in the iodine image using the Budker detector at the BMIT ID beamline when the incident fluxes of the above and below energies are on average 839 times higher than that of the 99.51 keV. The fluxes for the three beams of equal height were calculated (Table 5.4). The efficiency in Table 5.4 is the flux of certain energy collected in one beam over that in all three beams. It was noted that there is a negligible amount of 99.51 *keV* in the above and below beams and great amount of 33.17 *keV* in the middle beams that needed to be dealt with.

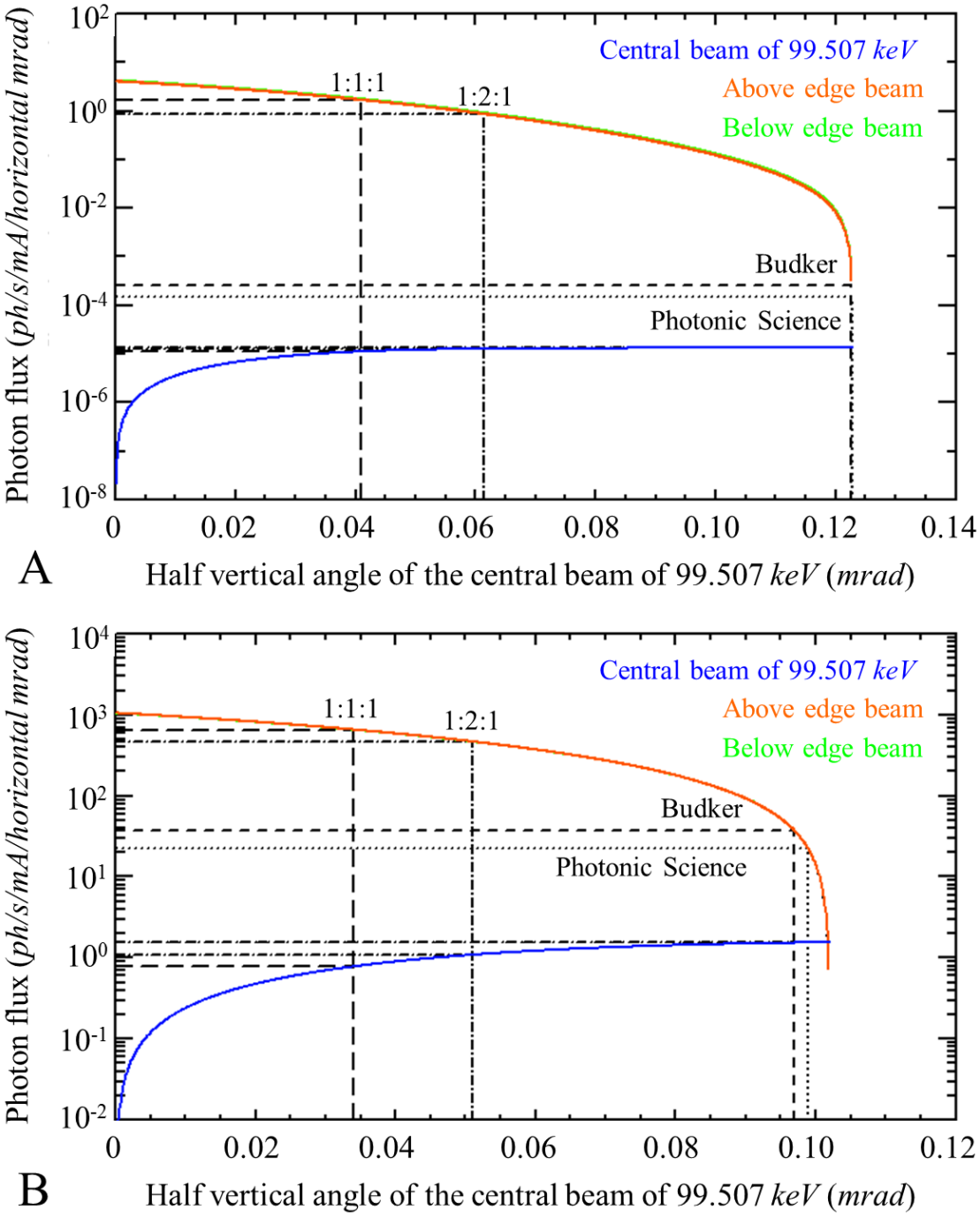

Figure 5.9 Three-beam fluxes vs. central beam height in half vertical angle from the source point for the BMIT BM (A) and ID (B) beamline. The dotted lines indicate the flux ratio requirements for the best SNR in iodine image using Photonic Science detector, and the dashed lines indicate the best SNR in iodine image using Budker detector. The dash-dotted lines indicate the flux ratio for three-beam height ratio of 1:2:1 (Above: 99.51 *keV*: Below), and the long dashed lines indicate the flux ratio for the three beams of equal height.

Table 5.4 Energies, fluxes and efficiencies of the three beams of equal height just after the BLM

Beam position after BLM	*BMIT BM*			*BMIT ID*		
	Energy (keV)	*Photon flux ratio*	*Efficiency (%)*	*Energy (keV)*	*Photon flux ratio*	*Efficiency (%)*
Above E_A	33.35	150,735	41	33.32	840	62
Middle E_K	33.17	431,863	58	33.17	1018	38
Below E_B	32.99	156,308	42	33.02	838	62
Middle E_{3K}	99.51	1	85	99.51	1	50
Above E_{3KA} *or Below* E_{3KB}	99.51	0.09	8	99.51	0.5	25

5.2.2.5 Three-Beam Chopper Design

Each of the three beams at the chopper position would be 1.593 *mm* high and 70 *mm* or 100 *mm* wide depending on the BLM crystal. The cross-section of the three-beam chopper was designed to aim at 60° opening time for each beam and 120° spacing between the successive beam centers in one revolution (Figure 5.10). The hexagonal chopper prepared an open tunnel of about 60° of rotation freedom for the above or below edge beam.

A 1.1 *mm* thick absorber was designed to block the 33.17 *keV* but let through most of the 99.51 *keV* in the middle beam. The material used for the absorber and actually the entire three-beam chopper was the tin bronze alloy C907 [ASTM-B505] which contains 11% of tin and 89% of copper by weight. This tin bronze provided great rigidness for fast rotation of the chopper and excellent stopping power of 33 *keV* while transmitting 99 *keV* which is quantified as a high ratio of the linear absorption coefficient $\mu_{E_K}/\mu_{E_{3K}}$ in Table 5.5. After the 1.1 *mm* thick absorber, 99.99659% of the 33.17 *keV* flux would be stopped while letting through 56.536% of the 99.51 *keV* flux. Given the middle beam incident flux ratio ($N_{0E_K}/N_{0E_{3K}}$) of 431,863 at the BMIT BM and 1,018 at BMIT ID beamline (Table 5.4), the transmitted flux ratio ($N_{E_K}/N_{E_{3K}}$) after the 1.1

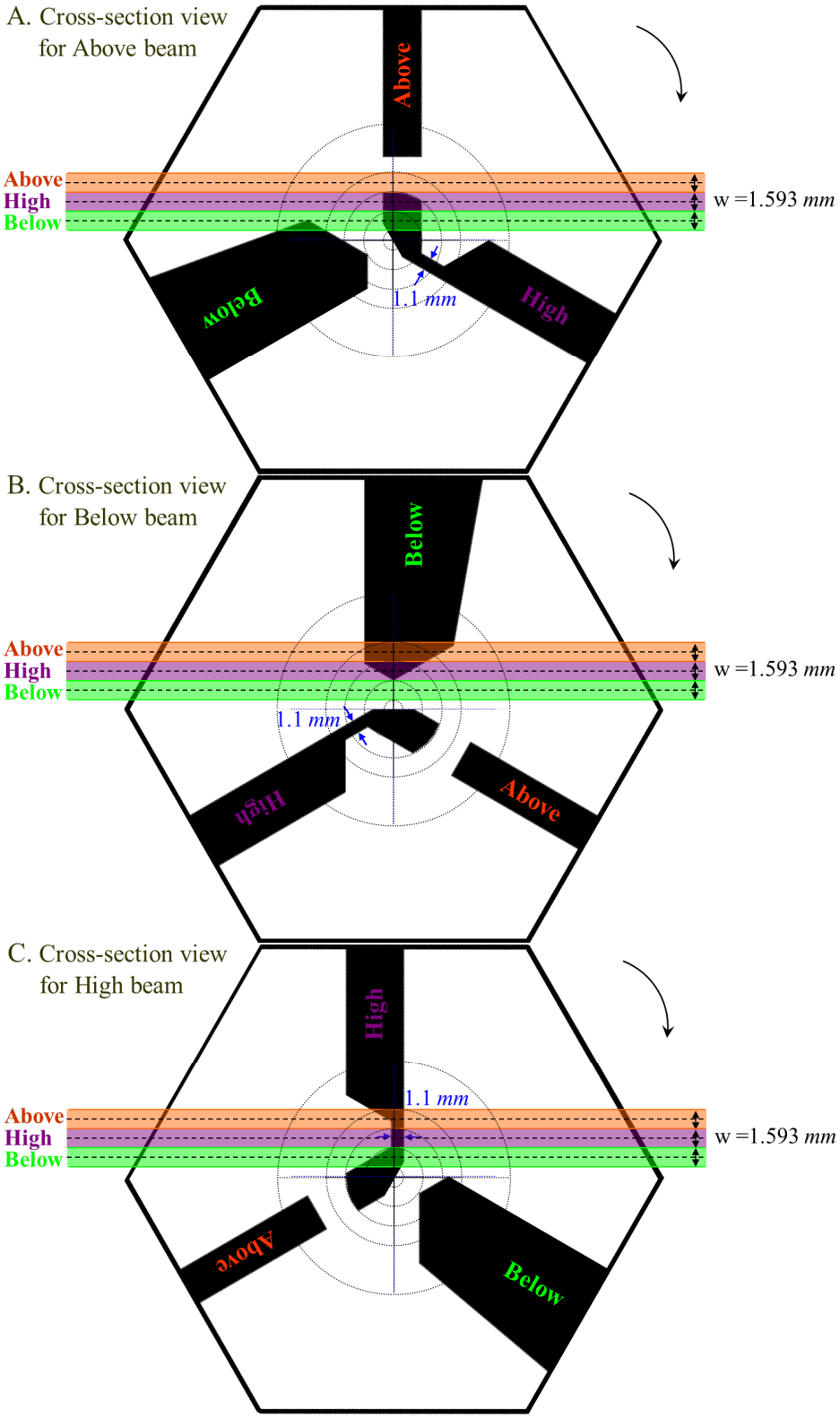

Figure 5.10 Cross-section views of the three-beam chopper for penetrating Above edge beam (A), Below edge beam (B) and High energy beam of 99.51 *keV* (C).

Table 5.5 Material selection for the three-beam chopper

Linear absorption coefficient μ (1/cm)	*Iodine K-edge* E_K *(33.17 keV)*	*2nd Hamonic* E_{3K} *(99.51 keV)*	*Linear absorption coefficient ratio* ($\mu_{E_K}/\mu_{E_{3K}}$)
Silver	296	15	19.2
Tin	231	12	18.8
Tin bronze alloy C907	93	5	18.0
Tin bronze alloy C913	108	6	17.9
Tin bronze alloy C903	88	5	17.6
Lead	263	64	4.1

mm thick absorber would be 26 at the BMIT BM beamline and 0.06 at the BMIT ID beamline, respectively. This factor would degrade the performance of the third image in the three-energy KES at the BMIT BM beamline.

The average transmission ratios (Figure 5.11) and the relative intensity distributions (Figure 5.12) of different beam energies were simulated for a 420° revolution of the three-beam chopper at the BMIT BM and ID beamlines. The photon flux results for both beamlines in Chapter 5.2.2.4 were input as the incident fluxes of different beam energies while the beam transmission through the three-beam chopper was calculated at every chopper rotation angle. The peaks of the above edge beam E_A and the below edge beam E_B had about 60° of on-duty time and characteristic shapes due to the cross-sectional design of the three-beam chopper. The third imaging energy E_{3K} could not be seen in the linear scale profiles at both the BMIT BM and ID beamlines (Figure 5.11A and C, Figure 5.12A and C), but they showed up in the logarithmic scale profiles (Figure 5.11B and D, Figure 5.12D). The edge energy E_K in the middle beam emerged a little (less than 10%) along with the above edge beam E_A or the below edge beam E_B,

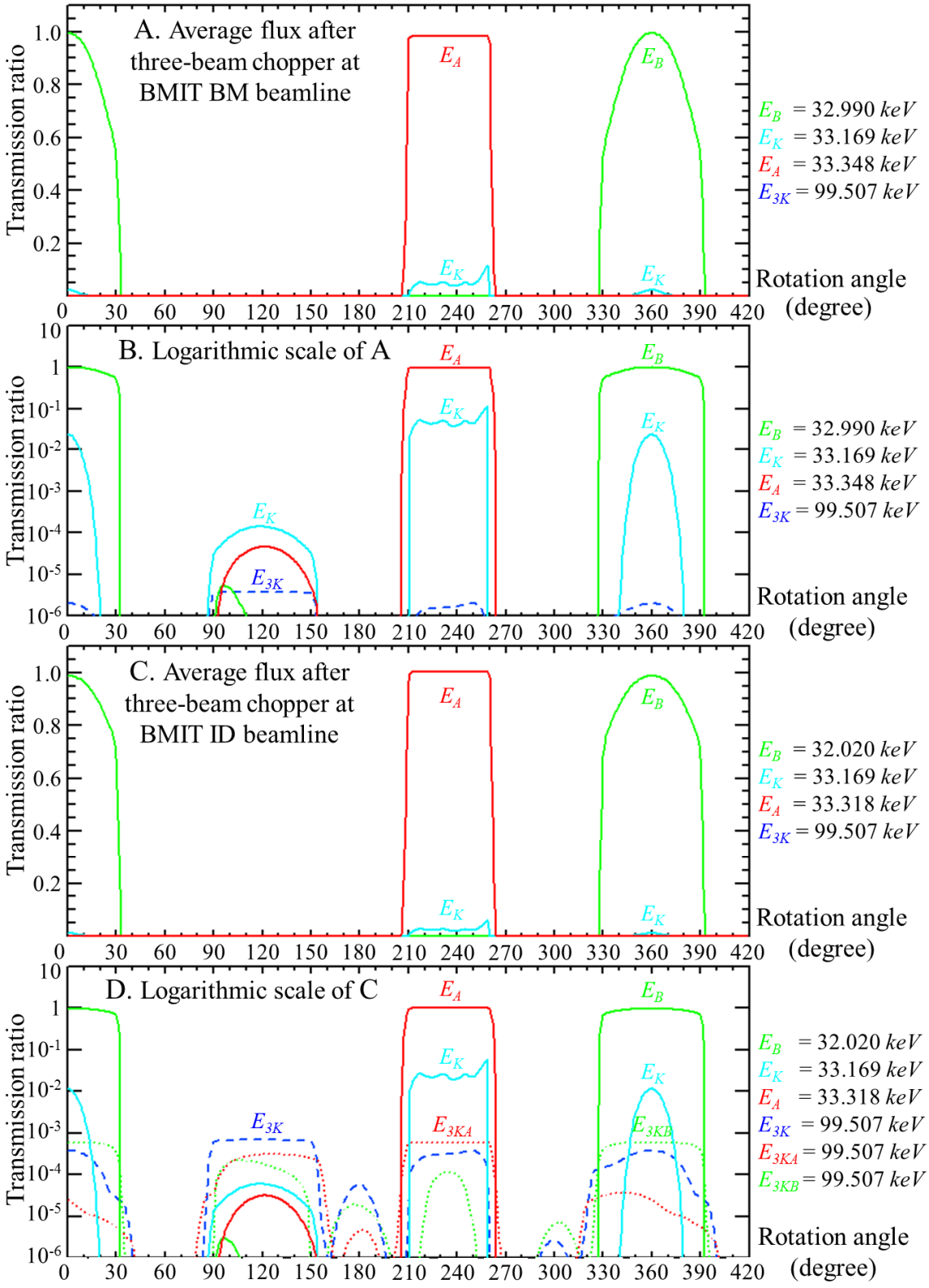

Figure 5.11 Simulated average beam fluxes after the three-beam chopper vs. chopper rotation angle at the BMIT BM (A, B in logarithmic scale) and ID (C, D in logarithmic scale) beamlines.

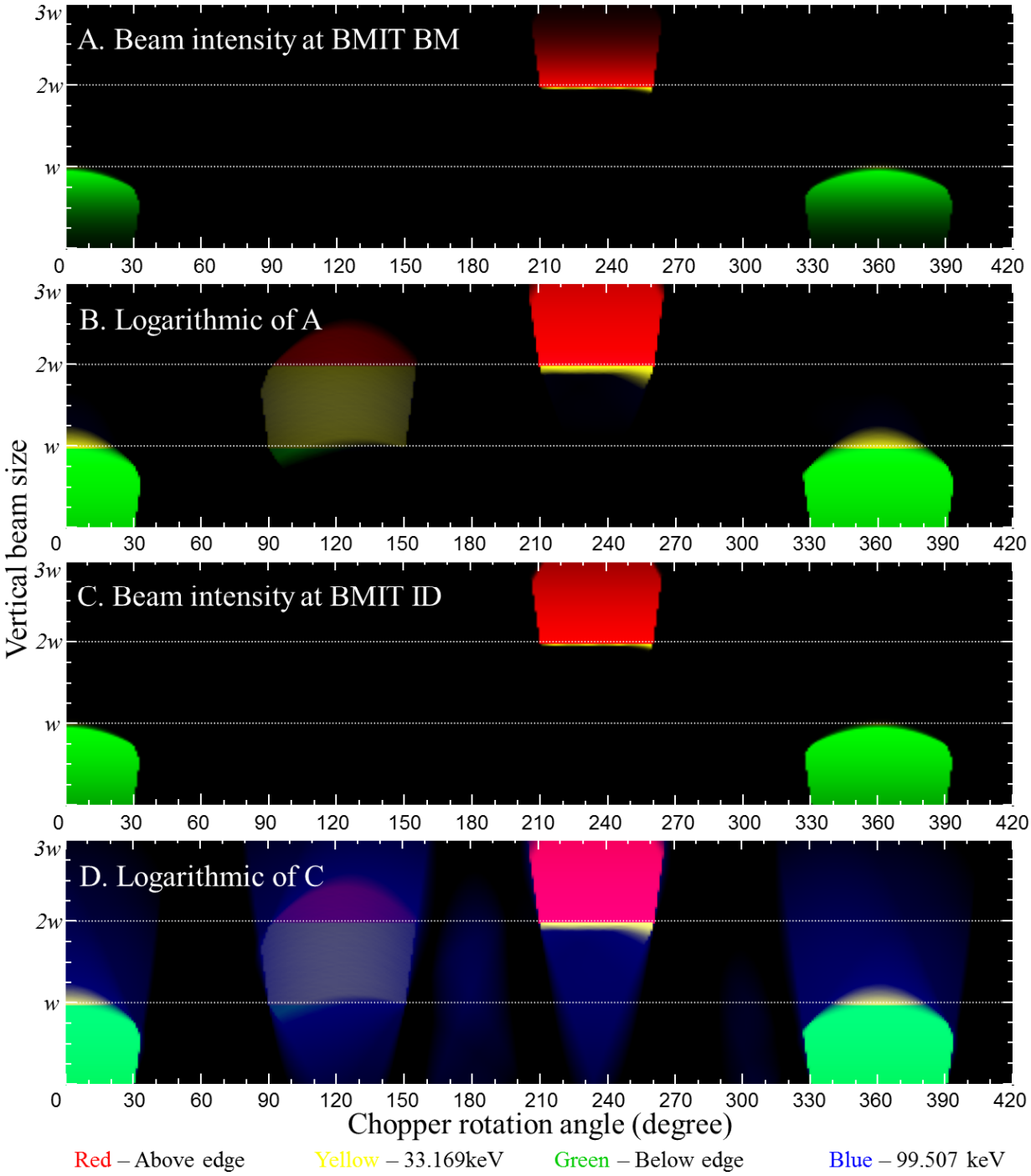

Figure 5.12 The relative intensity distributions of different beam energies in RGB false-colors were simulated just after the three-beam chopper vs. chopper rotation angle at the BMIT BM (A, B in logarithmic scale) and BMIT ID (C, D in logarithmic scale) beamline. The vertical axes denote the three equal beam heights of *w* which is 1.593 *mm*.

but it would not matter much since it is mostly distributed just near the edge of the E_A or E_B beam (Figure 5.12). This means that the emerged E_K is still well above or below the 33.17 *keV* since the diffracted energies are changing all along the BLM. As previously pointed out, the edge energy E_K in the middle beam of the BMIT BM beamline even suppressed the third imaging energy E_{3K} which would not provide an acceptable third image for the three-energy KES at the BMIT BM beamline. This would be much better at the BMIT ID beamline since E_{3K} was the most prominent energy within the opening for the third imaging energy. E_{3KA} and E_{3KB} from the above and below beam would contribute as well to the third imaging energy while the E_K, E_A and E_B energies were well controlled.

To balance the weight, two opposite three-beam choppers were attached to make the center of mass coincide with the center of rotation (Figure 5.13). The three-beam chopper was inserted into a segment of slotted aluminum rail (XT95, Thorlabs Inc., Newton NJ USA) which held a step motor (PK564BW, Oriental Motor USA Crop., CA USA) and an encoder (ROC413 /ROQ425, Heidenhain Inc., Germany) on both ends. The three-beam chopper was machined with great precision (±0.04 *mm*) by Daniel Vessey at the Engineering machine shop of U of S.

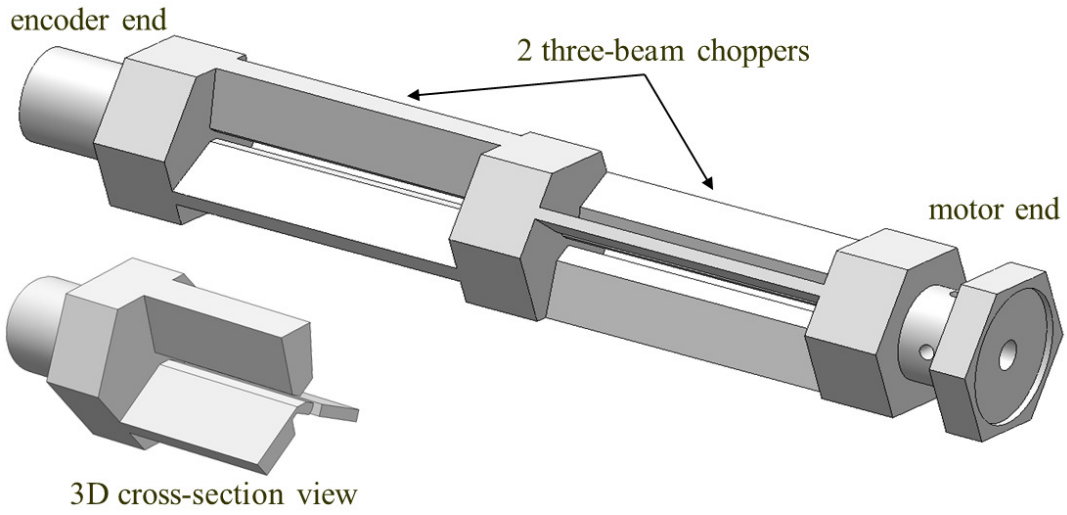

Figure 5.13 Three-beam chopper in 3D view and 3D cross-section view

5.2.3 Implementation

5.2.3.1 Experimental Setup

The three-energy KES experiments were set up at the BMIT BM beamline at the CLS starting in July 2010 (Figure 5.14 and Figure 5.15), when the preferred BMIT ID beamline was still under construction. The incident white beam was set as 5 *mm* high and 40 ~ 100 *mm* wide depending on the widths of the BLM, the sample and the detector. After a front end ion chamber and an imaging shutter, the incident white beam was diffracted by the 9.9° vertically inclined BLM and tilted upwards 13.1°. An aluminum rail system pivoting on the BLM center without touching the BLM was set up to hold all the equipment at a 13.1° angle. The equipment on the rail included the three-beam chopper at 100 *mm* after the BLM, a monitor ion chamber, a sample stage at about 1.5 meters away from the BLM and the detector stages afterwards.

The system alignment started from the BLM which was set on a vertical stage, a horizontal (inboard-outboard or in-out paper direction in Figure 5.14) stage and two cradle stages sharing the same center of rotation at the beam height. One cradle stage was the rotation for the Bragg angle θ_B and the second cradle stage was an orthometric rotation for an azimuthal angle. The BLM center was first vertically and horizontally aligned to the incident white beam position.

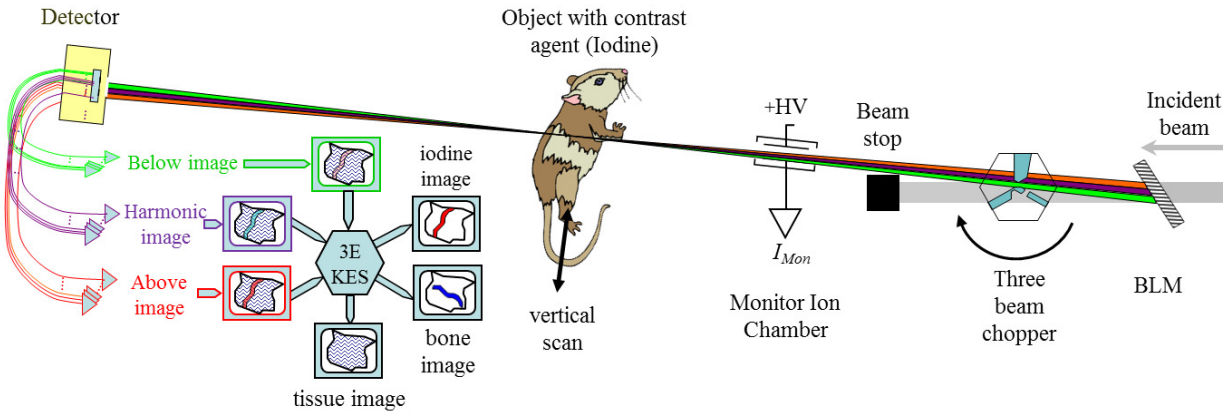

Figure 5.14 Diagram of the three-energy KES (adapted figure from Dr. Dean Chapman)

A box of iodine solution of 30 *mg/ml* in front of a fluorescence screen was used to find the iodine K-edge while the BLM was adjusted in Bragg angle θ_B. An abrupt change of the intensity on the fluorescence screen corresponded to the iodine K-edge energy and the corresponding height was marked as the diffracted beam height above the rails. Precise measurement of the iodine K-edge was performed using the ion chamber reading while scanning the Bragg angle θ_B. The Photonic Science area detector was set up to image the beams after the iodine solution and to make the K-edge line horizontally flat through appropriate adjustment of the azimuthal angle if necessary. Imaging the beams after the iodine solution was also performed using the Budker line detector while the Bragg angle θ_B of the BLM was gradually changed across the iodine K-edge within a small range. Any adjustment of the azimuthal angle required the θ_B to be tuned afterwards to refine the iodine K-edge again.

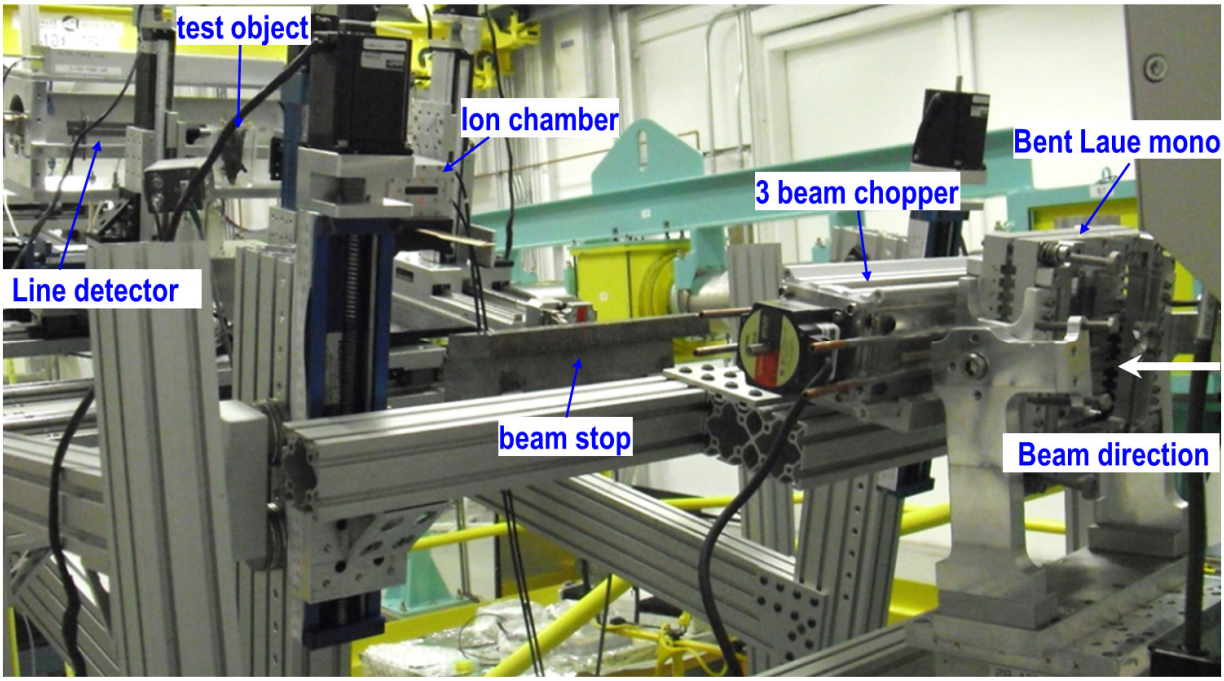

Figure 5.15 Experimental setup of the three-energy KES imaging at the BMIT BM beamline, showing the BLM, the three-beam chopper, a transmission beam stop, a diffraction ion chamber, a mouse with iodine injection, a Budker line detector and a pivoted rail which held the equipment and provided a tilt angle of 13.1° upwards.

The next step was the alignment of the detector, especially the Budker line detector. Considering the diffracted beam divergence of 3.5 *mrad* at the BMIT BM beamline (Table 5.2), any beam through the 6 *mm* gap hitting the 20 *mm* long ion chamber plates produced variable background features in the images which could not be easily eliminated by image processing afterwards.

The three-beam chopper was aligned to balance the above and below edge beams using a digital level and the ion chamber. Combined with an iodine solution of known thickness and concentration, the real energy difference δE for the above and below edge beams were estimated (Chapter 5.2.3.2).

The final step was the alignment of the sample stage which was critical for the KES CT experiment. To level the sample stage parallel to the beam plane, sinograms of the tip of a pin which was set on the edge of the rotating sample stage were examined using full beams and the Budker detector. Two methods could find the beam focus position after the alignment of the sample stage (Figure 5.16). The pin's position relative to the beam focus could be determined from the pin dip profile in the full beam sinogram, the same setup for the sample stage

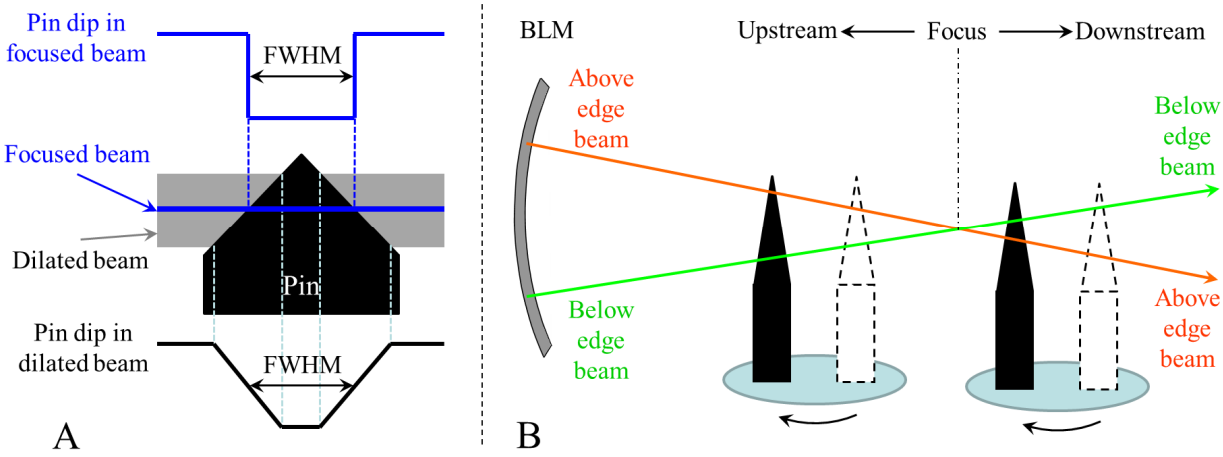

Figure 5.16 The beam focus position could be determined by either the slop of the pin dip profile by the full beam irradiation (A) or through the FWHM comparison of the pin dip profiles between the above edge and below edge beam irradiations (B).

alignment. Steep edges in the pin dip profile indicated closeness to the beam focus, while gradual slopes in the pin dip profile implied that the beam was farther from focus (Figure 5.16A). Combined with the three-beam chopper, sinograms of the pin tip using the above beam only and the below beam only were compared to find the beam focus position and set the sample stage at the beam focus accordingly. A big FWHM difference of the pin dip profile at the same sinogram position between the above and below sinograms indicated that the beam was farther from focus, while small FWHM difference between the above and below sinograms implied closeness to the beam focus (Figure 5.16B). Two methods were used to determine the beam focus size at the beam focus position. One was based on the derivative of a blade scan profile and the other was based on the FWHM of the slits scan profile. Three blade or slits scans along the beam path would estimate the beam focus position as well, without the requirement of the perfectly aligned sample stage.

5.2.3.2 Three-Beam Chopper Profile

The photon fluxes after the three-beam chopper were monitored by the ion chamber for

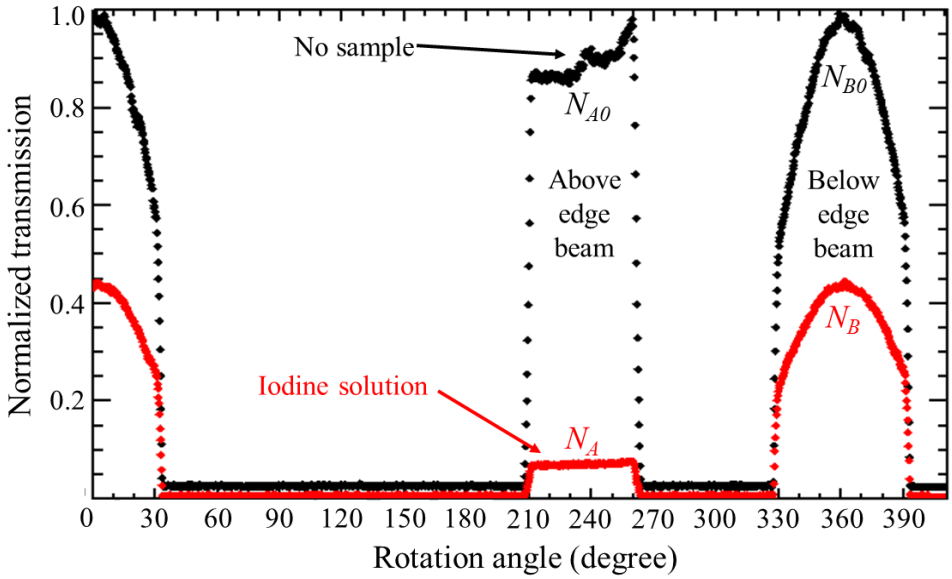

Figure 5.17 Measured normalized transmissions after the three-beam chopper vs. chopper rotation angle at BMIT BM beamline, with and without a 2 *cm* thick iodine solution of 30 *mg/ml.*

more than a full revolution either with or without a 2 *cm* thick iodine solution of 30 *mg/ml* in front (Figure 5.17). The data was collected at an increment of 0.25° rotation per ion chamber reading while the three-beam chopper was continuously rotating at a speed of 10*°/s*. The data were normalized by the maximal ion chamber reading without the iodine solution and the ring current decay was taken into account. As expected from the simulation in Figure 5.11, the round-head peak was the below edge beam and the flat-head peak was the above edge beam which was highly absorbed when the iodine solution was present. The ratios of the transmission drop in both the above and below edge beams as shown in Figure 5.17 can be used to calculate the concentration of the iodine solution through

$$\rho = \frac{\ln\left(\frac{N_{A0}}{N_A}\frac{N_B}{N_{B0}}\right)}{\left(\frac{\mu}{\rho}_A - \frac{\mu}{\rho}_B\right)t} \tag{5.15}$$

where N_{A0}/N_A is the ratio of averaged fluxes in the above edge beam without (N_{A0}) and with (N_A) iodine, N_{B0}/N_B is the ratio of maximal fluxes in the below edge beam without (N_{B0}) and with (N_B) iodine, $\frac{\mu}{\rho}_{A,B}$ is the mass absorption coefficient of iodine at above (A) or below (B) beam energy and t is the thickness of the iodine solution. Given the iodine solution thickness of 2 *cm* and the energy difference δE of 179 *eV* (Table 5.3), the measured flux ratio N_{A0}/N_A of 12.5 and N_{B0}/N_B of 2.2 directly determined an iodine concentration of 29.983 *mg/ml*, with an error of 0.57‰.

Equation (5.15) could be rearranged as

$$\frac{\mu}{\rho}_A - \frac{\mu}{\rho}_B = \frac{\ln\left(\frac{N_{A0}}{N_A}\frac{N_B}{N_{B0}}\right)}{\rho t} \tag{5.16}$$

Interpolation of the absorption coefficient difference in iodine would estimate the real energy difference δE under the assumption of equal energy difference δE of the above and below edge

beams from the edge energy. Given the 30 *mg/ml* concentration and 2 *cm* thickness of the iodine solution, the measured flux ratio N_{A0}/N_A of 12.5 and N_{B0}/N_B of 2.2 directly estimated an energy difference δE of 184 *eV*, an error of 2.8% compared with the 179 *eV* calculated in Table 5.3, for the chopper prepared above and below edge beams.

In summary, the agreement between the prepared iodine solution and the transmission measurements were quite good. Any differences were easily explained by small variations in the prepared solution concentration or subtle differences in the average imaging energies.

The beam intensity distribution after the three-beam chopper was monitored by the Photonic science area detector without any sample while the three-beam chopper was rotating 420º at a speed of 10*º/s* and a step size of 0.5*º/step* (Figure 5.18). Every image out of the area detector was horizontally summed and averaged into one vertical line at the corresponding chopper rotation angle. Adding all the averaged vertical flux distribution line at every angle built up the Figure 5.18. This real flux distribution matched well with the simulation in Figure 5.12A except that the above and below beams switched the position vertically since the detector was put downstream of the beam focus while the simulation was calculated for upstream of the beam focus. The vertical beam size on the detector depended on the distance of the downstream detector from the beam focus. The vertical beam size of 0.22 *mm* for each beam shown in the

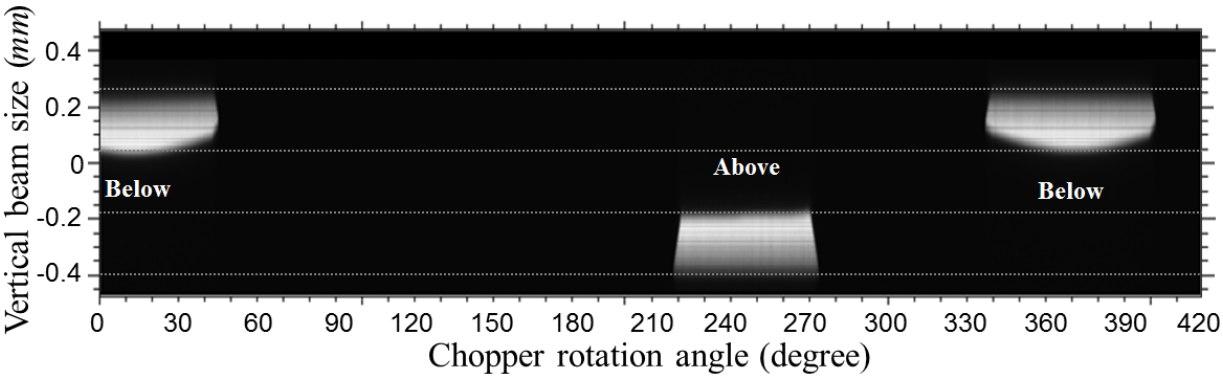

Figure 5.18 Beam intensity distributions vs. chopper rotation angle measured by the Photonic science detector after the beam focus at the BMIT BM beamline.

ordinate would estimate a detector distance of about 0.2 *m* from the beam focus and about 1.7 *m* away from the BLM.

5.2.3.3 Beam Focus Profile

The beam focus profile was measured using Huber slits and an ion chamber at the BMIT BM beamline on July 10, 2010. The incident white beam was set 2.5 *mm* wide and 5 *mm* high at the BLM position. Huber slits with a vertical gap setting of 6.25 μm was used to vertically scan across the beam at a 5 μm step size while an ion chamber after the Huber slits was averaging 20 voltage readings for each vertical step. The same vertical slits scan was repeated 36 times along the beam path at a 5 *mm* step size. The ion chamber readings were normalized by the ring current decay and plotted in Figure 5.19A, after an adjustment for the sagging aluminum rails along the beam path. The FWHM of each vertical scan was calculated and plotted as the solid curve, and the FWHM of Gaussian-fitted vertical scan was plotted as the dashed curve (Figure 5.19B). At 95 *mm* relative distance, both curves reached the minimal FWHM which means a focus size of 91 μm from the real scan and a focus size of 84 μm from the Gaussian-fitted scan. Over all the measured beam focus sizes were in the range of 80 ~ 100 μm for the several prepared BLMs.

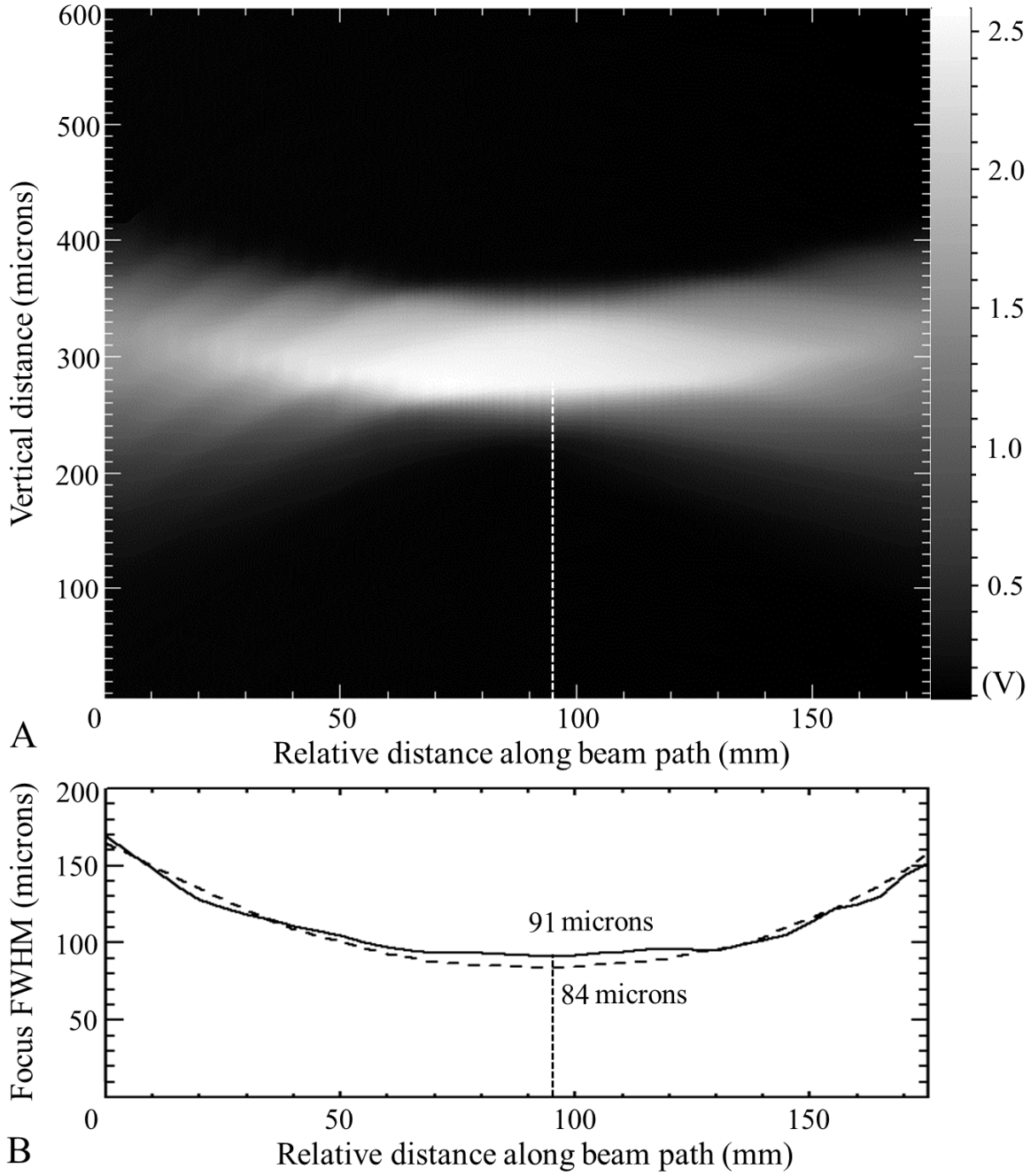

Figure 5.19 Figure A is the normalized ion chamber readings (*V*) after the Huber slits vs. the relative distance along the beam path (*mm*) and the vertical scanning range (μm). Figure B is the FWHM of the slits scan (solid curve) and FWHM of the Gaussian-fitted data (dashed curve) vs. relative distance along the beam path (*mm*) with the minimal FWHM noted (dashed line).

5.2.4 Results

5.2.4.1 First Simultaneous Iodine KES in Canada - a "Physics Rat" Head

The first simultaneous KES imaging was performed using the Photonic Science area detector without the three-beam chopper at the BMIT BM beamline at the CLS on July 10, 2010. The test object was a "physics rat" head which was printed by a rapid prototyper based on a CT scan data of a rat, the same technique described in Chapter 3.1. The rat head restraint was filled with water and sealed at neck position with a cuvette and a step wedge inserted (Figure 5.20A and B). An iodine solution filled the cuvette and occupied the space left by the step wedge.

The incident white beam was set 40 *mm* wide and 5 *mm* high at the BLM position. The Photonic Science area detector (18.7 μm pixel size) was set up looking at the beam at 0.67 *m* away from the beam focus position. While the test object was line-scanned 50 *mm* at a vertical speed of 0.033 *mm/s*, the Photonic Science detector was taking 1000 images at an acquisition time of 1.5 *s* per image. An "iodine" image was taken with a box of 30 *mg/ml* iodine solution in the beam path to find the iodine K-edge line, the arbitrarily defined above edge and below edge regions. The energy distribution within the beam region was estimated based on

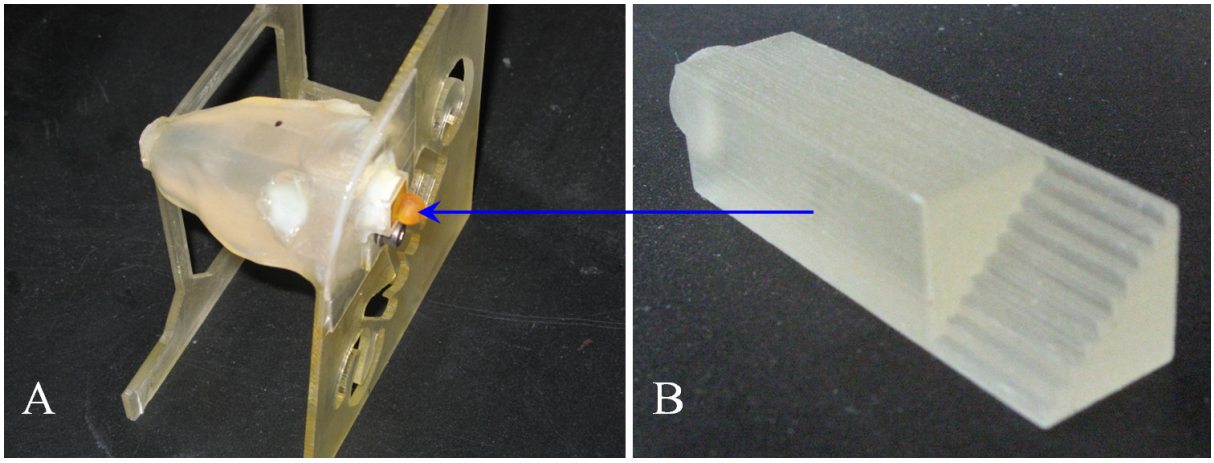

Figure 5.20 The "physics rat" head sample (A) was filled with water and a cuvette of 30 *mg/ml* iodine solution inside which a step wedge (B) was inserted.

$$\Delta E = \frac{E_K}{tg\theta_B}\Delta\theta \tag{5.17}$$

which indicates that a $\Delta\theta$ angle away from the K-edge line corresponds to a ΔE energy away from the K-edge energy (E_K). An average above and below edge energies were thus estimated as 171 *eV* above and 254 *eV* below the iodine K-edge energy, respectively. The above edge and below edge regions in every image of the test object were averaged into two lines. Stacking the above edge and below edge lines from the 1000 images built up the above edge and below edge images, respectively. The dual-energy KES algorithm (Equation (5.3)) was applied and the first simultaneous iodine KES image was produced at the BMIT BM beamline and in Canada (Figure 5.21). The iodine image clearly showed the gradually changing projected density of iodine and a big air bubble in the iodine solution.

After a refill of the iodine solution, a similar data set was collected and processed. While the test object was line-scanned 43.75 *mm* at a speed of 0.25 *mm/s*, the Photonic Science detector was taking 875 images at an acquisition time of 0.2 *s* per image. It took 175 *s* for one scan to

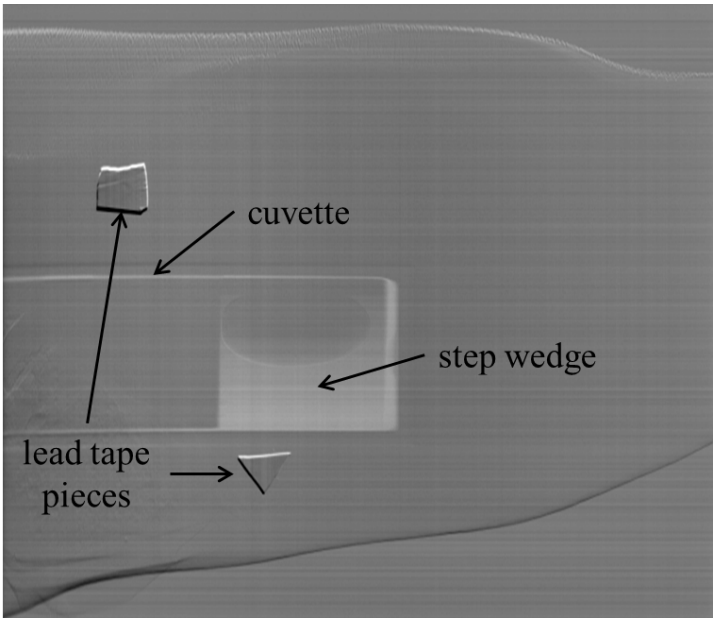

Figure 5.21 The first simultaneous iodine KES image in Canada at the BMIT BM beamline

simultaneously get the above and below edge images which were taken on average 178 *eV* above and 271 *eV* below the iodine K-edge energy, respectively. The water-equivalent image showed a plain matrix within the outline of the cuvette, while the iodine image clearly showed the projected iodine gradient due to the step wedge in the beam path (Figure 5.22 A and B). The horizontally averaged profile in the step wedge region showed the little steps in the projected iodine gradient and the vertical dimension matched with the step wedge's size of 1 *mm* per step (Figure 5.22C and D). The scale in the iodine image indicated that the iodine concentration was

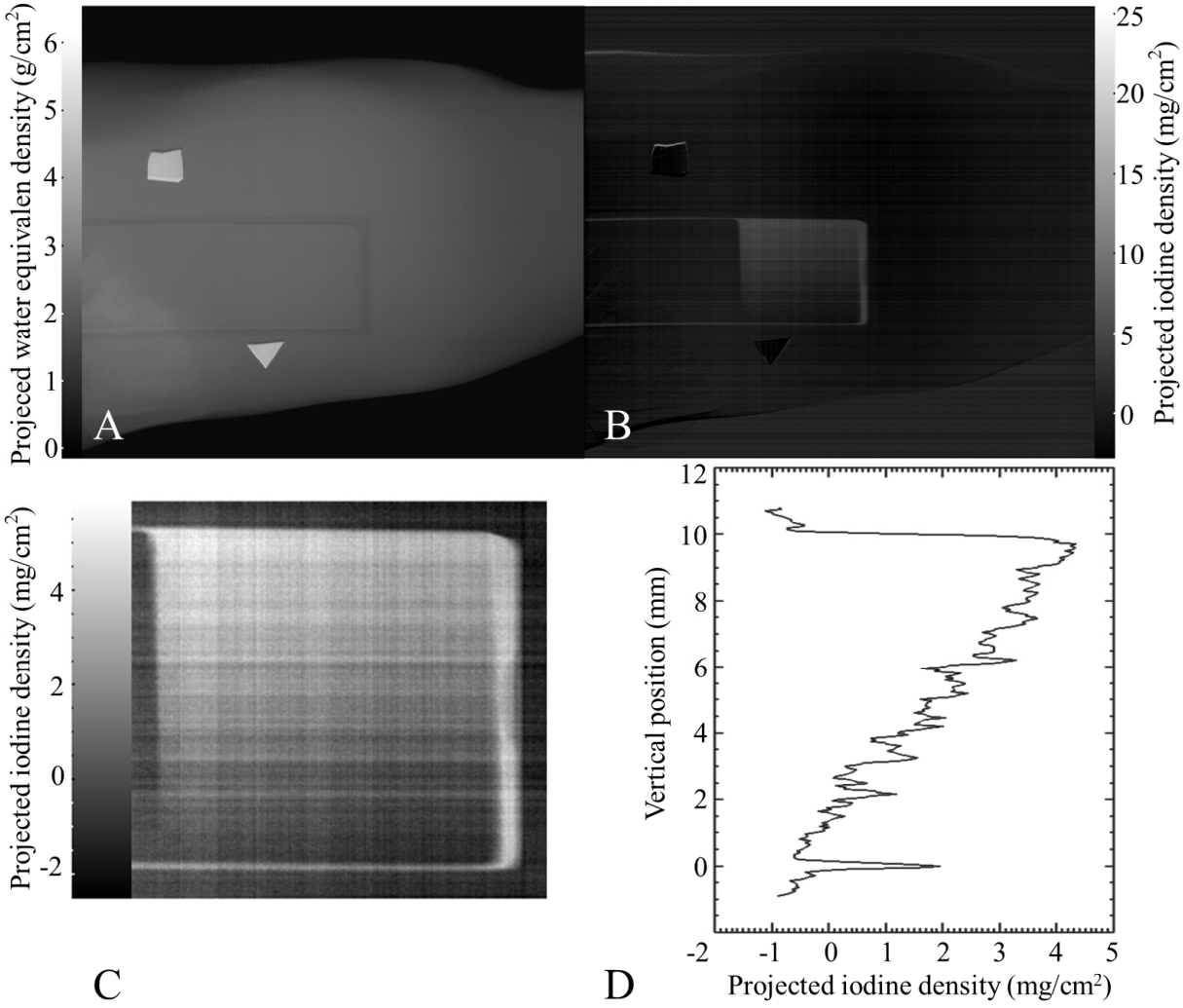

Figure 5.22 The water-equivalent image (A) and iodine image (B) of a "physics rat" head using simultaneous dual-energy KES imaging. The enlarged iodine image in the step wedge region (C) is shown with its horizontally averaged gradient of the projected iodine density (D).

about 5 *mg/ml* based on the 1 cm^2dimension of the cuvette. Some iodine was found in the gap between the cuvette and the inserted step wedge which led to an abrupt peak in the averaged gradient profile at 0 *mm* vertical position (Figure5.22D).

5.2.4.2 Iodine Uptake Three-Energy KES imaging of a Live Mouse

Three-energy KES imaging of a live mouse was performed using the three-beam chopper and Budker line detector (100 μm pixel size, 2560 pixels) at the BMIT BM beamline at the CLS on Aug 17, 2010. After intraperitoneal injection of the sodium iodine (NaI) solution, the mouse was anesthetized and KES imaged by one vertical scan which was repeated at 52, 55, 61, 66, 69, 75, 78, 83, 88, 94 and 112 minutes after the NaI injection to explore the iodine uptake process. The mouse was treated under Animal Care protocol #20050096 approved by UCACS.

The incident white beam was set 40 *mm* wide and 5 *mm* high at the BLM position. While the three-beam chopper was continuously rotating at a speed of 400 *RPM*, the anesthetized mouse was line-scanned 32 *mm* at a vertical speed of 0.667 *mm/s* and the Budker detector read 4800 lines with an acquisition time of 10 *ms/line*. For each chopper revolution the Budker detector took 15 lines of data and the sample stage vertically moved 100 μm, about the beam focus size. The raw data appeared like many stripes corresponding to the fast switching of the three beams. A closer view of the raw data indicated the very weak third beam (E_{3K}) of 99.51 *keV* which appeared as a bigger black gap between the above (E_A) and below (E_B) edge beams (Figure 5.23A and B). Data from each energy beam was curve-fit based on the chopper rotation profile and averaged to one line of data for each of the three energies. Adding all the data lines for each of the three energies produced a projection image taken by the corresponding energy beam. It took 48 *s* for one 32 *mm* scan of the live mouse to get three images of the above edge, below edge and harmonic energies all at once.

The projected density images of iodine and water were then calculated from the above and below edge images based on the dual-energy KES equation (5.3) (Figure5.24). The three energy KES algorithm, equation (5.11), was not used and the bone image was not produced due to the lack of 99.51 *keV* flux at the BMIT BM beamline. The iodine images showed the progressive accumulation of iodine in the bladder as it was cleared from the blood by the kidneys into the urine. This increase of the iodine in the bladder of a live mouse was tracked over time (Figure5.25).

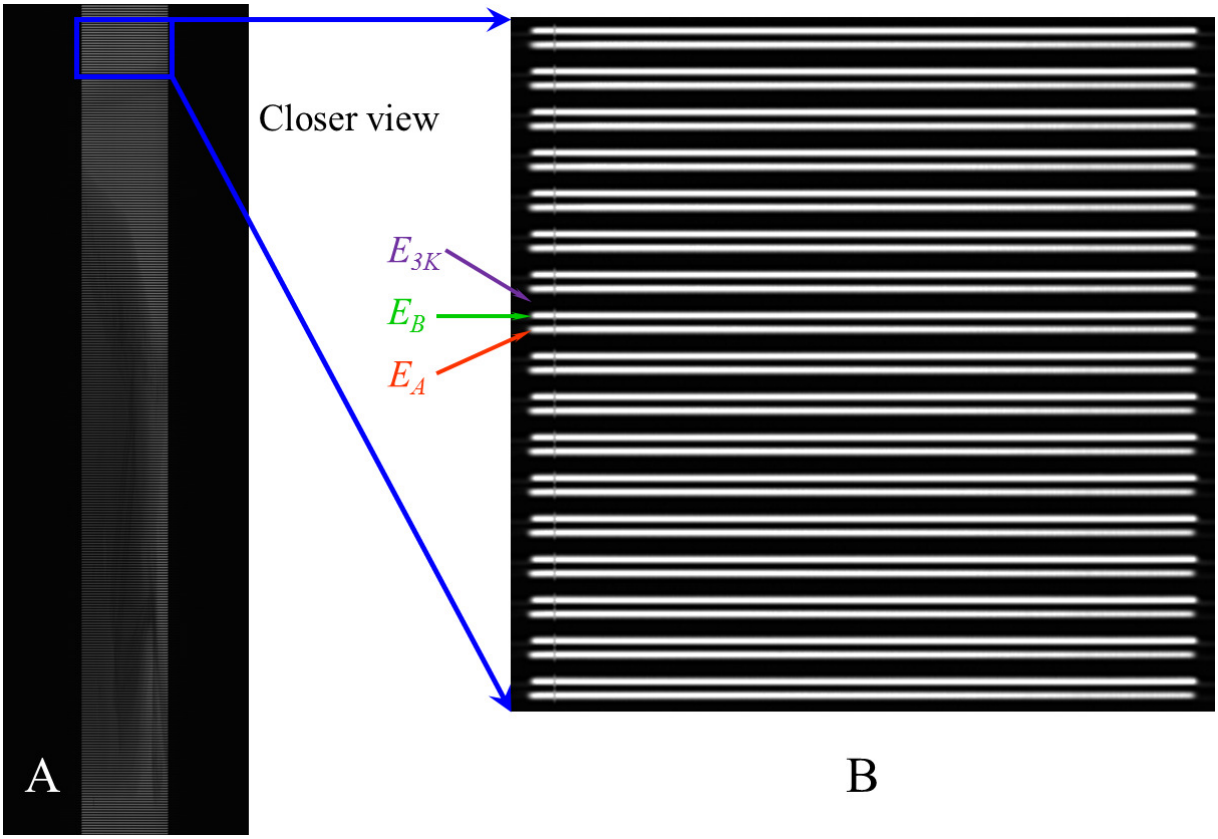

Figure 5.23 The raw data (A) and its closer view (B) of the three-energy KES performed at the BMIT BM beamline. The sample was a live mouse after NaI injection and anesthesia.

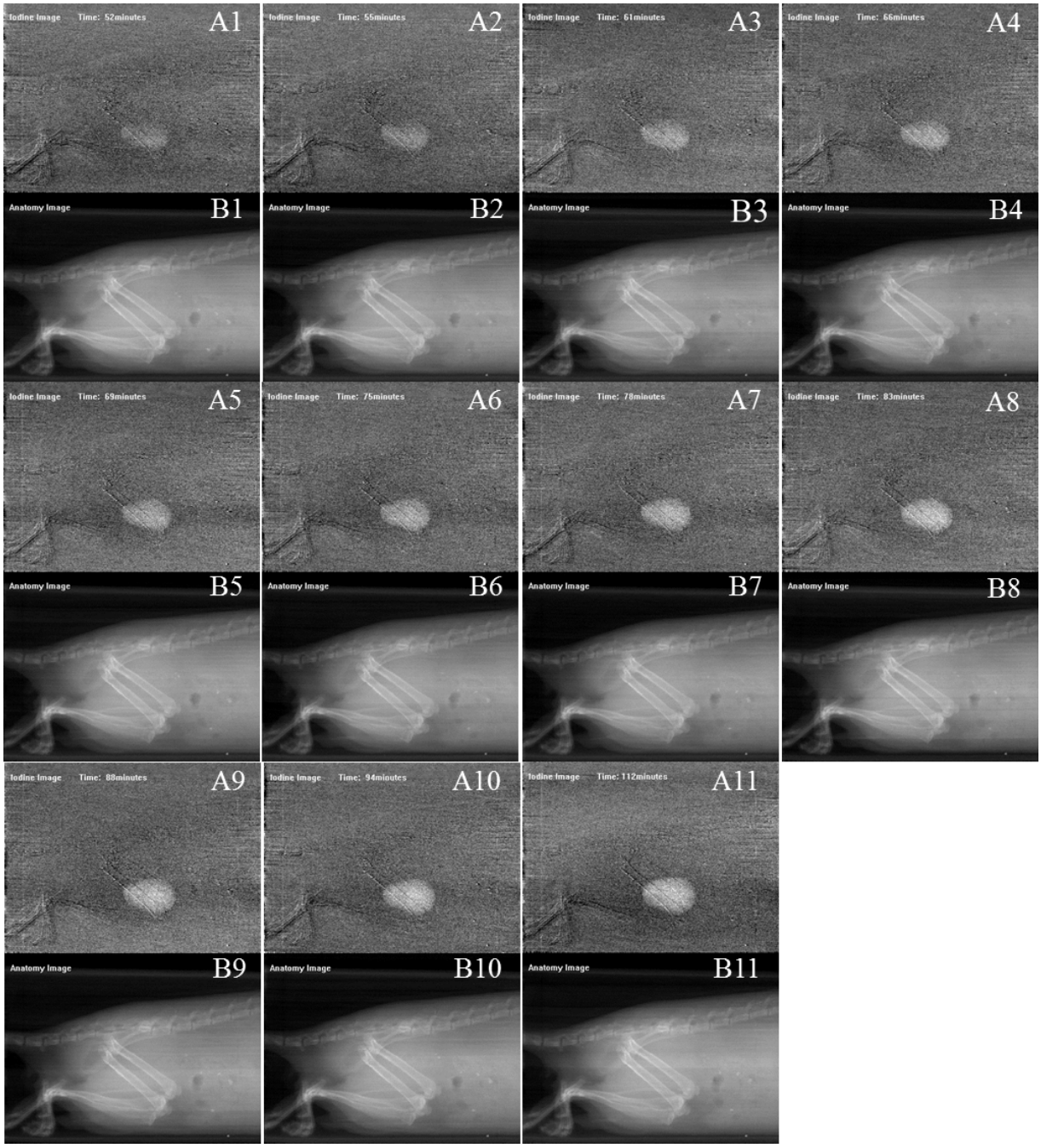

Figure 5.24 The projected density images of iodine (A) and water (B) of a live mouse using chopper enabled KES imaging. The image group 1~11 were taken at 52, 55, 61, 66, 69, 75, 78, 83, 88, 94, 112 minutes after the NaI injection, respectively.

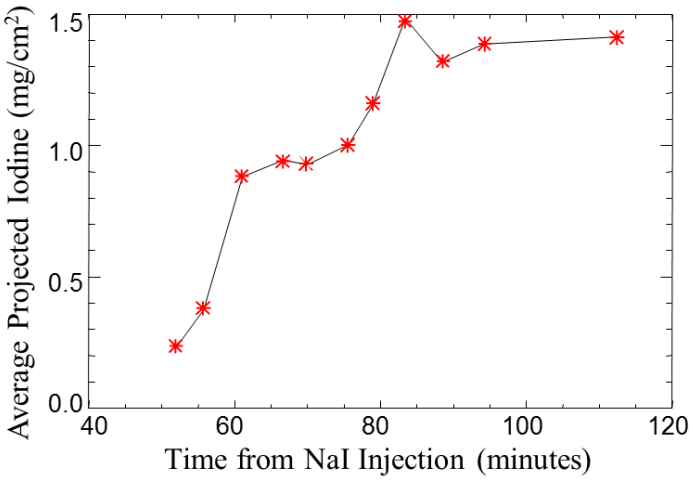

Figure 5.25 Averaged iodine content in the bladder of a live mouse vs. time after NaI injection

5.2.4.3 First KES CT in Canada - a "Physics Rat" Head

The first KES CT imaging was performed using the three-beam chopper and Budker line detector at the BMIT BM beamline on Nov 24, 2010. The same "physics rat" head sample (Fig5.20) was KES-CT imaged with the iodine solution of different concentrations, 5 *mg/ml*, 2.5 *mg/ml*, 1 *mg/ml* and 0.5 *mg/ml* which were diluted from the organically bound iodine (Optiray^{TM} 240 ioversol contrast agent, 240 *mg/ml*).

The incident white beam was set 52 *mm* wide and 5 *mm* high at the BLM position. The "physics rat" head sample was KES-CT scanned 120 slices with one scan for each slice. For each slice of image, while the sample was rotated 400° at a speed of 20.8*°/s* and the Budker detector read 3850 lines with an acquisition time of 5 *ms/line*, the three-beam chopper stayed at the "Above" beam position for half turn of sample, rotated 120º to switch to the "Below" beam position at a speed of 120*°/s* and stayed for another half turn of sample. After one scan for each slice, both the three-beam chopper and the sample stage rotated to the same starting point and the sample stage vertically moved 100 μm, about the beam focus size, for the next slice. Each slice of data took 19.25 *s* to get two sinograms using the above and below edge energies. If there were

enough 99.51 *keV* flux for the third imaging energy, each slice of data could get three sinograms using three energies all at once.

A 180º rotation section of the sinogram which was 1731 lines of data was picked for each energy to do the CT reconstruction. The sinogram was first normalized by a flat sinogram (no sample) and then reconstructed to an image slice. The reconstructed above and below edge slices were rotated and translated to match and the image slices of iodine density and water density were then calculated by the dual-energy KES algorithm (Figure 5.26). The measured iodine density within the cuvette of the iodine image and the measured water density outside of the cuvette in the water image were averaged and listed in Table 5.6. It is noted that the estimated iodine density matched well with the prepared iodine concentrations with errors in a range of -6% ~ 9%. The errors may come from the inaccuracy of the prepared iodine solutions, not perfectly balanced three-beam chopper and the error of energy difference δE which was 2.8% in one measurement (see Chapter 5.2.3.2). An unbalanced three-beam chopper would change the averaged beam energy and thus the energy difference δE. The inaccurate beam energy would introduce differences between the real attenuation coefficients and the tabulated values based on the designed δE which were used in the density image calculations from the measured data. The beam energy error was thus transferred to the density errors measured in the density images.

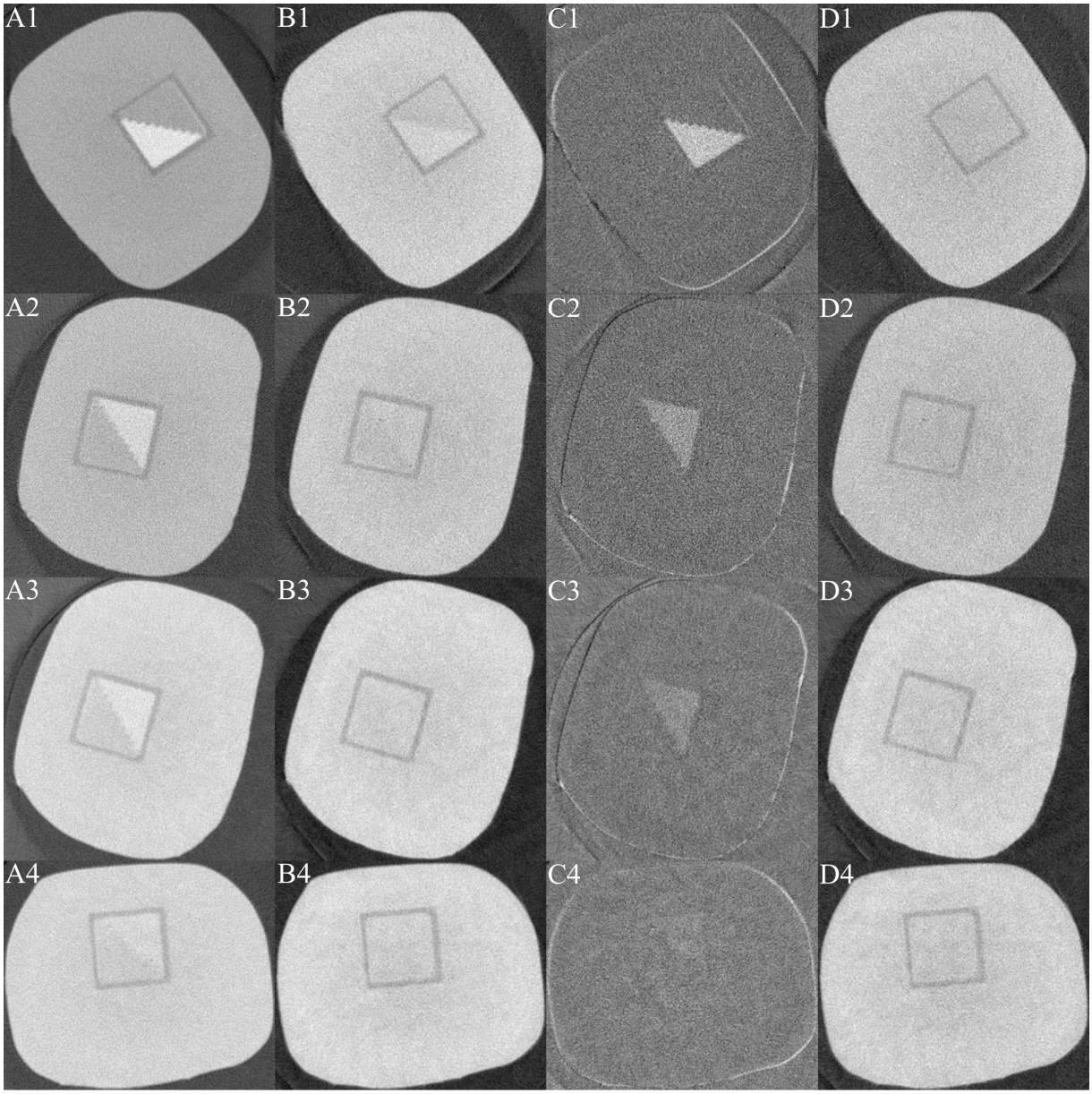

Figure 5.26 The above edge (A), below edge (B), iodine density (C) and equivalent water density (D) KES-CT slice images of a "physics rat" head with iodine solution of 5 *mg/ml* (1), 2.5 *mg/ml* (2), 1 *mg/ml* (3) and 0.5 *mg/ml* (4).

Table 5.6 Iodine density measurements for the KES CT data of a "physics rat" head

Prepared iodine concentration (mg/ml)	*Averaged iodine density in iodine image (mg/ml)*	*Averaged water density in water image (g/ml)*	*Estimated iodine density (mg/ml)*	*Relative error (%)*
ρ_{t0}	ρ_t	ρ_w	$\rho_{te} = \rho_t / (\rho_w / 1)$	$(\rho_{te} - \rho_{t0}) / \rho_{t0}$
0.5	0.46	0.97	0.47	-5.5
1	1.07	0.98	1.09	9.0
2.5	2.21	0.93	2.37	-5.1
5	4.53	0.94	4.85	-3.1

5.2.5 Discussions and Conclusions

To overcome the image artifacts from motion and the presence of bone in conventional dual-energy KES, a BLM-based three-energy KES was suggested and the third imaging energy of 99.51 *keV* was chosen based on an optimization calculation. Two BLMs specific for iodine KES at the BMIT BM and ID beamlines were designed to meet the conditions of sub-micron focus size in theory.

A novel three-beam chopper was designed and machined using tin bronze to operate with both BLMs and perform the three-energy KES at both beamlines. It was the first beam chopper for fast switching among three beams. The decision of three beam heights finally arrived at a simple result of three equal beam heights after a detailed optimization based on the maximal SNR in the contrast image, the same total dose for three energies, the beamline flux distribution, the detector response and the BLM reflectivity. The three-beam chopper profiles measured in the experiment matched well with the simulations of the beam fluxes and distributions. The three-beam chopper was successfully used in the three-energy KES setup which did not produce the bone image due to the lack of 99.51 *keV* flux at the BMIT BM beamline as expected from the

flux calculation. It would be straightforward to use the three-beam chopper and perform three-energy KES at the BMIT ID beamline which could provide ample 99.51 *keV* flux when it is available for commissioning.

Considering the source size of the BMIT BM beamline, the practical limit of the beam size that could be focused by optics is 8.5 μm when the theoretical condition of sub-micron focus size was met. Great effort was put on the BLM crystal preparations to aim for precise and even bending of the crystal including crystal orientation, off-cut measurement, cutting, etching, checking surface flatness, bending and measuring bending radius and uniformity. The measured beam focus size were in the range of 80 ~ 100 μm for the several prepared BLMs. The error may come from the errors of crystal asymmetry angle and alignment errors. Based on the available crystals and apparatus for crystal preparation, the focus size of 100 μm is good enough for KES imaging of small animals and matched well with the 100 μm pixel size of the Budker detector. It still leaves great room to explore the potential focus size of a few microns in the future to provide high resolution KES imaging to a variety of applications.

Using the BLM, the first simultaneous dual-energy KES imaging was performed at the BMIT BM beamline, and in Canada. It took 175 *s* for one 43.75 *mm* scan to simultaneously get the above and below edge images of the "physics rat" head. The projected iodine image clearly showed the density gradient with little steps due to the step wedge. This method would remove the motion artifact and provide better KES imaging for live animals.

Three-energy KES imaging of a live mouse was successfully performed using the three-beam chopper which was continuously rotating at 400 *RPM*. It took 48 *s* for one 32 *mm* scan of the live mouse to get three images of the above edge, below edge and harmonic energies all at once. It was a useful technique to track the iodine accumulation in the bladder of a live mouse

with time, because it was quick (48 *s/scan*), free of motion artifact by the nearly simultaneous KES imaging (50 *ms* between the successive three energies) and free of the artifact due to the presence of bone if enough harmonic flux were provided to make the three-energy KES algorithm feasible.

The first KES CT imaging was performed on the "physics rat" head sample at the BMIT BM beamline. Each slice of data took 19.25 *s* to get two sinograms of the above and below edge energies successively. If there were enough flux for the third imaging energy, each slice of data could easily get three sinograms using three energies successively. After CT reconstruction, image registration and KES algorithm, the iodine images of the "physics rat" head clearly showed the density variations produced by the different iodine concentrations within the cuvette.

Given the 45 *mm* diameter of the "physics rat" head sample, the 1731 lines of data for a half turn which means 0.104º angle between measurements was more than double sampling (2.448 times sampling) of the CT resolution requirement. If the single sampling which requires 707 lines of data for a half turn and 0.255º angle between measurements was performed, it only needs 8.64 *s* for one slice of data assuming 440º of sample rotation. So the KES CT could perform even faster. For example it will take two and half hours to collect 800 KES CT slices of an 80 *mm* long mouse.

Three motions were involved in the KES CT scan, the sample vertical scanning (S_V), the sample rotation (S_R) and the chopper rotation for energy iteration (C_E). The KES CT imaging was performed in the priority sequence of S_R - C_E - S_V and this is not the only way to perform the KES CT imaging. If the motion artifact from a live animal is the major concern, the KES CT could use continuous rotation of the three-beam chopper for each sample rotation angle. That is the KES CT imaging performed in the priority sequence of C_E - S_R - S_V or C_E - S_V - S_R depending

on the major direction of the concerned motion relative to the orientation of sample. The latter priority sequence of C_E - S_V - S_R is actually the three-energy KES imaging described in Chapter 5.2.4.2 repeated at every sample rotation angle. The reasons to choose the priority sequence of S_R - C_E - S_V to perform the KES CT of the "physics rat" head are that the sample was not a live animal and the three-beam chopper did not need to continuously rotate since the third energy was skipped due to lack of flux at the BMIT BM beamline. For live animal imaging, these forms of KES CT methods would be performed in the future to explore their potential.

In summary, this BLM and three-beam chopper enabled three-energy KES imaging system would easily overcome the image artifacts from motion and the presence of bone, but it introduced a cross-over artifact as a result of the focusing beam. On the other hand, the BLM greatly increased the flux and dose onto the sample due to the focusing beam. This high resolution and high flux KES setup after achieving a focus size of a few microns would open a door to a new level of applications such as cell level imaging and radiation therapy investigations. The three-energy KES imaging system would produce an additional image of bone which might be useful for anatomy or calcification determinations when enough flux of the third imaging energy is provided at the BMIT ID beamline in the near future. Besides the tissue and contrast material, this imaging system could be used to image other material that is important in the test object as the third component instead of bone, for example the iron.

5.3 Near Edge Spectral Imaging

5.3.1 Introduction

Similar to the dual-energy KES taking a two-color image and the three-energy KES taking a false-color image from three colors, a new spectrum-based imaging method was conceived to take a true-color image of an object using typically hundreds of colors (energy - E).

Its raw data output is a data cube of (*x, y, E*). Its resulting data is visualized as an image cube containing density distribution images of various material components in the object. Since this spectral imaging method is optimally applied with the spectrum encompassing an absorption edge of an element within the object, it is named as Near Edge Spectral Imaging (NESI). The NESI algorithm showed that it is a generalized version of KES imaging and the KES is a special case of NESI.

As mentioned in Chapter 5.2.2.2, the BLMs were designed by matching the geometric and single ray focal lengths. An important consequence of the matching of the single ray and geometric foci is that each ray has a unique energy. Thus the designed BLMs prepared a convergent beam whose energy changed linearly across the beam. The designed BLMs can be used to interrogate the absorption properties of materials such as is done with XAS where a detailed spectral measurement of the absorption of an element in the vicinity of the absorption edge can elucidate the oxidation state and local environment of that element. The powerful XAS method has resulted in structural and chemical state information of many systems. In the case of the structural information, the material need not be crystallized to determine the local environment which is very powerful for biological systems.

Such a BLM-based NESI system (Figure 1.1) was built up for small animal imaging at the BMIT BM beamline at the CLS which is exactly the same setup as described in chapter 5.2.4.1. An algorithm was developed to determine different components including the contrast species in the object using the spectral information. Preliminary results of NESI projection and NESI CT imaging of test objects and biological systems were presented along with a direct comparison with KES imaging.

5.3.2 Rationale

Projection images taken by *n* number of energies could resolve *n* number of components in an object as long as the attenuation coefficients of the components have enough variations during the energy range to distinguish themselves and achieve precise resolving accuracy. Assuming a sample system containing components less than *n*, the components are over-determined by the NESI algorithm and should achieve better results since more flux is involved.

5.3.2.1 Two-Component NESI

If the NESI system assumes an object as a two-component system, a contrast material (*C*) and a matrix material (*M*), each vertical line in the pixelated detector is a measurement of the number of photons transmitted through the object as a function of energy.

$$N_i = N_{0i} e^{-\frac{\mu}{\rho}_{Mi}\rho_M t_M - \frac{\mu}{\rho}_{Ci}\rho_C t_C} \qquad (1 \le i \le n) \tag{5.18}$$

where the index *i* corresponds to the energy of photon detected across the vertical extent of the beam on the detector and *n* is the number of energy points. The detailed attenuation characteristics of the two materials ($\frac{\mu}{\rho}_{Mi}, \frac{\mu}{\rho}_{Ci}$) can be easily measured, tabulated or modeled.

As in the case of KES, equation (5.18) can be recast by taking the negative logarithm to give a linear equation of the projected materials,

$$r_i = -\ln\left(\frac{N_i}{N_{0i}}\right) = \frac{\mu}{\rho}_{Mi}\rho_M t_M + \frac{\mu}{\rho}_{Ci}\rho_C t_C \qquad (1 \le i \le n) \tag{5.19}$$

The task now is to find the projected densities ($\rho_M t_M$, $\rho_C t_C$) that lead to the best fit to the measured values. A least-squares fit can be used in the derivation (see Appendix A) and results in the projected density equations,

$$\rho_M t_M = \frac{\sum_i \frac{\mu}{\rho}_{Ci}^2 \sum_i \left(\frac{\mu}{\rho}_{Mi} r_i\right) - \sum_i \left(\frac{\mu}{\rho}_{Ci} \frac{\mu}{\rho}_{Mi}\right) \sum_i \left(\frac{\mu}{\rho}_{Ci} r_i\right)}{\sum_i \frac{\mu}{\rho}_{Ci}^2 \sum_i \frac{\mu}{\rho}_{Mi}^2 - \left[\sum_i \left(\frac{\mu}{\rho}_{Ci} \frac{\mu}{\rho}_{Mi}\right)\right]^2} \qquad (1 \le i \le n)$$

$$\rho_C t_C = \frac{\sum_i \frac{\mu}{\rho}_{Mi}^2 \sum_i \left(\frac{\mu}{\rho}_{Ci} r_i\right) - \sum_i \left(\frac{\mu}{\rho}_{Ci} \frac{\mu}{\rho}_{Mi}\right) \sum_i \left(\frac{\mu}{\rho}_{Mi} r_i\right)}{\sum_i \frac{\mu}{\rho}_{Ci}^2 \sum_i \frac{\mu}{\rho}_{Mi}^2 - \left[\sum_i \left(\frac{\mu}{\rho}_{Ci} \frac{\mu}{\rho}_{Mi}\right)\right]^2} \qquad (5.20)$$

Introducing the average of the $\frac{\mu}{\rho}$ products as

$$\frac{\mu}{\rho}_{CC} \equiv \frac{1}{n}\sum_i \frac{\mu}{\rho}_{Ci}^2 \qquad \frac{\mu}{\rho}_{MM} \equiv \frac{1}{n}\sum_i \frac{\mu}{\rho}_{Mi}^2 \qquad \frac{\mu}{\rho}_{CM} \equiv \frac{1}{n}\sum_i \left(\frac{\mu}{\rho}_{Ci} \frac{\mu}{\rho}_{Mi}\right) \qquad (5.21)$$

leads to

$$\rho_M t_M = \frac{1}{n} \frac{\frac{\mu}{\rho}_{CC} \sum_i \left(\frac{\mu}{\rho}_{Mi} r_i\right) - \frac{\mu}{\rho}_{CM} \sum_i \left(\frac{\mu}{\rho}_{Ci} r_i\right)}{\frac{\mu}{\rho}_{CC} \frac{\mu}{\rho}_{MM} - \frac{\mu}{\rho}_{CM}^2} \qquad (1 \le i \le n)$$

$$\rho_C t_C = \frac{1}{n} \frac{\frac{\mu}{\rho}_{MM} \sum_i \left(\frac{\mu}{\rho}_{Ci} r_i\right) - \frac{\mu}{\rho}_{CM} \sum_i \left(\frac{\mu}{\rho}_{Mi} r_i\right)}{\frac{\mu}{\rho}_{CC} \frac{\mu}{\rho}_{MM} - \frac{\mu}{\rho}_{CM}^2} \qquad (5.22)$$

This is the equation that is used to extract projected contrast and matrix density images from the NESI raw data cube. As derived in Appendix B, the dual-energy KES is a special case of the two-component NESI when two energies are chosen, that is $n = 2$.

Under the assumptions of Poisson counting statistics to represent the noise from the detected signals, the SNR of the projected density images are calculated as (see Appendix C)

$$SNR_C = \frac{n\left(\frac{\mu}{\rho}_{CC} \frac{\mu}{\rho}_{MM} - \frac{\mu}{\rho}_{CM}^2\right)}{\sqrt{\sum_i \left[\left(\frac{\mu}{\rho}_{MM} \frac{\mu}{\rho}_{Ci} - \frac{\mu}{\rho}_{CM} \frac{\mu}{\rho}_{Mi}\right)^2 \left(\frac{1}{N_i} + \frac{1}{N_{0i}}\right)\right]}} \rho_C t_C$$

$$SNR_M = \frac{n\left(\frac{\mu}{\rho}_{CC} \frac{\mu}{\rho}_{MM} - \frac{\mu}{\rho}_{CM}^2\right)}{\sqrt{\sum_i \left[\left(\frac{\mu}{\rho}_{CC} \frac{\mu}{\rho}_{Mi} - \frac{\mu}{\rho}_{CM} \frac{\mu}{\rho}_{Ci}\right)^2 \left(\frac{1}{N_i} + \frac{1}{N_{0i}}\right)\right]}} \rho_M t_M \qquad (5.23)$$

In order to better understand what parameters affect the SNR with this NESI algorithm we made three simplifications: 1) equal incident flux N_{0i} for all energies, 2) equal transmitted flux N_i for all the energies and 3) dilute contrast material in the object. These lead to simplified SNR expressions for the projected density images as (see Appendix C)

$$\begin{aligned} SNR_C &\approx \sqrt{\frac{nN_0}{1+e^{\mu t}}}\sqrt{1-\frac{\frac{\mu}{\rho}_{CM}^{2}}{\frac{\mu}{\rho}_{MM}\frac{\mu}{\rho}_{CC}}}\sqrt{\frac{\mu}{\rho}_{CC}}\ \rho_C t_C \\ SNR_M &\approx \sqrt{\frac{nN_0}{1+e^{\mu t}}}\sqrt{1-\frac{\frac{\mu}{\rho}_{CM}^{2}}{\frac{\mu}{\rho}_{MM}\frac{\mu}{\rho}_{CC}}}\sqrt{\frac{\mu}{\rho}_{MM}}\,\rho_M t_M \end{aligned} \tag{5.24}$$

As expected, the SNR is proportional to the amount of material present ($\rho_C t_C$, $\rho_M t_M$) and proportional to the square root of the incident photon count, that is $SNR \propto \sqrt{nN_0}$ where nN_0 is the total number of incident photons at each pixel width at the sample position. Both SNR equations are dimensionless and both contain the root-mean-square (RMS) average of $\frac{\mu}{\rho}_C$ and $\frac{\mu}{\rho}_M$. Introducing $\frac{\mu}{\rho}_{C_{RMS}}$ and $\frac{\mu}{\rho}_{M_{RMS}}$ for the RMS values and Γ_2 term for the two-component NESI,

$$\frac{\mu}{\rho}_{C_{RMS}} \equiv \sqrt{\frac{\mu}{\rho}_{CC}} \qquad \frac{\mu}{\rho}_{M_{RMS}} \equiv \sqrt{\frac{\mu}{\rho}_{MM}} \qquad \Gamma_2 \equiv \sqrt{1-\frac{\frac{\mu}{\rho}_{CM}^{2}}{\frac{\mu}{\rho}_{MM}\frac{\mu}{\rho}_{CC}}} \tag{5.25}$$

the simplified SNR equations are then expressed as,

$$\begin{aligned} SNR_C &\approx \sqrt{\frac{nN_0}{1+e^{\mu t}}}\Gamma_2\,\frac{\mu}{\rho}_{C_{RMS}}\ \rho_C t_C \\ SNR_M &\approx \sqrt{\frac{nN_0}{1+e^{\mu t}}}\Gamma_2\,\frac{\mu}{\rho}_{M_{RMS}}\ \rho_M t_M \end{aligned} \tag{5.26}$$

For reference, a comparison between the RMS values and the normal values of the attenuation coefficients of iodine and water are simulated in Figure 5.27. The simulated RMS values are averaged over an energy span of 450 eV which approximately matched the measured

NESI data. As seen from this figure, the RMS plot of the water attenuation is overlapped with its normal values while the RMS curve of the iodine attenuation is a smoothed version of its normal values. The SNR for 1 mg/cm^2 of projected iodine content and 1 g/cm^2 of projected water content are simulated from equation (5.23) over an energy span of 450 eV while changing the imaging energy of the center beam (Figure 5.28A). The calculation assumes using the BLM for BMIT BM beamline to focus an incident flux of 1×10^6 photon/pixel width on the sample. Instead of the equal incident flux assumption for the simplified SNR derivations, the SNR calculations here use the simulated vertical flux distribution from the BMIT BM source and after the BLM (Figure 5.28B) as the incident beam, the total of which add up to 1×10^6 photons. Again, the RMS values of the attenuation coefficients are averaged over this 450 eV energy range. Quite different from Figure 5.27, the SNR plot clearly indicates that imaging near the iodine K-edge, i.e. 33.17 keV or

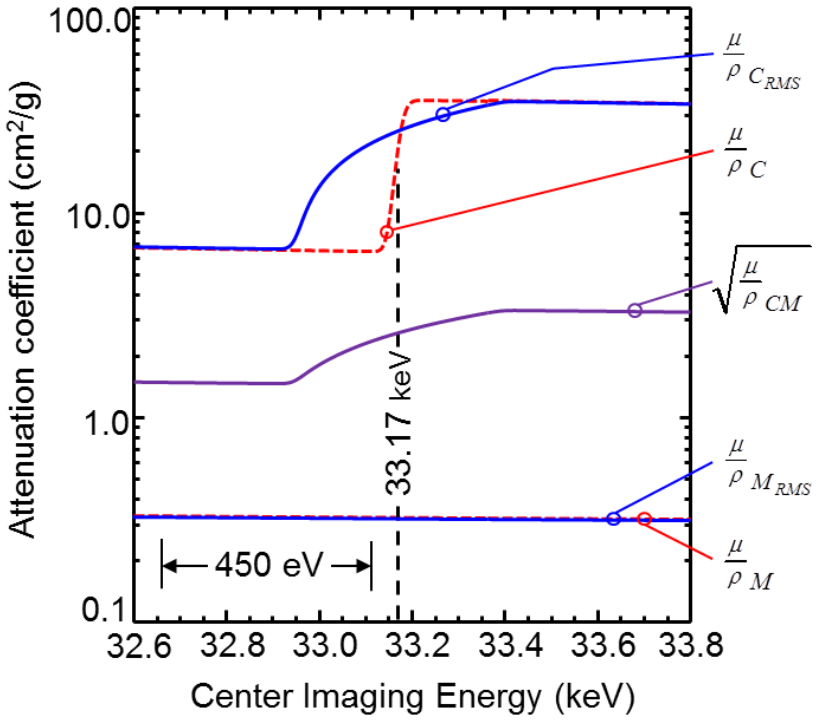

Figure 5.27 The RMS values (blue solid curves) and normal values (read dashed curves) of the iodine (C subscript) and water (M subscript) attenuation coefficients with relation to the imaging energy of the center beam. The RMS values are averaged over an energy span of 450 eV. The iodine K-edge at 33.17 keV is indicated for reference.

33.06 *keV*, achieves an optimal SNR for the iodine image or water image, respectively. It is the Γ_2 term that significantly alters the SNR curves and promotes an optimum SNR near an absorption edge of the contrast material. This calculation indicates that the two-component NESI algorithm is best applied near an absorption edge of the contrast material to achieve the best SNR in the component images and that is where the name "near edge" spectral imaging comes from.

All of the above simulations are based on the RMS averaging of the attenuation coefficients on the 450 *eV* energy span. To investigate the optimal energy span that could achieve the best SNR in the two-component NESI, the same calculation described in Figure 5.28 was repeated for a series of energy spans, ranging from 27 *eV* to 900 *eV* (Figure 5.29). The solid curves of $SNR_{C\text{-}NESI2}$ and $SNR_{M\text{-}NESI2}$ in Figure 5.29A indicate that there is an optimal energy span of 252 *eV* or 270 *eV* that reaches the maximal SNR for the projected iodine or water, respectively. Figure 5.29B shows that the center imaging energies that reach the optimal SNR for the

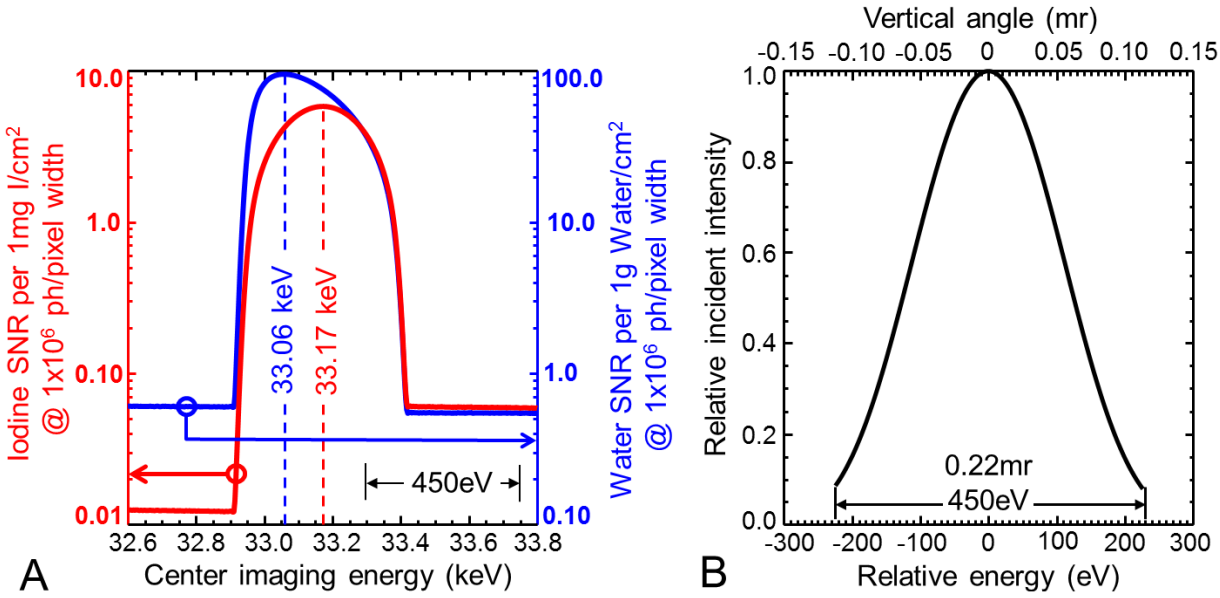

Figure 5.28 Figure A is the simulated iodine (red) and water (blue) SNR from Equation (5.23) vs. the center NESI energy. The SNR calculations assume 1 mg/cm^2 iodine material, 1 g/cm^2 water material and an incident flux of $1x10^6$ photon/pixel width. A significant peak is achieved at 33.17 *keV* or 33.06 *keV* for the iodine or water SNR, respectively. Figure B is the relative incident intensity distribution used in the SNR calculation.

projected iodine and water (such as in Figure 5.28A) are deviating away from the iodine K-edge energy with increasing imaging energy span. For comparison, the SNR for the dual-energy KES are simulated as well from equation (5.4) for the same 1 mg/cm^2 of projected iodine and 1 g/cm^2 of projected water. The SNR calculations for KES always assume one third of the vertical beam

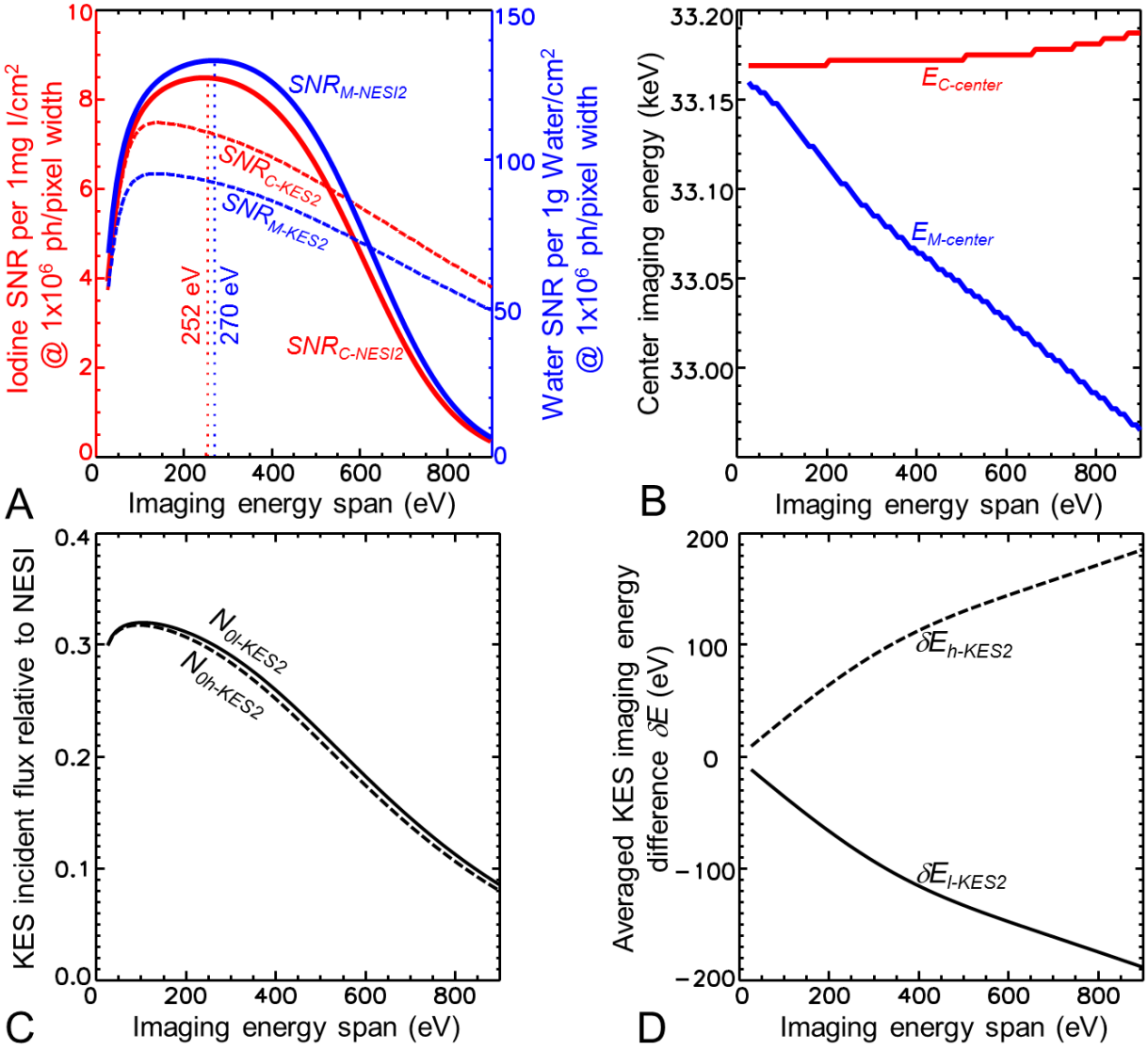

Figure 5.29 Figure A is the simulated iodine (red) and water (blue) SNR for two-component NESI (solid curve) and dual-energy KES (dashed curve) vs. the imaging energy span. The SNR calculations assume 1 mg/cm^2 iodine material, 1 g/cm^2 water material, an incident flux of $1x10^6$ photon/pixel width for NESI and KES incident fluxes relative to that of NESI as shown in Figure C. Figure B shows the center imaging energy that achieves the maximal SNR (such as in Figure 5.28A) at every imaging energy span. Figure D is the averaged energy difference of the above ($\delta E_{h\text{-}KES2}$) and below ($\delta E_{l\text{-}KES2}$) beams used in the KES SNR calculation.

on both shoulders of the full energy span (such as Figure 5.28B) as the incident above and below beams. The total incident fluxes for the above ($N_{0h\text{-}KES2}$) and below ($N_{0l\text{-}KES2}$) beams are plotted with scales relative to the total incident flux of the NESI full beam which is rescaled to 1 (Figure 5.29C). Since the incident flux is not equal along energies (Figure 5.28B), the averaged energy difference δE of the above and below beams which are used in the KES SNR calculations are significantly smaller than the total energy span for the NESI (Figure 5.29D). The simulated SNR comparison in Figure 5.29A indicates that the two-component NESI performs better than dual-energy KES only in a certain energy span. Even though the 450 eV energy span in some data is not optimal for NESI SNR under the simulation assumptions, it still has a better SNR than dual-energy KES.

5.3.2.2 Three-Component NESI

If the NESI assumes an object as a three-component system, a contrast material (C), soft tissue (T) and bone (B), equation (5.18) would be changed as.

$$N_i = N_{0i} e^{-\frac{\mu}{\rho_{Ti}}\rho_T t_T} e^{-\frac{\mu}{\rho_{Bi}}\rho_B t_B} e^{-\frac{\mu}{\rho_{Ci}}\rho_C t_C} \qquad (1 \le i \le n) \tag{5.27}$$

where the index i corresponds to the energy of photon and n is the number of energy points. Taking the negative logarithm gives a linear equation as,

$$r_i = -\ln\left(\frac{N_i}{N_{0i}}\right) = \frac{\mu}{\rho_{Ti}}\rho_T t_T + \frac{\mu}{\rho_{Bi}}\rho_B t_B + \frac{\mu}{\rho_{Ci}}\rho_C t_C \qquad (1 \le i \le n) \tag{5.28}$$

Using the left inverse (a pseudoinverse [Str09]) of an $n \times 3$ matrix, the projected densities of the three components are derived (see Appendix D) as the following equation (5.29),

$$\rho_T t_T = \frac{1}{n}\frac{\left(\frac{\mu}{\rho}_{BB}\frac{\mu}{\rho}_{CC} - \frac{\mu}{\rho}_{BC}^2\right)\sum_i\left(\frac{\mu}{\rho}_{Ti} r_i\right) + \left(\frac{\mu}{\rho}_{BC}\frac{\mu}{\rho}_{TC} - \frac{\mu}{\rho}_{TB}\frac{\mu}{\rho}_{CC}\right)\sum_i\left(\frac{\mu}{\rho}_{Bi} r_i\right) + \left(\frac{\mu}{\rho}_{TB}\frac{\mu}{\rho}_{BC} - \frac{\mu}{\rho}_{TC}\frac{\mu}{\rho}_{BB}\right)\sum_i\left(\frac{\mu}{\rho}_{Ci} r_i\right)}{\frac{\mu}{\rho}_{TT}\left(\frac{\mu}{\rho}_{BB}\frac{\mu}{\rho}_{CC} - \frac{\mu}{\rho}_{BC}^2\right) + \frac{\mu}{\rho}_{TB}\left(\frac{\mu}{\rho}_{BC}\frac{\mu}{\rho}_{TC} - \frac{\mu}{\rho}_{TB}\frac{\mu}{\rho}_{CC}\right) + \frac{\mu}{\rho}_{TC}\left(\frac{\mu}{\rho}_{TB}\frac{\mu}{\rho}_{BC} - \frac{\mu}{\rho}_{TC}\frac{\mu}{\rho}_{BB}\right)}$$

$$\rho_B t_B = \frac{1}{n}\frac{\left(\frac{\mu}{\rho}_{BC}\frac{\mu}{\rho}_{TC} - \frac{\mu}{\rho}_{TB}\frac{\mu}{\rho}_{CC}\right)\sum_i\left(\frac{\mu}{\rho}_{Ti} r_i\right) + \left(\frac{\mu}{\rho}_{TT}\frac{\mu}{\rho}_{CC} - \frac{\mu}{\rho}_{TC}^2\right)\sum_i\left(\frac{\mu}{\rho}_{Bi} r_i\right) + \left(\frac{\mu}{\rho}_{TB}\frac{\mu}{\rho}_{TC} - \frac{\mu}{\rho}_{TT}\frac{\mu}{\rho}_{BC}\right)\sum_i\left(\frac{\mu}{\rho}_{Ci} r_i\right)}{\frac{\mu}{\rho}_{TT}\left(\frac{\mu}{\rho}_{BB}\frac{\mu}{\rho}_{CC} - \frac{\mu}{\rho}_{BC}^2\right) + \frac{\mu}{\rho}_{TB}\left(\frac{\mu}{\rho}_{BC}\frac{\mu}{\rho}_{TC} - \frac{\mu}{\rho}_{TB}\frac{\mu}{\rho}_{CC}\right) + \frac{\mu}{\rho}_{TC}\left(\frac{\mu}{\rho}_{TB}\frac{\mu}{\rho}_{BC} - \frac{\mu}{\rho}_{TC}\frac{\mu}{\rho}_{BB}\right)}$$

$$\rho_C t_C = \frac{1}{n}\frac{\left(\frac{\mu}{\rho}_{TB}\frac{\mu}{\rho}_{BC} - \frac{\mu}{\rho}_{TC}\frac{\mu}{\rho}_{BB}\right)\sum_i\left(\frac{\mu}{\rho}_{Ti} r_i\right) + \left(\frac{\mu}{\rho}_{TB}\frac{\mu}{\rho}_{TC} - \frac{\mu}{\rho}_{TT}\frac{\mu}{\rho}_{BC}\right)\sum_i\left(\frac{\mu}{\rho}_{Bi} r_i\right) + \left(\frac{\mu}{\rho}_{TT}\frac{\mu}{\rho}_{BB} - \frac{\mu}{\rho}_{TB}^2\right)\sum_i\left(\frac{\mu}{\rho}_{Ci} r_i\right)}{\frac{\mu}{\rho}_{TT}\left(\frac{\mu}{\rho}_{BB}\frac{\mu}{\rho}_{CC} - \frac{\mu}{\rho}_{BC}^2\right) + \frac{\mu}{\rho}_{TB}\left(\frac{\mu}{\rho}_{BC}\frac{\mu}{\rho}_{TC} - \frac{\mu}{\rho}_{TB}\frac{\mu}{\rho}_{CC}\right) + \frac{\mu}{\rho}_{TC}\left(\frac{\mu}{\rho}_{TB}\frac{\mu}{\rho}_{BC} - \frac{\mu}{\rho}_{TC}\frac{\mu}{\rho}_{BB}\right)}$$

where the averages of the $\frac{\mu}{\rho}$ products are defined as,

$$\begin{aligned}
&\frac{\mu}{\rho}_{TT} \equiv \frac{1}{n}\sum_i \frac{\mu}{\rho}_{Ti}^2 && \frac{\mu}{\rho}_{BB} \equiv \frac{1}{n}\sum_i \frac{\mu}{\rho}_{Bi}^2 && \frac{\mu}{\rho}_{CC} \equiv \frac{1}{n}\sum_i \frac{\mu}{\rho}_{Ci}^2 \\
&\frac{\mu}{\rho}_{TB} \equiv \frac{1}{n}\sum_i \left(\frac{\mu}{\rho}_{Ti}\frac{\mu}{\rho}_{Bi}\right) && \frac{\mu}{\rho}_{TC} \equiv \frac{1}{n}\sum_i \left(\frac{\mu}{\rho}_{Ti}\frac{\mu}{\rho}_{Ci}\right) && \frac{\mu}{\rho}_{BC} \equiv \frac{1}{n}\sum_i \left(\frac{\mu}{\rho}_{Bi}\frac{\mu}{\rho}_{Ci}\right)
\end{aligned} \tag{5.30}$$

Or a simpler expression as,

$$\begin{aligned}
\rho_T t_T &= \frac{1}{nD_{33}}\left[R_{T1}\sum_i\left(\frac{\mu}{\rho}_{Ti} r_i\right) + R_{T2}\sum_i\left(\frac{\mu}{\rho}_{Bi} r_i\right) + R_{T3}\sum_i\left(\frac{\mu}{\rho}_{Ci} r_i\right)\right] \\
\rho_B t_B &= \frac{1}{nD_{33}}\left[R_{B1}\sum_i\left(\frac{\mu}{\rho}_{Ti} r_i\right) + R_{B2}\sum_i\left(\frac{\mu}{\rho}_{Bi} r_i\right) + R_{B3}\sum_i\left(\frac{\mu}{\rho}_{Ci} r_i\right)\right] \\
\rho_C t_C &= \frac{1}{nD_{33}}\left[R_{C1}\sum_i\left(\frac{\mu}{\rho}_{Ti} r_i\right) + R_{C2}\sum_i\left(\frac{\mu}{\rho}_{Bi} r_i\right) + R_{C3}\sum_i\left(\frac{\mu}{\rho}_{Ci} r_i\right)\right]
\end{aligned} \tag{5.31}$$

where
$$\begin{bmatrix} \frac{\mu}{\rho}_{TT} & \frac{\mu}{\rho}_{TB} & \frac{\mu}{\rho}_{TC} \\ \frac{\mu}{\rho}_{TB} & \frac{\mu}{\rho}_{BB} & \frac{\mu}{\rho}_{BC} \\ \frac{\mu}{\rho}_{TC} & \frac{\mu}{\rho}_{BC} & \frac{\mu}{\rho}_{CC} \end{bmatrix}^{-1} = \frac{1}{D_{33}}\begin{bmatrix} R_{T1} & R_{T2} & R_{T3} \\ R_{B1} & R_{B2} & R_{B3} \\ R_{C1} & R_{C2} & R_{C3} \end{bmatrix}$$

These are the equations that are used to extract projected density images from the NESI raw data cube. As derived in Appendix E, the three-energy KES is a special case of the three-component NESI when three energies are chosen, that is $n = 3$.

Under the assumptions of Poisson counting statistics to represent the noise from the detected signals, the SNR of the projected density images are calculated as (see Appendix F)

$$SNR_T = \frac{nD_{33}}{\sqrt{\sum_i \left[\left(R_{T1}\frac{\mu}{\rho}_{Ti} + R_{T2}\frac{\mu}{\rho}_{Bi} + R_{T3}\frac{\mu}{\rho}_{Ci} \right)^2 \left(\frac{1}{N_i} + \frac{1}{N_{0i}} \right) \right]}} \rho_T t_T$$

$$SNR_B = \frac{nD_{33}}{\sqrt{\sum_i \left[\left(R_{B1}\frac{\mu}{\rho}_{Ti} + R_{B2}\frac{\mu}{\rho}_{Bi} + R_{B3}\frac{\mu}{\rho}_{Ci} \right)^2 \left(\frac{1}{N_i} + \frac{1}{N_{0i}} \right) \right]}} \rho_B t_B \tag{5.32}$$

$$SNR_C = \frac{nD_{33}}{\sqrt{\sum_i \left[\left(R_{C1}\frac{\mu}{\rho}_{Ti} + R_{C2}\frac{\mu}{\rho}_{Bi} + R_{C3}\frac{\mu}{\rho}_{Ci} \right)^2 \left(\frac{1}{N_i} + \frac{1}{N_{0i}} \right) \right]}} \rho_C t_C$$

In order to better understand what parameters affect the SNR with this NESI algorithm we made three simplifications: 1) equal incident flux N_{0i} for all energies, 2) equal transmitted flux N_i for all the energies and 3) dilute contrast material in the object. These lead to simplified SNR expressions for the projected density images as (see in Appendix F),

$$SNR_T \approx \sqrt{\frac{nN_0}{1+e^{\mu t}}} \sqrt{1 - \frac{\frac{\mu}{\rho}_{BB}\frac{\mu}{\rho}_{TC}^2 + \frac{\mu}{\rho}_{CC}\frac{\mu}{\rho}_{TB}^2 - 2\frac{\mu}{\rho}_{TB}\frac{\mu}{\rho}_{TC}\frac{\mu}{\rho}_{BC}}{\frac{\mu}{\rho}_{TT}\left(\frac{\mu}{\rho}_{BB}\frac{\mu}{\rho}_{CC} - \frac{\mu}{\rho}_{BC}^2\right)}} \sqrt{\frac{\mu}{\rho}_{TT}} \rho_T t_T$$

$$SNR_B \approx \sqrt{\frac{nN_0}{1+e^{\mu t}}} \sqrt{1 - \frac{\frac{\mu}{\rho}_{TT}\frac{\mu}{\rho}_{BC}^2 + \frac{\mu}{\rho}_{CC}\frac{\mu}{\rho}_{TB}^2 - 2\frac{\mu}{\rho}_{TB}\frac{\mu}{\rho}_{TC}\frac{\mu}{\rho}_{BC}}{\frac{\mu}{\rho}_{BB}\left(\frac{\mu}{\rho}_{TT}\frac{\mu}{\rho}_{CC} - \frac{\mu}{\rho}_{TC}^2\right)}} \sqrt{\frac{\mu}{\rho}_{BB}} \rho_B t_B \tag{5.33}$$

$$SNR_C \approx \sqrt{\frac{nN_0}{1+e^{\mu t}}} \sqrt{1 - \frac{\frac{\mu}{\rho}_{TT}\frac{\mu}{\rho}_{BC}^2 + \frac{\mu}{\rho}_{BB}\frac{\mu}{\rho}_{TC}^2 - 2\frac{\mu}{\rho}_{TB}\frac{\mu}{\rho}_{TC}\frac{\mu}{\rho}_{BC}}{\frac{\mu}{\rho}_{CC}\left(\frac{\mu}{\rho}_{TT}\frac{\mu}{\rho}_{BB} - \frac{\mu}{\rho}_{TB}^2\right)}} \sqrt{\frac{\mu}{\rho}_{CC}} \rho_C t_C$$

Introducing $\frac{\mu}{\rho}_{T_{RMS}}$, $\frac{\mu}{\rho}_{B_{RMS}}$ and $\frac{\mu}{\rho}_{C_{RMS}}$ for the RMS values, Γ_{3T}, Γ_{3B} and Γ_{3C} terms for the three-component NESI,

$$\frac{\mu}{\rho}_{T_{RMS}} \equiv \sqrt{\frac{\mu}{\rho}_{TT}} \qquad \frac{\mu}{\rho}_{B_{RMS}} \equiv \sqrt{\frac{\mu}{\rho}_{BB}} \qquad \frac{\mu}{\rho}_{C_{RMS}} \equiv \sqrt{\frac{\mu}{\rho}_{CC}}$$

$$\Gamma_{3T} \equiv \sqrt{1 - \frac{\frac{\mu}{\rho}_{BB}\frac{\mu}{\rho}_{TC}^{2} + \frac{\mu}{\rho}_{CC}\frac{\mu}{\rho}_{TB}^{2} - 2\frac{\mu}{\rho}_{TB}\frac{\mu}{\rho}_{TC}\frac{\mu}{\rho}_{BC}}{\frac{\mu}{\rho}_{TT}\left(\frac{\mu}{\rho}_{BB}\frac{\mu}{\rho}_{CC} - \frac{\mu}{\rho}_{BC}^{2}\right)}}$$

$$\Gamma_{3B} \equiv \sqrt{1 - \frac{\frac{\mu}{\rho}_{TT}\frac{\mu}{\rho}_{BC}^{2} + \frac{\mu}{\rho}_{CC}\frac{\mu}{\rho}_{TB}^{2} - 2\frac{\mu}{\rho}_{TB}\frac{\mu}{\rho}_{TC}\frac{\mu}{\rho}_{BC}}{\frac{\mu}{\rho}_{BB}\left(\frac{\mu}{\rho}_{TT}\frac{\mu}{\rho}_{CC} - \frac{\mu}{\rho}_{TC}^{2}\right)}} \tag{5.34}$$

$$\Gamma_{3C} \equiv \sqrt{1 - \frac{\frac{\mu}{\rho}_{TT}\frac{\mu}{\rho}_{BC}^{2} + \frac{\mu}{\rho}_{BB}\frac{\mu}{\rho}_{TC}^{2} - 2\frac{\mu}{\rho}_{TB}\frac{\mu}{\rho}_{TC}\frac{\mu}{\rho}_{BC}}{\frac{\mu}{\rho}_{CC}\left(\frac{\mu}{\rho}_{TT}\frac{\mu}{\rho}_{BB} - \frac{\mu}{\rho}_{TB}^{2}\right)}}$$

the simplified SNR equations are then expressed as,

$$SNR_T \approx \sqrt{\frac{nN_0}{1+e^{\mu t}}}\Gamma_{3T}\frac{\mu}{\rho}_{T_{RMS}}\rho_T t_T$$

$$SNR_B \approx \sqrt{\frac{nN_0}{1+e^{\mu t}}}\Gamma_{3B}\frac{\mu}{\rho}_{B_{RMS}}\rho_B t_B \tag{5.35}$$

$$SNR_C \approx \sqrt{\frac{nN_0}{1+e^{\mu t}}}\Gamma_{3C}\frac{\mu}{\rho}_{C_{RMS}}\rho_C t_C$$

Similarly, the SNR is proportional to the amount of material present ($\rho_T t_T$, $\rho_B t_B$ and $\rho_C t_C$) and proportional to the square root of the incident photon count $\sqrt{nN_0}$. The SNR equations are dimensionless and contain the RMS averages of the attenuation coefficients.

5.3.2.3 *m*-Component NESI

In a general case, the NESI assumes an object as an *m*-component system with a subscript *j* for different materials and contrast species. Each vertical line in the pixelated detector is a measurement of the number of photons transmitted through the object as a function of energy.

$$N_i = N_{0i}e^{\sum_j -\frac{\mu}{\rho}_{ji}\rho_j t_j} \qquad (1 \le i \le n,\ 1 \le j \le m,\ n \ge m) \tag{1.36}$$

where the index *i* corresponds to the energy of photon and *n* is the number of energy points. Taking the negative logarithm gives a linear equation as,

$$r_i = -\ln\left(\frac{N_i}{N_{0i}}\right) = \sum_j \frac{\mu}{\rho}_{ji} \rho_j t_j \qquad (1 \le i \le n,\ 1 \le j \le m,\ n \ge m) \tag{2.37}$$

Using the left inverse of an $n \times m$ matrix, the projected densities of the components are derived (see Appendix G) as,

$$\rho_j t_j = \frac{1}{nD_{mm}}\left[R_{j1}\sum_i \left(\frac{\mu}{\rho}_{1i} r_i\right) + \ldots + R_{jj}\sum_i \left(\frac{\mu}{\rho}_{ji} r_i\right) + \ldots + R_{jm}\sum_i \left(\frac{\mu}{\rho}_{mi} r_i\right)\right]$$

$$\text{where} \quad \begin{bmatrix} \frac{\mu}{\rho}_{\langle 11\rangle} & \cdot\cdot & \frac{\mu}{\rho}_{\langle 1j\rangle} & \cdot\cdot & \frac{\mu}{\rho}_{\langle 1m\rangle} \\ \vdots & & \vdots & & \vdots \\ \frac{\mu}{\rho}_{\langle j1\rangle} & \cdot\cdot & \frac{\mu}{\rho}_{\langle jj\rangle} & \cdot\cdot & \frac{\mu}{\rho}_{\langle jm\rangle} \\ \vdots & & \vdots & & \vdots \\ \frac{\mu}{\rho}_{\langle m1\rangle} & \cdot\cdot & \frac{\mu}{\rho}_{\langle mj\rangle} & \cdot\cdot & \frac{\mu}{\rho}_{\langle mm\rangle} \end{bmatrix}^{-1} = \frac{1}{D_{mm}} \begin{bmatrix} R_{11} & \cdot\cdot & R_{1j} & \cdot\cdot & R_{1m} \\ \vdots & & \vdots & & \vdots \\ R_{j1} & \cdot\cdot & R_{jj} & \cdot\cdot & R_{jm} \\ \vdots & & \vdots & & \vdots \\ R_{m1} & \cdot\cdot & R_{mj} & \cdot\cdot & R_{mm} \end{bmatrix} \tag{5.38}$$

and the averages of the $\frac{\mu}{\rho}$ products are defined as,

$$\begin{aligned} &\frac{\mu}{\rho}_{\langle 11\rangle} \equiv \frac{1}{n}\sum_i \frac{\mu}{\rho}_{1i}^2 \qquad \frac{\mu}{\rho}_{\langle jj\rangle} \equiv \frac{1}{n}\sum_i \frac{\mu}{\rho}_{ji}^2 \qquad \frac{\mu}{\rho}_{\langle mm\rangle} \equiv \frac{1}{n}\sum_i \frac{\mu}{\rho}_{mi}^2 \\ &\frac{\mu}{\rho}_{\langle 1m\rangle} \equiv \frac{1}{n}\sum_i \left(\frac{\mu}{\rho}_{1i} \frac{\mu}{\rho}_{mi}\right) = \frac{1}{n}\sum_i \left(\frac{\mu}{\rho}_{mi} \frac{\mu}{\rho}_{1i}\right) \equiv \frac{\mu}{\rho}_{\langle m1\rangle} \\ &\frac{\mu}{\rho}_{\langle j1\rangle} \equiv \frac{1}{n}\sum_i \left(\frac{\mu}{\rho}_{ji} \frac{\mu}{\rho}_{1i}\right) \equiv \frac{\mu}{\rho}_{\langle 1j\rangle} \qquad \frac{\mu}{\rho}_{\langle mj\rangle} \equiv \frac{1}{n}\sum_i \left(\frac{\mu}{\rho}_{mi} \frac{\mu}{\rho}_{ji}\right) \equiv \frac{\mu}{\rho}_{\langle jm\rangle} \end{aligned} \tag{5.39}$$

Under the assumptions of Poisson counting statistics to represent the noise from the detected signals, the SNR of the projected density images are calculated (see Appendix H) as,

$$SNR_j = \frac{\rho_j t_j}{\sigma_{\rho_j t_j}} = \frac{nD_{mm}}{\sqrt{\sum_i \left[\left(R_{j1} \frac{\mu}{\rho}_{1i} + \ldots + R_{jj} \frac{\mu}{\rho}_{ji} + \ldots + R_{jm} \frac{\mu}{\rho}_{mi}\right)^2 \left(\frac{1}{N_i} + \frac{1}{N_{0i}}\right)\right]}} \rho_j t_j \tag{5.40}$$

Assuming equal incident flux N_{0i} for all the energy i, equal transmitted flux N_i for all the energy i and $N \approx N_0 e^{-\mu t}$, the simplified SNR for the projected material would be,

$$SNR_j \approx \sqrt{\frac{nN_0}{1+e^{\mu t}}} \frac{\sqrt{n} D_{mm}}{\sqrt{\sum_i \left(R_{j1} \frac{\mu}{\rho}_{1i} + ... + R_{jj} \frac{\mu}{\rho}_{ji} + ... + R_{jm} \frac{\mu}{\rho}_{mi} \right)^2}} \rho_j t_j \tag{5.41}$$

As expected, the SNR is proportional to the amount of material present ($\rho_j t_j$) and proportional to the square root of the incident photon count $\sqrt{nN_0}$.

5.3.3 Implementation

5.3.3.1 Experimental Setup

The same BLM described in chapter 5.2.2.2 was used to prepare the beam for the NESI system. This BLM was used with a pixelated area detector without the three-beam chopper to block the X-ray energies at and near the contrast element K-edge. This has an advantage that the imaging flux is higher and the possibility of faster imaging due to increased dose rate. This is especially an advantage on beamlines with low critical energy devices such as bend magnets. For example, the experiments were performed on the BMIT BM beamline (1.354 *T* magnetic field) at the CLS (2.9 *GeV*) which has a critical energy of 7.5 *keV*. At such a low critical energy source, the high energy component, for example 33.17 keV for iodine K-edge energy, is more compressed to the orbital plane where the traditional KES beam splitter would block most of the flux.

A schematic diagram and the experimental setup of the NESI system are shown in Figure 5.30. While the BLM was placed in a filtered white X-ray beam from the BMIT BM beamline, the {311} diffraction near the iodine K-edge of 33.17 *keV* was selected by an aperture in a leaded wall which was set between the BLM and the object. This leaded wall prevented other X-ray diffractions from the crystal and the scatter from the direct beam stop from giving background and unnecessary dose to the object, beam monitoring ionization chamber and the detection systems. The photon rate was monitored by an air-filled ionization chamber and was found to be

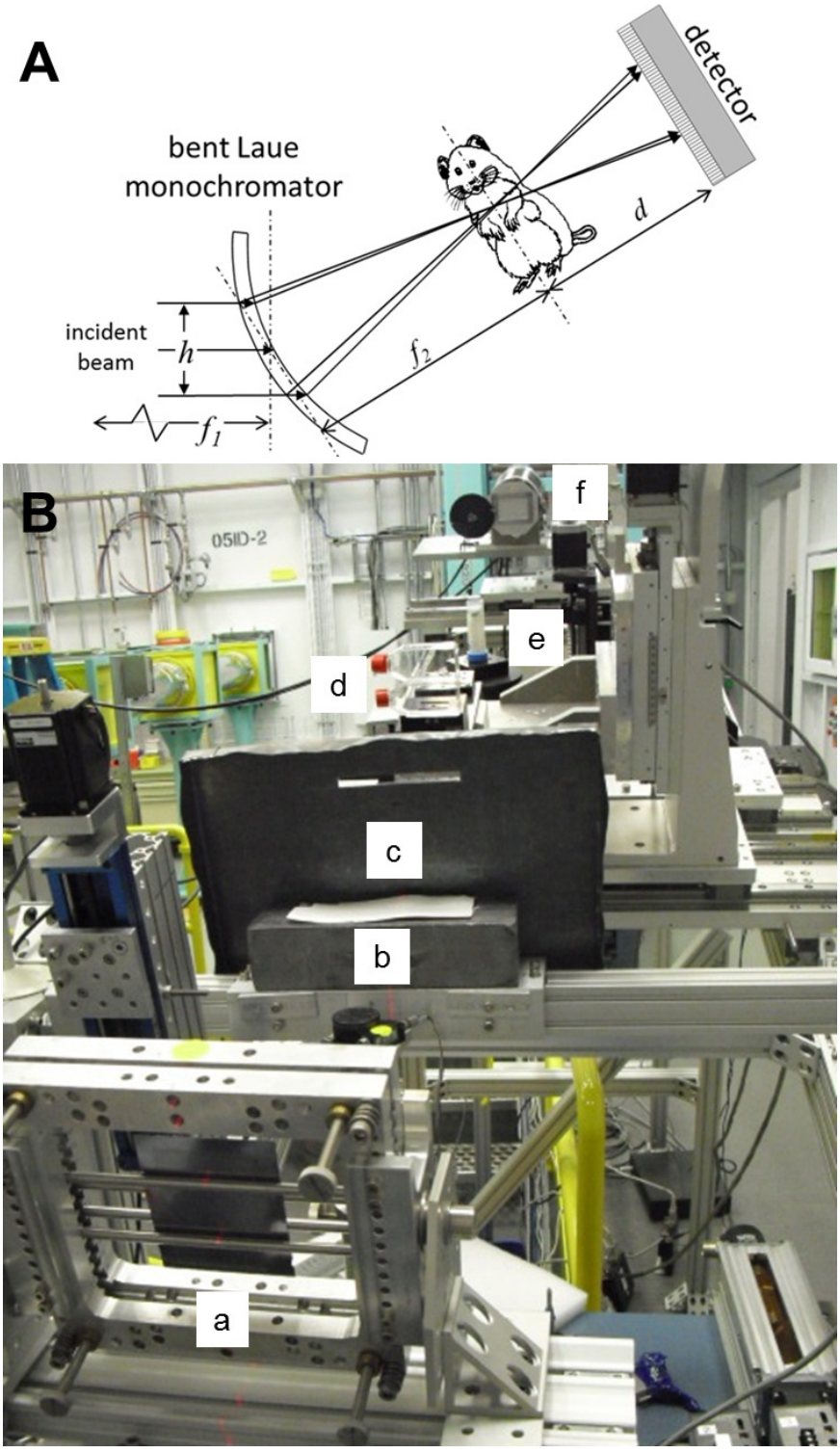

Figure 5.30 NESI schematic diagram (A) and the experimental setup (B) including a BLM (a) on a four-bar bender, direct beam stop (b), lead shielding (c) with an aperture, two bottles of 30 *mg/ml* NaI and organic iodine solution (d) stacked on top of an ion chamber, tubes of iodine solution (e) on a sample stage and the Photonic Science detector (f) at the very back.

2.31×10^9 photons/sec/horizontal *mr*/*mA* ring current with 0.11 *mm* of copper filter and 0.883 *mm* of aluminum filter in the beamline. This flux rate corresponds to a minimal energy bandwidth of 1.67%. The vertical beam size at the BLM position was about 5 *mm*. At the focus the vertical beam size was measured as approximately 0.1 *mm* which corresponds to a maximum dose rate of 14.4 *mGy/s* at a ring current of 250 *mA*. The sample was placed at or near the focus. The maximal dimension of the sample was typically less than 50 *mm* which allowed for minimal beam enlargement along the beam path due to convergence and divergence over the size of the object. The Photonic Science detector (FDI VHR 90 *mm*, 18.7 μm pixel size, Photonic Science Ltd., UK) was placed about 2.53 *m* downstream of the crystal and 1.03 *m* downstream of the object. Two bottles of 63 mg/cm^2 iodine filters, NaI and organic iodine (from Optiray®240 Ioversol) solution, were used to analyze the K-edge lines and beam features.

5.3.3.2 Beam Profile

An image of the beam with no object in the way is shown in Figure 5.31A with the intensity bar on the right side. Figure 5.31B shows the image of beam obtained when a 63 mg/cm^2 organic iodine filter was placed in the beam. Figure 5.31C is a negative logarithm image of the measured beam (Figure 5.31B) divided by the flat field beam (Figure 5.31A) both of which were first corrected by a dark image subtraction. Thus this image (Figure 5.31C) is proportional to the linear attenuation coefficient of the object since the thickness of the object is a constant all over the image area.

The attenuation jump line in Figure 5.31B and 5.31C near the vertical middle of the image was identified as the K-edge of iodine which was roughly the midpoint of the attenuation transition. This line corresponds to the maximal slope vertically across the image in Figure 5.31C. The measured K-edge line was plotted as a cyan line in Figure 5.31D which was nearly

overlapped by its fitted black line. The measured maximal intensity line across the beam width from Figure 5.31A was plotted as a blue line in Figure 5.31D which was nearly overlapped by its fitted orange line. The -3.3° angle of slope in the peak intensity line may come from the not exactly horizontal axis of the {311} diffraction plane, an azimuthal angle adjustment for the

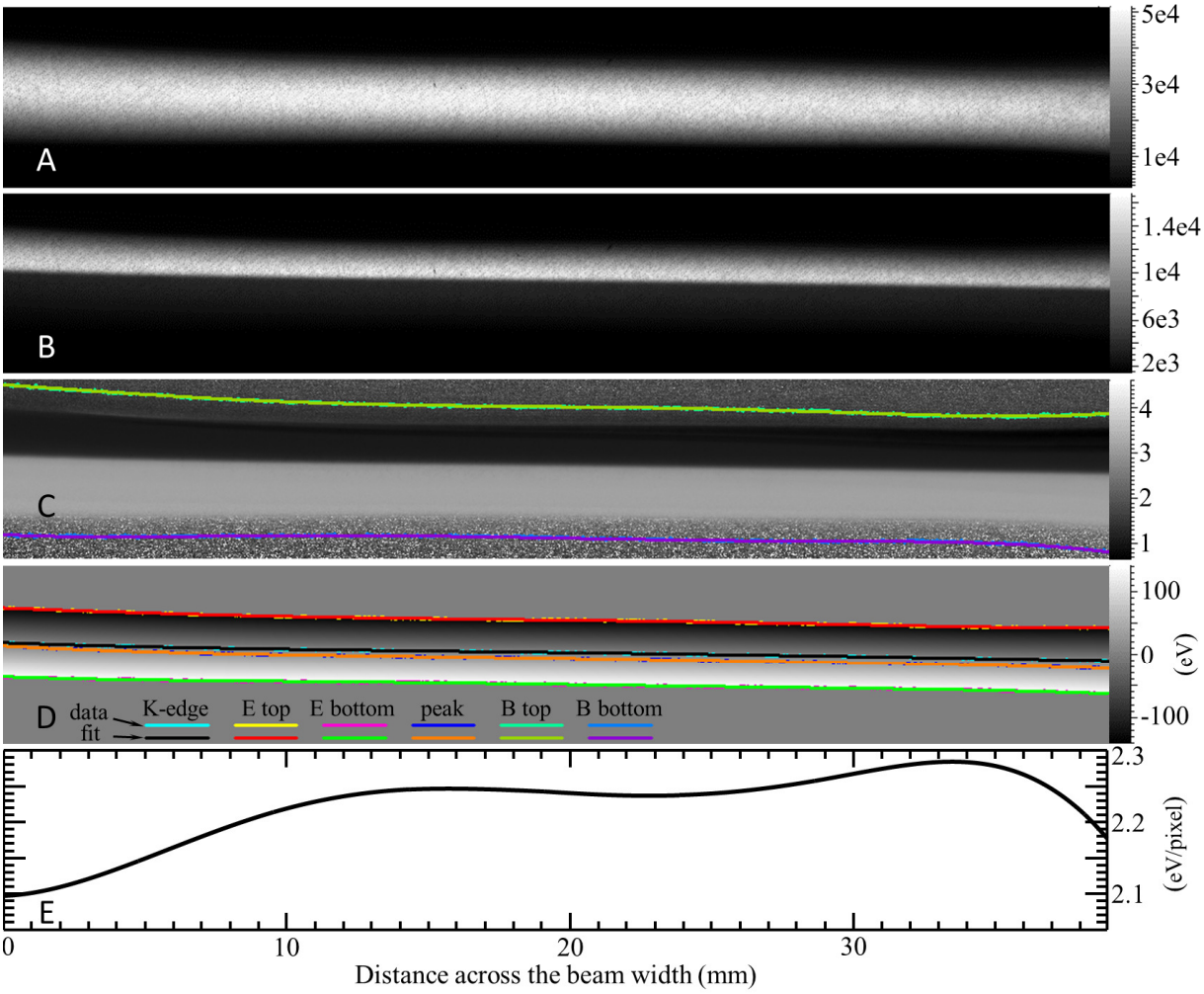

Figure 5.31 Images of the x-ray beam were acquired using the Photonic Science detector. Figure A and B are intensity based images of the beam in the absence of an object (A) and after an organic iodine filter of 63 mg/cm^2 (B), respectively. An attenuation image (C) was then obtained through a negative logarithm of the ratio of Figure B to Figure A. The beam energy distribution (D) within the selected beam region of 275 *eV* energy span was plotted relative to the iodine K-edge energy. The measured and fitted K-edge lines, peak intensity lines, top and bottom beam edge lines based on 1% peak intensity ("B top" and "B bottom"), top and bottom energy edge lines based on 275 *eV* energy span ("E top" and "E bottom") were plotted with their color mapping noted. The outside of the selected energy region was arbitrarily set to 0 just for viewing. Figure E is the change of energy resolution per vertical pixel width across the beam width.

BLM or a misaligned detector window. A 1.2° angle between the slightly mismatched K-edge line and the peak intensity line indicated a crystal mounting error that the axis of the {311} diffraction plane was not exactly parallel to the bending bars.

As more noises appeared on the both sides of the beam (Figure 5.31C) where the incident beam intensity was low, the beam edges were defined according to an arbitrary threshold of 1% of the maximal intensity along each vertical line of the data. The measured top or bottom beam edge was plotted as a celeste or azure line in Figure 5.31C which was overlapped by its fitted green-yellow or purple line, respectively. Most of the flux diverged into the region between the top and bottom beam edge lines in Figure 5.31C which had an average vertical size of 4.69 *mm* and an average top-to-bottom energy spread of 557 *eV*. The variations of the top and bottom beam edge lines implied non-uniform bending across the BLM width which resulted in an energy resolution change across the beam width with a standard deviation of 0.05 *eV* (Figure 5.31E). The detector's effective pixel size of 18.7 μm corresponds to an average energy resolution of 2.2 *eV* energy change per vertical pixel width and 2.4 *eV*/pixel after consideration of the Darwin width of a perfect crystal. The energy resolution was calculated based on the estimated focus-to-detector distance, beam height from 1% of the peak intensity and the equation (5.17).

Within the 557 *eV* energy range, only 275 *eV* energy span was selected to be analyzed in the NESI algorithm for better SNR performance (Figure 5.29A). The measured top or bottom edges of 137.5 *eV* below or above the K-edge energy was plotted as a yellow or magenta line in Figure 5.31D which was overlapped by its fitted red or green line, respectively. In the beam energy distribution relative to the iodine K-edge energy (Figure 5.31D), the above measured and fitted lines were plotted with color mapping noted and the outside of the selected energy region was arbitrarily set to 0 just for easy viewing.

The measured mass attenuation coefficient $\frac{\mu}{\rho}$ of iodine was calculated and averaged from the K-edge transition data in Figure 5.31C and then plotted in black in Figure 5.32A. The tabulated mass attenuation coefficient of iodine was convolved with an energy spread function (a Gaussian function with a Gaussian width of 20 *eV*) to give a good match with the measured data and it was plotted in blue in Figure 5.32A. The same convolution was applied to the tabulated mass attenuation coefficients of other components including the matrix material which is assumed to be water.

For comparison, the XANES data of sodium iodide measured by M.C. Feiters [Fei05] with a 2 *eV* energy resolution was plotted in red in Figure 5.32A. The fact that our measured data showed less near edge features than the Feiters' data indicated that our energy resolution should be worse than Feiters' 2 *eV* energy resolution which matched well with the estimated energy resolution of 2.4 *eV*/pixel. The slopes of the three iodine K-edge transitions were plotted

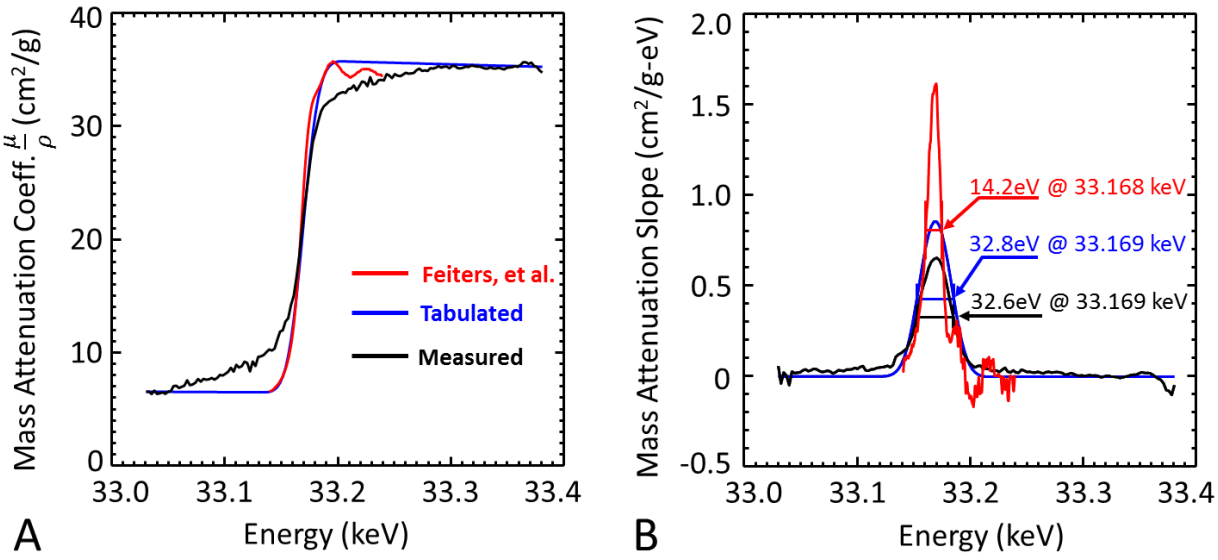

Figure 5.32 Iodine mass attenuation coefficients $\frac{\mu}{\rho}$ (A) and their slopes (B) of the measured data (black) from Figure 5.31C, the tabulated data after convolution (blue) and the Feiters' XANES data of the sodium iodine (red) acquired at an energy resolution of 2 *eV* [Fei05] (see the data use permission in Appendix I.6).

in Figure 5.32B. The Feiters' data had the steeper slope with a FWHM of 14.2 *eV* centered at 33.168 *keV* energy, while our measured data had a milder slope with a FWHM of 32.6 *eV* centered at 33.169 keV which matched well with the tabulated data after convolution. Besides, the NESI method definitely covered a much wider energy range than the standard XANES measurements and would be promising to obtain more sensitive data when better energy resolution is achieved.

5.3.4 Results

5.3.4.1 NESI of a "Physics Rat" Head

The same "physics rat" head sample with 30 *mg/ml* iodine solution as shown in Figure 5.20 was imaged by projection NESI (described in chapter 5.3.3.1) at the BMIT BM beamline in January 2012. While the sample was vertically line-scanned 800 steps with a step size of 50 μm/step, the Photonic Science detector took an image of the beam transmitted through the sample at each step. With each projection image of 2300 (x) × 301 (E) pixels, the raw data cube of 2300 (x) × 800 (y) × 301 (E) pixels covered a physical cube of 43 *mm* (x) × 40 *mm* (y) × 555 *eV* (E), while only half of the energies, 275 *eV* of the beam, was used in the data analysis. Besides 10 "dark" images without the beam and 10 "flat" images without the sample, 10 "edge" images of a 63 mg/cm^2 organic iodide filter were taken before and after the 800 projection images to analyze the beam parameters, such as the K-edge line, beam region and energy mapping as described in Figure 5.31.

Since the tabulated mass attenuation coefficients $\frac{\mu}{\rho}$ of iodine matched best with the measured transitions in the "edge" images after a 20 *eV* blurring through a convolution with a Gaussian function (as seen in Figure 5.32A), the tabulated mass attenuation coefficients of the matrix material which is assumed to be water was also blurred with a 20 *eV* Gaussian function.

Since the energy mapping within the beam region is known (Figure 5.31D), the maps of the mass attenuation coefficients of iodine $\frac{\mu}{\rho}_{Ci}$ and water $\frac{\mu}{\rho}_{Mi}$ within the beam region were obtained as well as their mean square maps $\frac{\mu}{\rho}_{CC}$, $\frac{\mu}{\rho}_{MM}$ and $\frac{\mu}{\rho}_{CM}$. Based on the NESI two-component theory, the projected density images of the iodine (Figure 5.33A) and water (Figure 5.33B) were obtained using the equation (5.22). The iodine image clearly showed 10 steps of the projected iodine variations in the step wedge region and the iodine sandwiched between the cuvette and its insert. The water image showed no density variations in the step wedge region. A big air bubble appeared in both images. The SNR of the projected density images were then calculated using the NESI SNR equation (5.23) and shown in Figure 5.34A and B without image processing.

For comparison, conventional KES images (Figure 5.33C and D) were obtained from the same data cube. The high and low beams were set within the selected beam region after one third of the region around the K-edge line was blocked away. The energy lines of the high and low beams were set by averaging the energy mapping vertically while considering the beam flux contributions. The average beam energies for the high and low beams were 33.26 k*eV* and 33.09 k*eV*. Each projection image was then averaged into two lines of high and low data and the projected density images were obtained using the KES equation (5.3). Similarly, the SNR of the KES images were calculated using the equation (5.4) and shown in Figure 5.34C and D.

The step wedge region in Figure 5.33 and 5.34 were plotted in Figure 5.35 after horizontal shifting and vertical averaging to compare the two-component NESI with KES imaging. Figure 5.35A clearly showed the 10 steps of the projected iodine density with about 2.8 mg/cm^2/step for the NESI and 2.7 mg/cm^2/step for the KES imaging both of which were supposed to be 3 mg/cm^2/step. The error may come from not accurately prepared iodine concentration and energy mapping errors. The plot was found to be downward shifted about a

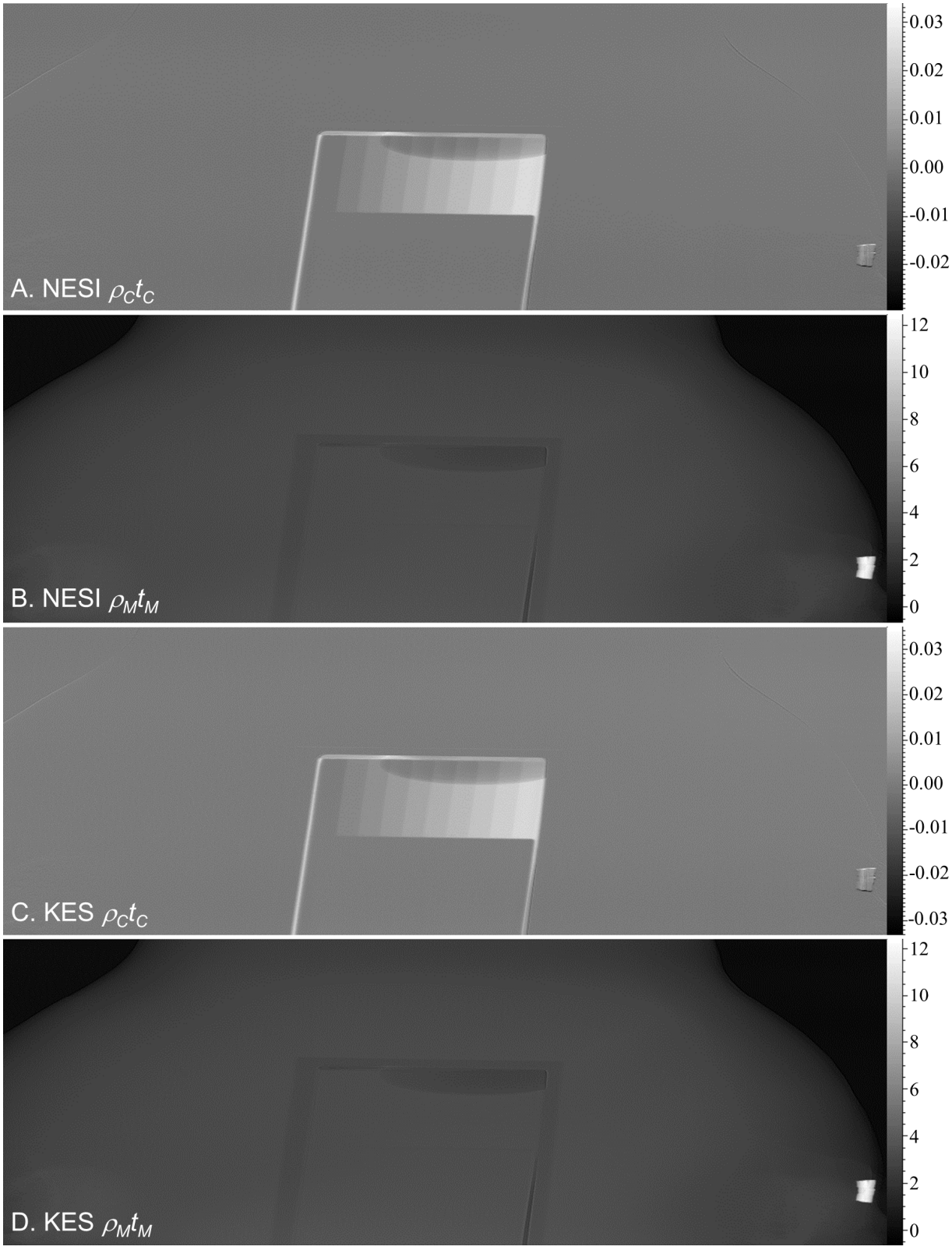

Figure 5.33 NESI and KES projected density images of a "physics rat" head in unit of g/cm^2

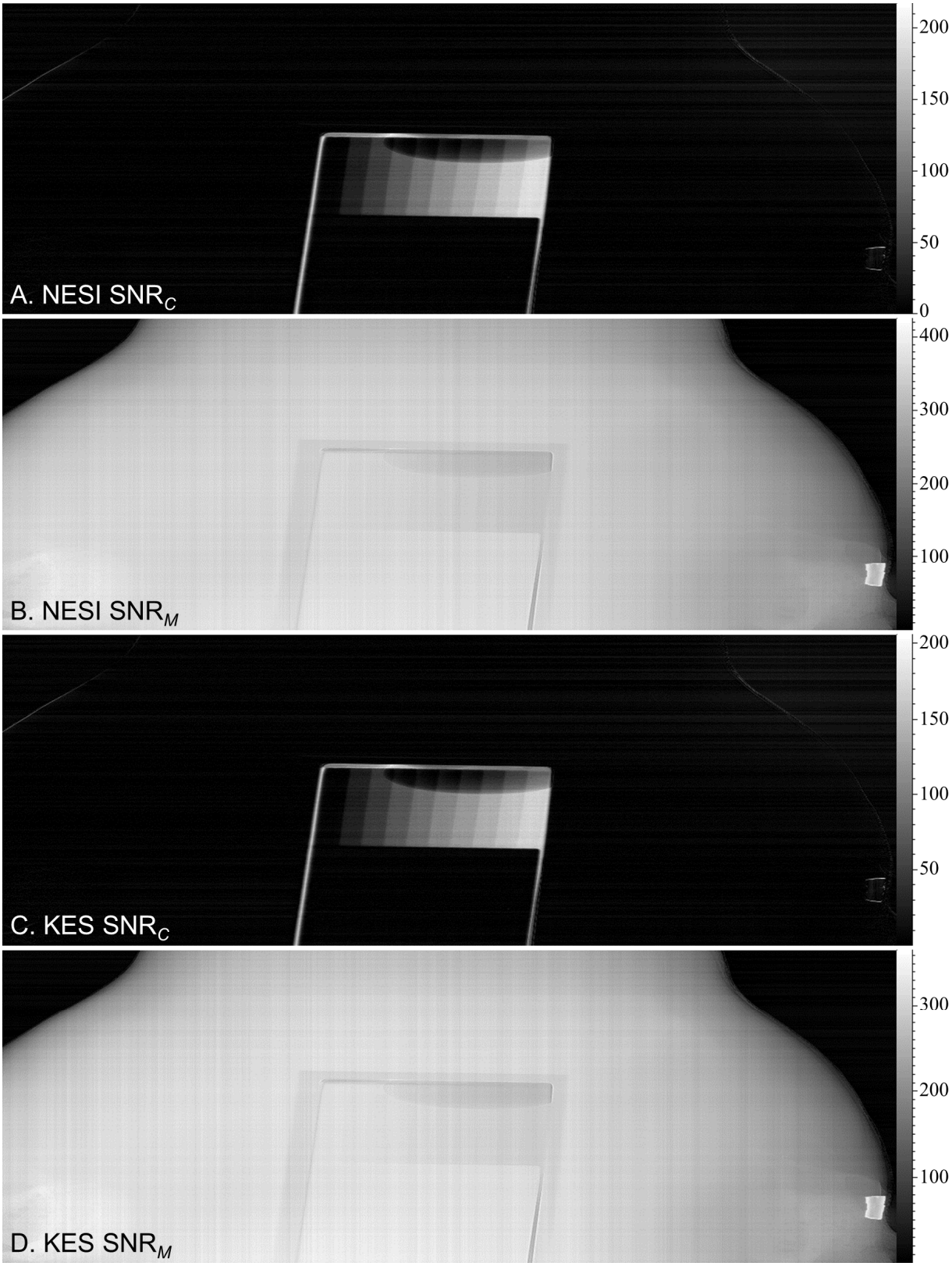

Figure 5.34 SNR of the projected density images of the “physics rat” head in Figure 5.33

step depth and the error may come from the over subtracted water and plastic container attenuations. Figure 5.35A indicated that the NESI is more sensitive in iodine detection than the KES processing partially because the NESI utilized the beam energy more accurately while the KES application used here simply averaged the energy bands for the high and low beams. The NESI projected density plots of water exactly matched with the KES plots (Figure 5.35B) both of

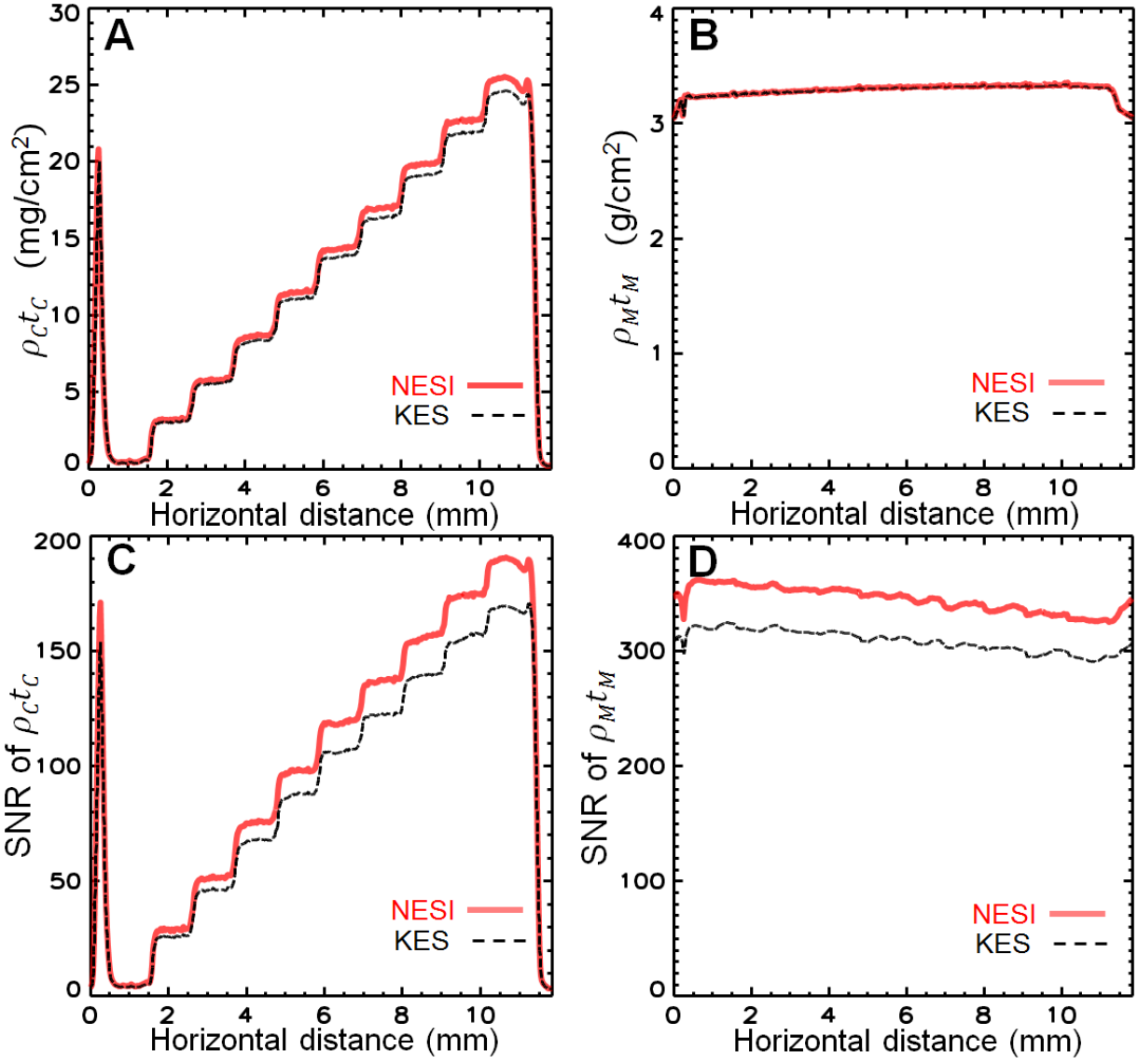

Figure 5.35 The step wedge region in Figure 5.33 and 5.34 were plotted vs. horizontal distance including the projected density of iodine (A), projected density of water (B), the SNR of the iodine image (C) and the water image (D) for both two-component NESI (red solid curves) and KES imaging (black dashed curves).

which showed no signs of iodine. The NESI showed higher SNR performance on both iodine (Figure 5.35C) and water (Figure 5.35D) images. And the SNR plot of iodine image (Figure 5.35C) directly showed that the SNR is proportional to the detected iodine amount.

5.3.4.2 NESI of a mouse with injected iodine

The same NESI projection imaging was successfully performed on a euthanized mouse injected with iodine solution in the lung region at the BMIT BM beamline in January 2012. While the mouse within a centrifuge tube was vertically scanned 2100 steps at 50 μm/step, the Photonic Science detector took an image at each step and collected a raw data cube of 2300 (x) × 2100 (y) × 301 (E) pixels which covered a physical cube of 43 *mm* (x) × 105 *mm* (y) × 555 *eV* (E). Again only 275 *eV* energy span of the beam was used in the data analysis for better SNR performance.

After the same analysis as described in Chapter 5.3.4.1, the NESI and KES projected density images of the mouse were obtained in both Dorsal-Ventral (DV) view (Figure 5.36) and lateral view (Figure 5.37). The iodine images indicated that the most amount of iodine located within the lung region while the water images did not show signs of iodine in the same region. The NESI and KES images were so close that only the statistics in Table 5.7 could tell the difference. Table 5.7 showed that the NESI picked up a little bit more iodine than KES, the total amount of water was pretty close between the two methods and the NESI images had better SNR than KES in both the DV and lateral views. It was also noted that the total amount of materials in the two views were not exactly matched with each other. The reason may come from the different averaged flat image (without sample), ring current decay and variations, different beam height at the detector (4.685 *mm* for DV view and 4.635 *mm* for lateral view) and thus the energy resolution (2.224 *eV* for DV view and 2.236 *eV* for lateral view) based on the different beam

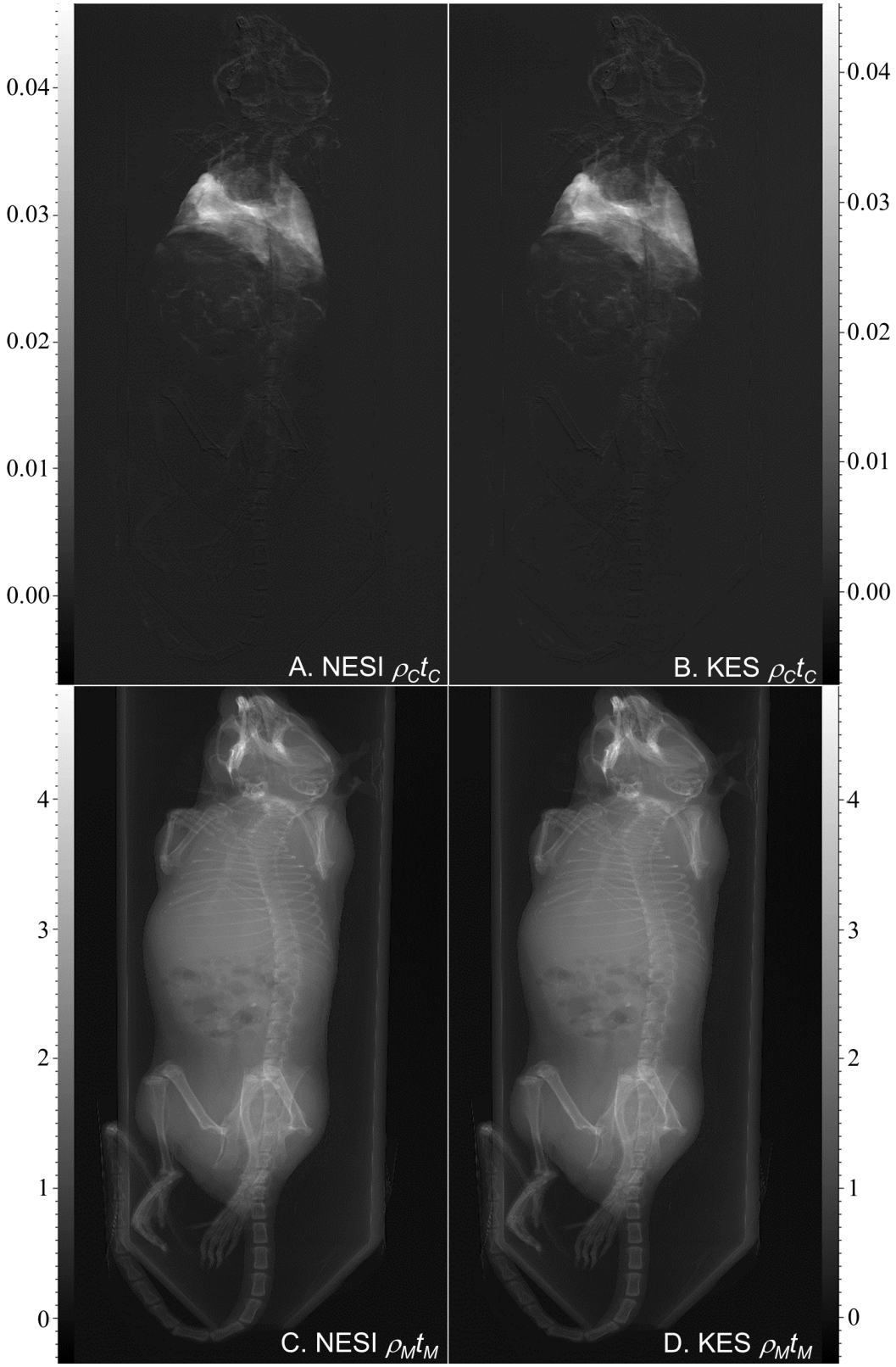

Figure 5.36 NESI and KES images of a mouse in DV view with injected iodine in unit of g/cm^2

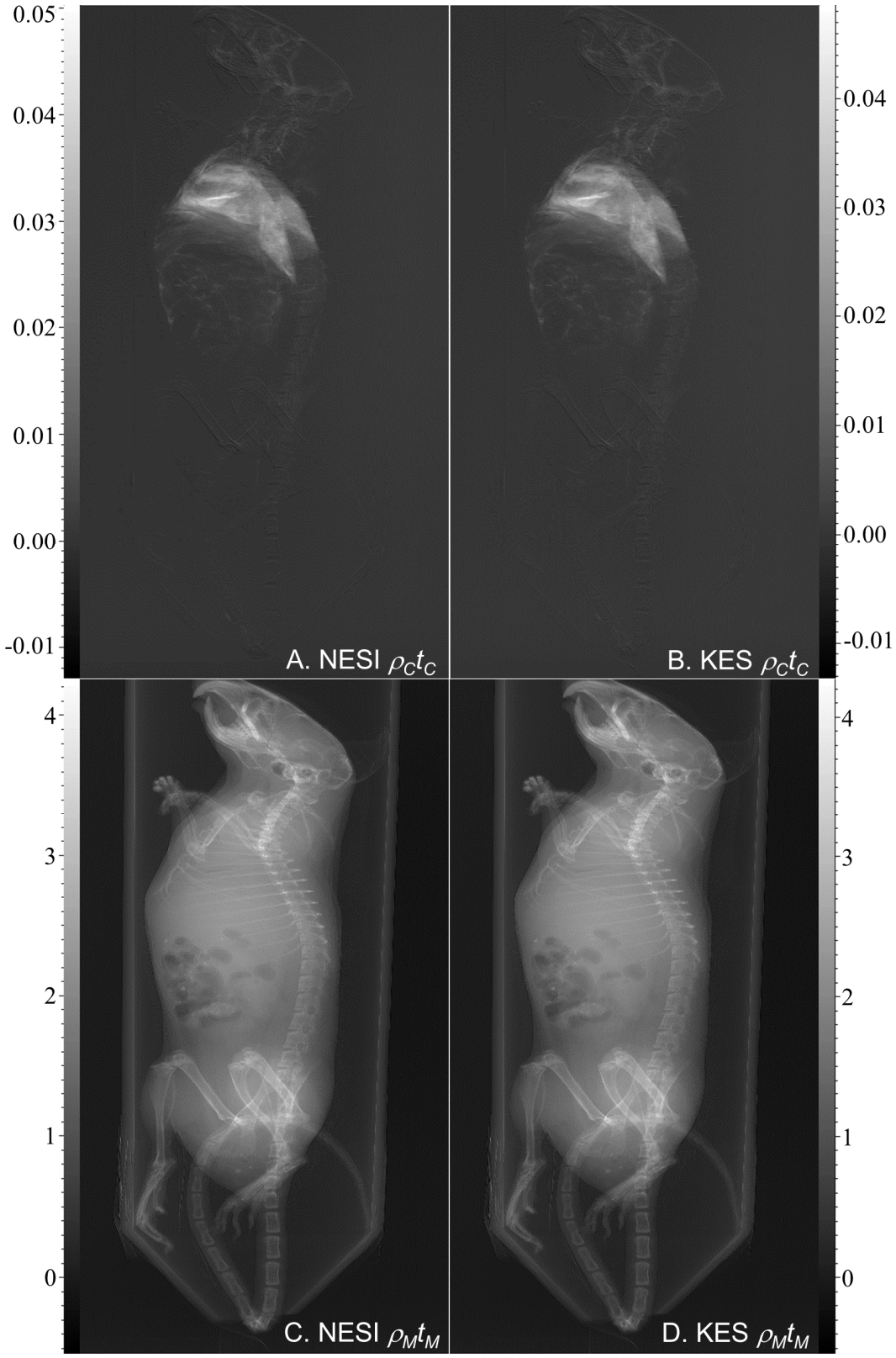

Figure 5.37 NESI and KES images of a mouse in lateral view with iodine in unit of g/cm^2

Table 5.7 NESI vs. KES respecting to the total amount of material detected and SNR

		NESI	*KES*
DV view	*Total amount of iodine in $\rho_C t_C$ image (mg)*	49.6	47.2
	Total amount of water in $\rho_M t_M$ image (g)	29.8	29.8
	Average SNR of $\rho_C t_C$ image	13.4	12.1
	Average SNR of $\rho_M t_M$ image	83.4	74.9
Lateral view	*Total amount of iodine in $\rho_C t_C$ image (mg)*	54.6	52.2
	Total amount of water in $\rho_M t_M$ image (g)	29.6	29.4
	Average SNR of $\rho_C t_C$ image	14.8	13.5
	Average SNR of $\rho_M t_M$ image	82.8	73.9

edges of 1% peak intensity.

5.3.4.3 NESI CT of Tubing with Organic Iodine

A bundle of tubing segments (Intramedic® non-radiopaque polyethylene tubing PE330, 2.92 *mm* I.D. and 3.73 *mm* O.D., Becton Dickinson and Company, USA) were sealed with organic iodine solution (diluted from Optiray®240 Ioversol) at concentrations of 0 ~ 2 *mg/ml* and were packed into a centrifuge tube (Figure 5.38) as the test object for the NESI CT experiment at the BMIT BM beamline in November 2011. While the tubing was continuously rotating, the Photonic Science detector took 2500 projections at a step angle of 0.072° and exposure time of 120 *ms* for each projection image of 2084 (x) × 341 (E) pixels. The collected raw data cube of 2084 (x) × 2500 (θ) × 341 (E) pixels covered a physical cube of 39 *mm* (x) × 180° (θ) × 557 *eV* (E). Again only 275 *eV* energy span of the beam was used in the data analysis.

After the same analysis as described in Chapter 5.3.3.2 and Chapter 5.3.4.1, sinograms of the iodine and water projected density were obtained from the NESI and KES algorithm. After the filtered back projection, the sinograms were reconstructed into iodine and water CT slice

images (Figure 5.39). The variations of the iodine concentration in the 35 tubes (Figure 5.39A and B) are obviously observed and well matched with the tubing packing patterns (Figure 5.38B) in both NESI and KES images. No such variations were observed in the water images (Figure 5.39C and D) and the water amount in the tubes with iodine solutions were exactly the same as the tube containing pure water (a smaller tube on the top right). This statement was confirmed by the measurements shown in Figure 5.40B which clearly indicated that no iodine showed up in the water images of both NESI and KES algorithms. Even though the CT images suffered the ring artifact mostly from the nonlinear distribution of the ring current and the artifact of enhanced edges due to the phase contrast, the averaged projected iodine amount displayed a linear concentration changes among the tube (Figure 5.40A). The fact that a little bit more iodine was detected in the NESI iodine images than the KES indicated a better sensitivity of NESI algorithm to detect iodine. Due to the image artifacts the SNR measurements of iodine and water within the tubes were quite noisy (Figure 5.40C and D), but the overall trend of

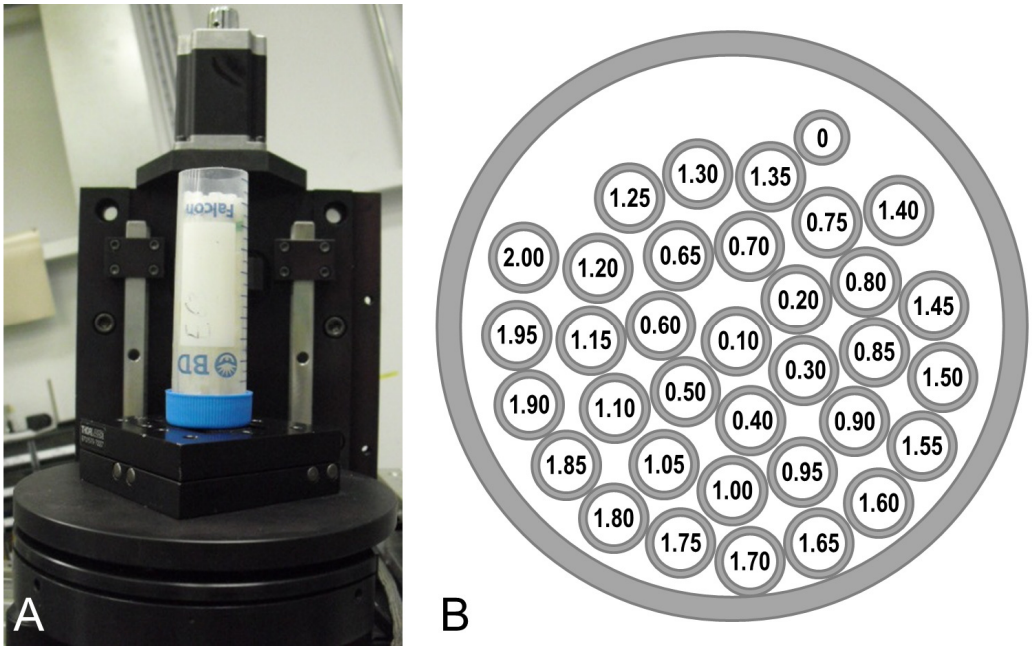

Figure 5.38 The photo (A) and cross-section view (B) of the tubing sample with organic iodine concentration noted in *mg/ml*.

proportionality to the iodine amount was still noticeable and better SNR in NESI over the KES was observed in many of the measurements (Figure 5.40C). If we define the iodine detection limit of an imaging system as the detectable iodine concentration with SNR better than one, the detection limit of this NESI and KES imaging system was achieved by the tube of 0.2 *mg/ml* iodine concentration with SNR of 1.29 in NESI and 1.25 in KES imaging. Considering the slice

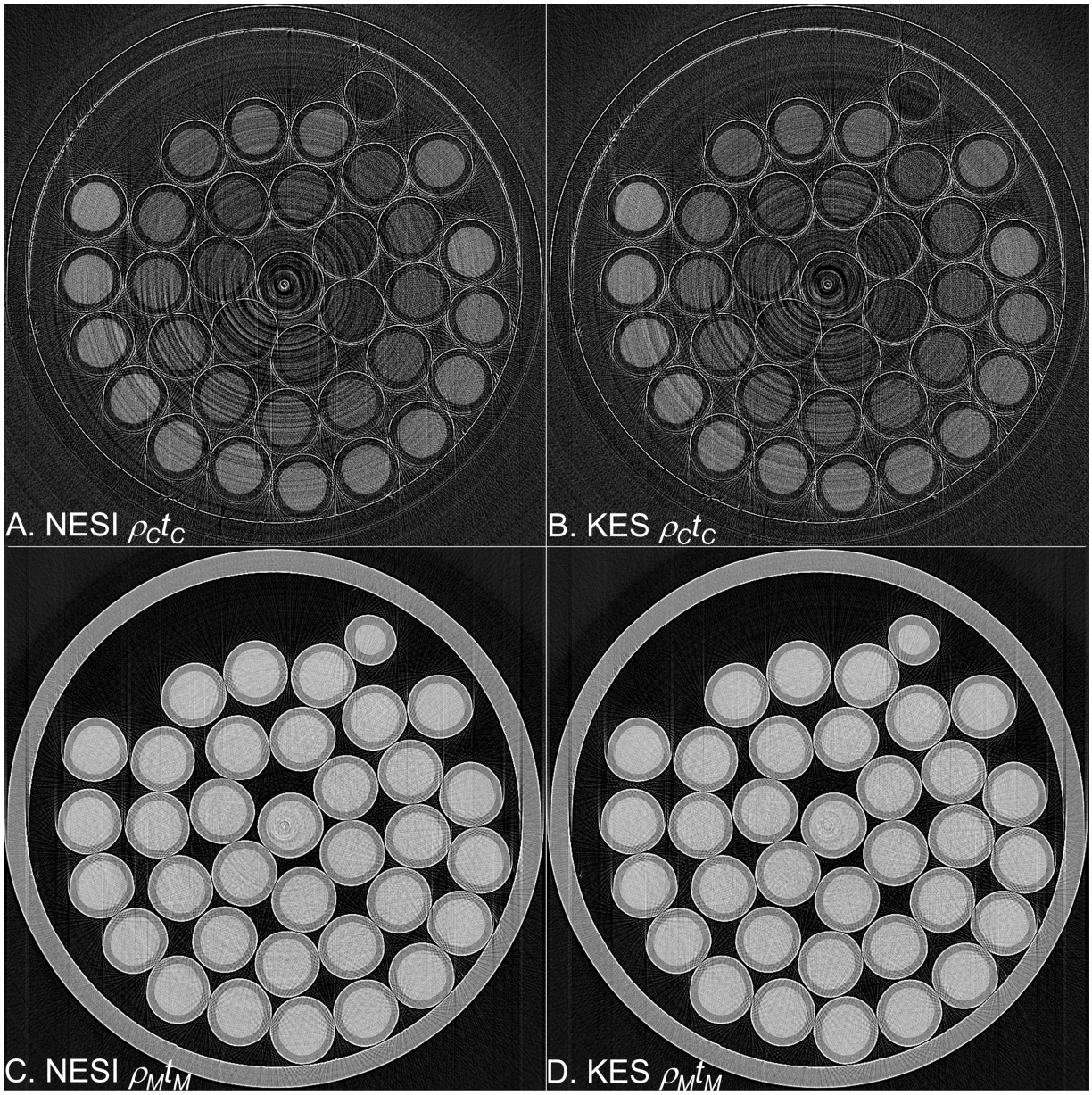

Figure 5.39 NESI and KES CT images of the tubing with different iodine concentrations

thickness defined by the beam height at the focus which was roughly 100 μm, the detection limit would be 2 $\mu g/cm^2$. Assuming a slice thickness of 100 μm, the measured projected water density was 5 times smaller and the measured projected iodine densities were 4~5 times smaller than the theoretical value. The reason may come from the image processing and still needs further investigation.

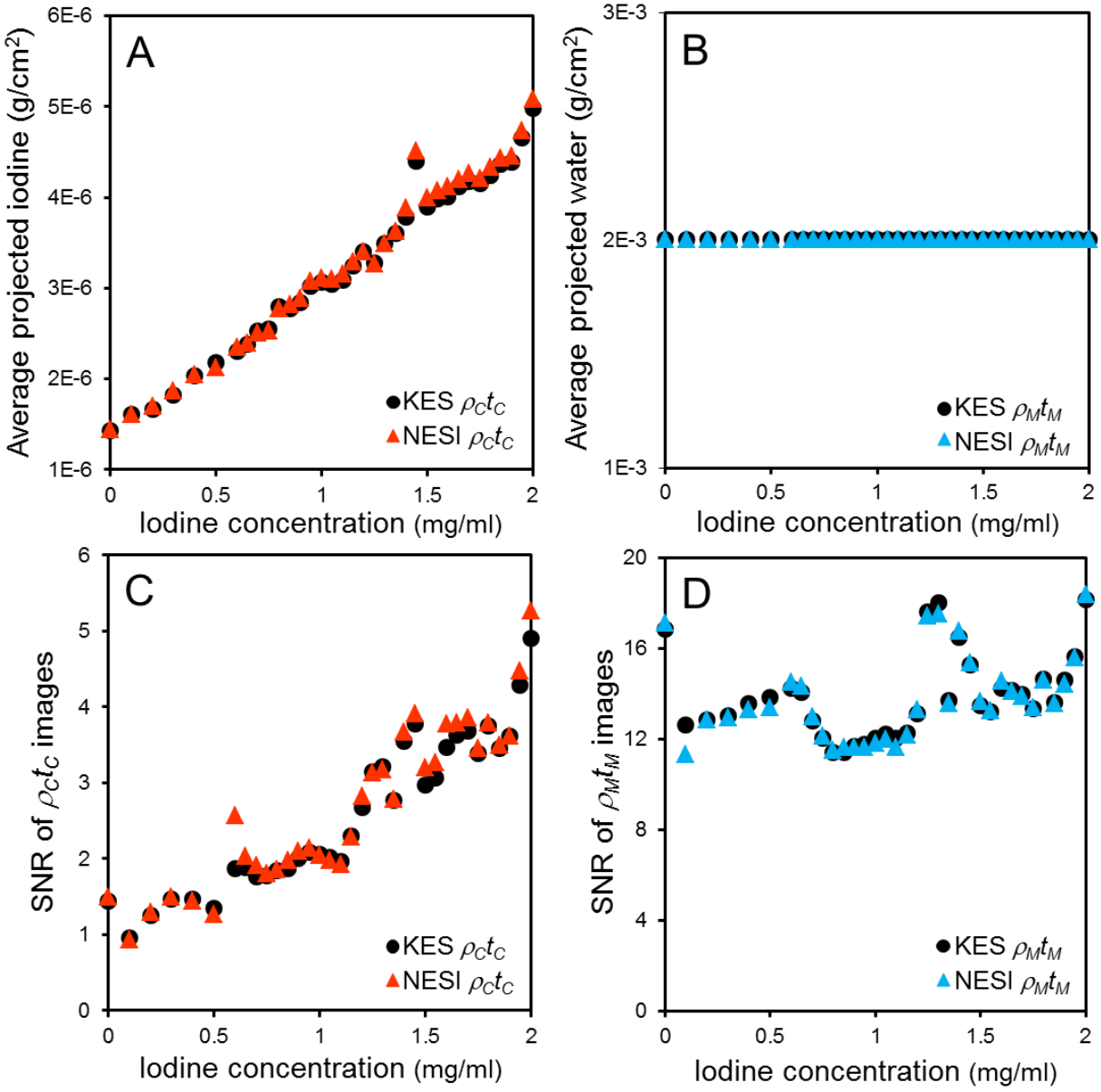

Figure 5.40 Projected iodine (A) and water (B) densities were averaged in every tube. SNR of the iodine (C) and water (D) within each tube were measured in both NESI and KES images.

5.3.5 Discussion and Future Work

In this chapter, a novel idea of NESI was conceived and a full set of its theoretical equations were derived. Preliminary experiments were performed on both NESI projection and CT imaging. The imaging results showed its sensitivity to detect dilute iodine and better SNR performance over a certain energy span compared with the conventional KES imaging. Besides, the setup for NESI is simpler and the alignments are easier compared with the three-energy KES and BLM-based KES imaging.

While two-component NESI analysis was successfully performed, the three-component NESI analysis of the real data encountered singular matrix problem and needs alternative mathematical manipulation on the matrix inverse. The sensitivity of NESI for resolving components of more than two still needs further investigation.

Through the theoretical simulation (Figure 5.29) and the data analysis, the NESI was found to have better performance within a certain energy span, such as 275 eV instead of 557 eV which nearly corresponded to the full beam. Besides its contribution to better SNR performance, imaging closer to the edge energy minimizes the image blurring due to bone in the two-component analysis where the sensitivity coefficient of bone to contrast image S_{CB} decreases with small δE (Figure 5.2). Also, narrower energy span corresponds to smaller vertical beam size and an overall smaller crossover angle to the beams which will minimize the crossover artifact that plagues the conventional BLM-based KES method. All these benefits promote the NESI for imaging applications of dilute contrast materials.

This narrowed energy span is still more than enough for the XANES analysis as seen in Figure 5.32. The spectral imaging to resolve different species of iodine was limited by the current energy resolution of 2.4 eV/pixel. An improvement in energy resolution can be achieved

by switching to a high resolution imaging detector and/or increasing the sample-to-detector distance. Since these actions will worsen the image artifact due to the phase contrast, it would be better pursued after figuring out a way to remove the phase artifact through proper image processing. The improvement of energy resolution would be limited by the BLM's intrinsic energy resolution of 0.95 *eV* or 1.29 *eV* considering the Darwin width of a perfect crystal at the BMIT BM beamline (Table 5.2). Improvement on the intrinsic energy resolution of a BLM while maintaining the sub-micron focus condition still needs further investigation.

Another promising application of NESI would be the EXAFS analysis which requires a different optimization of the NESI system towards wide energy span and high energy resolution. The overwhelming impact of NESI is that it will bring together contrast imaging and elemental speciation imaging through XANES and EXAFS analysis which have been totally different realms. It will be interesting the see what the merging of these two fields bring and what promising applications will be revealed in the near future.

Chapter 6 Conclusions and Further Research

6.1 Conclusions

The aim of this research is to use bent Laue crystals to develop biomedical X-ray imaging modalities and to solve biomedical X-ray imaging problems. The main conclusions of this research are summarized as follows.

1. The novel NESI system showed high sensitivity for iodine with a detection limit of 2 $\mu g/cm^2$ and a slightly better SNR performance than the conventional KES imaging. The NESI setup was simpler and the alignments were easier. Its narrower energy span showed great promise to minimize the crossover artifact in BLM-based KES imaging and the image artifact due to bone in the two-component analysis.
2. The novel three-beam chopper was successfully used in the three-energy KES imaging with measured profiles matched well with the simulations.
3. The BLM and three-beam chopper-enabled three-energy KES imaging was quick, free of motion artifact and the artifact due to the presence of bone at a cost of cross-over artifact. The first simultaneous dual-energy KES imaging and the first KES CT imaging were successfully performed in Canada at the BMIT BM beamline.
4. The BLA improved Mn specificity in XRF imaging and achieved a Mn detection limit of 0.5 mM concentration, 50 μm vertical size of the detectable region and 34.5 eV energy resolution.

5. A novel confocal XRF imaging system with a probing voxel of $100 \times 100 \times 124\ \mu m^3$ showed great promise to perform 3D iodine fluorescence mapping of a small animal. This method provides an alternative to perform the confocal XRF imaging and opens up a new application for BLAs.
6. Rapid prototyping is a simple, fast and relatively inexpensive method to fabricate humane custom animal restraints, field flatteners and crystal bender frames. The rapid-prototyped BLA frames provided a new method of log-spiral bending of crystals.
7. The rapid-prototyped animal restraint holds great promise in improving the image quality and repeatability while reducing stress on experimental animals.
8. The field flattener improved the image SNR and decreased the wide dynamic range and linear response requirements on the imaging detector at a cost of raised maximum exposure to some regions of the subject and reduced anatomical information in the images. This method holds great promise to visualize low concentrations of contrast agents.

6.2 Recommendations for Future Work

Based on the research presented in this dissertation, directions for future work are recommended according to different projects.

6.2.1 Small Animal Restraints and Field Flatteners

1. Standardize the animal restraints and field flatteners for ‘‘generic’’ rats;
2. Raise the compressed range of incident photon flux to the high end of the detector linearity to further improve the SNR;
3. Investigate clinical applications of animal restraints and field flatteners.

6.2.2 Mn XRF imaging and Confocal XRF Imaging

1. Employ a focused micro-probe source, stabilize the support of the detector system and develop a precise alignment procedure to quickly lock onto the focused position for the Mn XRF imaging project;
2. Apply the Mn XRF imaging system to EXAFS measurements and a thorough study of Mn in the substantia nigra of a larger number of human brains;
3. Compare the four BLA detectors for the Mn XRF imaging;
4. The confocal XRF imaging method needs further system validation and experimental application to small animals.

6.2.3 Three-Energy KES

1. Perform three-energy KES imaging at the BMIT ID beamline to obtain an image of bone;
2. Explore applications for other third component besides bone;
3. Improve the BLM focus size down to a few microns;
4. Explore the high resolution and high flux KES imaging and therapy applications.

6.2.4 NESI

1. Remove the phase contrast artifact and ring artifact in the NESI images;
2. Analyze m-component NESI ($m \geq 3$) and its sensitivity to resolve components of more than two;
3. Improve energy resolution and the intrinsic energy resolution of a BLM while maintaining the sub-micron focus size condition;
4. Improve spatial resolution to sub-ten microns;
5. Spectral imaging through XANES and EXAFS analysis;
6. Consider time resolved spectroscopy;
7. Combine contrast imaging and elemental speciation imaging into one system.

Appendix A Least Squares Fit Derivation for Two-Component NESI

The NESI data can be transformed into the values that represent the measured total attenuation r_i at each energy *i*. Ideally there is a combination of mass attenuation coefficients and projected density values that constitute these measured data. Due to the statistics of these measured data there may not be a solution that exactly matches. For a two-component NESI system, a contrast material (*C*) and a matrix material (*M*), the mass attenuation coefficients of the components ($\frac{\mu}{\rho}_{Mi}, \frac{\mu}{\rho}_{Ci}$) are either known, easily modeled or measured. We assume there is a single projected density value, $\rho_C t_C$ for the contrast material and $\rho_M t_M$ for the matrix material, that best fits the measured data. The calculated fit to the measured data could be presented as,

$$r_i' = \frac{\mu}{\rho}_{Mi} \rho_M t_M + \frac{\mu}{\rho}_{Ci} \rho_C t_C \tag{A.1}$$

Define an error function as the difference between the measured data and calculated values,

$$e \equiv \sum_i \left(r_i - r_i'\right)^2 = \sum_i \left(r_i - \frac{\mu}{\rho}_{Mi} \rho_M t_M - \frac{\mu}{\rho}_{Ci} \rho_C t_C\right)^2 \tag{A.2}$$

This function is to be minimized by varying the projected density values. Taking a partial derivative with respect to these two variables and setting the resulting equation to zero finds the minimum of the error function.

$$\begin{aligned} \frac{\partial e}{\partial(\rho_M t_M)} &= -2\sum_i \left(r_i - \frac{\mu}{\rho}_{Mi} \rho_M t_M - \frac{\mu}{\rho}_{Ci} \rho_C t_C\right)\frac{\mu}{\rho}_{Mi} = 0 \\ \frac{\partial e}{\partial(\rho_C t_C)} &= -2\sum_i \left(r_i - \frac{\mu}{\rho}_{Mi} \rho_M t_M - \frac{\mu}{\rho}_{Ci} \rho_C t_C\right)\frac{\mu}{\rho}_{Ci} = 0 \end{aligned} \tag{A.3}$$

These are easily recast into a solvable set of two equations as,

$$\sum_i r_i \frac{\mu}{\rho}_{Mi} = \rho_M t_M \sum_i \frac{\mu}{\rho}_{Mi}^2 + \rho_C t_C \sum_i \frac{\mu}{\rho}_{Ci} \frac{\mu}{\rho}_{Mi}$$
$$\sum_i r_i \frac{\mu}{\rho}_{Ci} = \rho_M t_M \sum_i \frac{\mu}{\rho}_{Ci} \frac{\mu}{\rho}_{Mi} + \rho_C t_C \sum_i \frac{\mu}{\rho}_{Ci}^2 \qquad \text{(A.4)}$$

The sums of the $\frac{\mu}{\rho}$ products can be replaced by their averages

$$\frac{\mu}{\rho}_{CC} \equiv \frac{1}{n}\sum_i \frac{\mu}{\rho}_{Ci}^2 \qquad \frac{\mu}{\rho}_{MM} \equiv \frac{1}{n}\sum_i \frac{\mu}{\rho}_{Mi}^2 \qquad \frac{\mu}{\rho}_{CM} \equiv \frac{1}{n}\sum_i \left(\frac{\mu}{\rho}_{Ci} \frac{\mu}{\rho}_{Mi}\right) \qquad \text{(5.21)}$$

where n is the number of energy points. Equation (A.4) can be represented as a matrix form,

$$\begin{bmatrix} \sum_i r_i \frac{\mu}{\rho}_{Mi} \\ \sum_i r_i \frac{\mu}{\rho}_{Ci} \end{bmatrix} = n \begin{bmatrix} \frac{\mu}{\rho}_{MM} & \frac{\mu}{\rho}_{CM} \\ \frac{\mu}{\rho}_{CM} & \frac{\mu}{\rho}_{CC} \end{bmatrix} \begin{bmatrix} \rho_M t_M \\ \rho_C t_C \end{bmatrix}$$
$$\begin{bmatrix} \rho_M t_M \\ \rho_C t_C \end{bmatrix} = \frac{1}{n} \begin{bmatrix} \frac{\mu}{\rho}_{MM} & \frac{\mu}{\rho}_{CM} \\ \frac{\mu}{\rho}_{CM} & \frac{\mu}{\rho}_{CC} \end{bmatrix}^{-1} \begin{bmatrix} \sum_i r_i \frac{\mu}{\rho}_{Mi} \\ \sum_i r_i \frac{\mu}{\rho}_{Ci} \end{bmatrix} \qquad \text{(A.5)}$$

This equation is easily solved for the projected density values,

$$\begin{bmatrix} \rho_M t_M \\ \rho_C t_C \end{bmatrix} = \frac{1}{n} \frac{\begin{bmatrix} \frac{\mu}{\rho}_{CC} & -\frac{\mu}{\rho}_{CM} \\ -\frac{\mu}{\rho}_{CM} & \frac{\mu}{\rho}_{MM} \end{bmatrix}}{\frac{\mu}{\rho}_{CC}\frac{\mu}{\rho}_{MM} - \frac{\mu}{\rho}_{CM}^2} \begin{bmatrix} \sum_i r_i \frac{\mu}{\rho}_{Mi} \\ \sum_i r_i \frac{\mu}{\rho}_{Ci} \end{bmatrix} \qquad \text{(A.6)}$$

This is the equation (5.22) for the two-component NESI in chapter 5.3.2.1,

$$\rho_M t_M = \frac{1}{n} \frac{\frac{\mu}{\rho}_{CC} \sum_i \left(\frac{\mu}{\rho}_{Mi} r_i\right) - \frac{\mu}{\rho}_{CM} \sum_i \left(\frac{\mu}{\rho}_{Ci} r_i\right)}{\frac{\mu}{\rho}_{CC}\frac{\mu}{\rho}_{MM} - \frac{\mu}{\rho}_{CM}^2}$$
$$\rho_C t_C = \frac{1}{n} \frac{\frac{\mu}{\rho}_{MM} \sum_i \left(\frac{\mu}{\rho}_{Ci} r_i\right) - \frac{\mu}{\rho}_{CM} \sum_i \left(\frac{\mu}{\rho}_{Mi} r_i\right)}{\frac{\mu}{\rho}_{CC}\frac{\mu}{\rho}_{MM} - \frac{\mu}{\rho}_{CM}^2} \qquad \text{(5.22)}$$

Appendix B Dual-Energy KES from Two-Component NESI

In theory, dual-energy KES equation (5.3) should be a special case of the two-component NESI equation (5.20). For a consistency check, setting the index i to two values, h for above the edge energy and l for below the edge energy,

$$\rho_M t_M = \frac{\sum_i \frac{\mu}{\rho}_{Ci}^2 \sum_i \left(\frac{\mu}{\rho}_{Mi} r_i\right) - \sum_i \left(\frac{\mu}{\rho}_{Ci} \frac{\mu}{\rho}_{Mi}\right) \sum_i \left(\frac{\mu}{\rho}_{Ci} r_i\right)}{\sum_i \frac{\mu}{\rho}_{Ci}^2 \sum_i \frac{\mu}{\rho}_{Mi}^2 - \left[\sum_i \left(\frac{\mu}{\rho}_{Ci} \frac{\mu}{\rho}_{Mi}\right)\right]^2} \tag{5.20}$$

$$\rho_M t_M = \frac{(\frac{\mu}{\rho}_{Cl}^2 + \frac{\mu}{\rho}_{Ch}^2)(\frac{\mu}{\rho}_{Ml} r_l + \frac{\mu}{\rho}_{Mh} r_h) - (\frac{\mu}{\rho}_{Ml} \frac{\mu}{\rho}_{Cl} + \frac{\mu}{\rho}_{Mh} \frac{\mu}{\rho}_{Ch})(\frac{\mu}{\rho}_{Cl} r_l + \frac{\mu}{\rho}_{Ch} r_h)}{(\frac{\mu}{\rho}_{Ml}^2 + \frac{\mu}{\rho}_{Mh}^2)(\frac{\mu}{\rho}_{Cl}^2 + \frac{\mu}{\rho}_{Ch}^2) - (\frac{\mu}{\rho}_{Ml} \frac{\mu}{\rho}_{Cl} + \frac{\mu}{\rho}_{Mh} \frac{\mu}{\rho}_{Ch})^2}$$

$$\rho_M t_M = \frac{\begin{array}{c}(\frac{\mu}{\rho}_{Ml} \frac{\mu}{\rho}_{Cl}^2 r_l + \frac{\mu}{\rho}_{Mh} \frac{\mu}{\rho}_{Cl}^2 r_h + \frac{\mu}{\rho}_{Ml} \frac{\mu}{\rho}_{Ch}^2 r_l + \frac{\mu}{\rho}_{Mh} \frac{\mu}{\rho}_{Ch}^2 r_h) - \\ (\frac{\mu}{\rho}_{Ml} \frac{\mu}{\rho}_{Cl}^2 r_l + \frac{\mu}{\rho}_{Ml} \frac{\mu}{\rho}_{Cl} \frac{\mu}{\rho}_{Ch} r_h + \frac{\mu}{\rho}_{Mh} \frac{\mu}{\rho}_{Ch} \frac{\mu}{\rho}_{Cl} r_l + \frac{\mu}{\rho}_{Mh} \frac{\mu}{\rho}_{Ch}^2 r_h)\end{array}}{\begin{array}{c}(\frac{\mu}{\rho}_{Ml}^2 \frac{\mu}{\rho}_{Cl}^2 + \frac{\mu}{\rho}_{Mh}^2 \frac{\mu}{\rho}_{Cl}^2 + \frac{\mu}{\rho}_{Ml}^2 \frac{\mu}{\rho}_{Ch}^2 + \frac{\mu}{\rho}_{Mh}^2 \frac{\mu}{\rho}_{Ch}^2) - \\ (\frac{\mu}{\rho}_{Ml}^2 \frac{\mu}{\rho}_{Cl}^2 + 2 \frac{\mu}{\rho}_{Ml} \frac{\mu}{\rho}_{Cl} \frac{\mu}{\rho}_{Mh} \frac{\mu}{\rho}_{Ch} + \frac{\mu}{\rho}_{Mh}^2 \frac{\mu}{\rho}_{Ch}^2)\end{array}}$$

$$\rho_M t_M = \frac{\frac{\mu}{\rho}_{Mh} \frac{\mu}{\rho}_{Cl}^2 r_h + \frac{\mu}{\rho}_{Ml} \frac{\mu}{\rho}_{Ch}^2 r_l - \frac{\mu}{\rho}_{Ml} \frac{\mu}{\rho}_{Cl} \frac{\mu}{\rho}_{Ch} r_h - \frac{\mu}{\rho}_{Mh} \frac{\mu}{\rho}_{Cl} \frac{\mu}{\rho}_{Ch} r_l}{\frac{\mu}{\rho}_{Mh}^2 \frac{\mu}{\rho}_{Cl}^2 + \frac{\mu}{\rho}_{Ml}^2 \frac{\mu}{\rho}_{Ch}^2 - 2 \frac{\mu}{\rho}_{Ml} \frac{\mu}{\rho}_{Cl} \frac{\mu}{\rho}_{Mh} \frac{\mu}{\rho}_{Ch}}$$

$$\rho_M t_M = \frac{(\frac{\mu}{\rho}_{Ml} \frac{\mu}{\rho}_{Ch} - \frac{\mu}{\rho}_{Mh} \frac{\mu}{\rho}_{Cl}) \frac{\mu}{\rho}_{Ch} r_l - (\frac{\mu}{\rho}_{Ml} \frac{\mu}{\rho}_{Ch} - \frac{\mu}{\rho}_{Mh} \frac{\mu}{\rho}_{Cl}) \frac{\mu}{\rho}_{Cl} r_h}{(\frac{\mu}{\rho}_{Ml} \frac{\mu}{\rho}_{Ch} - \frac{\mu}{\rho}_{Mh} \frac{\mu}{\rho}_{Cl})^2}$$

$$\rho_M t_M = \frac{\frac{\mu}{\rho}_{Ch} r_l - \frac{\mu}{\rho}_{Cl} r_h}{\frac{\mu}{\rho}_{Ml} \frac{\mu}{\rho}_{Ch} - \frac{\mu}{\rho}_{Mh} \frac{\mu}{\rho}_{Cl}} \tag{5.3}$$

$$\rho_C t_C = \frac{\sum_i \frac{\mu}{\rho}_{Mi}^2 \sum_i \left(\frac{\mu}{\rho}_{Ci} r_i\right) - \sum_i \left(\frac{\mu}{\rho}_{Ci} \frac{\mu}{\rho}_{Mi}\right) \sum_i \left(\frac{\mu}{\rho}_{Mi} r_i\right)}{\sum_i \frac{\mu}{\rho}_{Ci}^2 \sum_i \frac{\mu}{\rho}_{Mi}^2 - \left[\sum_i \left(\frac{\mu}{\rho}_{Ci} \frac{\mu}{\rho}_{Mi}\right)\right]^2} \tag{5.20}$$

$$\rho_C t_C = \frac{(\frac{\mu}{\rho}_{Ml}^2 + \frac{\mu}{\rho}_{Mh}^2)(\frac{\mu}{\rho}_{Cl} r_l + \frac{\mu}{\rho}_{Ch} r_h) - (\frac{\mu}{\rho}_{Ml} \frac{\mu}{\rho}_{Cl} + \frac{\mu}{\rho}_{Mh} \frac{\mu}{\rho}_{Ch})(\frac{\mu}{\rho}_{Ml} r_l + \frac{\mu}{\rho}_{Mh} r_h)}{(\frac{\mu}{\rho}_{Ml}^2 + \frac{\mu}{\rho}_{Mh}^2)(\frac{\mu}{\rho}_{Cl}^2 + \frac{\mu}{\rho}_{Ch}^2) - (\frac{\mu}{\rho}_{Ml} \frac{\mu}{\rho}_{Cl} + \frac{\mu}{\rho}_{Mh} \frac{\mu}{\rho}_{Ch})^2}$$

$$\rho_C t_C = \frac{\begin{array}{c}(\frac{\mu}{\rho}_{Ml}^2 \frac{\mu}{\rho}_{Cl} r_l + \frac{\mu}{\rho}_{Mh}^2 \frac{\mu}{\rho}_{Cl} r_l + \frac{\mu}{\rho}_{Ml}^2 \frac{\mu}{\rho}_{Ch} r_h + \frac{\mu}{\rho}_{Mh}^2 \frac{\mu}{\rho}_{Ch} r_h) - \\ (\frac{\mu}{\rho}_{Ml}^2 \frac{\mu}{\rho}_{Cl} r_l + \frac{\mu}{\rho}_{Ml} \frac{\mu}{\rho}_{Mh} \frac{\mu}{\rho}_{Ch} r_l + \frac{\mu}{\rho}_{Ml} \frac{\mu}{\rho}_{Mh} \frac{\mu}{\rho}_{Cl} r_h + \frac{\mu}{\rho}_{Mh}^2 \frac{\mu}{\rho}_{Ch} r_h)\end{array}}{\begin{array}{c}(\frac{\mu}{\rho}_{Ml}^2 \frac{\mu}{\rho}_{Cl}^2 + \frac{\mu}{\rho}_{Mh}^2 \frac{\mu}{\rho}_{Cl}^2 + \frac{\mu}{\rho}_{Ml}^2 \frac{\mu}{\rho}_{Ch}^2 + \frac{\mu}{\rho}_{Mh}^2 \frac{\mu}{\rho}_{Ch}^2) - \\ (\frac{\mu}{\rho}_{Ml}^2 \frac{\mu}{\rho}_{Cl}^2 + 2\frac{\mu}{\rho}_{Ml} \frac{\mu}{\rho}_{Cl} \frac{\mu}{\rho}_{Mh} \frac{\mu}{\rho}_{Ch} + \frac{\mu}{\rho}_{Mh}^2 \frac{\mu}{\rho}_{Ch}^2)\end{array}}$$

$$\rho_C t_C = \frac{\frac{\mu}{\rho}_{Mh}^2 \frac{\mu}{\rho}_{Cl} r_l + \frac{\mu}{\rho}_{Ml}^2 \frac{\mu}{\rho}_{Ch} r_h - \frac{\mu}{\rho}_{Ml} \frac{\mu}{\rho}_{Mh} \frac{\mu}{\rho}_{Ch} r_l - \frac{\mu}{\rho}_{Ml} \frac{\mu}{\rho}_{Mh} \frac{\mu}{\rho}_{Cl} r_h}{\frac{\mu}{\rho}_{Mh}^2 \frac{\mu}{\rho}_{Cl}^2 + \frac{\mu}{\rho}_{Ml}^2 \frac{\mu}{\rho}_{Ch}^2 - 2\frac{\mu}{\rho}_{Ml} \frac{\mu}{\rho}_{Cl} \frac{\mu}{\rho}_{Mh} \frac{\mu}{\rho}_{Ch}}$$

$$\rho_C t_C = \frac{(\frac{\mu}{\rho}_{Mh} \frac{\mu}{\rho}_{Cl} - \frac{\mu}{\rho}_{Ml} \frac{\mu}{\rho}_{Ch}) \frac{\mu}{\rho}_{Mh} r_l + (\frac{\mu}{\rho}_{Ml} \frac{\mu}{\rho}_{Ch} - \frac{\mu}{\rho}_{Mh} \frac{\mu}{\rho}_{Cl}) \frac{\mu}{\rho}_{Ml} r_h}{(\frac{\mu}{\rho}_{Ml} \frac{\mu}{\rho}_{Ch} - \frac{\mu}{\rho}_{Mh} \frac{\mu}{\rho}_{Cl})^2}$$

$$\rho_C t_C = \frac{\frac{\mu}{\rho}_{Ml} r_h - \frac{\mu}{\rho}_{Mh} r_l}{\frac{\mu}{\rho}_{Ml} \frac{\mu}{\rho}_{Ch} - \frac{\mu}{\rho}_{Mh} \frac{\mu}{\rho}_{Cl}} \tag{5.3}$$

Appendix C SNR derivation for Two-Component NESI

Starting from the projected density equations for the two-component NESI,

$$\rho_C t_C = \frac{1}{n}\frac{\frac{\mu}{\rho}_{MM}\sum_i\left(\frac{\mu}{\rho}_{Ci} r_i\right) - \frac{\mu}{\rho}_{CM}\sum_i\left(\frac{\mu}{\rho}_{Mi} r_i\right)}{\frac{\mu}{\rho}_{CC}\frac{\mu}{\rho}_{MM} - \frac{\mu}{\rho}_{CM}^2} \qquad (1 \le i \le n)$$

$$\rho_M t_M = \frac{1}{n}\frac{\frac{\mu}{\rho}_{CC}\sum_i\left(\frac{\mu}{\rho}_{Mi} r_i\right) - \frac{\mu}{\rho}_{CM}\sum_i\left(\frac{\mu}{\rho}_{Ci} r_i\right)}{\frac{\mu}{\rho}_{CC}\frac{\mu}{\rho}_{MM} - \frac{\mu}{\rho}_{CM}^2} \qquad (5.22)$$

$$\text{where} \quad r_i = -\ln\left(\frac{N_i}{N_{0i}}\right) = \frac{\mu}{\rho}_{Mi}\rho_M t_M + \frac{\mu}{\rho}_{Ci}\rho_C t_C \qquad (1 \le i \le n) \qquad (5.19)$$

applying propagation of error on equation (5.22) assumes independent measurements of both the incident beam at each energy N_{0i} and the transmitted beam at each energy N_i,

$$\sigma^2_{\rho_C t_C} = \sum_i\left[\left(\frac{\partial\rho_C t_C}{\partial N_i}\right)^2(\delta N_i)^2 + \left(\frac{\partial\rho_C t_C}{\partial N_{0i}}\right)^2(\delta N_{0i})^2\right]$$

$$\sigma^2_{\rho_M t_M} = \sum_i\left[\left(\frac{\partial\rho_M t_M}{\partial N_i}\right)^2(\delta N_i)^2 + \left(\frac{\partial\rho_M t_M}{\partial N_{0i}}\right)^2(\delta N_{0i})^2\right] \qquad (C.1)$$

With Poisson statistics, the variance in the photon counts,

$$(\delta N_i)^2 = N_i \qquad (\delta N_{0i})^2 = N_{0i}$$

The included partial derivatives are,

$$\frac{\partial\rho_C t_C}{\partial N_i} = \frac{\partial\rho_C t_C}{\partial r_i}\frac{\partial r_i}{\partial N_i} \qquad \frac{\partial\rho_C t_C}{\partial N_{0i}} = \frac{\partial\rho_C t_C}{\partial r_i}\frac{\partial r_i}{\partial N_{0i}}$$

$$\frac{\partial\rho_M t_M}{\partial N_i} = \frac{\partial\rho_M t_M}{\partial r_i}\frac{\partial r_i}{\partial N_i} \qquad \frac{\partial\rho_M t_M}{\partial N_{0i}} = \frac{\partial\rho_M t_M}{\partial r_i}\frac{\partial r_i}{\partial N_{0i}}$$

$$\frac{\partial r_i}{\partial N_i} = -\frac{\partial}{\partial N_i}\left(\ln\frac{N_i}{N_{0i}}\right) = -\frac{1}{N_i} \qquad \frac{\partial r_i}{\partial N_{0i}} = -\frac{\partial}{\partial N_{0i}}\left(\ln\frac{N_i}{N_{0i}}\right) = \frac{1}{N_{0i}}$$

$$\frac{\partial \rho_C t_C}{\partial r_i} = \frac{1}{n}\frac{\partial}{\partial r_i}\left[\frac{\frac{\mu}{\rho}_{MM}\sum_i\left(\frac{\mu}{\rho}_{Ci} r_i\right) - \frac{\mu}{\rho}_{CM}\sum_i\left(\frac{\mu}{\rho}_{Mi} r_i\right)}{\frac{\mu}{\rho}_{CC}\frac{\mu}{\rho}_{MM} - \frac{\mu}{\rho}_{CM}^2}\right] = \frac{1}{n}\frac{\frac{\mu}{\rho}_{MM}\frac{\mu}{\rho}_{Ci} - \frac{\mu}{\rho}_{CM}\frac{\mu}{\rho}_{Mi}}{\frac{\mu}{\rho}_{CC}\frac{\mu}{\rho}_{MM} - \frac{\mu}{\rho}_{CM}^2}$$

$$\frac{\partial \rho_M t_M}{\partial r_i} = \frac{1}{n}\frac{\partial}{\partial r_i}\left[\frac{\frac{\mu}{\rho}_{CC}\sum_i\left(\frac{\mu}{\rho}_{Mi} r_i\right) - \frac{\mu}{\rho}_{CM}\sum_i\left(\frac{\mu}{\rho}_{Ci} r_i\right)}{\frac{\mu}{\rho}_{CC}\frac{\mu}{\rho}_{MM} - \frac{\mu}{\rho}_{CM}^2}\right] = \frac{1}{n}\frac{\frac{\mu}{\rho}_{CC}\frac{\mu}{\rho}_{Mi} - \frac{\mu}{\rho}_{CM}\frac{\mu}{\rho}_{Ci}}{\frac{\mu}{\rho}_{CC}\frac{\mu}{\rho}_{MM} - \frac{\mu}{\rho}_{CM}^2}$$

Combining these derived items the image noise from equation (C.1) could be determined.

$$\sigma^2_{\rho_C t_C} = \sum_i\left[\left(\frac{\partial \rho_C t_C}{\partial N_i}\right)^2(\delta N_i)^2 + \left(\frac{\partial \rho_C t_C}{\partial N_{0i}}\right)^2(\delta N_{0i})^2\right]$$

$$= \frac{1}{n^2}\sum_i\left[\left(\frac{\frac{\mu}{\rho}_{MM}\frac{\mu}{\rho}_{Ci} - \frac{\mu}{\rho}_{CM}\frac{\mu}{\rho}_{Mi}}{\frac{\mu}{\rho}_{CC}\frac{\mu}{\rho}_{MM} - \frac{\mu}{\rho}_{CM}^2}\right)^2\left(\left(-\frac{1}{N_i}\right)^2 N_i + \left(\frac{1}{N_{0i}}\right)^2 N_{0i}\right)\right]$$

$$\sigma^2_{\rho_C t_C} = \frac{1}{n^2\left(\frac{\mu}{\rho}_{CC}\frac{\mu}{\rho}_{MM} - \frac{\mu}{\rho}_{CM}^2\right)^2}\sum_i\left[\left(\frac{\mu}{\rho}_{MM}\frac{\mu}{\rho}_{Ci} - \frac{\mu}{\rho}_{CM}\frac{\mu}{\rho}_{Mi}\right)^2\left(\frac{1}{N_i} + \frac{1}{N_{0i}}\right)\right] \tag{C.2}$$

The SNR for the projected contrast image will be,

$$SNR_C = \frac{\rho_C t_C}{\sigma_{\rho_C t_C}} = \frac{n\left(\frac{\mu}{\rho}_{CC}\frac{\mu}{\rho}_{MM} - \frac{\mu}{\rho}_{CM}^2\right)}{\sqrt{\sum_i\left[\left(\frac{\mu}{\rho}_{MM}\frac{\mu}{\rho}_{Ci} - \frac{\mu}{\rho}_{CM}\frac{\mu}{\rho}_{Mi}\right)^2\left(\frac{1}{N_i} + \frac{1}{N_{0i}}\right)\right]}}\rho_C t_C \tag{5.23}$$

Similarly, image noise for the matrix image is determined from equation (C.1).

$$\sigma^2_{\rho_M t_M} = \sum_i\left[\left(\frac{\partial \rho_M t_M}{\partial N_i}\right)^2(\delta N_i)^2 + \left(\frac{\partial \rho_M t_M}{\partial N_{0i}}\right)^2(\delta N_{0i})^2\right]$$

$$= \frac{1}{n^2}\sum_i\left[\left(\frac{\frac{\mu}{\rho}_{CC}\frac{\mu}{\rho}_{Mi} - \frac{\mu}{\rho}_{CM}\frac{\mu}{\rho}_{Ci}}{\frac{\mu}{\rho}_{CC}\frac{\mu}{\rho}_{MM} - \frac{\mu}{\rho}_{CM}^2}\right)^2\left(\left(-\frac{1}{N_i}\right)^2 N_i + \left(\frac{1}{N_{0i}}\right)^2 N_{0i}\right)\right]$$

$$\sigma^2_{\rho_M t_M} = \frac{1}{n^2\left(\frac{\mu}{\rho}_{CC}\frac{\mu}{\rho}_{MM} - \frac{\mu}{\rho}_{CM}^2\right)^2}\sum_i\left[\left(\frac{\mu}{\rho}_{CC}\frac{\mu}{\rho}_{Mi} - \frac{\mu}{\rho}_{CM}\frac{\mu}{\rho}_{Ci}\right)^2\left(\frac{1}{N_i} + \frac{1}{N_{0i}}\right)\right] \tag{C.3}$$

The SNR for the projected matrix image will be,

$$SNR_M = \frac{\rho_M t_M}{\sigma_{\rho_M t_M}} = \frac{n\left(\frac{\mu}{\rho}_{CC}\frac{\mu}{\rho}_{MM} - \frac{\mu}{\rho}^2_{CM}\right)}{\sqrt{\sum_i \left[\left(\frac{\mu}{\rho}_{CC}\frac{\mu}{\rho}_{Mi} - \frac{\mu}{\rho}_{CM}\frac{\mu}{\rho}_{Ci}\right)^2\left(\frac{1}{N_i}+\frac{1}{N_{0i}}\right)\right]}}\rho_M t_M \tag{5.23}$$

To simplify the SNR equation (5.23), equal incident flux N_{0i} and equal transmitted flux N_i for all the energy *i* at each pixel are assumed. The noise equation (C.2) is simplified as,

$$\begin{aligned}
\sigma^2_{\rho_C t_C} &\approx \frac{1}{n^2(\frac{\mu}{\rho}_{CC}\frac{\mu}{\rho}_{MM} - \frac{\mu}{\rho}^2_{CM})^2}\left(\frac{1}{N}+\frac{1}{N_0}\right)\sum_i\left(\frac{\mu}{\rho}_{MM}\frac{\mu}{\rho}_{Ci} - \frac{\mu}{\rho}_{CM}\frac{\mu}{\rho}_{Mi}\right)^2 \\
&= \frac{1}{n^2(\frac{\mu}{\rho}_{CC}\frac{\mu}{\rho}_{MM} - \frac{\mu}{\rho}^2_{CM})^2}\left(\frac{1}{N}+\frac{1}{N_0}\right)\sum_i\left(\frac{\mu}{\rho}^2_{MM}\frac{\mu}{\rho}^2_{Ci} + \frac{\mu}{\rho}^2_{CM}\frac{\mu}{\rho}^2_{Mi} - 2\frac{\mu}{\rho}_{MM}\frac{\mu}{\rho}_{CM}\frac{\mu}{\rho}_{Ci}\frac{\mu}{\rho}_{Mi}\right) \\
&= \frac{1}{n^2(\frac{\mu}{\rho}_{CC}\frac{\mu}{\rho}_{MM} - \frac{\mu}{\rho}^2_{CM})^2}\left(\frac{1}{N}+\frac{1}{N_0}\right)\left[\frac{\mu}{\rho}^2_{MM}\sum_i\frac{\mu}{\rho}^2_{Ci} + \frac{\mu}{\rho}^2_{CM}\sum_i\frac{\mu}{\rho}^2_{Mi} - 2\frac{\mu}{\rho}_{MM}\frac{\mu}{\rho}_{CM}\sum_i\left(\frac{\mu}{\rho}_{Ci}\frac{\mu}{\rho}_{Mi}\right)\right] \\
&= \frac{1}{n^2(\frac{\mu}{\rho}_{CC}\frac{\mu}{\rho}_{MM} - \frac{\mu}{\rho}^2_{CM})^2}\left(\frac{1}{N}+\frac{1}{N_0}\right)\left(\frac{\mu}{\rho}^2_{MM}\,n\frac{\mu}{\rho}_{CC} + \frac{\mu}{\rho}^2_{CM}\,n\frac{\mu}{\rho}_{MM} - 2\frac{\mu}{\rho}_{MM}\frac{\mu}{\rho}_{CM}\,n\frac{\mu}{\rho}_{CM}\right) \\
&= \frac{1}{n(\frac{\mu}{\rho}_{CC}\frac{\mu}{\rho}_{MM} - \frac{\mu}{\rho}^2_{CM})^2}\left(\frac{1}{N}+\frac{1}{N_0}\right)\frac{\mu}{\rho}_{MM}\left(\frac{\mu}{\rho}_{MM}\frac{\mu}{\rho}_{CC} + \frac{\mu}{\rho}^2_{CM} - 2\frac{\mu}{\rho}^2_{CM}\right) \\
&= \frac{1}{n(\frac{\mu}{\rho}_{CC}\frac{\mu}{\rho}_{MM} - \frac{\mu}{\rho}^2_{CM})^2}\left(\frac{1}{N}+\frac{1}{N_0}\right)\frac{\mu}{\rho}_{MM}\left(\frac{\mu}{\rho}_{MM}\frac{\mu}{\rho}_{CC} - \frac{\mu}{\rho}^2_{CM}\right) \\
\sigma^2_{\rho_C t_C} &\approx \frac{1}{n}\left(\frac{1}{N}+\frac{1}{N_0}\right)\frac{\frac{\mu}{\rho}_{MM}}{\frac{\mu}{\rho}_{CC}\frac{\mu}{\rho}_{MM} - \frac{\mu}{\rho}^2_{CM}}
\end{aligned} \tag{C.4}$$

The simplified SNR for the projected contrast image will be,

$$SNR^2_C = \frac{(\rho_C t_C)^2}{\sigma^2_{\rho_C t_C}} \approx \frac{(\rho_C t_C)^2}{\frac{1}{n}\left(\frac{1}{N}+\frac{1}{N_0}\right)}\frac{\frac{\mu}{\rho}_{CC}\frac{\mu}{\rho}_{MM} - \frac{\mu}{\rho}^2_{CM}}{\frac{\mu}{\rho}_{MM}} = n\frac{NN_0}{N+N_0}\frac{\mu}{\rho}_{CC}(\rho_C t_C)^2\frac{\frac{\mu}{\rho}_{CC}\frac{\mu}{\rho}_{MM} - \frac{\mu}{\rho}^2_{CM}}{\frac{\mu}{\rho}_{MM}\frac{\mu}{\rho}_{CC}}$$

Assuming dilute contrast material in the object $N \approx N_0 e^{-\mu t}$ where $\mu = \frac{\mu}{\rho}_M \rho_M$ and $t = t_M + t_C$

$$SNR_C^2 \approx \frac{nN_0}{1+e^{\mu t}}\left(1-\frac{\frac{\mu}{\rho}_{CM}^{2}}{\frac{\mu}{\rho}_{MM}\ \frac{\mu}{\rho}_{CC}}\right)\frac{\mu}{\rho}_{CC}\left(\rho_C t_C\right)^2 \tag{C.5}$$

Similarly, the simplified SNR for the matrix material is,

$$SNR_M^2 \approx \frac{nN_0}{1+e^{\mu t}}\left(1-\frac{\frac{\mu}{\rho}_{CM}^{2}}{\frac{\mu}{\rho}_{MM}\ \frac{\mu}{\rho}_{CC}}\right)\frac{\mu}{\rho}_{MM}\left(\rho_M t_M\right)^2 \tag{C.6}$$

Then the equations (C.5) and (C.6) give out the simplified SNR equation (5.24) in chapter 5.3.2.1. As expected, both SNR values are dependent upon the square root of the incident photon count (nN_0) and amount of material present. Also both values have a dimensionless common term in the brackets as well as having a sum over the squares of the mass attenuation coefficients over the photon energy range.

Appendix D Left Inverse Derivation for Three-Component NESI

For a three-component NESI system, a contrast material (*C*), soft tissue (*T*) and bone material (*B*), the negative logarithm of the normalized signals could be arranged in a matrix form as,

$$\begin{bmatrix} r_1 \\ \vdots \\ r_n \end{bmatrix} = \begin{bmatrix} -\ln\left(\frac{N_1}{N_{01}}\right) \\ \vdots \\ -\ln\left(\frac{N_n}{N_{0n}}\right) \end{bmatrix} = \begin{bmatrix} \frac{\mu}{\rho}_{T1}\rho_T t_T + \frac{\mu}{\rho}_{B1}\rho_B t_B + \frac{\mu}{\rho}_{C1}\rho_C t_C \\ \vdots \\ \frac{\mu}{\rho}_{Tn}\rho_T t_T + \frac{\mu}{\rho}_{Bn}\rho_B t_B + \frac{\mu}{\rho}_{Cn}\rho_C t_C \end{bmatrix} = \begin{bmatrix} \frac{\mu}{\rho}_{T1} & \frac{\mu}{\rho}_{B1} & \frac{\mu}{\rho}_{C1} \\ \vdots & \vdots & \vdots \\ \frac{\mu}{\rho}_{Tn} & \frac{\mu}{\rho}_{Bn} & \frac{\mu}{\rho}_{Cn} \end{bmatrix} \begin{bmatrix} \rho_T t_T \\ \rho_B t_B \\ \rho_C t_C \end{bmatrix} \quad \text{(D.1)}$$

Multiplying the left inverse (a pseudoinverse [Str09]) of the $n \times 3$ matrix of the $\frac{\mu}{\rho}$, the projected densities are derived as,

$$\begin{bmatrix} \rho_T t_T \\ \rho_B t_B \\ \rho_C t_C \end{bmatrix} = \begin{bmatrix} \frac{\mu}{\rho}_{T1} & \frac{\mu}{\rho}_{B1} & \frac{\mu}{\rho}_{C1} \\ \vdots & \vdots & \vdots \\ \frac{\mu}{\rho}_{Tn} & \frac{\mu}{\rho}_{Bn} & \frac{\mu}{\rho}_{Cn} \end{bmatrix}_{left}^{-1} \begin{bmatrix} r_1 \\ \vdots \\ r_n \end{bmatrix}$$

$$= \left(\begin{bmatrix} \frac{\mu}{\rho}_{T1} & \frac{\mu}{\rho}_{B1} & \frac{\mu}{\rho}_{C1} \\ \vdots & \vdots & \vdots \\ \frac{\mu}{\rho}_{Tn} & \frac{\mu}{\rho}_{Bn} & \frac{\mu}{\rho}_{Cn} \end{bmatrix}^T \begin{bmatrix} \frac{\mu}{\rho}_{T1} & \frac{\mu}{\rho}_{B1} & \frac{\mu}{\rho}_{C1} \\ \vdots & \vdots & \vdots \\ \frac{\mu}{\rho}_{Tn} & \frac{\mu}{\rho}_{Bn} & \frac{\mu}{\rho}_{Cn} \end{bmatrix} \right)^{-1} \begin{bmatrix} \frac{\mu}{\rho}_{T1} & \frac{\mu}{\rho}_{B1} & \frac{\mu}{\rho}_{C1} \\ \vdots & \vdots & \vdots \\ \frac{\mu}{\rho}_{Tn} & \frac{\mu}{\rho}_{Bn} & \frac{\mu}{\rho}_{Cn} \end{bmatrix}^T \begin{bmatrix} r_1 \\ \vdots \\ r_n \end{bmatrix}$$

$$= \left(\begin{bmatrix} \frac{\mu}{\rho}_{T1} & \cdots & \frac{\mu}{\rho}_{Tn} \\ \frac{\mu}{\rho}_{B1} & \cdots & \frac{\mu}{\rho}_{Bn} \\ \frac{\mu}{\rho}_{C1} & \cdots & \frac{\mu}{\rho}_{Cn} \end{bmatrix} \begin{bmatrix} \frac{\mu}{\rho}_{T1} & \frac{\mu}{\rho}_{B1} & \frac{\mu}{\rho}_{C1} \\ \vdots & \vdots & \vdots \\ \frac{\mu}{\rho}_{Tn} & \frac{\mu}{\rho}_{Bn} & \frac{\mu}{\rho}_{Cn} \end{bmatrix} \right)^{-1} \begin{bmatrix} \frac{\mu}{\rho}_{T1} & \cdots & \frac{\mu}{\rho}_{Tn} \\ \frac{\mu}{\rho}_{B1} & \cdots & \frac{\mu}{\rho}_{Bn} \\ \frac{\mu}{\rho}_{C1} & \cdots & \frac{\mu}{\rho}_{Cn} \end{bmatrix} \begin{bmatrix} r_1 \\ \vdots \\ r_n \end{bmatrix}$$

$$= \begin{bmatrix} \sum_i \frac{\mu}{\rho}_{Ti}^2 & \sum_i \left(\frac{\mu}{\rho}_{Ti}\frac{\mu}{\rho}_{Bi}\right) & \sum_i \left(\frac{\mu}{\rho}_{Ti}\frac{\mu}{\rho}_{Ci}\right) \\ \sum_i \left(\frac{\mu}{\rho}_{Ti}\frac{\mu}{\rho}_{Bi}\right) & \sum_i \frac{\mu}{\rho}_{Bi}^2 & \sum_i \left(\frac{\mu}{\rho}_{Bi}\frac{\mu}{\rho}_{Ci}\right) \\ \sum_i \left(\frac{\mu}{\rho}_{Ti}\frac{\mu}{\rho}_{Ci}\right) & \sum_i \left(\frac{\mu}{\rho}_{Bi}\frac{\mu}{\rho}_{Ci}\right) & \sum_i \frac{\mu}{\rho}_{Ci}^2 \end{bmatrix}^{-1} \begin{bmatrix} \sum_i \left(\frac{\mu}{\rho}_{Ti} r_i\right) \\ \sum_i \left(\frac{\mu}{\rho}_{Bi} r_i\right) \\ \sum_i \left(\frac{\mu}{\rho}_{Ci} r_i\right) \end{bmatrix}$$

The sums of the $\frac{\mu}{\rho}$ products can be replaced by their averages

$$\begin{aligned}
&\frac{\mu}{\rho}_{TT} \equiv \frac{1}{n}\sum_i \frac{\mu}{\rho}_{Ti}^2 && \frac{\mu}{\rho}_{BB} \equiv \frac{1}{n}\sum_i \frac{\mu}{\rho}_{Bi}^2 && \frac{\mu}{\rho}_{CC} \equiv \frac{1}{n}\sum_i \frac{\mu}{\rho}_{Ci}^2 \\
&\frac{\mu}{\rho}_{TB} \equiv \frac{1}{n}\sum_i \left(\frac{\mu}{\rho}_{Ti}\ \frac{\mu}{\rho}_{Bi}\right) && \frac{\mu}{\rho}_{TC} \equiv \frac{1}{n}\sum_i \left(\frac{\mu}{\rho}_{Ti}\ \frac{\mu}{\rho}_{Ci}\right) && \frac{\mu}{\rho}_{BC} \equiv \frac{1}{n}\sum_i \left(\frac{\mu}{\rho}_{Bi}\ \frac{\mu}{\rho}_{Ci}\right)
\end{aligned} \tag{5.30}$$

$$\begin{bmatrix} \rho_T t_T \\ \rho_B t_B \\ \rho_C t_C \end{bmatrix} = \begin{bmatrix} n\frac{\mu}{\rho}_{TT} & n\frac{\mu}{\rho}_{TB} & n\frac{\mu}{\rho}_{TC} \\ n\frac{\mu}{\rho}_{TB} & n\frac{\mu}{\rho}_{BB} & n\frac{\mu}{\rho}_{BC} \\ n\frac{\mu}{\rho}_{TC} & n\frac{\mu}{\rho}_{BC} & n\frac{\mu}{\rho}_{CC} \end{bmatrix}^{-1} \begin{bmatrix} \sum_i \left(\frac{\mu}{\rho}_{Ti} r_i\right) \\ \sum_i \left(\frac{\mu}{\rho}_{Bi} r_i\right) \\ \sum_i \left(\frac{\mu}{\rho}_{Ci} r_i\right) \end{bmatrix}$$

$$\begin{bmatrix} \rho_T t_T \\ \rho_B t_B \\ \rho_C t_C \end{bmatrix} = \frac{\frac{1}{n}\begin{bmatrix} \frac{\mu}{\rho}_{BB}\frac{\mu}{\rho}_{CC} - \frac{\mu}{\rho}_{BC}^2 & \frac{\mu}{\rho}_{BC}\frac{\mu}{\rho}_{TC} - \frac{\mu}{\rho}_{TB}\frac{\mu}{\rho}_{CC} & \frac{\mu}{\rho}_{TB}\frac{\mu}{\rho}_{BC} - \frac{\mu}{\rho}_{TC}\frac{\mu}{\rho}_{BB} \\ \frac{\mu}{\rho}_{BC}\frac{\mu}{\rho}_{TC} - \frac{\mu}{\rho}_{TB}\frac{\mu}{\rho}_{CC} & \frac{\mu}{\rho}_{TT}\frac{\mu}{\rho}_{CC} - \frac{\mu}{\rho}_{TC}^2 & \frac{\mu}{\rho}_{TB}\frac{\mu}{\rho}_{TC} - \frac{\mu}{\rho}_{TT}\frac{\mu}{\rho}_{BC} \\ \frac{\mu}{\rho}_{TB}\frac{\mu}{\rho}_{BC} - \frac{\mu}{\rho}_{TC}\frac{\mu}{\rho}_{BB} & \frac{\mu}{\rho}_{TB}\frac{\mu}{\rho}_{TC} - \frac{\mu}{\rho}_{TT}\frac{\mu}{\rho}_{BC} & \frac{\mu}{\rho}_{TT}\frac{\mu}{\rho}_{BB} - \frac{\mu}{\rho}_{TB}^2 \end{bmatrix} \begin{bmatrix} \sum_i \left(\frac{\mu}{\rho}_{Ti} r_i\right) \\ \sum_i \left(\frac{\mu}{\rho}_{Bi} r_i\right) \\ \sum_i \left(\frac{\mu}{\rho}_{Ci} r_i\right) \end{bmatrix}}{\frac{\mu}{\rho}_{TT}\left(\frac{\mu}{\rho}_{BB}\frac{\mu}{\rho}_{CC} - \frac{\mu}{\rho}_{BC}^2\right) + \frac{\mu}{\rho}_{TB}\left(\frac{\mu}{\rho}_{BC}\frac{\mu}{\rho}_{TC} - \frac{\mu}{\rho}_{TB}\frac{\mu}{\rho}_{CC}\right) + \frac{\mu}{\rho}_{TC}\left(\frac{\mu}{\rho}_{TB}\frac{\mu}{\rho}_{BC} - \frac{\mu}{\rho}_{TC}\frac{\mu}{\rho}_{BB}\right)} \tag{D.2}$$

$$\begin{bmatrix} \rho_T t_T \\ \rho_B t_B \\ \rho_C t_C \end{bmatrix} = \frac{1}{nD_{33}} \begin{bmatrix} R_{T1} & R_{T2} & R_{T3} \\ R_{B1} & R_{B2} & R_{B3} \\ R_{C1} & R_{C2} & R_{C3} \end{bmatrix} \begin{bmatrix} \sum_i \left(\frac{\mu}{\rho}_{Ti} r_i\right) \\ \sum_i \left(\frac{\mu}{\rho}_{Bi} r_i\right) \\ \sum_i \left(\frac{\mu}{\rho}_{Ci} r_i\right) \end{bmatrix} \tag{D.3}$$

Then the projected density equations (5.29) and (5.31) in chapter 5.3.2.2 are obtained from the above equation (D.2) and (D.3), respectively.

Appendix E Three-Energy KES from Three-Component NESI

In theory, three-energy KES equation (5.11) should be a special case of the three-component NESI equation (5.29). For a consistency check, setting n = 3 and the index *i* to three values, subscript 1, 2 and 3 for three energies, the equation (5.29) in chapter 5.3.2.2

$$\rho_C t_C = \frac{1}{n}\frac{\left(\frac{\mu}{\rho}_{TB}\frac{\mu}{\rho}_{BC} - \frac{\mu}{\rho}_{TC}\frac{\mu}{\rho}_{BB}\right)\sum_i\left(\frac{\mu}{\rho}_{Ti} r_i\right) + \left(\frac{\mu}{\rho}_{TB}\frac{\mu}{\rho}_{TC} - \frac{\mu}{\rho}_{TT}\frac{\mu}{\rho}_{BC}\right)\sum_i\left(\frac{\mu}{\rho}_{Bi} r_i\right) + \left(\frac{\mu}{\rho}_{TT}\frac{\mu}{\rho}_{BB} - \frac{\mu}{\rho}^2_{TB}\right)\sum_i\left(\frac{\mu}{\rho}_{Ci} r_i\right)}{\frac{\mu}{\rho}_{TT}\left(\frac{\mu}{\rho}_{BB}\frac{\mu}{\rho}_{CC} - \frac{\mu}{\rho}^2_{BC}\right) + \frac{\mu}{\rho}_{TB}\left(\frac{\mu}{\rho}_{BC}\frac{\mu}{\rho}_{TC} - \frac{\mu}{\rho}_{TB}\frac{\mu}{\rho}_{CC}\right) + \frac{\mu}{\rho}_{TC}\left(\frac{\mu}{\rho}_{TB}\frac{\mu}{\rho}_{BC} - \frac{\mu}{\rho}_{TC}\frac{\mu}{\rho}_{BB}\right)}$$

could be expressed as

$$\rho_C t_C = \frac{1}{3}\frac{Nume}{Deno} \tag{E.1}$$

The denominator is derived as,

$$\begin{aligned}
Deno &= \frac{\mu}{\rho}_{TT}\left(\frac{\mu}{\rho}_{BB}\frac{\mu}{\rho}_{CC} - \frac{\mu}{\rho}^2_{BC}\right) + \frac{\mu}{\rho}_{TB}\left(\frac{\mu}{\rho}_{BC}\frac{\mu}{\rho}_{TC} - \frac{\mu}{\rho}_{TB}\frac{\mu}{\rho}_{CC}\right) + \frac{\mu}{\rho}_{TC}\left(\frac{\mu}{\rho}_{TB}\frac{\mu}{\rho}_{BC} - \frac{\mu}{\rho}_{TC}\frac{\mu}{\rho}_{BB}\right) \\
&= \left(\frac{\mu}{\rho}_{TT}\frac{\mu}{\rho}_{BB}\frac{\mu}{\rho}_{CC} - \frac{\mu}{\rho}_{TT}\frac{\mu}{\rho}^2_{BC}\right) + \left(\frac{\mu}{\rho}_{BC}\frac{\mu}{\rho}_{TC}\frac{\mu}{\rho}_{TB} - \frac{\mu}{\rho}^2_{TB}\frac{\mu}{\rho}_{CC}\right) + \left(\frac{\mu}{\rho}_{TC}\frac{\mu}{\rho}_{TB}\frac{\mu}{\rho}_{BC} - \frac{\mu}{\rho}^2_{TC}\frac{\mu}{\rho}_{BB}\right) \\
&= \frac{\mu}{\rho}_{TT}\frac{\mu}{\rho}_{BB}\frac{\mu}{\rho}_{CC} - \frac{\mu}{\rho}_{TT}\frac{\mu}{\rho}^2_{BC} - \frac{\mu}{\rho}_{BB}\frac{\mu}{\rho}^2_{TC} - \frac{\mu}{\rho}_{CC}\frac{\mu}{\rho}^2_{TB} + 2\frac{\mu}{\rho}_{BC}\frac{\mu}{\rho}_{TC}\frac{\mu}{\rho}_{TB} \\
&= \frac{1}{27}\left(\frac{\mu}{\rho}^2_{T1} + \frac{\mu}{\rho}^2_{T2} + \frac{\mu}{\rho}^2_{T3}\right)\left(\frac{\mu}{\rho}^2_{B1} + \frac{\mu}{\rho}^2_{B2} + \frac{\mu}{\rho}^2_{B3}\right)\left(\frac{\mu}{\rho}^2_{C1} + \frac{\mu}{\rho}^2_{C2} + \frac{\mu}{\rho}^2_{C3}\right) \\
&\quad - \frac{1}{27}\left(\frac{\mu}{\rho}^2_{T1} + \frac{\mu}{\rho}^2_{T2} + \frac{\mu}{\rho}^2_{T3}\right)\left(\frac{\mu}{\rho}_{B1}\frac{\mu}{\rho}_{C1} + \frac{\mu}{\rho}_{B2}\frac{\mu}{\rho}_{C2} + \frac{\mu}{\rho}_{B3}\frac{\mu}{\rho}_{C3}\right)^2 \\
&\quad - \frac{1}{27}\left(\frac{\mu}{\rho}^2_{B1} + \frac{\mu}{\rho}^2_{B2} + \frac{\mu}{\rho}^2_{B3}\right)\left(\frac{\mu}{\rho}_{T1}\frac{\mu}{\rho}_{C1} + \frac{\mu}{\rho}_{T2}\frac{\mu}{\rho}_{C2} + \frac{\mu}{\rho}_{T3}\frac{\mu}{\rho}_{C3}\right)^2 \\
&\quad - \frac{1}{27}\left(\frac{\mu}{\rho}^2_{C1} + \frac{\mu}{\rho}^2_{C2} + \frac{\mu}{\rho}^2_{C3}\right)\left(\frac{\mu}{\rho}_{T1}\frac{\mu}{\rho}_{B1} + \frac{\mu}{\rho}_{T2}\frac{\mu}{\rho}_{B2} + \frac{\mu}{\rho}_{T3}\frac{\mu}{\rho}_{B3}\right)^2 \\
&\quad + \frac{2}{27}\left(\frac{\mu}{\rho}_{B1}\frac{\mu}{\rho}_{C1} + \frac{\mu}{\rho}_{B2}\frac{\mu}{\rho}_{C2} + \frac{\mu}{\rho}_{B3}\frac{\mu}{\rho}_{C3}\right)\left(\frac{\mu}{\rho}_{T1}\frac{\mu}{\rho}_{C1} + \frac{\mu}{\rho}_{T2}\frac{\mu}{\rho}_{C2} + \frac{\mu}{\rho}_{T3}\frac{\mu}{\rho}_{C3}\right)\left(\frac{\mu}{\rho}_{T1}\frac{\mu}{\rho}_{B1} + \frac{\mu}{\rho}_{T2}\frac{\mu}{\rho}_{B2} + \frac{\mu}{\rho}_{T3}\frac{\mu}{\rho}_{B3}\right)
\end{aligned}$$

$$
\begin{aligned}
27Deno = {} & \frac{\mu^2}{\rho_{T1}}\frac{\mu^2}{\rho_{B1}}\frac{\mu^2}{\rho_{C1}} + \frac{\mu^2}{\rho_{T2}}\frac{\mu^2}{\rho_{B1}}\frac{\mu^2}{\rho_{C1}} + \frac{\mu^2}{\rho_{T3}}\frac{\mu^2}{\rho_{B1}}\frac{\mu^2}{\rho_{C1}} + \frac{\mu^2}{\rho_{T1}}\frac{\mu^2}{\rho_{B2}}\frac{\mu^2}{\rho_{C1}} + \frac{\mu^2}{\rho_{T2}}\frac{\mu^2}{\rho_{B2}}\frac{\mu^2}{\rho_{C1}} + \frac{\mu^2}{\rho_{T3}}\frac{\mu^2}{\rho_{B2}}\frac{\mu^2}{\rho_{C1}} \\
& + \frac{\mu^2}{\rho_{T1}}\frac{\mu^2}{\rho_{B3}}\frac{\mu^2}{\rho_{C1}} + \frac{\mu^2}{\rho_{T2}}\frac{\mu^2}{\rho_{B3}}\frac{\mu^2}{\rho_{C1}} + \frac{\mu^2}{\rho_{T3}}\frac{\mu^2}{\rho_{B3}}\frac{\mu^2}{\rho_{C1}} + \frac{\mu^2}{\rho_{T1}}\frac{\mu^2}{\rho_{B1}}\frac{\mu^2}{\rho_{C2}} + \frac{\mu^2}{\rho_{T2}}\frac{\mu^2}{\rho_{B1}}\frac{\mu^2}{\rho_{C2}} + \frac{\mu^2}{\rho_{T3}}\frac{\mu^2}{\rho_{B1}}\frac{\mu^2}{\rho_{C2}} \\
& + \frac{\mu^2}{\rho_{T1}}\frac{\mu^2}{\rho_{B2}}\frac{\mu^2}{\rho_{C2}} + \frac{\mu^2}{\rho_{T2}}\frac{\mu^2}{\rho_{B2}}\frac{\mu^2}{\rho_{C2}} + \frac{\mu^2}{\rho_{T3}}\frac{\mu^2}{\rho_{B2}}\frac{\mu^2}{\rho_{C2}} + \frac{\mu^2}{\rho_{T1}}\frac{\mu^2}{\rho_{B3}}\frac{\mu^2}{\rho_{C2}} + \frac{\mu^2}{\rho_{T2}}\frac{\mu^2}{\rho_{B3}}\frac{\mu^2}{\rho_{C2}} + \frac{\mu^2}{\rho_{T3}}\frac{\mu^2}{\rho_{B3}}\frac{\mu^2}{\rho_{C2}} \\
& + \frac{\mu^2}{\rho_{T1}}\frac{\mu^2}{\rho_{B1}}\frac{\mu^2}{\rho_{C3}} + \frac{\mu^2}{\rho_{T2}}\frac{\mu^2}{\rho_{B1}}\frac{\mu^2}{\rho_{C3}} + \frac{\mu^2}{\rho_{T3}}\frac{\mu^2}{\rho_{B1}}\frac{\mu^2}{\rho_{C3}} + \frac{\mu^2}{\rho_{T1}}\frac{\mu^2}{\rho_{B2}}\frac{\mu^2}{\rho_{C3}} + \frac{\mu^2}{\rho_{T2}}\frac{\mu^2}{\rho_{B2}}\frac{\mu^2}{\rho_{C3}} + \frac{\mu^2}{\rho_{T3}}\frac{\mu^2}{\rho_{B2}}\frac{\mu^2}{\rho_{C3}} \\
& + \frac{\mu^2}{\rho_{T1}}\frac{\mu^2}{\rho_{B3}}\frac{\mu^2}{\rho_{C3}} + \frac{\mu^2}{\rho_{T2}}\frac{\mu^2}{\rho_{B3}}\frac{\mu^2}{\rho_{C3}} + \frac{\mu^2}{\rho_{T3}}\frac{\mu^2}{\rho_{B3}}\frac{\mu^2}{\rho_{C3}} - \frac{\mu^2}{\rho_{T1}}\frac{\mu^2}{\rho_{B1}}\frac{\mu^2}{\rho_{C1}} - \frac{\mu^2}{\rho_{T1}}\frac{\mu^2}{\rho_{B2}}\frac{\mu^2}{\rho_{C2}} - \frac{\mu^2}{\rho_{T1}}\frac{\mu^2}{\rho_{B3}}\frac{\mu^2}{\rho_{C3}} \\
& - 2\frac{\mu^2}{\rho_{T1}}\frac{\mu}{\rho_{B1}}\frac{\mu}{\rho_{B2}}\frac{\mu}{\rho_{C1}}\frac{\mu}{\rho_{C2}} - 2\frac{\mu^2}{\rho_{T1}}\frac{\mu}{\rho_{B2}}\frac{\mu}{\rho_{B3}}\frac{\mu}{\rho_{C2}}\frac{\mu}{\rho_{C3}} - 2\frac{\mu^2}{\rho_{T1}}\frac{\mu}{\rho_{B1}}\frac{\mu}{\rho_{B3}}\frac{\mu}{\rho_{C1}}\frac{\mu}{\rho_{C3}} - \frac{\mu^2}{\rho_{T2}}\frac{\mu^2}{\rho_{B1}}\frac{\mu^2}{\rho_{C1}} \\
& - \frac{\mu^2}{\rho_{T2}}\frac{\mu^2}{\rho_{B2}}\frac{\mu^2}{\rho_{C2}} - \frac{\mu^2}{\rho_{T2}}\frac{\mu^2}{\rho_{B3}}\frac{\mu^2}{\rho_{C3}} - 2\frac{\mu^2}{\rho_{T2}}\frac{\mu}{\rho_{B1}}\frac{\mu}{\rho_{B2}}\frac{\mu}{\rho_{C1}}\frac{\mu}{\rho_{C2}} - 2\frac{\mu^2}{\rho_{T2}}\frac{\mu}{\rho_{B2}}\frac{\mu}{\rho_{B3}}\frac{\mu}{\rho_{C2}}\frac{\mu}{\rho_{C3}} \\
& - 2\frac{\mu^2}{\rho_{T2}}\frac{\mu}{\rho_{B1}}\frac{\mu}{\rho_{B3}}\frac{\mu}{\rho_{C1}}\frac{\mu}{\rho_{C3}} - \frac{\mu^2}{\rho_{T3}}\frac{\mu^2}{\rho_{B1}}\frac{\mu^2}{\rho_{C1}} - \frac{\mu^2}{\rho_{T3}}\frac{\mu^2}{\rho_{B2}}\frac{\mu^2}{\rho_{C2}} - \frac{\mu^2}{\rho_{T3}}\frac{\mu^2}{\rho_{B3}}\frac{\mu^2}{\rho_{C3}} - 2\frac{\mu^2}{\rho_{T3}}\frac{\mu}{\rho_{B1}}\frac{\mu}{\rho_{B2}}\frac{\mu}{\rho_{C1}}\frac{\mu}{\rho_{C2}} \\
& - 2\frac{\mu^2}{\rho_{T3}}\frac{\mu}{\rho_{B2}}\frac{\mu}{\rho_{B3}}\frac{\mu}{\rho_{C2}}\frac{\mu}{\rho_{C3}} - 2\frac{\mu^2}{\rho_{T3}}\frac{\mu}{\rho_{B1}}\frac{\mu}{\rho_{B3}}\frac{\mu}{\rho_{C1}}\frac{\mu}{\rho_{C3}} - \frac{\mu^2}{\rho_{T1}}\frac{\mu^2}{\rho_{B1}}\frac{\mu^2}{\rho_{C1}} - \frac{\mu^2}{\rho_{T2}}\frac{\mu^2}{\rho_{B1}}\frac{\mu^2}{\rho_{C2}} - \frac{\mu^2}{\rho_{T3}}\frac{\mu^2}{\rho_{B1}}\frac{\mu^2}{\rho_{C3}} \\
& - 2\frac{\mu^2}{\rho_{B1}}\frac{\mu}{\rho_{T1}}\frac{\mu}{\rho_{T2}}\frac{\mu}{\rho_{C1}}\frac{\mu}{\rho_{C2}} - 2\frac{\mu^2}{\rho_{B1}}\frac{\mu}{\rho_{T2}}\frac{\mu}{\rho_{T3}}\frac{\mu}{\rho_{C2}}\frac{\mu}{\rho_{C3}} - 2\frac{\mu^2}{\rho_{B1}}\frac{\mu}{\rho_{T1}}\frac{\mu}{\rho_{T3}}\frac{\mu}{\rho_{C1}}\frac{\mu}{\rho_{C3}} - \frac{\mu^2}{\rho_{T1}}\frac{\mu^2}{\rho_{B2}}\frac{\mu^2}{\rho_{C1}} \\
& - \frac{\mu^2}{\rho_{T2}}\frac{\mu^2}{\rho_{B2}}\frac{\mu^2}{\rho_{C2}} - \frac{\mu^2}{\rho_{T3}}\frac{\mu^2}{\rho_{B2}}\frac{\mu^2}{\rho_{C3}} - 2\frac{\mu^2}{\rho_{B2}}\frac{\mu}{\rho_{T1}}\frac{\mu}{\rho_{T2}}\frac{\mu}{\rho_{C1}}\frac{\mu}{\rho_{C2}} - 2\frac{\mu^2}{\rho_{B2}}\frac{\mu}{\rho_{T2}}\frac{\mu}{\rho_{T3}}\frac{\mu}{\rho_{C2}}\frac{\mu}{\rho_{C3}} \\
& - 2\frac{\mu^2}{\rho_{B2}}\frac{\mu}{\rho_{T1}}\frac{\mu}{\rho_{T3}}\frac{\mu}{\rho_{C1}}\frac{\mu}{\rho_{C3}} - \frac{\mu^2}{\rho_{T1}}\frac{\mu^2}{\rho_{B3}}\frac{\mu^2}{\rho_{C1}} - \frac{\mu^2}{\rho_{T2}}\frac{\mu^2}{\rho_{B3}}\frac{\mu^2}{\rho_{C2}} - \frac{\mu^2}{\rho_{T3}}\frac{\mu^2}{\rho_{B3}}\frac{\mu^2}{\rho_{C3}} - 2\frac{\mu^2}{\rho_{B3}}\frac{\mu}{\rho_{T1}}\frac{\mu}{\rho_{T2}}\frac{\mu}{\rho_{C1}}\frac{\mu}{\rho_{C2}} \\
& - 2\frac{\mu^2}{\rho_{B3}}\frac{\mu}{\rho_{T2}}\frac{\mu}{\rho_{T3}}\frac{\mu}{\rho_{C2}}\frac{\mu}{\rho_{C3}} - 2\frac{\mu^2}{\rho_{B3}}\frac{\mu}{\rho_{T1}}\frac{\mu}{\rho_{T3}}\frac{\mu}{\rho_{C1}}\frac{\mu}{\rho_{C3}} - \frac{\mu^2}{\rho_{T1}}\frac{\mu^2}{\rho_{B1}}\frac{\mu^2}{\rho_{C1}} - \frac{\mu^2}{\rho_{T2}}\frac{\mu^2}{\rho_{B2}}\frac{\mu^2}{\rho_{C1}} - \frac{\mu^2}{\rho_{T3}}\frac{\mu^2}{\rho_{B3}}\frac{\mu^2}{\rho_{C1}} \\
& - 2\frac{\mu^2}{\rho_{C1}}\frac{\mu}{\rho_{T1}}\frac{\mu}{\rho_{T2}}\frac{\mu}{\rho_{B1}}\frac{\mu}{\rho_{B2}} - 2\frac{\mu^2}{\rho_{C1}}\frac{\mu}{\rho_{T2}}\frac{\mu}{\rho_{T3}}\frac{\mu}{\rho_{B2}}\frac{\mu}{\rho_{B3}} - 2\frac{\mu^2}{\rho_{C1}}\frac{\mu}{\rho_{T1}}\frac{\mu}{\rho_{T3}}\frac{\mu}{\rho_{B1}}\frac{\mu}{\rho_{B3}} - \frac{\mu^2}{\rho_{T1}}\frac{\mu^2}{\rho_{B1}}\frac{\mu^2}{\rho_{C2}} \\
& - \frac{\mu^2}{\rho_{T2}}\frac{\mu^2}{\rho_{B2}}\frac{\mu^2}{\rho_{C2}} - \frac{\mu^2}{\rho_{T3}}\frac{\mu^2}{\rho_{B3}}\frac{\mu^2}{\rho_{C2}} - 2\frac{\mu^2}{\rho_{C2}}\frac{\mu}{\rho_{T1}}\frac{\mu}{\rho_{T2}}\frac{\mu}{\rho_{B1}}\frac{\mu}{\rho_{B2}} - 2\frac{\mu^2}{\rho_{C2}}\frac{\mu}{\rho_{T2}}\frac{\mu}{\rho_{T3}}\frac{\mu}{\rho_{B2}}\frac{\mu}{\rho_{B3}} \\
& - 2\frac{\mu^2}{\rho_{C2}}\frac{\mu}{\rho_{T1}}\frac{\mu}{\rho_{T3}}\frac{\mu}{\rho_{B1}}\frac{\mu}{\rho_{B3}} - \frac{\mu^2}{\rho_{T1}}\frac{\mu^2}{\rho_{B1}}\frac{\mu^2}{\rho_{C3}} - \frac{\mu^2}{\rho_{T2}}\frac{\mu^2}{\rho_{B2}}\frac{\mu^2}{\rho_{C3}} - \frac{\mu^2}{\rho_{T3}}\frac{\mu^2}{\rho_{B3}}\frac{\mu^2}{\rho_{C3}} - 2\frac{\mu^2}{\rho_{C3}}\frac{\mu}{\rho_{T1}}\frac{\mu}{\rho_{T2}}\frac{\mu}{\rho_{B1}}\frac{\mu}{\rho_{B2}} \\
& - 2\frac{\mu^2}{\rho_{C3}}\frac{\mu}{\rho_{T2}}\frac{\mu}{\rho_{T3}}\frac{\mu}{\rho_{B2}}\frac{\mu}{\rho_{B3}} - 2\frac{\mu^2}{\rho_{C3}}\frac{\mu}{\rho_{T1}}\frac{\mu}{\rho_{T3}}\frac{\mu}{\rho_{B1}}\frac{\mu}{\rho_{B3}} + 2\frac{\mu^2}{\rho_{T1}}\frac{\mu^2}{\rho_{B1}}\frac{\mu^2}{\rho_{C1}} + 2\frac{\mu^2}{\rho_{T1}}\frac{\mu}{\rho_{B1}}\frac{\mu}{\rho_{B2}}\frac{\mu}{\rho_{C1}}\frac{\mu}{\rho_{C2}} \\
& + 2\frac{\mu^2}{\rho_{T1}}\frac{\mu}{\rho_{B1}}\frac{\mu}{\rho_{B3}}\frac{\mu}{\rho_{C1}}\frac{\mu}{\rho_{C3}} + 2\frac{\mu^2}{\rho_{B1}}\frac{\mu}{\rho_{T1}}\frac{\mu}{\rho_{T2}}\frac{\mu}{\rho_{C1}}\frac{\mu}{\rho_{C2}} + 2\frac{\mu^2}{\rho_{C2}}\frac{\mu}{\rho_{T1}}\frac{\mu}{\rho_{T2}}\frac{\mu}{\rho_{B1}}\frac{\mu}{\rho_{B2}} \\
& + 2\frac{\mu}{\rho_{T1}}\frac{\mu}{\rho_{T2}}\frac{\mu}{\rho_{B1}}\frac{\mu}{\rho_{B3}}\frac{\mu}{\rho_{C2}}\frac{\mu}{\rho_{C3}} + 2\frac{\mu^2}{\rho_{B1}}\frac{\mu}{\rho_{T1}}\frac{\mu}{\rho_{T3}}\frac{\mu}{\rho_{C1}}\frac{\mu}{\rho_{C3}} + 2\frac{\mu}{\rho_{T1}}\frac{\mu}{\rho_{T3}}\frac{\mu}{\rho_{B1}}\frac{\mu}{\rho_{B2}}\frac{\mu}{\rho_{C2}}\frac{\mu}{\rho_{C3}} \\
& + 2\frac{\mu^2}{\rho_{C3}}\frac{\mu}{\rho_{T1}}\frac{\mu}{\rho_{T3}}\frac{\mu}{\rho_{B1}}\frac{\mu}{\rho_{B3}} + 2\frac{\mu^2}{\rho_{C1}}\frac{\mu}{\rho_{T1}}\frac{\mu}{\rho_{T2}}\frac{\mu}{\rho_{B1}}\frac{\mu}{\rho_{B2}} + 2\frac{\mu^2}{\rho_{B2}}\frac{\mu}{\rho_{T1}}\frac{\mu}{\rho_{T2}}\frac{\mu}{\rho_{C1}}\frac{\mu}{\rho_{C2}} \\
& + 2\frac{\mu}{\rho_{T1}}\frac{\mu}{\rho_{T2}}\frac{\mu}{\rho_{B2}}\frac{\mu}{\rho_{B3}}\frac{\mu}{\rho_{C1}}\frac{\mu}{\rho_{C3}} + 2\frac{\mu^2}{\rho_{T2}}\frac{\mu}{\rho_{B1}}\frac{\mu}{\rho_{B2}}\frac{\mu}{\rho_{C1}}\frac{\mu}{\rho_{C2}} + 2\frac{\mu^2}{\rho_{T2}}\frac{\mu^2}{\rho_{B2}}\frac{\mu^2}{\rho_{C2}} \\
& + 2\frac{\mu^2}{\rho_{T2}}\frac{\mu}{\rho_{B2}}\frac{\mu}{\rho_{B3}}\frac{\mu}{\rho_{C2}}\frac{\mu}{\rho_{C3}} + 2\frac{\mu}{\rho_{T2}}\frac{\mu}{\rho_{T3}}\frac{\mu}{\rho_{B1}}\frac{\mu}{\rho_{B2}}\frac{\mu}{\rho_{C1}}\frac{\mu}{\rho_{C3}} + 2\frac{\mu^2}{\rho_{B2}}\frac{\mu}{\rho_{T2}}\frac{\mu}{\rho_{T3}}\frac{\mu}{\rho_{C2}}\frac{\mu}{\rho_{C3}} \\
& + 2\frac{\mu^2}{\rho_{C3}}\frac{\mu}{\rho_{T2}}\frac{\mu}{\rho_{T3}}\frac{\mu}{\rho_{B2}}\frac{\mu}{\rho_{B3}} + 2\frac{\mu^2}{\rho_{C1}}\frac{\mu}{\rho_{T1}}\frac{\mu}{\rho_{T3}}\frac{\mu}{\rho_{B1}}\frac{\mu}{\rho_{B3}} + 2\frac{\mu}{\rho_{T1}}\frac{\mu}{\rho_{T3}}\frac{\mu}{\rho_{B2}}\frac{\mu}{\rho_{B3}}\frac{\mu}{\rho_{C1}}\frac{\mu}{\rho_{C2}} \\
& + 2\frac{\mu^2}{\rho_{B3}}\frac{\mu}{\rho_{T1}}\frac{\mu}{\rho_{T3}}\frac{\mu}{\rho_{C1}}\frac{\mu}{\rho_{C3}} + 2\frac{\mu}{\rho_{T2}}\frac{\mu}{\rho_{T3}}\frac{\mu}{\rho_{B1}}\frac{\mu}{\rho_{B3}}\frac{\mu}{\rho_{C1}}\frac{\mu}{\rho_{C2}} + 2\frac{\mu^2}{\rho_{C2}}\frac{\mu}{\rho_{T2}}\frac{\mu}{\rho_{T3}}\frac{\mu}{\rho_{B2}}\frac{\mu}{\rho_{B3}} \\
& + 2\frac{\mu^2}{\rho_{B3}}\frac{\mu}{\rho_{T2}}\frac{\mu}{\rho_{T3}}\frac{\mu}{\rho_{C2}}\frac{\mu}{\rho_{C3}} + 2\frac{\mu^2}{\rho_{T3}}\frac{\mu}{\rho_{B1}}\frac{\mu}{\rho_{B3}}\frac{\mu}{\rho_{C1}}\frac{\mu}{\rho_{C3}} + 2\frac{\mu^2}{\rho_{T3}}\frac{\mu}{\rho_{B2}}\frac{\mu}{\rho_{B3}}\frac{\mu}{\rho_{C2}}\frac{\mu}{\rho_{C3}} + 2\frac{\mu^2}{\rho_{C3}}\frac{\mu^2}{\rho_{T3}}\frac{\mu^2}{\rho_{B3}}
\end{aligned}
$$

$$
\begin{aligned}
27Deno = & \frac{\mu^2}{\rho_{T3}}\frac{\mu^2}{\rho_{B2}}\frac{\mu^2}{\rho_{C1}} + \frac{\mu^2}{\rho_{T2}}\frac{\mu^2}{\rho_{B3}}\frac{\mu^2}{\rho_{C1}} + \frac{\mu^2}{\rho_{T3}}\frac{\mu^2}{\rho_{B1}}\frac{\mu^2}{\rho_{C2}} + \frac{\mu^2}{\rho_{T1}}\frac{\mu^2}{\rho_{B3}}\frac{\mu^2}{\rho_{C2}} + \frac{\mu^2}{\rho_{T2}}\frac{\mu^2}{\rho_{B1}}\frac{\mu^2}{\rho_{C3}} + \frac{\mu^2}{\rho_{T1}}\frac{\mu^2}{\rho_{B2}}\frac{\mu^2}{\rho_{C3}} \\
& - 2\frac{\mu^2}{\rho_{T1}}\frac{\mu}{\rho_{B2}}\frac{\mu}{\rho_{B3}}\frac{\mu}{\rho_{C2}}\frac{\mu}{\rho_{C3}} - 2\frac{\mu^2}{\rho_{T2}}\frac{\mu}{\rho_{B1}}\frac{\mu}{\rho_{B3}}\frac{\mu}{\rho_{C1}}\frac{\mu}{\rho_{C3}} - 2\frac{\mu^2}{\rho_{T3}}\frac{\mu}{\rho_{B1}}\frac{\mu}{\rho_{B2}}\frac{\mu}{\rho_{C1}}\frac{\mu}{\rho_{C2}} \\
& - 2\frac{\mu^2}{\rho_{B1}}\frac{\mu}{\rho_{T2}}\frac{\mu}{\rho_{T3}}\frac{\mu}{\rho_{C2}}\frac{\mu}{\rho_{C3}} - 2\frac{\mu^2}{\rho_{B2}}\frac{\mu}{\rho_{T1}}\frac{\mu}{\rho_{T3}}\frac{\mu}{\rho_{C1}}\frac{\mu}{\rho_{C3}} - 2\frac{\mu^2}{\rho_{B3}}\frac{\mu}{\rho_{T1}}\frac{\mu}{\rho_{T2}}\frac{\mu}{\rho_{C1}}\frac{\mu}{\rho_{C2}} \\
& - 2\frac{\mu^2}{\rho_{C1}}\frac{\mu}{\rho_{T2}}\frac{\mu}{\rho_{T3}}\frac{\mu}{\rho_{B2}}\frac{\mu}{\rho_{B3}} - 2\frac{\mu^2}{\rho_{C2}}\frac{\mu}{\rho_{T1}}\frac{\mu}{\rho_{T3}}\frac{\mu}{\rho_{B1}}\frac{\mu}{\rho_{B3}} - 2\frac{\mu^2}{\rho_{C3}}\frac{\mu}{\rho_{T1}}\frac{\mu}{\rho_{T2}}\frac{\mu}{\rho_{B1}}\frac{\mu}{\rho_{B2}} \\
& + 2\frac{\mu}{\rho_{T1}}\frac{\mu}{\rho_{T2}}\frac{\mu}{\rho_{B1}}\frac{\mu}{\rho_{B3}}\frac{\mu}{\rho_{C2}}\frac{\mu}{\rho_{C3}} + 2\frac{\mu}{\rho_{T1}}\frac{\mu}{\rho_{T3}}\frac{\mu}{\rho_{B1}}\frac{\mu}{\rho_{B2}}\frac{\mu}{\rho_{C2}}\frac{\mu}{\rho_{C3}} + 2\frac{\mu}{\rho_{T1}}\frac{\mu}{\rho_{T2}}\frac{\mu}{\rho_{B2}}\frac{\mu}{\rho_{B3}}\frac{\mu}{\rho_{C1}}\frac{\mu}{\rho_{C3}} \\
& + 2\frac{\mu}{\rho_{T2}}\frac{\mu}{\rho_{T3}}\frac{\mu}{\rho_{B1}}\frac{\mu}{\rho_{B2}}\frac{\mu}{\rho_{C1}}\frac{\mu}{\rho_{C3}} + 2\frac{\mu}{\rho_{T1}}\frac{\mu}{\rho_{T3}}\frac{\mu}{\rho_{B2}}\frac{\mu}{\rho_{B3}}\frac{\mu}{\rho_{C1}}\frac{\mu}{\rho_{C2}} + 2\frac{\mu}{\rho_{T2}}\frac{\mu}{\rho_{T3}}\frac{\mu}{\rho_{B1}}\frac{\mu}{\rho_{B3}}\frac{\mu}{\rho_{C1}}\frac{\mu}{\rho_{C2}} \\
= & \frac{\mu^2}{\rho_{T1}}\left(\frac{\mu^2}{\rho_{B3}}\frac{\mu^2}{\rho_{C2}} - 2\frac{\mu}{\rho_{B2}}\frac{\mu}{\rho_{B3}}\frac{\mu}{\rho_{C2}}\frac{\mu}{\rho_{C3}} + \frac{\mu^2}{\rho_{B2}}\frac{\mu^2}{\rho_{C3}}\right) \\
& + \frac{\mu^2}{\rho_{B1}}\left(\frac{\mu^2}{\rho_{T3}}\frac{\mu^2}{\rho_{C2}} - 2\frac{\mu}{\rho_{T2}}\frac{\mu}{\rho_{T3}}\frac{\mu}{\rho_{C2}}\frac{\mu}{\rho_{C3}} + \frac{\mu^2}{\rho_{T2}}\frac{\mu^2}{\rho_{C3}}\right) \\
& + \frac{\mu^2}{\rho_{C1}}\left(\frac{\mu^2}{\rho_{T3}}\frac{\mu^2}{\rho_{B2}} - 2\frac{\mu}{\rho_{T2}}\frac{\mu}{\rho_{T3}}\frac{\mu}{\rho_{B2}}\frac{\mu}{\rho_{B3}} + \frac{\mu^2}{\rho_{T2}}\frac{\mu^2}{\rho_{B3}}\right) \\
& + 2\frac{\mu}{\rho_{T1}}\frac{\mu}{\rho_{B1}}\left(\frac{\mu}{\rho_{T2}}\frac{\mu}{\rho_{B3}}\frac{\mu}{\rho_{C2}}\frac{\mu}{\rho_{C3}} + \frac{\mu}{\rho_{T3}}\frac{\mu}{\rho_{B2}}\frac{\mu}{\rho_{C2}}\frac{\mu}{\rho_{C3}} - \frac{\mu^2}{\rho_{C2}}\frac{\mu}{\rho_{T3}}\frac{\mu}{\rho_{B3}} - \frac{\mu^2}{\rho_{C3}}\frac{\mu}{\rho_{T2}}\frac{\mu}{\rho_{B2}}\right) \\
& + 2\frac{\mu}{\rho_{T1}}\frac{\mu}{\rho_{C1}}\left(\frac{\mu}{\rho_{T2}}\frac{\mu}{\rho_{B2}}\frac{\mu}{\rho_{B3}}\frac{\mu}{\rho_{C3}} + \frac{\mu}{\rho_{T3}}\frac{\mu}{\rho_{B2}}\frac{\mu}{\rho_{B3}}\frac{\mu}{\rho_{C2}} - \frac{\mu^2}{\rho_{B2}}\frac{\mu}{\rho_{T3}}\frac{\mu}{\rho_{C3}} - \frac{\mu^2}{\rho_{B3}}\frac{\mu}{\rho_{T2}}\frac{\mu}{\rho_{C2}}\right) \\
& + 2\frac{\mu}{\rho_{B1}}\frac{\mu}{\rho_{C1}}\left(\frac{\mu}{\rho_{T2}}\frac{\mu}{\rho_{T3}}\frac{\mu}{\rho_{B2}}\frac{\mu}{\rho_{C3}} + \frac{\mu}{\rho_{T2}}\frac{\mu}{\rho_{T3}}\frac{\mu}{\rho_{B3}}\frac{\mu}{\rho_{C2}} - \frac{\mu^2}{\rho_{T2}}\frac{\mu}{\rho_{B3}}\frac{\mu}{\rho_{C3}} - \frac{\mu^2}{\rho_{T3}}\frac{\mu}{\rho_{B2}}\frac{\mu}{\rho_{C2}}\right) \\
= & \frac{\mu^2}{\rho_{T1}}\left(\frac{\mu}{\rho_{B2}}\frac{\mu}{\rho_{C3}} - \frac{\mu}{\rho_{B3}}\frac{\mu}{\rho_{C2}}\right)^2 + \frac{\mu^2}{\rho_{B1}}\left(\frac{\mu}{\rho_{C2}}\frac{\mu}{\rho_{T3}} - \frac{\mu}{\rho_{C3}}\frac{\mu}{\rho_{T2}}\right)^2 + \frac{\mu^2}{\rho_{C1}}\left(\frac{\mu}{\rho_{T2}}\frac{\mu}{\rho_{B3}} - \frac{\mu}{\rho_{T3}}\frac{\mu}{\rho_{B2}}\right)^2 \\
& + 2\frac{\mu}{\rho_{T1}}\frac{\mu}{\rho_{B1}}\left(\frac{\mu}{\rho_{B2}}\frac{\mu}{\rho_{C3}}\left(\frac{\mu}{\rho_{T3}}\frac{\mu}{\rho_{C2}} - \frac{\mu}{\rho_{C3}}\frac{\mu}{\rho_{T2}}\right) + \frac{\mu}{\rho_{B3}}\frac{\mu}{\rho_{C2}}\left(\frac{\mu}{\rho_{T2}}\frac{\mu}{\rho_{C3}} - \frac{\mu}{\rho_{C2}}\frac{\mu}{\rho_{T3}}\right)\right) \\
& + 2\frac{\mu}{\rho_{T1}}\frac{\mu}{\rho_{C1}}\left(\frac{\mu}{\rho_{B2}}\frac{\mu}{\rho_{C3}}\left(\frac{\mu}{\rho_{T2}}\frac{\mu}{\rho_{B3}} - \frac{\mu}{\rho_{B2}}\frac{\mu}{\rho_{T3}}\right) + \frac{\mu}{\rho_{B3}}\frac{\mu}{\rho_{C2}}\left(\frac{\mu}{\rho_{T3}}\frac{\mu}{\rho_{B2}} - \frac{\mu}{\rho_{B3}}\frac{\mu}{\rho_{T2}}\right)\right) \\
& + 2\frac{\mu}{\rho_{B1}}\frac{\mu}{\rho_{C1}}\left(\frac{\mu}{\rho_{C3}}\frac{\mu}{\rho_{T2}}\left(\frac{\mu}{\rho_{T3}}\frac{\mu}{\rho_{B2}} - \frac{\mu}{\rho_{T2}}\frac{\mu}{\rho_{B3}}\right) + \frac{\mu}{\rho_{C2}}\frac{\mu}{\rho_{T3}}\left(\frac{\mu}{\rho_{T2}}\frac{\mu}{\rho_{B3}} - \frac{\mu}{\rho_{T3}}\frac{\mu}{\rho_{B2}}\right)\right) \\
= & \frac{\mu^2}{\rho_{T1}}\left(\frac{\mu}{\rho_{B2}}\frac{\mu}{\rho_{C3}} - \frac{\mu}{\rho_{B3}}\frac{\mu}{\rho_{C2}}\right)^2 + \frac{\mu^2}{\rho_{B1}}\left(\frac{\mu}{\rho_{C2}}\frac{\mu}{\rho_{T3}} - \frac{\mu}{\rho_{C3}}\frac{\mu}{\rho_{T2}}\right)^2 + \frac{\mu^2}{\rho_{C1}}\left(\frac{\mu}{\rho_{T2}}\frac{\mu}{\rho_{B3}} - \frac{\mu}{\rho_{T3}}\frac{\mu}{\rho_{B2}}\right)^2 \\
& + 2\frac{\mu}{\rho_{T1}}\frac{\mu}{\rho_{B1}}\left(\frac{\mu}{\rho_{C2}}\frac{\mu}{\rho_{T3}} - \frac{\mu}{\rho_{C3}}\frac{\mu}{\rho_{T2}}\right)\left(\frac{\mu}{\rho_{B2}}\frac{\mu}{\rho_{C3}} - \frac{\mu}{\rho_{B3}}\frac{\mu}{\rho_{C2}}\right) \\
& + 2\frac{\mu}{\rho_{T1}}\frac{\mu}{\rho_{C1}}\left(\frac{\mu}{\rho_{T2}}\frac{\mu}{\rho_{B3}} - \frac{\mu}{\rho_{T3}}\frac{\mu}{\rho_{B2}}\right)\left(\frac{\mu}{\rho_{B2}}\frac{\mu}{\rho_{C3}} - \frac{\mu}{\rho_{B3}}\frac{\mu}{\rho_{C2}}\right) \\
& + 2\frac{\mu}{\rho_{B1}}\frac{\mu}{\rho_{C1}}\left(\frac{\mu}{\rho_{T2}}\frac{\mu}{\rho_{B3}} - \frac{\mu}{\rho_{T3}}\frac{\mu}{\rho_{B2}}\right)\left(\frac{\mu}{\rho_{C2}}\frac{\mu}{\rho_{T3}} - \frac{\mu}{\rho_{C3}}\frac{\mu}{\rho_{T2}}\right)
\end{aligned}
$$

$$
\begin{aligned}
Deno &= \frac{1}{27}\left[\frac{\mu}{\rho_{T1}}\left(\frac{\mu}{\rho_{B2}}\frac{\mu}{\rho_{C3}} - \frac{\mu}{\rho_{B3}}\frac{\mu}{\rho_{C2}}\right) + \frac{\mu}{\rho_{B1}}\left(\frac{\mu}{\rho_{C2}}\frac{\mu}{\rho_{T3}} - \frac{\mu}{\rho_{C3}}\frac{\mu}{\rho_{T2}}\right) + \frac{\mu}{\rho_{C1}}\left(\frac{\mu}{\rho_{T2}}\frac{\mu}{\rho_{B3}} - \frac{\mu}{\rho_{T3}}\frac{\mu}{\rho_{B2}}\right)\right]^2 \\
&= \frac{1}{27}D_3^2
\end{aligned}
\tag{E.2}
$$

where D_3 is defined in equation (5.12) for the three-energy KES.

The numerator in equaiton (E.1) could be expressed as,

$$
\begin{aligned}
Nume &= \left(\frac{\mu}{\rho_{TB}}\frac{\mu}{\rho_{BC}} - \frac{\mu}{\rho_{TC}}\frac{\mu}{\rho_{BB}}\right)\sum_i\left(\frac{\mu}{\rho_{Ti}}r_i\right) + \left(\frac{\mu}{\rho_{TB}}\frac{\mu}{\rho_{TC}} - \frac{\mu}{\rho_{TT}}\frac{\mu}{\rho_{BC}}\right)\sum_i\left(\frac{\mu}{\rho_{Bi}}r_i\right) + \left(\frac{\mu}{\rho_{TT}}\frac{\mu}{\rho_{BB}} - \frac{\mu^2}{\rho_{TB}}\right)\sum_i\left(\frac{\mu}{\rho_{Ci}}r_i\right) \\
&= \left(\frac{\mu}{\rho_{TB}}\frac{\mu}{\rho_{BC}} - \frac{\mu}{\rho_{TC}}\frac{\mu}{\rho_{BB}}\right)\left(\frac{\mu}{\rho_{T1}}r_1 + \frac{\mu}{\rho_{T2}}r_2 + \frac{\mu}{\rho_{T3}}r_3\right) \\
&\quad + \left(\frac{\mu}{\rho_{TB}}\frac{\mu}{\rho_{TC}} - \frac{\mu}{\rho_{TT}}\frac{\mu}{\rho_{BC}}\right)\left(\frac{\mu}{\rho_{B1}}r_1 + \frac{\mu}{\rho_{B2}}r_2 + \frac{\mu}{\rho_{B3}}r_3\right) \\
&\quad + \left(\frac{\mu}{\rho_{TT}}\frac{\mu}{\rho_{BB}} - \frac{\mu^2}{\rho_{TB}}\right)\left(\frac{\mu}{\rho_{C1}}r_1 + \frac{\mu}{\rho_{C2}}r_2 + \frac{\mu}{\rho_{C3}}r_3\right) \\
&= \left(\frac{\mu}{\rho_{T1}}\frac{\mu}{\rho_{TB}}\frac{\mu}{\rho_{BC}} - \frac{\mu}{\rho_{T1}}\frac{\mu}{\rho_{TC}}\frac{\mu}{\rho_{BB}} + \frac{\mu}{\rho_{B1}}\frac{\mu}{\rho_{TB}}\frac{\mu}{\rho_{TC}} - \frac{\mu}{\rho_{B1}}\frac{\mu}{\rho_{TT}}\frac{\mu}{\rho_{BC}} + \frac{\mu}{\rho_{C1}}\frac{\mu}{\rho_{TT}}\frac{\mu}{\rho_{BB}} - \frac{\mu}{\rho_{C1}}\frac{\mu^2}{\rho_{TB}}\right)r_1 \\
&\quad + \left(\frac{\mu}{\rho_{T2}}\frac{\mu}{\rho_{TB}}\frac{\mu}{\rho_{BC}} - \frac{\mu}{\rho_{T2}}\frac{\mu}{\rho_{TC}}\frac{\mu}{\rho_{BB}} + \frac{\mu}{\rho_{B2}}\frac{\mu}{\rho_{TB}}\frac{\mu}{\rho_{TC}} - \frac{\mu}{\rho_{B2}}\frac{\mu}{\rho_{TT}}\frac{\mu}{\rho_{BC}} + \frac{\mu}{\rho_{C2}}\frac{\mu}{\rho_{TT}}\frac{\mu}{\rho_{BB}} - \frac{\mu}{\rho_{C2}}\frac{\mu^2}{\rho_{TB}}\right)r_2 \\
&\quad + \left(\frac{\mu}{\rho_{T3}}\frac{\mu}{\rho_{TB}}\frac{\mu}{\rho_{BC}} - \frac{\mu}{\rho_{T3}}\frac{\mu}{\rho_{TC}}\frac{\mu}{\rho_{BB}} + \frac{\mu}{\rho_{B3}}\frac{\mu}{\rho_{TB}}\frac{\mu}{\rho_{TC}} - \frac{\mu}{\rho_{B3}}\frac{\mu}{\rho_{TT}}\frac{\mu}{\rho_{BC}} + \frac{\mu}{\rho_{C3}}\frac{\mu}{\rho_{TT}}\frac{\mu}{\rho_{BB}} - \frac{\mu}{\rho_{C3}}\frac{\mu^2}{\rho_{TB}}\right)r_3
\end{aligned}
$$

Define $Nume = X_1 r_1 + X_2 r_2 + X_3 r_3$ (E.3)

$$
\begin{aligned}
X_1 &= \frac{\mu}{\rho_{T1}}\frac{\mu}{\rho_{TB}}\frac{\mu}{\rho_{BC}} - \frac{\mu}{\rho_{T1}}\frac{\mu}{\rho_{TC}}\frac{\mu}{\rho_{BB}} + \frac{\mu}{\rho_{B1}}\frac{\mu}{\rho_{TB}}\frac{\mu}{\rho_{TC}} - \frac{\mu}{\rho_{B1}}\frac{\mu}{\rho_{TT}}\frac{\mu}{\rho_{BC}} + \frac{\mu}{\rho_{C1}}\frac{\mu}{\rho_{TT}}\frac{\mu}{\rho_{BB}} - \frac{\mu}{\rho_{C1}}\frac{\mu^2}{\rho_{TB}} \\
&= \frac{\mu}{\rho_{T1}}\tfrac{1}{3}\left(\frac{\mu}{\rho_{T1}}\frac{\mu}{\rho_{B1}} + \frac{\mu}{\rho_{T2}}\frac{\mu}{\rho_{B2}} + \frac{\mu}{\rho_{T3}}\frac{\mu}{\rho_{B3}}\right)\tfrac{1}{3}\left(\frac{\mu}{\rho_{B1}}\frac{\mu}{\rho_{C1}} + \frac{\mu}{\rho_{B2}}\frac{\mu}{\rho_{C2}} + \frac{\mu}{\rho_{B3}}\frac{\mu}{\rho_{C3}}\right) \\
&\quad - \frac{\mu}{\rho_{T1}}\tfrac{1}{3}\left(\frac{\mu}{\rho_{T1}}\frac{\mu}{\rho_{C1}} + \frac{\mu}{\rho_{T2}}\frac{\mu}{\rho_{C2}} + \frac{\mu}{\rho_{T3}}\frac{\mu}{\rho_{C3}}\right)\tfrac{1}{3}\left(\frac{\mu^2}{\rho_{B1}} + \frac{\mu^2}{\rho_{B2}} + \frac{\mu^2}{\rho_{B3}}\right) \\
&\quad + \frac{\mu}{\rho_{B1}}\tfrac{1}{3}\left(\frac{\mu}{\rho_{T1}}\frac{\mu}{\rho_{B1}} + \frac{\mu}{\rho_{T2}}\frac{\mu}{\rho_{B2}} + \frac{\mu}{\rho_{T3}}\frac{\mu}{\rho_{B3}}\right)\tfrac{1}{3}\left(\frac{\mu}{\rho_{T1}}\frac{\mu}{\rho_{C1}} + \frac{\mu}{\rho_{T2}}\frac{\mu}{\rho_{C2}} + \frac{\mu}{\rho_{T3}}\frac{\mu}{\rho_{C3}}\right) \\
&\quad - \frac{\mu}{\rho_{B1}}\tfrac{1}{3}\left(\frac{\mu^2}{\rho_{T1}} + \frac{\mu^2}{\rho_{T2}} + \frac{\mu^2}{\rho_{T3}}\right)\tfrac{1}{3}\left(\frac{\mu}{\rho_{B1}}\frac{\mu}{\rho_{C1}} + \frac{\mu}{\rho_{B2}}\frac{\mu}{\rho_{C2}} + \frac{\mu}{\rho_{B3}}\frac{\mu}{\rho_{C3}}\right) \\
&\quad + \frac{\mu}{\rho_{C1}}\tfrac{1}{3}\left(\frac{\mu^2}{\rho_{T1}} + \frac{\mu^2}{\rho_{T2}} + \frac{\mu^2}{\rho_{T3}}\right)\tfrac{1}{3}\left(\frac{\mu^2}{\rho_{B1}} + \frac{\mu^2}{\rho_{B2}} + \frac{\mu^2}{\rho_{B3}}\right) - \frac{\mu}{\rho_{C1}}\tfrac{1}{9}\left(\frac{\mu}{\rho_{T1}}\frac{\mu}{\rho_{B1}} + \frac{\mu}{\rho_{T2}}\frac{\mu}{\rho_{B2}} + \frac{\mu}{\rho_{T3}}\frac{\mu}{\rho_{B3}}\right)^2
\end{aligned}
$$

$$
\begin{aligned}
9X_1 &= \frac{\mu^2}{\rho_{T1}}\frac{\mu^2}{\rho_{B1}}\frac{\mu}{\rho_{C1}} + \frac{\mu}{\rho_{T1}}\frac{\mu}{\rho_{T2}}\frac{\mu}{\rho_{B1}}\frac{\mu}{\rho_{B2}}\frac{\mu}{\rho_{C1}} + \frac{\mu}{\rho_{T1}}\frac{\mu}{\rho_{T3}}\frac{\mu}{\rho_{B1}}\frac{\mu}{\rho_{B3}}\frac{\mu}{\rho_{C1}} + \frac{\mu^2}{\rho_{T1}}\frac{\mu}{\rho_{B1}}\frac{\mu}{\rho_{B2}}\frac{\mu}{\rho_{C2}} + \frac{\mu}{\rho_{T1}}\frac{\mu}{\rho_{T2}}\frac{\mu^2}{\rho_{B2}}\frac{\mu}{\rho_{C2}} \\
&\quad + \frac{\mu}{\rho_{T1}}\frac{\mu}{\rho_{T3}}\frac{\mu}{\rho_{B2}}\frac{\mu}{\rho_{B3}}\frac{\mu}{\rho_{C2}} + \frac{\mu^2}{\rho_{T1}}\frac{\mu}{\rho_{B1}}\frac{\mu}{\rho_{B3}}\frac{\mu}{\rho_{C3}} + \frac{\mu}{\rho_{T1}}\frac{\mu}{\rho_{T2}}\frac{\mu}{\rho_{B2}}\frac{\mu}{\rho_{B3}}\frac{\mu}{\rho_{C3}} + \frac{\mu}{\rho_{T1}}\frac{\mu}{\rho_{T3}}\frac{\mu^2}{\rho_{B3}}\frac{\mu}{\rho_{C3}} \\
&\quad - \frac{\mu^2}{\rho_{T1}}\frac{\mu^2}{\rho_{B1}}\frac{\mu}{\rho_{C1}} - \frac{\mu^2}{\rho_{B1}}\frac{\mu}{\rho_{T1}}\frac{\mu}{\rho_{T2}}\frac{\mu}{\rho_{C2}} - \frac{\mu^2}{\rho_{B1}}\frac{\mu}{\rho_{T1}}\frac{\mu}{\rho_{T3}}\frac{\mu}{\rho_{C3}} - \frac{\mu^2}{\rho_{T1}}\frac{\mu^2}{\rho_{B2}}\frac{\mu}{\rho_{C1}} - \frac{\mu^2}{\rho_{B2}}\frac{\mu}{\rho_{T1}}\frac{\mu}{\rho_{T2}}\frac{\mu}{\rho_{C2}} \\
&\quad - \frac{\mu^2}{\rho_{B2}}\frac{\mu}{\rho_{T1}}\frac{\mu}{\rho_{T3}}\frac{\mu}{\rho_{C3}} - \frac{\mu^2}{\rho_{T1}}\frac{\mu^2}{\rho_{B3}}\frac{\mu}{\rho_{C1}} - \frac{\mu^2}{\rho_{B3}}\frac{\mu}{\rho_{T1}}\frac{\mu}{\rho_{T2}}\frac{\mu}{\rho_{C2}} - \frac{\mu^2}{\rho_{B3}}\frac{\mu}{\rho_{T1}}\frac{\mu}{\rho_{T3}}\frac{\mu}{\rho_{C3}} \\
&\quad + \frac{\mu^2}{\rho_{T1}}\frac{\mu^2}{\rho_{B1}}\frac{\mu}{\rho_{C1}} + \frac{\mu}{\rho_{T1}}\frac{\mu}{\rho_{T2}}\frac{\mu}{\rho_{B1}}\frac{\mu}{\rho_{B2}}\frac{\mu}{\rho_{C1}} + \frac{\mu}{\rho_{T1}}\frac{\mu}{\rho_{T3}}\frac{\mu}{\rho_{B1}}\frac{\mu}{\rho_{B3}}\frac{\mu}{\rho_{C1}} + \frac{\mu^2}{\rho_{B1}}\frac{\mu}{\rho_{T1}}\frac{\mu}{\rho_{T2}}\frac{\mu}{\rho_{C2}} + \frac{\mu^2}{\rho_{T2}}\frac{\mu}{\rho_{B1}}\frac{\mu}{\rho_{B2}}\frac{\mu}{\rho_{C2}} \\
&\quad + \frac{\mu}{\rho_{T2}}\frac{\mu}{\rho_{T3}}\frac{\mu}{\rho_{B1}}\frac{\mu}{\rho_{B3}}\frac{\mu}{\rho_{C2}} + \frac{\mu^2}{\rho_{B1}}\frac{\mu}{\rho_{T1}}\frac{\mu}{\rho_{T3}}\frac{\mu}{\rho_{C3}} + \frac{\mu}{\rho_{T2}}\frac{\mu}{\rho_{T3}}\frac{\mu}{\rho_{B1}}\frac{\mu}{\rho_{B2}}\frac{\mu}{\rho_{C3}} + \frac{\mu^2}{\rho_{T3}}\frac{\mu}{\rho_{B1}}\frac{\mu}{\rho_{B3}}\frac{\mu}{\rho_{C3}} \\
&\quad - \frac{\mu^2}{\rho_{T1}}\frac{\mu^2}{\rho_{B1}}\frac{\mu}{\rho_{C1}} - \frac{\mu^2}{\rho_{T2}}\frac{\mu^2}{\rho_{B1}}\frac{\mu}{\rho_{C1}} - \frac{\mu^2}{\rho_{T3}}\frac{\mu^2}{\rho_{B1}}\frac{\mu}{\rho_{C1}} - \frac{\mu^2}{\rho_{T1}}\frac{\mu}{\rho_{B1}}\frac{\mu}{\rho_{B2}}\frac{\mu}{\rho_{C2}} - \frac{\mu^2}{\rho_{T2}}\frac{\mu}{\rho_{B1}}\frac{\mu}{\rho_{B2}}\frac{\mu}{\rho_{C2}} \\
&\quad - \frac{\mu^2}{\rho_{T3}}\frac{\mu}{\rho_{B1}}\frac{\mu}{\rho_{B2}}\frac{\mu}{\rho_{C2}} - \frac{\mu^2}{\rho_{T1}}\frac{\mu}{\rho_{B1}}\frac{\mu}{\rho_{B3}}\frac{\mu}{\rho_{C3}} - \frac{\mu^2}{\rho_{T2}}\frac{\mu}{\rho_{B1}}\frac{\mu}{\rho_{B3}}\frac{\mu}{\rho_{C3}} - \frac{\mu^2}{\rho_{T3}}\frac{\mu}{\rho_{B1}}\frac{\mu}{\rho_{B3}}\frac{\mu}{\rho_{C3}} \\
&\quad + \frac{\mu^2}{\rho_{T1}}\frac{\mu^2}{\rho_{B1}}\frac{\mu}{\rho_{C1}} + \frac{\mu^2}{\rho_{T2}}\frac{\mu^2}{\rho_{B1}}\frac{\mu}{\rho_{C1}} + \frac{\mu^2}{\rho_{T3}}\frac{\mu^2}{\rho_{B1}}\frac{\mu}{\rho_{C1}} + \frac{\mu^2}{\rho_{T1}}\frac{\mu^2}{\rho_{B2}}\frac{\mu}{\rho_{C1}} + \frac{\mu^2}{\rho_{T2}}\frac{\mu^2}{\rho_{B2}}\frac{\mu}{\rho_{C1}} + \frac{\mu^2}{\rho_{T3}}\frac{\mu^2}{\rho_{B2}}\frac{\mu}{\rho_{C1}} \\
&\quad + \frac{\mu^2}{\rho_{T1}}\frac{\mu^2}{\rho_{B3}}\frac{\mu}{\rho_{C1}} + \frac{\mu^2}{\rho_{T2}}\frac{\mu^2}{\rho_{B3}}\frac{\mu}{\rho_{C1}} + \frac{\mu^2}{\rho_{T3}}\frac{\mu^2}{\rho_{B3}}\frac{\mu}{\rho_{C1}} - \frac{\mu^2}{\rho_{T1}}\frac{\mu^2}{\rho_{B1}}\frac{\mu}{\rho_{C1}} - \frac{\mu^2}{\rho_{T2}}\frac{\mu^2}{\rho_{B2}}\frac{\mu}{\rho_{C1}} - \frac{\mu^2}{\rho_{T3}}\frac{\mu^2}{\rho_{B3}}\frac{\mu}{\rho_{C1}} \\
&\quad - 2\frac{\mu}{\rho_{T1}}\frac{\mu}{\rho_{T2}}\frac{\mu}{\rho_{B1}}\frac{\mu}{\rho_{B2}}\frac{\mu}{\rho_{C1}} - 2\frac{\mu}{\rho_{T2}}\frac{\mu}{\rho_{T3}}\frac{\mu}{\rho_{B2}}\frac{\mu}{\rho_{B3}}\frac{\mu}{\rho_{C1}} - 2\frac{\mu}{\rho_{T1}}\frac{\mu}{\rho_{T3}}\frac{\mu}{\rho_{B1}}\frac{\mu}{\rho_{B3}}\frac{\mu}{\rho_{C1}}
\end{aligned}
$$

$$
\begin{aligned}
9X_1 &= \tfrac{\mu}{\rho_{T1}}\tfrac{\mu}{\rho_{T3}}\tfrac{\mu}{\rho_{B2}}\tfrac{\mu}{\rho_{B3}}\tfrac{\mu}{\rho_{C2}} + \tfrac{\mu}{\rho_{T1}}\tfrac{\mu}{\rho_{T2}}\tfrac{\mu}{\rho_{B2}}\tfrac{\mu}{\rho_{B3}}\tfrac{\mu}{\rho_{C3}} + \tfrac{\mu}{\rho_{T2}}\tfrac{\mu}{\rho_{T3}}\tfrac{\mu}{\rho_{B1}}\tfrac{\mu}{\rho_{B3}}\tfrac{\mu}{\rho_{C2}} + \tfrac{\mu}{\rho_{T2}}\tfrac{\mu}{\rho_{T3}}\tfrac{\mu}{\rho_{B1}}\tfrac{\mu}{\rho_{B2}}\tfrac{\mu}{\rho_{C3}} \\
&\quad - \tfrac{\mu^2}{\rho_{B2}}\tfrac{\mu}{\rho_{T1}}\tfrac{\mu}{\rho_{T3}}\tfrac{\mu}{\rho_{C3}} - \tfrac{\mu^2}{\rho_{B3}}\tfrac{\mu}{\rho_{T1}}\tfrac{\mu}{\rho_{T2}}\tfrac{\mu}{\rho_{C2}} - \tfrac{\mu^2}{\rho_{T3}}\tfrac{\mu}{\rho_{B1}}\tfrac{\mu}{\rho_{B2}}\tfrac{\mu}{\rho_{C2}} - \tfrac{\mu^2}{\rho_{T2}}\tfrac{\mu}{\rho_{B1}}\tfrac{\mu}{\rho_{B3}}\tfrac{\mu}{\rho_{C3}} \\
&\quad + \tfrac{\mu^2}{\rho_{T3}}\tfrac{\mu^2}{\rho_{B2}}\tfrac{\mu}{\rho_{C1}} + \tfrac{\mu^2}{\rho_{T2}}\tfrac{\mu^2}{\rho_{B3}}\tfrac{\mu}{\rho_{C1}} - 2\tfrac{\mu}{\rho_{T2}}\tfrac{\mu}{\rho_{T3}}\tfrac{\mu}{\rho_{B2}}\tfrac{\mu}{\rho_{B3}}\tfrac{\mu}{\rho_{C1}} \\
&= \tfrac{\mu}{\rho_{T1}}(\tfrac{\mu}{\rho_{T3}}\tfrac{\mu}{\rho_{B2}}\tfrac{\mu}{\rho_{B3}}\tfrac{\mu}{\rho_{C2}} + \tfrac{\mu}{\rho_{T2}}\tfrac{\mu}{\rho_{B2}}\tfrac{\mu}{\rho_{B3}}\tfrac{\mu}{\rho_{C3}} - \tfrac{\mu^2}{\rho_{B2}}\tfrac{\mu}{\rho_{T3}}\tfrac{\mu}{\rho_{C3}} - \tfrac{\mu^2}{\rho_{B3}}\tfrac{\mu}{\rho_{T2}}\tfrac{\mu}{\rho_{C2}}) \\
&\quad + \tfrac{\mu}{\rho_{B1}}(\tfrac{\mu}{\rho_{T2}}\tfrac{\mu}{\rho_{T3}}\tfrac{\mu}{\rho_{B3}}\tfrac{\mu}{\rho_{C2}} + \tfrac{\mu}{\rho_{T2}}\tfrac{\mu}{\rho_{T3}}\tfrac{\mu}{\rho_{B2}}\tfrac{\mu}{\rho_{C3}} - \tfrac{\mu^2}{\rho_{T3}}\tfrac{\mu}{\rho_{B2}}\tfrac{\mu}{\rho_{C2}} - \tfrac{\mu^2}{\rho_{T2}}\tfrac{\mu}{\rho_{B3}}\tfrac{\mu}{\rho_{C3}}) \\
&\quad + \tfrac{\mu}{\rho_{C1}}(\tfrac{\mu^2}{\rho_{T3}}\tfrac{\mu^2}{\rho_{B2}} + \tfrac{\mu^2}{\rho_{T2}}\tfrac{\mu^2}{\rho_{B3}} - 2\tfrac{\mu}{\rho_{T2}}\tfrac{\mu}{\rho_{T3}}\tfrac{\mu}{\rho_{B2}}\tfrac{\mu}{\rho_{B3}}) \\
&= \tfrac{\mu}{\rho_{T1}}(\tfrac{\mu}{\rho_{B2}}\tfrac{\mu}{\rho_{C3}}(\tfrac{\mu}{\rho_{T2}}\tfrac{\mu}{\rho_{B3}} - \tfrac{\mu}{\rho_{B2}}\tfrac{\mu}{\rho_{T3}}) + \tfrac{\mu}{\rho_{B3}}\tfrac{\mu}{\rho_{C2}}(\tfrac{\mu}{\rho_{T3}}\tfrac{\mu}{\rho_{B2}} - \tfrac{\mu}{\rho_{B3}}\tfrac{\mu}{\rho_{T2}})) \\
&\quad + \tfrac{\mu}{\rho_{B1}}(\tfrac{\mu}{\rho_{C2}}\tfrac{\mu}{\rho_{T3}}(\tfrac{\mu}{\rho_{T2}}\tfrac{\mu}{\rho_{B3}} - \tfrac{\mu}{\rho_{T3}}\tfrac{\mu}{\rho_{B2}}) + \tfrac{\mu}{\rho_{C3}}\tfrac{\mu}{\rho_{T2}}(\tfrac{\mu}{\rho_{T3}}\tfrac{\mu}{\rho_{B2}} - \tfrac{\mu}{\rho_{T2}}\tfrac{\mu}{\rho_{B3}})) \\
&\quad + \tfrac{\mu}{\rho_{C1}}(\tfrac{\mu^2}{\rho_{T3}}\tfrac{\mu^2}{\rho_{B2}} + \tfrac{\mu^2}{\rho_{T2}}\tfrac{\mu^2}{\rho_{B3}} - 2\tfrac{\mu}{\rho_{T2}}\tfrac{\mu}{\rho_{T3}}\tfrac{\mu}{\rho_{B2}}\tfrac{\mu}{\rho_{B3}}) \\
&= \tfrac{\mu}{\rho_{T1}}(\tfrac{\mu}{\rho_{T2}}\tfrac{\mu}{\rho_{B3}} - \tfrac{\mu}{\rho_{B2}}\tfrac{\mu}{\rho_{T3}})(\tfrac{\mu}{\rho_{B2}}\tfrac{\mu}{\rho_{C3}} - \tfrac{\mu}{\rho_{B3}}\tfrac{\mu}{\rho_{C2}}) + \tfrac{\mu}{\rho_{B1}}(\tfrac{\mu}{\rho_{T2}}\tfrac{\mu}{\rho_{B3}} - \tfrac{\mu}{\rho_{T3}}\tfrac{\mu}{\rho_{B2}})(\tfrac{\mu}{\rho_{C2}}\tfrac{\mu}{\rho_{T3}} - \tfrac{\mu}{\rho_{C3}}\tfrac{\mu}{\rho_{T2}}) \\
&\quad + \tfrac{\mu}{\rho_{C1}}(\tfrac{\mu}{\rho_{T2}}\tfrac{\mu}{\rho_{B3}} - \tfrac{\mu}{\rho_{T3}}\tfrac{\mu}{\rho_{B2}})^2
\end{aligned}
$$

$$
\begin{aligned}
X_1 &= \frac{1}{9}(\tfrac{\mu}{\rho_{T2}}\tfrac{\mu}{\rho_{B3}} - \tfrac{\mu}{\rho_{T3}}\tfrac{\mu}{\rho_{B2}})\begin{pmatrix} \tfrac{\mu}{\rho_{T1}}(\tfrac{\mu}{\rho_{B2}}\tfrac{\mu}{\rho_{C3}} - \tfrac{\mu}{\rho_{B3}}\tfrac{\mu}{\rho_{C2}}) + \tfrac{\mu}{\rho_{B1}}(\tfrac{\mu}{\rho_{C2}}\tfrac{\mu}{\rho_{T3}} - \tfrac{\mu}{\rho_{C3}}\tfrac{\mu}{\rho_{T2}}) \\ + \tfrac{\mu}{\rho_{C1}}(\tfrac{\mu}{\rho_{T2}}\tfrac{\mu}{\rho_{B3}} - \tfrac{\mu}{\rho_{T3}}\tfrac{\mu}{\rho_{B2}}) \end{pmatrix} \\
&= \frac{1}{9}(\tfrac{\mu}{\rho_{T2}}\tfrac{\mu}{\rho_{B3}} - \tfrac{\mu}{\rho_{T3}}\tfrac{\mu}{\rho_{B2}})D_3
\end{aligned}
\tag{E.4}
$$

Similarly,

$$
X_2 = \frac{1}{9}(\tfrac{\mu}{\rho_{T3}}\tfrac{\mu}{\rho_{B1}} - \tfrac{\mu}{\rho_{T1}}\tfrac{\mu}{\rho_{B3}})D_3 \tag{E.5}
$$

$$
X_3 = \frac{1}{9}(\tfrac{\mu}{\rho_{T1}}\tfrac{\mu}{\rho_{B2}} - \tfrac{\mu}{\rho_{T2}}\tfrac{\mu}{\rho_{B1}})D_3 \tag{E.6}
$$

Substituting the above X_1, X_2 and X_3 into equation (E.3), the numerator is expressed as

$$
Nume = \frac{1}{9}D_3\left[(\tfrac{\mu}{\rho_{T2}}\tfrac{\mu}{\rho_{B3}} - \tfrac{\mu}{\rho_{T3}}\tfrac{\mu}{\rho_{B2}})r_1 + (\tfrac{\mu}{\rho_{T3}}\tfrac{\mu}{\rho_{B1}} - \tfrac{\mu}{\rho_{T1}}\tfrac{\mu}{\rho_{B3}})r_2 + (\tfrac{\mu}{\rho_{T1}}\tfrac{\mu}{\rho_{B2}} - \tfrac{\mu}{\rho_{T2}}\tfrac{\mu}{\rho_{B1}})r_3\right] \tag{E.7}
$$

Substituting the numerator (E.7) and denominator (E.2) into equation (E.1) obtains the three-energy KES equation (5.11) with silimar derivations for the other two components.

Appendix F SNR derivation for Three-Component NESI

Starting from the projected density equations for the three-component NESI,

$$\begin{aligned}
\rho_T t_T &= \frac{1}{nD_{33}}\left[R_{T1}\sum_i\left(\tfrac{\mu}{\rho}_{Ti}\, r_i\right)+R_{T2}\sum_i\left(\tfrac{\mu}{\rho}_{Bi}\, r_i\right)+R_{T3}\sum_i\left(\tfrac{\mu}{\rho}_{Ci}\, r_i\right)\right]\\
\rho_B t_B &= \frac{1}{nD_{33}}\left[R_{B1}\sum_i\left(\tfrac{\mu}{\rho}_{Ti}\, r_i\right)+R_{B2}\sum_i\left(\tfrac{\mu}{\rho}_{Bi}\, r_i\right)+R_{B3}\sum_i\left(\tfrac{\mu}{\rho}_{Ci}\, r_i\right)\right] \qquad (1\le i\le n) \qquad (5.31)\\
\rho_C t_C &= \frac{1}{nD_{33}}\left[R_{C1}\sum_i\left(\tfrac{\mu}{\rho}_{Ti}\, r_i\right)+R_{C2}\sum_i\left(\tfrac{\mu}{\rho}_{Bi}\, r_i\right)+R_{C3}\sum_i\left(\tfrac{\mu}{\rho}_{Ci}\, r_i\right)\right]
\end{aligned}$$

$$\text{where}\quad r_i = -\ln\left(\frac{N_i}{N_{0i}}\right) = \tfrac{\mu}{\rho}_{Ti}\,\rho_T t_T + \tfrac{\mu}{\rho}_{Bi}\,\rho_B t_B + \tfrac{\mu}{\rho}_{Ci}\,\rho_C t_C \qquad (1\le i\le n) \qquad (1.28)$$

applying propagation of error on equation (5.31) assumes independent measurements of both the incident beam at each energy N_{0i} and the transmitted beam at each energy N_i,

$$\begin{aligned}
\sigma^2_{\rho_T t_T} &= \sum_i\left[\left(\frac{\partial \rho_T t_T}{\partial N_i}\right)^2(\delta N_i)^2+\left(\frac{\partial \rho_T t_T}{\partial N_{0i}}\right)^2(\delta N_{0i})^2\right]\\
\sigma^2_{\rho_B t_B} &= \sum_i\left[\left(\frac{\partial \rho_B t_B}{\partial N_i}\right)^2(\delta N_i)^2+\left(\frac{\partial \rho_B t_B}{\partial N_{0i}}\right)^2(\delta N_{0i})^2\right] \qquad (F.1)\\
\sigma^2_{\rho_C t_C} &= \sum_i\left[\left(\frac{\partial \rho_C t_C}{\partial N_i}\right)^2(\delta N_i)^2+\left(\frac{\partial \rho_C t_C}{\partial N_{0i}}\right)^2(\delta N_{0i})^2\right]
\end{aligned}$$

With Poisson statistics, the variance in the photon counts,

$$(\delta N_i)^2 = N_i \qquad\qquad (\delta N_{0i})^2 = N_{0i}$$

The included partial derivatives are,

$$\frac{\partial r_i}{\partial N_i} = -\frac{\partial}{\partial N_i}\left(\ln\frac{N_i}{N_{0i}}\right) = -\frac{1}{N_i} \qquad\qquad \frac{\partial r_i}{\partial N_{0i}} = -\frac{\partial}{\partial N_{0i}}\left(\ln\frac{N_i}{N_{0i}}\right) = \frac{1}{N_{0i}}$$

$$\frac{\partial \rho_T t_T}{\partial N_i} = \frac{\partial \rho_T t_T}{\partial r_i}\frac{\partial r_i}{\partial N_i} \qquad \frac{\partial \rho_T t_T}{\partial N_{0i}} = \frac{\partial \rho_T t_T}{\partial r_i}\frac{\partial r_i}{\partial N_{0i}}$$

$$\frac{\partial \rho_B t_B}{\partial N_i} = \frac{\partial \rho_B t_B}{\partial r_i}\frac{\partial r_i}{\partial N_i} \qquad \frac{\partial \rho_B t_B}{\partial N_{0i}} = \frac{\partial \rho_B t_B}{\partial r_i}\frac{\partial r_i}{\partial N_{0i}}$$

$$\frac{\partial \rho_C t_C}{\partial N_i} = \frac{\partial \rho_C t_C}{\partial r_i}\frac{\partial r_i}{\partial N_i} \qquad \frac{\partial \rho_C t_C}{\partial N_{0i}} = \frac{\partial \rho_C t_C}{\partial r_i}\frac{\partial r_i}{\partial N_{0i}}$$

$$\frac{\partial \rho_T t_T}{\partial r_i} = \frac{\partial}{\partial r_i}\left[\frac{R_{T1}\sum_i\left(\frac{\mu}{\rho_{Ti}}r_i\right)+R_{T2}\sum_i\left(\frac{\mu}{\rho_{Bi}}r_i\right)+R_{T3}\sum_i\left(\frac{\mu}{\rho_{Ci}}r_i\right)}{nD_{33}}\right]=\frac{R_{T1}\frac{\mu}{\rho_{Ti}}+R_{T2}\frac{\mu}{\rho_{Bi}}+R_{T3}\frac{\mu}{\rho_{Ci}}}{nD_{33}}$$

$$\frac{\partial \rho_B t_B}{\partial r_i} = \frac{\partial}{\partial r_i}\left[\frac{R_{B1}\sum_i\left(\frac{\mu}{\rho_{Ti}}r_i\right)+R_{B2}\sum_i\left(\frac{\mu}{\rho_{Bi}}r_i\right)+R_{B3}\sum_i\left(\frac{\mu}{\rho_{Ci}}r_i\right)}{nD_{33}}\right]=\frac{R_{B1}\frac{\mu}{\rho_{Ti}}+R_{B2}\frac{\mu}{\rho_{Bi}}+R_{B3}\frac{\mu}{\rho_{Ci}}}{nD_{33}}$$

$$\frac{\partial \rho_C t_C}{\partial r_i} = \frac{\partial}{\partial r_i}\left[\frac{R_{C1}\sum_i\left(\frac{\mu}{\rho_{Ti}}r_i\right)+R_{C2}\sum_i\left(\frac{\mu}{\rho_{Bi}}r_i\right)+R_{C3}\sum_i\left(\frac{\mu}{\rho_{Ci}}r_i\right)}{nD_{33}}\right]=\frac{R_{C1}\frac{\mu}{\rho_{Ti}}+R_{C2}\frac{\mu}{\rho_{Bi}}+R_{C3}\frac{\mu}{\rho_{Ci}}}{nD_{33}}$$

Combining these derived items the image noise from equation (F.1) could be determined.

$$\sigma^2_{\rho_C t_C} = \sum_i\left[\left(\frac{\partial \rho_C t_C}{\partial N_i}\right)^2(\delta N_i)^2+\left(\frac{\partial \rho_C t_C}{\partial N_{0i}}\right)^2(\delta N_{0i})^2\right]$$

$$= \sum_i\left[\left(\frac{R_{C1}\frac{\mu}{\rho_{Ti}}+R_{C2}\frac{\mu}{\rho_{Bi}}+R_{C3}\frac{\mu}{\rho_{Ci}}}{nD_{33}}\right)^2\left(\left(-\frac{1}{N_i}\right)^2 N_i+\left(\frac{1}{N_{0i}}\right)^2 N_{0i}\right)\right]$$

$$\sigma^2_{\rho_C t_C} = \frac{1}{n^2 D_{33}^2}\sum_i\left[\left(R_{C1}\frac{\mu}{\rho_{Ti}}+R_{C2}\frac{\mu}{\rho_{Bi}}+R_{C3}\frac{\mu}{\rho_{Ci}}\right)^2\left(\frac{1}{N_i}+\frac{1}{N_{0i}}\right)\right] \tag{F.2}$$

The SNR for the projected contrast image will be,

$$SNR_C = \frac{\rho_C t_C}{\sigma_{\rho_C t_C}} = \frac{nD_{33}}{\sqrt{\sum_i\left[\left(R_{C1}\frac{\mu}{\rho_{Ti}}+R_{C2}\frac{\mu}{\rho_{Bi}}+R_{C3}\frac{\mu}{\rho_{Ci}}\right)^2\left(\frac{1}{N_i}+\frac{1}{N_{0i}}\right)\right]}}\rho_C t_C \tag{5.32}$$

Similarly, image noise for the soft tissue and bone material are determined from equation (F.1).

And SNR of the soft tissue and bone material are derived as,

$$SNR_T = \frac{\rho_T t_T}{\sigma_{\rho_T t_T}} = \frac{nD_{33}}{\sqrt{\sum_i \left[\left(R_{T1} \frac{\mu}{\rho_{Ti}} + R_{T2} \frac{\mu}{\rho_{Bi}} + R_{T3} \frac{\mu}{\rho_{Ci}} \right)^2 \left(\frac{1}{N_i} + \frac{1}{N_{0i}} \right) \right]}} \rho_T t_T$$

$$SNR_B = \frac{\rho_B t_B}{\sigma_{\rho_B t_B}} = \frac{nD_{33}}{\sqrt{\sum_i \left[\left(R_{B1} \frac{\mu}{\rho_{Ti}} + R_{B2} \frac{\mu}{\rho_{Bi}} + R_{B3} \frac{\mu}{\rho_{Ci}} \right)^2 \left(\frac{1}{N_i} + \frac{1}{N_{0i}} \right) \right]}} \rho_B t_B \qquad (5.32)$$

To simplify the SNR equation (5.32), equal incident flux N_{0i} and equal transmitted flux N_i for all the energy *i* at each pixel are assumed. The noise equation (F.2) is simplified as,

$$\sigma^2_{\rho_C t_C} \approx \frac{1}{n^2 D_{33}^2} \left(\frac{1}{N} + \frac{1}{N_0} \right) \sum_i \left(R_{C1} \frac{\mu}{\rho_{Ti}} + R_{C2} \frac{\mu}{\rho_{Bi}} + R_{C3} \frac{\mu}{\rho_{Ci}} \right)^2 = \frac{1}{n^2 D_{33}^2} \left(\frac{1}{N} + \frac{1}{N_0} \right) X_C \qquad (F.3)$$

$$\begin{aligned}
X_C &= \sum_i \left(R_{C1} \frac{\mu}{\rho_{Ti}} + R_{C2} \frac{\mu}{\rho_{Bi}} + R_{C3} \frac{\mu}{\rho_{Ci}} \right)^2 \\
&= \sum_i \left(R_{C1}^2 \frac{\mu^2}{\rho_{Ti}} + R_{C2}^2 \frac{\mu^2}{\rho_{Bi}} + R_{C3}^2 \frac{\mu^2}{\rho_{Ci}} + 2R_{C1}R_{C2} \frac{\mu}{\rho_{Ti}} \frac{\mu}{\rho_{Bi}} + 2R_{C2}R_{C3} \frac{\mu}{\rho_{Bi}} \frac{\mu}{\rho_{Ci}} + 2R_{C1}R_{C3} \frac{\mu}{\rho_{Ti}} \frac{\mu}{\rho_{Ci}} \right) \\
&= R_{C1}^2 \sum_i \frac{\mu^2}{\rho_{Ti}} + R_{C2}^2 \sum_i \frac{\mu^2}{\rho_{Bi}} + R_{C3}^2 \sum_i \frac{\mu^2}{\rho_{Ci}} + 2R_{C1}R_{C2} \sum_i \frac{\mu}{\rho_{Ti}} \frac{\mu}{\rho_{Bi}} + 2R_{C2}R_{C3} \sum_i \frac{\mu}{\rho_{Bi}} \frac{\mu}{\rho_{Ci}} + 2R_{C1}R_{C3} \sum_i \frac{\mu}{\rho_{Ti}} \frac{\mu}{\rho_{Ci}} \\
&= n \frac{\mu}{\rho_{TT}} R_{C1}^2 + n \frac{\mu}{\rho_{BB}} R_{C2}^2 + n \frac{\mu}{\rho_{CC}} R_{C3}^2 + 2n \frac{\mu}{\rho_{TB}} R_{C1}R_{C2} + 2n \frac{\mu}{\rho_{BC}} R_{C2}R_{C3} + 2n \frac{\mu}{\rho_{TC}} R_{C1}R_{C3}
\end{aligned}$$

Replacing $R_{C1} = \left(\frac{\mu}{\rho_{TB}} \frac{\mu}{\rho_{BC}} - \frac{\mu}{\rho_{TC}} \frac{\mu}{\rho_{BB}} \right)$ $R_{C2} = \left(\frac{\mu}{\rho_{TB}} \frac{\mu}{\rho_{TC}} - \frac{\mu}{\rho_{TT}} \frac{\mu}{\rho_{BC}} \right)$ $R_{C3} = \left(\frac{\mu}{\rho_{TT}} \frac{\mu}{\rho_{BB}} - \frac{\mu^2}{\rho_{TB}} \right)$

$$\begin{aligned}
\frac{1}{n} X_C &= \frac{\mu}{\rho_{TT}} R_{C1}^2 + \frac{\mu}{\rho_{BB}} R_{C2}^2 + \frac{\mu}{\rho_{CC}} R_{C3}^2 + 2\frac{\mu}{\rho_{TB}} R_{C1}R_{C2} + 2\frac{\mu}{\rho_{BC}} R_{C2}R_{C3} + 2\frac{\mu}{\rho_{TC}} R_{C1}R_{C3} \\
&= \frac{\mu}{\rho_{TT}} \left(\frac{\mu}{\rho_{TB}} \frac{\mu}{\rho_{BC}} - \frac{\mu}{\rho_{TC}} \frac{\mu}{\rho_{BB}} \right)^2 + \frac{\mu}{\rho_{BB}} \left(\frac{\mu}{\rho_{TB}} \frac{\mu}{\rho_{TC}} - \frac{\mu}{\rho_{TT}} \frac{\mu}{\rho_{BC}} \right)^2 + \frac{\mu}{\rho_{CC}} \left(\frac{\mu}{\rho_{TT}} \frac{\mu}{\rho_{BB}} - \frac{\mu^2}{\rho_{TB}} \right)^2 \\
&\quad + 2\frac{\mu}{\rho_{TB}} \left(\frac{\mu}{\rho_{TB}} \frac{\mu}{\rho_{BC}} - \frac{\mu}{\rho_{TC}} \frac{\mu}{\rho_{BB}} \right) \left(\frac{\mu}{\rho_{TB}} \frac{\mu}{\rho_{TC}} - \frac{\mu}{\rho_{TT}} \frac{\mu}{\rho_{BC}} \right) + 2\frac{\mu}{\rho_{BC}} \left(\frac{\mu}{\rho_{TB}} \frac{\mu}{\rho_{TC}} - \frac{\mu}{\rho_{TT}} \frac{\mu}{\rho_{BC}} \right) \left(\frac{\mu}{\rho_{TT}} \frac{\mu}{\rho_{BB}} - \frac{\mu^2}{\rho_{TB}} \right) \\
&\quad + 2\frac{\mu}{\rho_{TC}} \left(\frac{\mu}{\rho_{TB}} \frac{\mu}{\rho_{BC}} - \frac{\mu}{\rho_{TC}} \frac{\mu}{\rho_{BB}} \right) \left(\frac{\mu}{\rho_{TT}} \frac{\mu}{\rho_{BB}} - \frac{\mu^2}{\rho_{TB}} \right) \\
&= \frac{\mu^2}{\rho_{TB}} \frac{\mu^2}{\rho_{BC}} \frac{\mu}{\rho_{TT}} + \frac{\mu^2}{\rho_{TC}} \frac{\mu^2}{\rho_{BB}} \frac{\mu}{\rho_{TT}} - 2\frac{\mu}{\rho_{TT}} \frac{\mu}{\rho_{TB}} \frac{\mu}{\rho_{TC}} \frac{\mu}{\rho_{BB}} \frac{\mu}{\rho_{BC}} + \frac{\mu^2}{\rho_{TB}} \frac{\mu^2}{\rho_{TC}} \frac{\mu}{\rho_{BB}} + \frac{\mu^2}{\rho_{TT}} \frac{\mu^2}{\rho_{BC}} \frac{\mu}{\rho_{BB}} \\
&\quad - 2\frac{\mu}{\rho_{TT}} \frac{\mu}{\rho_{TB}} \frac{\mu}{\rho_{TC}} \frac{\mu}{\rho_{BB}} \frac{\mu}{\rho_{BC}} + \frac{\mu}{\rho_{CC}} \left(\frac{\mu}{\rho_{TT}} \frac{\mu}{\rho_{BB}} - \frac{\mu^2}{\rho_{TB}} \right)^2 \\
&\quad + 2\frac{\mu^3}{\rho_{TB}} \frac{\mu}{\rho_{TC}} \frac{\mu}{\rho_{BC}} - 2\frac{\mu^2}{\rho_{TB}} \frac{\mu^2}{\rho_{TC}} \frac{\mu}{\rho_{BB}} - 2\frac{\mu^2}{\rho_{TB}} \frac{\mu^2}{\rho_{BC}} \frac{\mu}{\rho_{TT}} + 2\frac{\mu}{\rho_{TT}} \frac{\mu}{\rho_{TB}} \frac{\mu}{\rho_{TC}} \frac{\mu}{\rho_{BB}} \frac{\mu}{\rho_{BC}} \\
&\quad + 2\frac{\mu}{\rho_{BC}} \left(\frac{\mu}{\rho_{TB}} \frac{\mu}{\rho_{TC}} - \frac{\mu}{\rho_{TT}} \frac{\mu}{\rho_{BC}} \right) \left(\frac{\mu}{\rho_{TT}} \frac{\mu}{\rho_{BB}} - \frac{\mu^2}{\rho_{TB}} \right) + 2\frac{\mu}{\rho_{TC}} \left(\frac{\mu}{\rho_{TB}} \frac{\mu}{\rho_{BC}} - \frac{\mu}{\rho_{TC}} \frac{\mu}{\rho_{BB}} \right) \left(\frac{\mu}{\rho_{TT}} \frac{\mu}{\rho_{BB}} - \frac{\mu^2}{\rho_{TB}} \right) \\
&= \frac{\mu^2}{\rho_{TC}} \frac{\mu^2}{\rho_{BB}} \frac{\mu}{\rho_{TT}} + \frac{\mu^2}{\rho_{TT}} \frac{\mu^2}{\rho_{BC}} \frac{\mu}{\rho_{BB}} - 2\frac{\mu}{\rho_{TT}} \frac{\mu}{\rho_{TB}} \frac{\mu}{\rho_{TC}} \frac{\mu}{\rho_{BB}} \frac{\mu}{\rho_{BC}} + 2\frac{\mu^3}{\rho_{TB}} \frac{\mu}{\rho_{TC}} \frac{\mu}{\rho_{BC}} - \frac{\mu^2}{\rho_{TB}} \frac{\mu^2}{\rho_{TC}} \frac{\mu}{\rho_{BB}} - \frac{\mu^2}{\rho_{TB}} \frac{\mu^2}{\rho_{BC}} \frac{\mu}{\rho_{TT}} \\
&\quad + \frac{\mu}{\rho_{CC}} \left(\frac{\mu}{\rho_{TT}} \frac{\mu}{\rho_{BB}} - \frac{\mu^2}{\rho_{TB}} \right)^2 + 2\frac{\mu}{\rho_{BC}} \left(\frac{\mu}{\rho_{TB}} \frac{\mu}{\rho_{TC}} - \frac{\mu}{\rho_{TT}} \frac{\mu}{\rho_{BC}} \right) \left(\frac{\mu}{\rho_{TT}} \frac{\mu}{\rho_{BB}} - \frac{\mu^2}{\rho_{TB}} \right) + 2\frac{\mu}{\rho_{TC}} \left(\frac{\mu}{\rho_{TB}} \frac{\mu}{\rho_{BC}} - \frac{\mu}{\rho_{TC}} \frac{\mu}{\rho_{BB}} \right) \left(\frac{\mu}{\rho_{TT}} \frac{\mu}{\rho_{BB}} - \frac{\mu^2}{\rho_{TB}} \right)
\end{aligned}$$

$$
\begin{aligned}
\frac{1}{n}X_C &= \tfrac{\mu}{\rho_{TT}}\tfrac{\mu}{\rho_{BB}}\left(\tfrac{\mu^2}{\rho_{TC}}\tfrac{\mu}{\rho_{BB}}+\tfrac{\mu}{\rho_{TT}}\tfrac{\mu^2}{\rho_{BC}}-2\tfrac{\mu}{\rho_{TB}}\tfrac{\mu}{\rho_{TC}}\tfrac{\mu}{\rho_{BC}}\right)+\tfrac{\mu^2}{\rho_{TB}}\left(2\tfrac{\mu}{\rho_{TB}}\tfrac{\mu}{\rho_{TC}}\tfrac{\mu}{\rho_{BC}}-\tfrac{\mu^2}{\rho_{TC}}\tfrac{\mu}{\rho_{BB}}-\tfrac{\mu^2}{\rho_{BC}}\tfrac{\mu}{\rho_{TT}}\right)\\
&+\tfrac{\mu}{\rho_{CC}}\left(\tfrac{\mu}{\rho_{TT}}\tfrac{\mu}{\rho_{BB}}-\tfrac{\mu^2}{\rho_{TB}}\right)^2+2\tfrac{\mu}{\rho_{BC}}\left(\tfrac{\mu}{\rho_{TB}}\tfrac{\mu}{\rho_{TC}}-\tfrac{\mu}{\rho_{TT}}\tfrac{\mu}{\rho_{BC}}\right)\left(\tfrac{\mu}{\rho_{TT}}\tfrac{\mu}{\rho_{BB}}-\tfrac{\mu^2}{\rho_{TB}}\right)\\
&+2\tfrac{\mu}{\rho_{TC}}\left(\tfrac{\mu}{\rho_{TB}}\tfrac{\mu}{\rho_{BC}}-\tfrac{\mu}{\rho_{TC}}\tfrac{\mu}{\rho_{BB}}\right)\left(\tfrac{\mu}{\rho_{TT}}\tfrac{\mu}{\rho_{BB}}-\tfrac{\mu^2}{\rho_{TB}}\right)\\
&=\left(\tfrac{\mu}{\rho_{TT}}\tfrac{\mu}{\rho_{BB}}-\tfrac{\mu^2}{\rho_{TB}}\right)\left(\tfrac{\mu^2}{\rho_{TC}}\tfrac{\mu}{\rho_{BB}}+\tfrac{\mu^2}{\rho_{BC}}\tfrac{\mu}{\rho_{TT}}-2\tfrac{\mu}{\rho_{TB}}\tfrac{\mu}{\rho_{TC}}\tfrac{\mu}{\rho_{BC}}\right)+\tfrac{\mu}{\rho_{CC}}\left(\tfrac{\mu}{\rho_{TT}}\tfrac{\mu}{\rho_{BB}}-\tfrac{\mu^2}{\rho_{TB}}\right)^2\\
&+2\tfrac{\mu}{\rho_{BC}}\left(\tfrac{\mu}{\rho_{TB}}\tfrac{\mu}{\rho_{TC}}-\tfrac{\mu}{\rho_{TT}}\tfrac{\mu}{\rho_{BC}}\right)\left(\tfrac{\mu}{\rho_{TT}}\tfrac{\mu}{\rho_{BB}}-\tfrac{\mu^2}{\rho_{TB}}\right)+2\tfrac{\mu}{\rho_{TC}}\left(\tfrac{\mu}{\rho_{TB}}\tfrac{\mu}{\rho_{BC}}-\tfrac{\mu}{\rho_{TC}}\tfrac{\mu}{\rho_{BB}}\right)\left(\tfrac{\mu}{\rho_{TT}}\tfrac{\mu}{\rho_{BB}}-\tfrac{\mu^2}{\rho_{TB}}\right)\\
&=\left(\tfrac{\mu}{\rho_{TT}}\tfrac{\mu}{\rho_{BB}}-\tfrac{\mu^2}{\rho_{TB}}\right)\left[\begin{array}{l}\tfrac{\mu^2}{\rho_{TC}}\tfrac{\mu}{\rho_{BB}}+\tfrac{\mu^2}{\rho_{BC}}\tfrac{\mu}{\rho_{TT}}-2\tfrac{\mu}{\rho_{TB}}\tfrac{\mu}{\rho_{TC}}\tfrac{\mu}{\rho_{BC}}+\tfrac{\mu}{\rho_{CC}}\left(\tfrac{\mu}{\rho_{TT}}\tfrac{\mu}{\rho_{BB}}-\tfrac{\mu^2}{\rho_{TB}}\right)\\+2\tfrac{\mu}{\rho_{BC}}\left(\tfrac{\mu}{\rho_{TB}}\tfrac{\mu}{\rho_{TC}}-\tfrac{\mu}{\rho_{TT}}\tfrac{\mu}{\rho_{BC}}\right)+2\tfrac{\mu}{\rho_{TC}}\left(\tfrac{\mu}{\rho_{TB}}\tfrac{\mu}{\rho_{BC}}-\tfrac{\mu}{\rho_{TC}}\tfrac{\mu}{\rho_{BB}}\right)\end{array}\right]\\
&=\left(\tfrac{\mu}{\rho_{TT}}\tfrac{\mu}{\rho_{BB}}-\tfrac{\mu^2}{\rho_{TB}}\right)\left[\begin{array}{l}\tfrac{\mu^2}{\rho_{TC}}\tfrac{\mu}{\rho_{BB}}+\tfrac{\mu^2}{\rho_{BC}}\tfrac{\mu}{\rho_{TT}}-2\tfrac{\mu}{\rho_{TB}}\tfrac{\mu}{\rho_{TC}}\tfrac{\mu}{\rho_{BC}}+\tfrac{\mu}{\rho_{CC}}\tfrac{\mu}{\rho_{TT}}\tfrac{\mu}{\rho_{BB}}-\tfrac{\mu^2}{\rho_{TB}}\tfrac{\mu}{\rho_{CC}}\\+2\tfrac{\mu}{\rho_{BC}}\tfrac{\mu}{\rho_{TB}}\tfrac{\mu}{\rho_{TC}}-2\tfrac{\mu^2}{\rho_{BC}}\tfrac{\mu}{\rho_{TT}}+2\tfrac{\mu}{\rho_{TC}}\tfrac{\mu}{\rho_{TB}}\tfrac{\mu}{\rho_{BC}}-2\tfrac{\mu^2}{\rho_{TC}}\tfrac{\mu}{\rho_{BB}}\end{array}\right]\\
&=\left(\tfrac{\mu}{\rho_{TT}}\tfrac{\mu}{\rho_{BB}}-\tfrac{\mu^2}{\rho_{TB}}\right)\left[\tfrac{\mu}{\rho_{CC}}\tfrac{\mu}{\rho_{TT}}\tfrac{\mu}{\rho_{BB}}-\tfrac{\mu^2}{\rho_{TB}}\tfrac{\mu}{\rho_{CC}}-\tfrac{\mu^2}{\rho_{BC}}\tfrac{\mu}{\rho_{TT}}-\tfrac{\mu^2}{\rho_{TC}}\tfrac{\mu}{\rho_{BB}}+2\tfrac{\mu}{\rho_{BC}}\tfrac{\mu}{\rho_{TB}}\tfrac{\mu}{\rho_{TC}}\right]\\
&=\left(\tfrac{\mu}{\rho_{TT}}\tfrac{\mu}{\rho_{BB}}-\tfrac{\mu^2}{\rho_{TB}}\right)\left[\left(\tfrac{\mu}{\rho_{CC}}\tfrac{\mu}{\rho_{TT}}\tfrac{\mu}{\rho_{BB}}-\tfrac{\mu^2}{\rho_{BC}}\tfrac{\mu}{\rho_{TT}}\right)+\left(\tfrac{\mu}{\rho_{BC}}\tfrac{\mu}{\rho_{TB}}\tfrac{\mu}{\rho_{TC}}-\tfrac{\mu^2}{\rho_{TB}}\tfrac{\mu}{\rho_{CC}}\right)+\left(\tfrac{\mu}{\rho_{BC}}\tfrac{\mu}{\rho_{TB}}\tfrac{\mu}{\rho_{TC}}-\tfrac{\mu^2}{\rho_{TC}}\tfrac{\mu}{\rho_{BB}}\right)\right]\\
&=\left(\tfrac{\mu}{\rho_{TT}}\tfrac{\mu}{\rho_{BB}}-\tfrac{\mu^2}{\rho_{TB}}\right)\left[\tfrac{\mu}{\rho_{TT}}\left(\tfrac{\mu}{\rho_{BB}}\tfrac{\mu}{\rho_{CC}}-\tfrac{\mu^2}{\rho_{BC}}\right)+\tfrac{\mu}{\rho_{TB}}\left(\tfrac{\mu}{\rho_{BC}}\tfrac{\mu}{\rho_{TC}}-\tfrac{\mu}{\rho_{TB}}\tfrac{\mu}{\rho_{CC}}\right)+\tfrac{\mu}{\rho_{TC}}\left(\tfrac{\mu}{\rho_{TB}}\tfrac{\mu}{\rho_{BC}}-\tfrac{\mu}{\rho_{TC}}\tfrac{\mu}{\rho_{BB}}\right)\right]
\end{aligned}
$$

$$X_C = nD_{33}\left(\tfrac{\mu}{\rho_{TT}}\tfrac{\mu}{\rho_{BB}}-\tfrac{\mu^2}{\rho_{TB}}\right) \tag{F.4}$$

Substituting X_C into equation (F.3), the noise for the contrast material would be

$$\sigma^2_{\rho_C t_C} \approx \left(\frac{1}{N}+\frac{1}{N_0}\right)\frac{\left(\tfrac{\mu}{\rho_{TT}}\tfrac{\mu}{\rho_{BB}}-\tfrac{\mu^2}{\rho_{TB}}\right)}{nD_{33}} \tag{F.5}$$

Then the SNR equation would be

$$SNR_C = \frac{\rho_C t_C}{\sigma_{\rho_C t_C}} \approx \sqrt{\frac{nD_{33}}{\left(\frac{1}{N}+\frac{1}{N_0}\right)\left(\tfrac{\mu}{\rho_{TT}}\tfrac{\mu}{\rho_{BB}}-\tfrac{\mu^2}{\rho_{TB}}\right)}}\rho_C t_C = \sqrt{\frac{nNN_0}{N+N_0}}\sqrt{\frac{D_{33}}{\tfrac{\mu}{\rho_{TT}}\tfrac{\mu}{\rho_{BB}}-\tfrac{\mu^2}{\rho_{TB}}}}\rho_C t_C$$

Assuming dilute contrast material in the object $N \approx N_0 e^{-\mu t}$ where $\mu = \tfrac{\mu}{\rho_T}\rho_T$ and $t = t_T + t_B + t_C$, the simplified SNR for the projected contrast material would be,

$$
\begin{aligned}
SNR_C &\approx \sqrt{\frac{nN_0}{1+e^{\mu t}}}\sqrt{\frac{D_{33}}{\frac{\mu}{\rho_{TT}}\frac{\mu}{\rho_{BB}}-\frac{\mu^2}{\rho_{TB}}}}\rho_C t_C \\
&= \sqrt{\frac{nN_0}{1+e^{\mu t}}}\sqrt{\frac{\frac{\mu}{\rho_{TT}}(\frac{\mu}{\rho_{BB}}\frac{\mu}{\rho_{CC}}-\frac{\mu^2}{\rho_{BC}})+\frac{\mu}{\rho_{TB}}(\frac{\mu}{\rho_{BC}}\frac{\mu}{\rho_{TC}}-\frac{\mu}{\rho_{TB}}\frac{\mu}{\rho_{CC}})+\frac{\mu}{\rho_{TC}}(\frac{\mu}{\rho_{TB}}\frac{\mu}{\rho_{BC}}-\frac{\mu}{\rho_{TC}}\frac{\mu}{\rho_{BB}})}{\frac{\mu}{\rho_{TT}}\frac{\mu}{\rho_{BB}}-\frac{\mu^2}{\rho_{TB}}}}\rho_C t_C \\
&= \sqrt{\frac{nN_0}{1+e^{\mu t}}}\sqrt{\frac{\frac{\mu}{\rho_{TT}}\frac{\mu}{\rho_{BB}}\frac{\mu}{\rho_{CC}}-\frac{\mu^2}{\rho_{BC}}\frac{\mu}{\rho_{TT}}+\frac{\mu}{\rho_{TB}}\frac{\mu}{\rho_{BC}}\frac{\mu}{\rho_{TC}}-\frac{\mu^2}{\rho_{TB}}\frac{\mu}{\rho_{CC}}+\frac{\mu}{\rho_{TC}}\frac{\mu}{\rho_{TB}}\frac{\mu}{\rho_{BC}}-\frac{\mu^2}{\rho_{TC}}\frac{\mu}{\rho_{BB}}}{\frac{\mu}{\rho_{CC}}(\frac{\mu}{\rho_{TT}}\frac{\mu}{\rho_{BB}}-\frac{\mu^2}{\rho_{TB}})}}\sqrt{\frac{\mu}{\rho_{CC}}}\rho_C t_C \\
&= \sqrt{\frac{nN_0}{1+e^{\mu t}}}\sqrt{\frac{\frac{\mu}{\rho_{CC}}(\frac{\mu}{\rho_{TT}}\frac{\mu}{\rho_{BB}}-\frac{\mu^2}{\rho_{TB}})-\frac{\mu^2}{\rho_{BC}}\frac{\mu}{\rho_{TT}}+2\frac{\mu}{\rho_{TB}}\frac{\mu}{\rho_{TC}}\frac{\mu}{\rho_{BC}}-\frac{\mu^2}{\rho_{TC}}\frac{\mu}{\rho_{BB}}}{\frac{\mu}{\rho_{CC}}(\frac{\mu}{\rho_{TT}}\frac{\mu}{\rho_{BB}}-\frac{\mu^2}{\rho_{TB}})}}\sqrt{\frac{\mu}{\rho_{CC}}}\rho_C t_C \\
&= \sqrt{\frac{nN_0}{1+e^{\mu t}}}\sqrt{1-\frac{\frac{\mu^2}{\rho_{BC}}\frac{\mu}{\rho_{TT}}-2\frac{\mu}{\rho_{TB}}\frac{\mu}{\rho_{TC}}\frac{\mu}{\rho_{BC}}+\frac{\mu^2}{\rho_{TC}}\frac{\mu}{\rho_{BB}}}{\frac{\mu}{\rho_{CC}}(\frac{\mu}{\rho_{TT}}\frac{\mu}{\rho_{BB}}-\frac{\mu^2}{\rho_{TB}})}}\sqrt{\frac{\mu}{\rho_{CC}}}\rho_C t_C
\end{aligned}
$$

Then the simplified SNR equation for the contrast material is

$$
SNR_C \approx \sqrt{\frac{nN_0}{1+e^{\mu t}}}\sqrt{1-\frac{\frac{\mu}{\rho_{TT}}\frac{\mu^2}{\rho_{BC}}+\frac{\mu}{\rho_{BB}}\frac{\mu^2}{\rho_{TC}}-2\frac{\mu}{\rho_{TB}}\frac{\mu}{\rho_{TC}}\frac{\mu}{\rho_{BC}}}{\frac{\mu}{\rho_{CC}}(\frac{\mu}{\rho_{TT}}\frac{\mu}{\rho_{BB}}-\frac{\mu^2}{\rho_{TB}})}}\sqrt{\frac{\mu}{\rho_{CC}}}\rho_C t_C \tag{5.33}
$$

Similarly, the simplified SNR for the soft tissure and bone material are,

$$
\begin{aligned}
SNR_T &\approx \sqrt{\frac{nN_0}{1+e^{\mu t}}}\sqrt{1-\frac{\frac{\mu}{\rho_{BB}}\frac{\mu^2}{\rho_{TC}}+\frac{\mu}{\rho_{CC}}\frac{\mu^2}{\rho_{TB}}-2\frac{\mu}{\rho_{TB}}\frac{\mu}{\rho_{TC}}\frac{\mu}{\rho_{BC}}}{\frac{\mu}{\rho_{TT}}(\frac{\mu}{\rho_{BB}}\frac{\mu}{\rho_{CC}}-\frac{\mu^2}{\rho_{BC}})}}\sqrt{\frac{\mu}{\rho_{TT}}}\rho_T t_T \\
SNR_B &\approx \sqrt{\frac{nN_0}{1+e^{\mu t}}}\sqrt{1-\frac{\frac{\mu}{\rho_{TT}}\frac{\mu^2}{\rho_{BC}}+\frac{\mu}{\rho_{CC}}\frac{\mu^2}{\rho_{TB}}-2\frac{\mu}{\rho_{TB}}\frac{\mu}{\rho_{TC}}\frac{\mu}{\rho_{BC}}}{\frac{\mu}{\rho_{BB}}(\frac{\mu}{\rho_{TT}}\frac{\mu}{\rho_{CC}}-\frac{\mu^2}{\rho_{TC}})}}\sqrt{\frac{\mu}{\rho_{BB}}}\rho_B t_B
\end{aligned} \tag{5.33}
$$

As expected, all the SNR values are dependent upon the square root of the incident photon count (nN_0) and amount of material present. Also all the SNR values have a dimensionless common term as well as a RMS average of the mass attenuation coefficients over the photon energy range.

Appendix G Left Inverse Derivation for *m*-Component NESI

For a general NESI system containing *m* number of components, the negative logarithm of the normalized signals could be arranged in a matrix form as,

$$\begin{bmatrix} r_1 \\ \vdots \\ r_i \\ \vdots \\ r_n \end{bmatrix} = \begin{bmatrix} -\ln\left(\frac{N_1}{N_{01}}\right) \\ -\ln\left(\frac{N_i}{N_{0i}}\right) \\ -\ln\left(\frac{N_n}{N_{0n}}\right) \end{bmatrix} = \begin{bmatrix} \frac{\mu}{\rho}_{11}\rho_1 t_1 + .. + \frac{\mu}{\rho}_{j1}\rho_j t_j + .. + \frac{\mu}{\rho}_{m1}\rho_m t_m \\ .. \\ \frac{\mu}{\rho}_{1i}\rho_1 t_1 + .. + \frac{\mu}{\rho}_{ji}\rho_j t_j + .. + \frac{\mu}{\rho}_{mi}\rho_m t_m \\ .. \\ \frac{\mu}{\rho}_{1n}\rho_1 t_1 + .. + \frac{\mu}{\rho}_{jn}\rho_j t_j + .. + \frac{\mu}{\rho}_{mn}\rho_m t_m \end{bmatrix}$$

$$\begin{bmatrix} r_1 \\ \vdots \\ r_i \\ \vdots \\ r_n \end{bmatrix} = \begin{bmatrix} \frac{\mu}{\rho}_{11} & .. & \frac{\mu}{\rho}_{j1} & .. & \frac{\mu}{\rho}_{m1} \\ \vdots & & \vdots & & \vdots \\ \frac{\mu}{\rho}_{1i} & .. & \frac{\mu}{\rho}_{ji} & .. & \frac{\mu}{\rho}_{mi} \\ \vdots & & \vdots & & \vdots \\ \frac{\mu}{\rho}_{1n} & .. & \frac{\mu}{\rho}_{jn} & .. & \frac{\mu}{\rho}_{mn} \end{bmatrix} \begin{bmatrix} \rho_1 t_1 \\ \vdots \\ \rho_j t_j \\ \vdots \\ \rho_m t_m \end{bmatrix} \tag{G.1}$$

Multiplying the left inverse of the $n \times m$ matrix of the $\frac{\mu}{\rho}$, the projected densities are derived as,

$$\begin{bmatrix} \rho_1 t_1 \\ \vdots \\ \rho_j t_j \\ \vdots \\ \rho_m t_m \end{bmatrix} = \begin{bmatrix} \frac{\mu}{\rho}_{11} & .. & \frac{\mu}{\rho}_{j1} & .. & \frac{\mu}{\rho}_{m1} \\ \vdots & & \vdots & & \vdots \\ \frac{\mu}{\rho}_{1i} & .. & \frac{\mu}{\rho}_{ji} & .. & \frac{\mu}{\rho}_{mi} \\ \vdots & & \vdots & & \vdots \\ \frac{\mu}{\rho}_{1n} & .. & \frac{\mu}{\rho}_{jn} & .. & \frac{\mu}{\rho}_{mn} \end{bmatrix}_{left}^{-1} \begin{bmatrix} r_1 \\ \vdots \\ r_i \\ \vdots \\ r_n \end{bmatrix}$$

$$\begin{bmatrix}\rho_1 t_1\\ \vdots\\ \rho_j t_j\\ \vdots\\ \rho_m t_m\end{bmatrix}=\left(\begin{bmatrix}\frac{\mu}{\rho}_{11} & \cdots & \frac{\mu}{\rho}_{j1} & \cdots & \frac{\mu}{\rho}_{m1}\\ \vdots & & \vdots & & \vdots\\ \frac{\mu}{\rho}_{1i} & \cdots & \frac{\mu}{\rho}_{ji} & \cdots & \frac{\mu}{\rho}_{mi}\\ \vdots & & \vdots & & \vdots\\ \frac{\mu}{\rho}_{1n} & \cdots & \frac{\mu}{\rho}_{jn} & \cdots & \frac{\mu}{\rho}_{mn}\end{bmatrix}^T\begin{bmatrix}\frac{\mu}{\rho}_{11} & \cdots & \frac{\mu}{\rho}_{j1} & \cdots & \frac{\mu}{\rho}_{m1}\\ \vdots & & \vdots & & \vdots\\ \frac{\mu}{\rho}_{1i} & \cdots & \frac{\mu}{\rho}_{ji} & \cdots & \frac{\mu}{\rho}_{mi}\\ \vdots & & \vdots & & \vdots\\ \frac{\mu}{\rho}_{1n} & \cdots & \frac{\mu}{\rho}_{jn} & \cdots & \frac{\mu}{\rho}_{mn}\end{bmatrix}\right)^{-1}\begin{bmatrix}\frac{\mu}{\rho}_{11} & \cdots & \frac{\mu}{\rho}_{j1} & \cdots & \frac{\mu}{\rho}_{m1}\\ \vdots & & \vdots & & \vdots\\ \frac{\mu}{\rho}_{1i} & \cdots & \frac{\mu}{\rho}_{ji} & \cdots & \frac{\mu}{\rho}_{mi}\\ \vdots & & \vdots & & \vdots\\ \frac{\mu}{\rho}_{1n} & \cdots & \frac{\mu}{\rho}_{jn} & \cdots & \frac{\mu}{\rho}_{mn}\end{bmatrix}^T\begin{bmatrix}r_1\\ \vdots\\ r_i\\ \vdots\\ r_n\end{bmatrix}$$

$$=\left(\begin{bmatrix}\frac{\mu}{\rho}_{11} & \cdots & \frac{\mu}{\rho}_{1i} & \cdots & \frac{\mu}{\rho}_{1n}\\ \vdots & & \vdots & & \vdots\\ \frac{\mu}{\rho}_{j1} & \cdots & \frac{\mu}{\rho}_{ji} & \cdots & \frac{\mu}{\rho}_{jn}\\ \vdots & & \vdots & & \vdots\\ \frac{\mu}{\rho}_{m1} & \cdots & \frac{\mu}{\rho}_{mi} & \cdots & \frac{\mu}{\rho}_{mn}\end{bmatrix}\begin{bmatrix}\frac{\mu}{\rho}_{11} & \cdots & \frac{\mu}{\rho}_{j1} & \cdots & \frac{\mu}{\rho}_{m1}\\ \vdots & & \vdots & & \vdots\\ \frac{\mu}{\rho}_{1i} & \cdots & \frac{\mu}{\rho}_{ji} & \cdots & \frac{\mu}{\rho}_{mi}\\ \vdots & & \vdots & & \vdots\\ \frac{\mu}{\rho}_{1n} & \cdots & \frac{\mu}{\rho}_{jn} & \cdots & \frac{\mu}{\rho}_{mn}\end{bmatrix}\right)^{-1}\begin{bmatrix}\frac{\mu}{\rho}_{11} & \cdots & \frac{\mu}{\rho}_{1i} & \cdots & \frac{\mu}{\rho}_{1n}\\ \vdots & & \vdots & & \vdots\\ \frac{\mu}{\rho}_{j1} & \cdots & \frac{\mu}{\rho}_{ji} & \cdots & \frac{\mu}{\rho}_{jn}\\ \vdots & & \vdots & & \vdots\\ \frac{\mu}{\rho}_{m1} & \cdots & \frac{\mu}{\rho}_{mi} & \cdots & \frac{\mu}{\rho}_{mn}\end{bmatrix}\begin{bmatrix}r_1\\ \vdots\\ r_i\\ \vdots\\ r_n\end{bmatrix}$$

$$\begin{bmatrix}\rho_1 t_1\\ \vdots\\ \rho_j t_j\\ \vdots\\ \rho_m t_m\end{bmatrix}=\begin{bmatrix}\sum_i \frac{\mu}{\rho}_{1i}^2 & \cdots & \sum_i\left(\frac{\mu}{\rho}_{1i}\,\frac{\mu}{\rho}_{ji}\right) & \cdots & \sum_i\left(\frac{\mu}{\rho}_{1i}\,\frac{\mu}{\rho}_{mi}\right)\\ \vdots & & \vdots & & \vdots\\ \sum_i\left(\frac{\mu}{\rho}_{ji}\,\frac{\mu}{\rho}_{1i}\right) & \cdots & \sum_i \frac{\mu}{\rho}_{ji}^2 & \cdots & \sum_i\left(\frac{\mu}{\rho}_{ji}\,\frac{\mu}{\rho}_{mi}\right)\\ \vdots & & \vdots & & \vdots\\ \sum_i\left(\frac{\mu}{\rho}_{mi}\,\frac{\mu}{\rho}_{1i}\right) & \cdots & \sum_i\left(\frac{\mu}{\rho}_{mi}\,\frac{\mu}{\rho}_{ji}\right) & \cdots & \sum_i \frac{\mu}{\rho}_{mi}^2\end{bmatrix}^{-1}\begin{bmatrix}\sum_i\left(\frac{\mu}{\rho}_{1i}\,r_i\right)\\ \vdots\\ \sum_i\left(\frac{\mu}{\rho}_{ji}\,r_i\right)\\ \vdots\\ \sum_i\left(\frac{\mu}{\rho}_{mi}\,r_i\right)\end{bmatrix} \tag{G.2}$$

The sums of the $\frac{\mu}{\rho}$ products can be replaced by their averages

$$\begin{aligned}
&\frac{\mu}{\rho}_{\langle 11\rangle}\equiv\frac{1}{n}\sum_i \frac{\mu}{\rho}_{1i}^2 \qquad \frac{\mu}{\rho}_{\langle jj\rangle}\equiv\frac{1}{n}\sum_i \frac{\mu}{\rho}_{ji}^2 \qquad \frac{\mu}{\rho}_{\langle mm\rangle}\equiv\frac{1}{n}\sum_i \frac{\mu}{\rho}_{mi}^2\\
&\frac{\mu}{\rho}_{\langle 1m\rangle}\equiv\frac{1}{n}\sum_i\left(\frac{\mu}{\rho}_{1i}\,\frac{\mu}{\rho}_{mi}\right)=\frac{1}{n}\sum_i\left(\frac{\mu}{\rho}_{mi}\,\frac{\mu}{\rho}_{1i}\right)\equiv\frac{\mu}{\rho}_{\langle m1\rangle}\\
&\frac{\mu}{\rho}_{\langle j1\rangle}\equiv\frac{1}{n}\sum_i\left(\frac{\mu}{\rho}_{ji}\,\frac{\mu}{\rho}_{1i}\right)\equiv\frac{\mu}{\rho}_{\langle 1j\rangle} \qquad \frac{\mu}{\rho}_{\langle mj\rangle}\equiv\frac{1}{n}\sum_i\left(\frac{\mu}{\rho}_{mi}\,\frac{\mu}{\rho}_{ji}\right)\equiv\frac{\mu}{\rho}_{\langle jm\rangle}
\end{aligned} \tag{5.39}$$

Then

$$\begin{bmatrix}\rho_1 t_1\\ \vdots\\ \rho_j t_j\\ \vdots\\ \rho_m t_m\end{bmatrix}=\begin{bmatrix}n\frac{\mu}{\rho}_{\langle 11\rangle} & \cdots & n\frac{\mu}{\rho}_{\langle 1j\rangle} & \cdots & n\frac{\mu}{\rho}_{\langle 1m\rangle}\\ \vdots & & \vdots & & \vdots\\ n\frac{\mu}{\rho}_{\langle j1\rangle} & \cdots & n\frac{\mu}{\rho}_{\langle jj\rangle} & \cdots & n\frac{\mu}{\rho}_{\langle jm\rangle}\\ \vdots & & \vdots & & \vdots\\ n\frac{\mu}{\rho}_{\langle m1\rangle} & \cdots & n\frac{\mu}{\rho}_{\langle mj\rangle} & \cdots & n\frac{\mu}{\rho}_{\langle mm\rangle}\end{bmatrix}^{-1}\begin{bmatrix}\sum_i\left(\frac{\mu}{\rho}_{1i}\,r_i\right)\\ \vdots\\ \sum_i\left(\frac{\mu}{\rho}_{ji}\,r_i\right)\\ \vdots\\ \sum_i\left(\frac{\mu}{\rho}_{mi}\,r_i\right)\end{bmatrix} \tag{G.3}$$

$$\begin{bmatrix} \rho_1 t_1 \\ \vdots \\ \rho_j t_j \\ \vdots \\ \rho_m t_m \end{bmatrix} = \frac{1}{nD_{mm}} \begin{bmatrix} R_{11} & .. & R_{1j} & .. & R_{1m} \\ \vdots & & \vdots & & \vdots \\ R_{j1} & .. & R_{jj} & .. & R_{jm} \\ \vdots & & \vdots & & \vdots \\ R_{m1} & .. & R_{mj} & .. & R_{mm} \end{bmatrix} \begin{bmatrix} \sum_i \left(\frac{\mu}{\rho}_{1i} r_i\right) \\ \vdots \\ \sum_i \left(\frac{\mu}{\rho}_{ji} r_i\right) \\ \vdots \\ \sum_i \left(\frac{\mu}{\rho}_{mi} r_i\right) \end{bmatrix} \tag{G.4}$$

where $$\begin{bmatrix} \frac{\mu}{\rho}\langle 11\rangle & .. & \frac{\mu}{\rho}\langle 1j\rangle & .. & \frac{\mu}{\rho}\langle 1m\rangle \\ \vdots & & \vdots & & \vdots \\ \frac{\mu}{\rho}\langle j1\rangle & .. & \frac{\mu}{\rho}\langle jj\rangle & .. & \frac{\mu}{\rho}\langle jm\rangle \\ \vdots & & \vdots & & \vdots \\ \frac{\mu}{\rho}\langle m1\rangle & .. & \frac{\mu}{\rho}\langle mj\rangle & .. & \frac{\mu}{\rho}\langle mm\rangle \end{bmatrix}^{-1} = \frac{1}{D_{mm}} \begin{bmatrix} R_{11} & .. & R_{1j} & .. & R_{1m} \\ \vdots & & \vdots & & \vdots \\ R_{j1} & .. & R_{jj} & .. & R_{jm} \\ \vdots & & \vdots & & \vdots \\ R_{m1} & .. & R_{mj} & .. & R_{mm} \end{bmatrix}$$

Then the projected density equations (5.38) in chapter 5.3.2.3 are obtained.

$$\rho_1 t_1 = \frac{1}{nD_{mm}} \left[R_{11} \sum_i \left(\frac{\mu}{\rho}_{1i} r_i\right) + \ldots + R_{1j} \sum_i \left(\frac{\mu}{\rho}_{ji} r_i\right) + \ldots + R_{1m} \sum_i \left(\frac{\mu}{\rho}_{mi} r_i\right) \right]$$

...

$$\rho_j t_j = \frac{1}{nD_{mm}} \left[R_{j1} \sum_i \left(\frac{\mu}{\rho}_{1i} r_i\right) + \ldots + R_{jj} \sum_i \left(\frac{\mu}{\rho}_{ji} r_i\right) + \ldots + R_{jm} \sum_i \left(\frac{\mu}{\rho}_{mi} r_i\right) \right] \tag{5.38}$$

...

$$\rho_m t_m = \frac{1}{nD_{mm}} \left[R_{m1} \sum_i \left(\frac{\mu}{\rho}_{1i} r_i\right) + \ldots + R_{mj} \sum_i \left(\frac{\mu}{\rho}_{ji} r_i\right) + \ldots + R_{mm} \sum_i \left(\frac{\mu}{\rho}_{mi} r_i\right) \right]$$

Appendix H SNR derivation for *m*-Component NESI

Starting from the projected density equations for the *m*-component NESI,

$$\rho_j t_j = \frac{1}{nD_{mm}}\left[R_{j1}\sum_i\left(\frac{\mu}{\rho}_{1i} r_i\right)+\ldots+R_{jj}\sum_i\left(\frac{\mu}{\rho}_{ji} r_i\right)+\ldots+R_{jm}\sum_i\left(\frac{\mu}{\rho}_{mi} r_i\right)\right] \tag{5.38}$$

where $r_i = -\ln\left(\frac{N_i}{N_{0i}}\right) = \sum_j \frac{\mu}{\rho}_{ji}\rho_j t_j \qquad (1 \le i \le n,\ 1 \le j \le m,\ n \ge m)$ (1.37)

applying propagation of error on equation (5.38) assumes independent measurements of both the incident beam at each energy N_{0i} and the transmitted beam at each energy N_i,

$$\sigma^2_{\rho_j t_j} = \sum_i\left[\left(\frac{\partial \rho_j t_j}{\partial N_i}\right)^2(\delta N_i)^2+\left(\frac{\partial \rho_j t_j}{\partial N_{0i}}\right)^2(\delta N_{0i})^2\right] \tag{H.1}$$

With Poisson statistics, the variance in the photon counts,

$$(\delta N_i)^2 = N_i \qquad\qquad (\delta N_{0i})^2 = N_{0i}$$

The included partial derivatives are,

$$\frac{\partial \rho_j t_j}{\partial N_i} = \frac{\partial \rho_j t_j}{\partial r_i}\frac{\partial r_i}{\partial N_i} \qquad\qquad \frac{\partial \rho_j t_j}{\partial N_{0i}} = \frac{\partial \rho_j t_j}{\partial r_i}\frac{\partial r_i}{\partial N_{0i}}$$

$$\frac{\partial r_i}{\partial N_i} = -\frac{\partial}{\partial N_i}\left(\ln\frac{N_i}{N_{0i}}\right) = -\frac{1}{N_i} \qquad\qquad \frac{\partial r_i}{\partial N_{0i}} = -\frac{\partial}{\partial N_{0i}}\left(\ln\frac{N_i}{N_{0i}}\right) = \frac{1}{N_{0i}}$$

$$\frac{\partial \rho_j t_j}{\partial r_i} = \frac{\partial}{\partial r_i}\left[\frac{R_{j1}\sum_i\left(\frac{\mu}{\rho}_{1i} r_i\right)+\ldots+R_{jj}\sum_i\left(\frac{\mu}{\rho}_{ji} r_i\right)+\ldots+R_{jm}\sum_i\left(\frac{\mu}{\rho}_{mi} r_i\right)}{nD_{mm}}\right] = \frac{R_{j1}\frac{\mu}{\rho}_{1i}+\ldots+R_{jj}\frac{\mu}{\rho}_{ji}+\ldots+R_{jm}\frac{\mu}{\rho}_{mi}}{nD_{mm}}$$

Combining these derived items the image noise from equation (H.1) could be determined.

$$\sigma^2_{\rho_j t_j} = \sum_i \left[\left(\frac{\partial \rho_j t_j}{\partial N_i} \right)^2 (\delta N_i)^2 + \left(\frac{\partial \rho_j t_j}{\partial N_{0i}} \right)^2 (\delta N_{0i})^2 \right]$$

$$= \sum_i \left[\left(\frac{R_{j1} \frac{\mu}{\rho}_{1i} + \ldots + R_{jj} \frac{\mu}{\rho}_{ji} + \ldots + R_{jm} \frac{\mu}{\rho}_{mi}}{nD_{mm}} \right)^2 \left(\left(-\frac{1}{N_i} \right)^2 N_i + \left(\frac{1}{N_{0i}} \right)^2 N_{0i} \right) \right]$$

$$\sigma^2_{\rho_j t_j} = \frac{1}{n^2 D^2_{mm}} \sum_i \left[\left(R_{j1} \frac{\mu}{\rho}_{1i} + \ldots + R_{jj} \frac{\mu}{\rho}_{ji} + \ldots + R_{jm} \frac{\mu}{\rho}_{mi} \right)^2 \left(\frac{1}{N_i} + \frac{1}{N_{0i}} \right) \right] \tag{H.2}$$

The SNR for the projected contrast image will be,

$$SNR_j = \frac{\rho_j t_j}{\sigma_{\rho_j t_j}} = \frac{nD_{mm}}{\sqrt{\sum_i \left[\left(R_{j1} \frac{\mu}{\rho}_{1i} + \ldots + R_{jj} \frac{\mu}{\rho}_{ji} + \ldots + R_{jm} \frac{\mu}{\rho}_{mi} \right)^2 \left(\frac{1}{N_i} + \frac{1}{N_{0i}} \right) \right]}} \rho_j t_j \tag{5.40}$$

Assuming equal incident flux N_{0i} for all the energy i, equal transmitted flux N_i for all the energy i and $N \approx N_0 e^{-\mu t}$, the simplified SNR for the projected material would be,

$$SNR_j \approx \frac{1}{\sqrt{\frac{1}{N} + \frac{1}{N_0}}} \frac{nD_{mm}}{\sqrt{\sum_i \left(R_{j1} \frac{\mu}{\rho}_{1i} + \ldots + R_{jj} \frac{\mu}{\rho}_{ji} + \ldots + R_{jm} \frac{\mu}{\rho}_{mi} \right)^2}} \rho_j t_j$$

$$SNR_j \approx \sqrt{\frac{nN_0}{1 + e^{\mu t}}} \frac{\sqrt{n} D_{mm}}{\sqrt{\sum_i \left(R_{j1} \frac{\mu}{\rho}_{1i} + \ldots + R_{jj} \frac{\mu}{\rho}_{ji} + \ldots + R_{jm} \frac{\mu}{\rho}_{mi} \right)^2}} \rho_j t_j \tag{5.41}$$

Appendix I Reuse Licenses for Papers and Figures

Table I.1 Published papers and figures used in this dissertation with approved reuse licenses attached in the Appendix I.

License Number	*Paper reference*	*Author*	*Reuse content*	*Reuse location*
Appendix I.1	[Zhu07]	Zhu, Y. ect.	Full article with modifications	Chapter 3.1
Appendix I.2	[Zhu08]	Zhu, Y. ect.	Full article with modifications	Chapter 3.2
Appendix I.3	[Zhu10]	Zhu, Y. ect.	Full article with modifications	Chapter 4.1
Appendix I.4	[Mal05]	Malzer, W. ect.	Adapted Figure 1	Figure 1.4
Appendix I.5	[Tak09]	Takeuchi, A. ect.	Figure 2	Figure 1.5A
Appendix I.6	[Fei05]	Feiters, M.C. ect.	Figure 2 and 4	Figure 5.32
Appendix I.7	[Tak10]	Takeuchi, A. ect.	Figure 1	Figure 1.5B

Appendix I.1

ELSEVIER LICENSE
TERMS AND CONDITIONS

Jan 20, 2012

This is a License Agreement between Ying Zhu ("You") and Elsevier ("Elsevier") provided by Copyright Clearance Center ("CCC"). The license consists of your order details, the terms and conditions provided by Elsevier, and the payment terms and conditions.

All payments must be made in full to CCC. For payment instructions, please see information listed at the bottom of this form.

Supplier

Elsevier Limited
The Boulevard,Langford Lane
Kidlington,Oxford,OX5 1GB,UK

Registered Company Number	1982084
Customer name	Ying Zhu
Customer address	16 Hampstead Rd. NW Calgary, AB T3A 6E9
License number	2833401166190
License date	Jan 20, 2012
Licensed content publisher	Elsevier
Licensed content publication	Nuclear Instruments and Methods in Physics Research Section A: Accelerators, Spectrometers, Detectors and Associated Equipment
Licensed content title	Fabrication of a small animal restraint for synchrotron biomedical imaging using a rapid prototyper
Licensed content author	Ying Zhu,Honglin Zhang,Richard McCrea,Brian Bewer,Sheldon Wiebe,Helen Nichol,Christopher Ryan,Tomasz Wysokinski,Dean Chapman
Licensed content date	11 November 2007
Licensed content volume number	582
Licensed content issue number	1
Number of pages	4
Start Page	229
End Page	232
Type of Use	reuse in a thesis/dissertation
Intended publisher of new work	other
Portion	full article
Format	electronic
Are you the author of this Elsevier article?	Yes
Will you be translating?	No
Order reference number	
Title of your thesis/dissertation	Bent Laue Crystals in Biomedical Applications
Expected completion date	May 2012
Estimated size (number of pages)	200
Elsevier VAT number	GB 494 6272 12
Permissions price	0.00 USD
VAT/Local Sales Tax	0.0 USD / 0.0 GBP
Total	0.00 USD

Appendix I.2

ELSEVIER LICENSE
TERMS AND CONDITIONS

Jan 20, 2012

This is a License Agreement between Ying Zhu ("You") and Elsevier ("Elsevier") provided by Copyright Clearance Center ("CCC"). The license consists of your order details, the terms and conditions provided by Elsevier, and the payment terms and conditions.

All payments must be made in full to CCC. For payment instructions, please see information listed at the bottom of this form.

Supplier	Elsevier Limited The Boulevard,Langford Lane Kidlington,Oxford,OX5 1GB,UK
Registered Company Number	1982084
Customer name	Ying Zhu
Customer address	16 Hampstead Rd. NW Calgary, AB T3A 6E9
License number	2833401448543
License date	Jan 20, 2012
Licensed content publisher	Elsevier
Licensed content publication	Nuclear Instruments and Methods in Physics Research Section A: Accelerators, Spectrometers, Detectors and Associated Equipment
Licensed content title	Field flatteners fabricated with a rapid prototyper for K-edge subtraction imaging of small animals
Licensed content author	Ying Zhu,Honglin Zhang,Brian Bewer,Bogdan Florin Gh. Popescu,Helen Nichol,Dean Chapman
Licensed content date	11 April 2008
Licensed content volume number	588
Licensed content issue number	3
Number of pages	6
Start Page	442
End Page	447
Type of Use	reuse in a thesis/dissertation
Intended publisher of new work	other
Portion	full article

Format	electronic
Are you the author of this Elsevier article?	Yes
Will you be translating?	No
Order reference number	
Title of your thesis/dissertation	Bent Laue Crystals in Biomedical Applications
Expected completion date	May 2012
Estimated size (number of pages)	200
Elsevier VAT number	GB 494 6272 12
Permissions price	0.00 USD
VAT/Local Sales Tax	0.0 USD / 0.0 GBP
Total	0.00 USD

Appendix I.3

From: "AIPRights Permissions" <Rights@aip.org>
Date: August-26-11 12:45 PM
To: "Ying" <ying.zhu@usask.ca>
Subject: RE: Require permission to include my article into my dissertation

Dear Dr. Zhu:

Thank you for requesting permission to reproduce material from American Institute of Physics publications.

Permission is granted – subject to the conditions outlined below – for the following:

Zhu, Y.; Bewer, B.; Zhang, H.; Nichol, H.; Thomlinson, B.; Chapman, D., Bent Laue X-ray Fluorescence Imaging of Manganese in Biological Tissues – Preliminary Results, 10th International Conference on Radiation Instrumentation (SRI 2009), Melbourne, Australia, American Institute of Physics Conference Proceedings, 1234 (2010) 457-60

To be used in the following manner:

Reproduced as part of your dissertation.

1. The American Institute of Physics grants you the right to reproduce the material indicated above on a one-time, non-exclusive basis, solely for the purpose described. Permission must be requested separately for any future or additional use.

2. This permission pertains only to print use and its electronic equivalent, including CD-ROM or DVD.

3. The following copyright notice must appear with the material (please fill in the information indicated by capital letters): "Reprinted with permission from [FULL CITATION]. Copyright [PUBLICATION YEAR], American Institute of Physics."
Full citation format is as follows: Author names, journal title, Vol. #, Page #, (Year of publication).
For an article, the copyright notice must be printed on the first page of the article or book chapter. For figures, photographs, covers, or tables, the notice may appear with the material, in a footnote, or in the reference list.

4. This permission does not apply to any materials credited to sources other than the copyright holder.

5. If you have not already done so, please attempt to obtain permission from at least one of the authors. The author's address can be obtained from the article.

Please let us know if you have any questions.

Sincerely,
Susann Brailey

Manager, Rights and Permissions
Office of the Publisher, Journals and Technical Publications
American Institute of Physics
Suite 1NO1
2 Huntington Quadrangle
Melville, NY 11747-4502
Phone: 1-516-576-2268
Fax: 1-516-576-2450
Email: rights@aip.org

Appendix I.4

ELSEVIER LICENSE
TERMS AND CONDITIONS

Jan 20, 2012

This is a License Agreement between Ying Zhu ("You") and Elsevier ("Elsevier") provided by Copyright Clearance Center ("CCC"). The license consists of your order details, the terms and conditions provided by Elsevier, and the payment terms and conditions.

All payments must be made in full to CCC. For payment instructions, please see information listed at the bottom of this form.

Supplier	Elsevier Limited The Boulevard,Langford Lane Kidlington,Oxford,OX5 1GB,UK
Registered Company Number	1982084
Customer name	Ying Zhu
Customer address	16 Hampstead Rd. NW Calgary, AB T3A 6E9
License number	2833400034204
License date	Jan 20, 2012
Licensed content publisher	Elsevier
Licensed content publication	Spectrochimica Acta Part B: Atomic Spectroscopy

Licensed content title	A model for the confocal volume of 3D micro X-ray fluorescence spectrometer
Licensed content author	Wolfgang Malzer,Birgit Kanngießer
Licensed content date	October 2005
Licensed content volume number	60
Licensed content issue number	9–10
Number of pages	8
Start Page	1334
End Page	1341
Type of Use	reuse in a thesis/dissertation
Intended publisher of new work	other
Portion	figures/tables/illustrations
Number of figures/tables/illustrations	1
Format	electronic
Are you the author of this Elsevier article?	No
Will you be translating?	No
Order reference number	
Title of your thesis/dissertation	Bent Laue Crystals in Biomedical Applications
Expected completion date	May 2012
Estimated size (number of pages)	200
Elsevier VAT number	GB 494 6272 12
Permissions price	0.00 USD
VAT/Local Sales Tax	0.0 USD / 0.0 GBP
Total	0.00 USD

Appendix I.5

From: "Peter Strickland" <ps@iucr.org>
Date: January-23-12 6:25 AM
To: "Ying" <ying.zhu@usask.ca>
Cc: "Peter Strickland" <ps@iucr.org>
Subject: Re: Require permission to use a figure in my PhD dissertation

Dear Ying ZHU

Thank you for your email.

Permission is hereby granted, on behalf of the IUCr, for you to reproduce the material specified below, subject to the following conditions:

1. Reproduction is intended in a primary journal, secondary journal, CD-ROM, book or thesis.

2. The original article in which the material appeared is cited.

Best wishes
Peter Strickland

Managing Editor
IUCr Journals

IUCr Editorial Office, 5 Abbey Square, Chester CH1 2HU, England
Phone: 44 1244 342878 Fax: 44 1244 314888 Email: ps@iucr.org
Ftp: ftp.iucr.org WWW: http://journals.iucr.org/

> Dear Managing Editor of IUCr Journals,
>
> Could I ask for your permission to use the Figure 2 (page 618) of the following paper published in the Journal of Synchrotron Radiation? This figure will be used in my PhD dissertation as Figure 4.38A for literature review of confocal X-ray fluorescence imaging methods. The title of my PhD dissertation is "Bent Laue Crystals in Biomedical Applications" which is expected to publish in May 2012. A pdf version of my PhD Thesis will be posted as Electronic Theses & Dissertations (ETD) Collection at the University of Saskatchewan Library. A credit line acknowledging the original source will be included as a reference.
>
> Figure 2 at page 618 of the paper detailed below:
>
> Takeuchi, A.; Terada, Y.; Suzuki, Y.; Uesugi, K.; Aoki, S., Confocal full-field X-ray microscope for novel three-dimensional X-ray imaging, Journal of Synchrotron Radiation, 16 (5) (2009) 616-21
>
> Would you please email me your written permission so that it could be included into my dissertation for clarification of the copyright? Great thanks!
>
> Sincerely,
>
> Ying ZHU
> Biomedical Engineering
> University of Saskatchewan
> Saskatoon, SK, Canada

Appendix I.6

To: "Ying" <ying.zhu@usask.ca>
Cc: "Peter Strickland" <ps@iucr.org>
Subject: Re: Require permission to reuse data from 2 figures in my PhD dissertation

Dear Ying

Thank you for your email.

Permission is hereby granted, on behalf of the IUCr, for you
to reproduce the material specified below, subject to the following
conditions:

1. Reproduction is intended in a primary journal, secondary journal,
CD-ROM, book or thesis.

2. The original article in which the material appeared is cited.

3. IUCr's copyright permission is indicated next to the
Figure in print. In electronic form, this acknowledgement
must be visible at the same time as the Figure, and
must be hyperlinked to the article
(http://dx.doi.org/10.1107/S0909049504027815).

Best wishes
Peter Strickland
Managing Editor
IUCr Journals

IUCr Editorial Office, 5 Abbey Square, Chester CH1 2HU, England
Phone: 44 1244 342878 Fax: 44 1244 314888 Email: ps@iucr.org
Ftp: ftp.iucr.org WWW: http://journals.iucr.org/

> Dear Managing Editor of IUCr Journals,
>
> Could I ask for your permission to reuse some data in the Figure 2 and Figure 4 (page 88) of the following paper published in the Journal of Synchrotron Radiation? These data will be reused in my PhD dissertation to compare with our measured XAS data of Iodine. The title of my PhD dissertation is "Bent Laue Crystals in Biomedical Applications" which is expected to be published in 2012. A pdf version of my PhD Thesis will be posted as Electronic Theses & Dissertations (ETD) Collection at the University of Saskatchewan Library. A credit line acknowledging the original source will be included in the Appendix as a reference.

> Figure 2 and Figure 4 at page 88 of the following paper:
>
> M.C. Feiters; F.C. Küpper; W. Meyer-Klaucke, X-ray absorption spectroscopic studies on model compounds for biological iodine and bromine, Journal of Synchrotron Radiation, v 12, n 1, p 85-93, January 2005
>
> Would you please email me your written permission so that it could be included into my dissertation for clarification of the copyright? Great thanks!
>
> Sincerely,
>
> Ying ZHU
> Biomedical Engineering
> University of Saskatchewan
> Saskatoon, SK, Canada

Appendix I.7

ELSEVIER LICENSE
TERMS AND CONDITIONS

Jan 20, 2012

This is a License Agreement between Ying Zhu ("You") and Elsevier ("Elsevier") provided by Copyright Clearance Center ("CCC"). The license consists of your order details, the terms and conditions provided by Elsevier, and the payment terms and conditions.

All payments must be made in full to CCC. For payment instructions, please see information listed at the bottom of this form.

Supplier	Elsevier Limited The Boulevard,Langford Lane Kidlington,Oxford,OX5 1GB,UK
Registered Company Number	1982084
Customer name	Ying Zhu
Customer address	16 Hampstead Rd. NW Calgary, AB T3A 6E9
License number	2833390016993
License date	Jan 20, 2012
Licensed content publisher	Elsevier
Licensed content publication	Nuclear Instruments and Methods in Physics Research Section A: Accelerators, Spectrometers, Detectors and Associated Equipment
Licensed content title	Three-dimensional X-ray fluorescence imaging with confocal full-field X-ray microscope
Licensed content author	Akihisa Takeuchi,Yasuko Terada,Kentaro Uesugi,Yoshio Suzuki
Licensed content date	1 May 2010
Licensed content volume number	616
Licensed content issue number	2–3
Number of pages	5
Start Page	261
End Page	265
Type of Use	reuse in a thesis/dissertation
Portion	figures/tables/illustrations
Number of figures/tables/illustrations	1
Format	electronic
Are you the author of this Elsevier article?	No
Will you be translating?	No

Order reference number	
Title of your thesis/dissertation	Bent Laue Crystals in Biomedical Applications
Expected completion date	May 2012
Estimated size (number of pages)	200
Elsevier VAT number	GB 494 6272 12
Permissions price	0.00 USD
VAT/Local Sales Tax	0.0 USD / 0.0 GBP
Total	0.00 USD
Terms and Conditions	

INTRODUCTION

1. The publisher for this copyrighted material is Elsevier. By clicking "accept" in connection with completing this licensing transaction, you agree that the following terms and conditions apply to this transaction (along with the Billing and Payment terms and conditions established by Copyright Clearance Center, Inc. ("CCC"), at the time that you opened your Rightslink account and that are available at any time at http://myaccount.copyright.com).

GENERAL TERMS

2. Elsevier hereby grants you permission to reproduce the aforementioned material subject to the terms and conditions indicated.

3. Acknowledgement: If any part of the material to be used (for example, figures) has appeared in our publication with credit or acknowledgement to another source, permission must also be sought from that source. If such permission is not obtained then that material may not be included in your publication/copies. Suitable acknowledgement to the source must be made, either as a footnote or in a reference list at the end of your publication, as follows:

"Reprinted from Publication title, Vol /edition number, Author(s), Title of article / title of chapter, Pages No., Copyright (Year), with permission from Elsevier [OR APPLICABLE SOCIETY COPYRIGHT OWNER]." Also Lancet special credit - "Reprinted from The Lancet, Vol. number, Author(s), Title of article, Pages No., Copyright (Year), with permission from Elsevier."

4. Reproduction of this material is confined to the purpose and/or media for which permission is hereby given.

5. Altering/Modifying Material: Not Permitted. However figures and illustrations may be altered/adapted minimally to serve your work. Any other abbreviations, additions, deletions and/or any other alterations shall be made only with prior written authorization of Elsevier Ltd. (Please contact Elsevier at permissions@elsevier.com)

6. If the permission fee for the requested use of our material is waived in this instance,

please be advised that your future requests for Elsevier materials may attract a fee.

7. Reservation of Rights: Publisher reserves all rights not specifically granted in the combination of (i) the license details provided by you and accepted in the course of this licensing transaction, (ii) these terms and conditions and (iii) CCC's Billing and Payment terms and conditions.

8. License Contingent Upon Payment: While you may exercise the rights licensed immediately upon issuance of the license at the end of the licensing process for the transaction, provided that you have disclosed complete and accurate details of your proposed use, no license is finally effective unless and until full payment is received from you (either by publisher or by CCC) as provided in CCC's Billing and Payment terms and conditions. If full payment is not received on a timely basis, then any license preliminarily granted shall be deemed automatically revoked and shall be void as if never granted. Further, in the event that you breach any of these terms and conditions or any of CCC's Billing and Payment terms and conditions, the license is automatically revoked and shall be void as if never granted. Use of materials as described in a revoked license, as well as any use of the materials beyond the scope of an unrevoked license, may constitute copyright infringement and publisher reserves the right to take any and all action to protect its copyright in the materials.

9. Warranties: Publisher makes no representations or warranties with respect to the licensed material.

10. Indemnity: You hereby indemnify and agree to hold harmless publisher and CCC, and their respective officers, directors, employees and agents, from and against any and all claims arising out of your use of the licensed material other than as specifically authorized pursuant to this license.

11. No Transfer of License: This license is personal to you and may not be sublicensed, assigned, or transferred by you to any other person without publisher's written permission.

12. No Amendment Except in Writing: This license may not be amended except in a writing signed by both parties (or, in the case of publisher, by CCC on publisher's behalf).

13. Objection to Contrary Terms: Publisher hereby objects to any terms contained in any purchase order, acknowledgment, check endorsement or other writing prepared by you, which terms are inconsistent with these terms and conditions or CCC's Billing and Payment terms and conditions. These terms and conditions, together with CCC's Billing and Payment terms and conditions (which are incorporated herein), comprise the entire agreement between you and publisher (and CCC) concerning this licensing transaction. In the event of any conflict between your obligations established by these terms and conditions and those established by CCC's Billing and Payment terms and conditions, these terms and conditions shall control.

14. Revocation: Elsevier or Copyright Clearance Center may deny the permissions described in this License at their sole discretion, for any reason or no reason, with a full refund payable to you. Notice of such denial will be made using the contact information provided by you. Failure to receive such notice will not alter or invalidate the denial. In no event will Elsevier or Copyright Clearance Center be responsible or liable for any costs, expenses or damage

incurred by you as a result of a denial of your permission request, other than a refund of the amount(s) paid by you to Elsevier and/or Copyright Clearance Center for denied permissions.

LIMITED LICENSE

The following terms and conditions apply only to specific license types:

15. **Translation**: This permission is granted for non-exclusive world **English** rights only unless your license was granted for translation rights. If you licensed translation rights you may only translate this content into the languages you requested. A professional translator must perform all translations and reproduce the content word for word preserving the integrity of the article. If this license is to re-use 1 or 2 figures then permission is granted for non-exclusive world rights in all languages.

16. **Website**: The following terms and conditions apply to electronic reserve and author websites:
Electronic reserve: If licensed material is to be posted to website, the web site is to be password-protected and made available only to bona fide students registered on a relevant course if:
This license was made in connection with a course,
This permission is granted for 1 year only. You may obtain a license for future website posting,
All content posted to the web site must maintain the copyright information line on the bottom of each image,
A hyper-text must be included to the Homepage of the journal from which you are licensing at http://www.sciencedirect.com/science/journal/xxxxx or the Elsevier homepage for books at http://www.elsevier.com , and
Central Storage: This license does not include permission for a scanned version of the material to be stored in a central repository such as that provided by Heron/XanEdu.

17. **Author website** for journals with the following additional clauses:

All content posted to the web site must maintain the copyright information line on the bottom of each image, and
he permission granted is limited to the personal version of your paper. You are not allowed to download and post the published electronic version of your article (whether PDF or HTML, proof or final version), nor may you scan the printed edition to create an electronic version,
A hyper-text must be included to the Homepage of the journal from which you are licensing at http://www.sciencedirect.com/science/journal/xxxxx , As part of our normal production process, you will receive an e-mail notice when your article appears on Elsevier's online service ScienceDirect (www.sciencedirect.com). That e-mail will include the article's Digital Object Identifier (DOI). This number provides the electronic link to the published article and should be included in the posting of your personal version. We ask that you wait until you receive this e-mail and have the DOI to do any posting.
Central Storage: This license does not include permission for a scanned version of the material to be stored in a central repository such as that provided by Heron/XanEdu.

18. **Author website** for books with the following additional clauses:

Authors are permitted to place a brief summary of their work online only.
A hyper-text must be included to the Elsevier homepage at http://www.elsevier.com

All content posted to the web site must maintain the copyright information line on the bottom of each image
You are not allowed to download and post the published electronic version of your chapter, nor may you scan the printed edition to create an electronic version.
Central Storage: This license does not include permission for a scanned version of the material to be stored in a central repository such as that provided by Heron/XanEdu.

19. **Website** (regular and for author): A hyper-text must be included to the Homepage of the journal from which you are licensing at http://www.sciencedirect.com/science/journal/xxxxx. or for books to the Elsevier homepage at http://www.elsevier.com

20. **Thesis/Dissertation**: If your license is for use in a thesis/dissertation your thesis may be submitted to your institution in either print or electronic form. Should your thesis be published commercially, please reapply for permission. These requirements include permission for the Library and Archives of Canada to supply single copies, on demand, of the complete thesis and include permission for UMI to supply single copies, on demand, of the complete thesis. Should your thesis be published commercially, please reapply for permission.

21. **Other Conditions**:

v1.6

If you would like to pay for this license now, please remit this license along with your payment made payable to "COPYRIGHT CLEARANCE CENTER" otherwise you will be invoiced within 48 hours of the license date. Payment should be in the form of a check or money order referencing your account number and this invoice number RLNK500703466.
Once you receive your invoice for this order, you may pay your invoice by credit card. Please follow instructions provided at that time.

Make Payment To:
Copyright Clearance Center
Dept 001
P.O. Box 843006
Boston, MA 02284-3006

For suggestions or comments regarding this order, contact RightsLink Customer Support: customercare@copyright.com or +1-877-622-5543 (toll free in the US) or +1-978-646-2777.

Gratis licenses (referencing $0 in the Total field) are free. Please retain this printable license for your reference. No payment is required.

References

A

[Ade90] Ade, H.; Kirz, J.; Hulbert, S.L.; Johnson,E.D.; Anderson, E. et al, X-ray spectromicroscopy with a zone plate generated microprobe, Applied Physics Letters, 56 (19) (1990) 1841-4

[All57] Allen, J.W., On the mechanical properties of indium antimonide, Philosophical Magazine, 2 (1957) 1475-81

[Als01] Als-Nielsen, J.; McMorrow, D., Elements of modern X-ray physics, John Wiley & Sons Ltd., England, 2001

[ASTM-B505] Standard Specification for Copper Alloy Continuous Castings, ASTM B505 / B505M – 11, ASTM International, 2008 For referenced ASTM standards, visit the ASTM website, www.astm.org or contact ASTM Customer Service at Service@astm.org.

B

[Bal02] Baldazzi, G.; Bollini, D.; Celesti, E.; Gambaccini, M.; Gombia, M.; Labanti, C.; Taibi, A.; Tuffanelli, A., First results with a novel X-ray source for dual energy angiography, 2001 IEEE Nuclear Science Symposium Conference Record, 3 (2002) 1615-19

[Bal03] Baldazzi, G.; Bernardi, B.; Bollini, D.; Gambaccini, M.; Gombia, M.; Rossi, P.L.; Sarnelli, A.; Taibi, A.; Tuffanelli, A.; Pancaldi, G.; Zuffa, M., Imaging characterization of an experimental apparatus for dual energy angiography, 2002 IEEE Nuclear Science Symposium Conference Record, 3 (2003) 1829-31

[Bay77] Bayer, S.A.; Peters, P.J., A method for x-irradiating selected brain regions in infant rats, Brain research bulletin, 2 (2) (1977) 153-6

[Bid94] Bidez, M.W.; Mcloughlin, S.W.; Chen, Y.; Lakshminarayanan, A.V.; Jeffcoat, M.K., An adaptable head retention and alignment device for computed tomography scanning of Macaca mulatta, Journal of Biomechanics, 27 (10) (1994) 1271-5

[Boe78] Boeuf, A.; Rustichelli, F.; Lagomarsino, S.; Mazkedian, S.; Melone, S.; Puliti, P., X-ray diffraction characteristics of curved monochromators for synchrotron radiation, Journal of Applied Crystallography, 11 (5) (1978) 442-9

[Bra73] Brantley, W.A., Calculated elastic constants for stress problems associated with semiconductor devices, Journal of Applied Physics, 44 (1) (1973) 534-5

[Buc97] Buckley, C.J.; Khaleque, N.; Bellamy, S.J.; Robins, M.; Zhang, X., Mapping the organic and inorganic components of tissue using NEXAFS, Journal de Physique IV (Colloque), 7 (C2) (1997) 83-90

C

[Cam09] Cammarata, M.; Eybert, L.; Ewald, F.; Reichenbach, W.; Wulff, M.; Anfinrud, P.; Schotte, F.; Plech, A.; Qingyu Kong; Lorenc, M.; Lindenau, B.; Rabiger, J.; Polachowski, S., Chopper system for time resolved experiments with synchrotron radiation, Review of Scientific Instruments, 80 (1) (2009) 015101

[Cau32] Cauchois, Y., X ray spectrography by transmission of a nonchanneled beam through a curved crystal (I), Journal de Physique et le Radium, 3 (1932) 320-36

[Cre78] Cremer, C.; Cremer, T., Considerations on a laser-scanning microscope with high resolution and depth of field, Microscopica Acta, 81 (1) (1978) 31-44

[Cul56] Cullity, B.D., Elements of X-ray diffraction, Addison-Wesley publishing company Inc., London, England, 1956

D

[DeB14] De Broglie, M.; Lindemann, F.A., New method of rapidly obtaining spectra of röntgen rays, Comptes Rendus Hebdomadaires des Seances de l'Academie des Sciences, 158 (1914) 944

E

[Ero90] Erola, E.; Etelaniemi, V.; Suortti, P.; Pattison, P.; Thomlinson, W., X-ray reflectivity of bent perfect crystals in Bragg and Laue geometry, Journal of Applied Crystallography, 23 (1) (1990) 35-42

[Ete89] Etelaniemi, V.; Suortti, P.; Thomlinson, W., Reflect - A Computer Program for the X-Ray Reflectivity of Bent Perfect Crystals, BNL-43247 Report in National Synchrotron Light Source, Brookhaven National Laboratory, 1989.

F

[Fau75] Faulkner, K.D., A restraining device for irradiating rats, Australian Dental Journal, 20 (1) (1975) 19-21

[Fei05] Feiters, M.C.; Küpper, F.C.; Meyer-Klaucke, W., X-ray absorption spectroscopic studies on model compounds for biological iodine and bromine, Journal of Synchrotron Radiation, 12 (1) (2005) 85-93

G

[Gem07] Gembicky, M.; Adachi, S.I.; Coppens, P., KHz heat-load shutter for white-beam experiments at synchrotron sources, Journal of Synchrotron Radiation, 14 (3) (2007) 295-6

[Gui10] Guilarte, TR., Manganese and Parkinson's disease: a critical review and new findings, Environmental Health Perspectives, 118 (8) (2010) 1071-80

H

[Hit03] Hitchcock, A.P.; Araki, T.; Ikeura-Sekiguchi, H.; Iwata, N.; Tani, K., 3d chemical mapping of toners by serial section scanning transmission X-ray microscopy, Journal de Physique IV (Proceedings), 104 (2003) 509-12

[How01] Howell, L.L.; Hoffman, J.M.; Votaw, J.R.; Landrum, A.M.; Jordan, J.F., An apparatus and behavioral training protocol to conduct positron emission tomography (PET) neuroimaging in conscious rhesus monkeys, Journal of neuroscience methods, 106 (2) (2001) 161-9

I

[Ill95] Illing, G.; Heuer, J.; Reime, B.; Lohmann, M.; Menk, R.H.; Schildwachter, L.; Dix, W.-R.; Graeff, W., Double beam bent Laue monochromator for coronary angiography, Review of Scientific Instruments, 66 (2) (1995) 1379-81

[Irs06] Irsen, S.H.; Leukers, B.; Bruckschen, B.; Tille, C.; Seitz, H.; Beckmann, F.; Muller, B., Image-based analysis of the internal microstructure of bone replacement scaffolds fabricated by 3D printing, Proceedings of the SPIE - The International Society for Optical Engineering, 6318 (2006) 631809

J

[Jac53] Jacobson, B., Dichromatic absorption radiography: dichromography, Acta Radiologica, 39 (1953) 437-52

[Jac00] Jacobsen, C.; Wirick, S.; Flynn, G.; Zimba, C., Soft X-ray spectroscopy from image sequences with sub-100 nm spatial resolution, Journal of Microscopy, 197 (2) (2000) 173-84

[Jan04] Janssens, K.; Proost, K.; Falkenberg, G., Confocal microscopic X-ray fluorescence at the HASYLAB microfocus beamline: Characteristics and possibilities, 17th International Congress on X-Ray Optics and Microanalysis, Spectrochimica Acta - Part B Atomic Spectroscopy, 59 (10-11) (2004) 1637-45

[Joh07] Johansson, G.A.; Tyliszczak, T.; Mitchell, G.E.; Keefe, M.H.; Hitchcock, A.P., Three-dimensional chemical mapping by scanning transmission X-ray spectromicroscopy, Journal of Synchrotron Radiation, 14 (5) (2007) 395-402

[Jon88] Jonson, R.; Roos, B.; Hansson, T., Triple-photon energy absorptiometry in the measurement of bone mineral, Acta Radiologica, 29 (4) (1988) 461-4

K

[Kan03] Kanngiesser, B.; Malzer, W.; Reiche, I., A new 3D micro X-ray fluorescence analysis set-up - First archaeometric applications, Nuclear Instruments & Methods in Physics Research, Section B (Beam Interactions with Materials and Atoms), 211 (2) (2003) 259-64

[Kar00] Karanfil, C.; Zhong, Z.; Chapman, L.D.; Fischetti, R.; Bunker, G.B.; Segre, C.U.; Bunker, B.A., A bent Laue analyzer detection system for dilute fluorescence XAFS, AIP Conference Proceedings, 521 (2000) 178-82

[Kel76] Kelez, F.; Mistretta, C.A., Absorption-edge fluoroscopy using a three-spectrum technique, Medical Physics, 3 (3) (1976) 159-68

[Kel77] Kelcz, F.; Mistretla, C.A.; Riederer, S.J., Spectral considerations for absorption-edge fluoroscopy, Medical Physics, 4 (1) (1977) 26-35

[Kir09] Kirz, J.; Jacobsen, C., The history and future of X-ray microscopy, Journal of Physics: Conference Series, 186 (1) (2009) 012001

[Koz99] Kozul, N.; Davis, G.R.; Anderson, P.; Elliott, J.C., Elemental quantification using multiple-energy X-ray absorptiometry, Measurement Science & Technology, 10 (3) (1999) 252-9

[Kum84] Kumakhov, M.A., the Union of Soviet Socialist Republics (USSR) Certificate of Authorship, No. 1322888, July 26, 1984.

[Kum90] Kumakhov, M.A., Channeling of photons and new X-ray optics, Nuclear Instruments and Methods in Physics Research Section B, 48 (1–4) (1990) 283–6.

[Kum00] Kumakhov, M.A., Capillary optics and their use in X-ray analysis, X-ray Spectrometry, 29 (2000) 343-8

L

[Lah98] Lahti, K.M; Ferris, C.F; Li, Fuhai; Sotak, C.H; King, J.A, Imaging brain activity in conscious animals using functional MRI, Journal of neuroscience methods, 82 (1) (1998) 75-83

[Lew03] Lewis, R., Position sensitive detectors for synchrotron radiation studies: the tortoise and the hare? Nuclear Instruments and Methods in Physics Research, Section A: Accelerators, Spectrometers, Detectors and Associated Equipment, 513 (1-2) (2003) 172-7

[Lin08] Lin, X.; Wang, Z.; Sun, T.; Pan, Q.; Ding, X., Characterization and applications of a new tabletop confocal micro X-ray fluorescence setup, Nuclear Instruments and Methods in

Physics Research Section B: Beam Interactions with Materials and Atoms, 266 (11) (2008) 2638-42

[Lyt75] Lytle, F.W.; Sayers, D.E.; Stern, E.A., Extended X-ray-absorption fine-structure technique. II. Experimental practice and selected results, Physical Review B (Solid State), 11 (12) (1975) 4825-35

M

[Mal05] Malzer, W.; Kanngieer, B., A model for the confocal volume of 3D micro X-ray fluorescence spectrometer, Spectrochimica Acta - Part B Atomic Spectroscopy, 60 (9-10) (2005) 1334-41

[Men97] Menk, R.H.; Charvet, A.M.; Arfelli, F.; Chapman, L.; Thomlinson, W.; Zhong, Z., Three energy computed tomography with synchrotron radiation, Physica Medica, 13 (1) (1997) 26-9

[Min57] Marvin Minsky, Microscopy apparatus, US patent 3013467 (A), Filed in 1957 and granted 1961

O

[Oku98] Oku, Y.; Hyodo, K.; Ando, M.; Tada, J., Development of a rotating X-ray shutter for coronary angiography using synchrotron radiation, Journal of Synchrotron Radiation, 5 (2) (1998) 123-7

[Ola04] Olanow, CW., Manganese-induced parkinsonism and Parkinson's disease, Annals of the New York Academy of Sciences, 1012 (2004) 209-23

P

[Paw06] Pawley, JB., Handbook of Biological Confocal Microscopy (3rd ed.), 2006, Berlin

[Pil95] Pilipuf, M.N.; Goble, J.C.; Kassell, N.F., A noninvasive thermoplastic head immobilization system, Journal of Neurosurgery, 82 (6) (1995) 1082-5

[Pop09] Popescu, B.F.Gh.; George, M.J.; Bergmann, U.; Garachtchenko, A.V.; Kelly, M.E.; McCrea, R.P.; Luning, K.; Devon, R.M.; George, G.N.; Hanson, A.D.; Harder, S.M.; Chapman, L.D.; Pickering, I.J.; Nichol, H., Mapping metals in Parkinson's and normal brain using rapid-scanning x-ray fluorescence, Physics in Medicine and Biology, 54 (3) (2009) 651-63

R

[Rar88] Rarback, H.; Shu, D.; Feng, S.C.; Ade, H.; Kirz, J.; McNulty, I.; Kern, D.P.; Chang, T.H.P.; Vladimirsky, Y.; Iskander, N.; Attwood, D.; McQuaid, K.; Rothman, S., Scanning X-ray microscope with 75-nm resolution, Review of Scientific Instruments, 59 (1) (1988) 52-9

[Ren97] Ren, B., A bent Laue-Laue monochromator for a synchrotron-based monochromatic X-ray computed tomography system, PhD dissertation, State University of New York at Stony Brook, 1997

[Ren05] Renier, M.; Fiedler, S.; Nemoz, C.; Gonzalez, H.; Berruyer, G.; Bravin, A., A mechanical chopper with continuously adjustable duty cycle for a wide X-ray beam, Nuclear Instruments & Methods in Physics Research, Section A (Accelerators, Spectrometers, Detectors and Associated Equipment), 548 (1-2) (2005) 111-15

[Rie81] Riederer, S.J.; Kruger, R.A.; Mistretta, C.A., Three-beam K-edge imaging of iodine using differences between fluoroscopic video images: theoretical considerations, Medical Physics, 8 (4) (1981) 471-9

[Rie82] Riederer, S.J., Performance of X-ray imaging systems applied to intravenous angiography, IEEE Transactions on Medical Imaging, MI-1 (1) (1982) 48-62

[Rig05] Rigley, S.; Rigon, L.; Ataelmannan, K.; Chapman, D.; Doucette, R.; Griebel, R.; Juurlink, B.; Arfelli, F.; Menk, R.H.; Tromba, G.; Barroso, R.C.; Beveridge, T.; Lewis, R.; Pavlov, K.; Siu, K.; Hall, C.; Schültke, E., Absorption edge subtraction imaging for volumetric measurement in an animal model of malignant brain tumor, Nuclear Instruments and Methods in Physics Research Section A: Accelerators, Spectrometers, Detectors and Associated Equipment, 548 (1-2) (2005) 88-93

[Row83] Rowland, H.A., On concave gratings for optical purposes, Philosophical Magazine, 16 (1883) 197-210

[Rub85] Rubenstein, E.; Brown, G.S.; Harrison, D.C.; Hofstadter, R.; Hughes, E.B.; Kernoff, R.S.; Otis, J.N.; Thompson, A.C.; Zeman, H.D, Synchrotron radiation for transvenous coronary angiography, Transactions of the American Clinical and Climatological Association, 97 (1985) 27-31

S

[Sak82] Sakayanagi, Y., Bragg optics of a logarithmic spiral surface, Japanese Journal of Applied Physics, Part 2 (Letters), 21 (4) (1982) L225-6

[San02] Sanghera, B.; Amis, A.; McGurk, M., Preliminary study of potential for rapid prototype and surface scanned radiotherapy facemask production technique, Journal of Medical Engineering and Technology, 26 (1) (2002) 16-21

[Sch97] Schulze, C.; Lienert, U.; Hanfland, M.; Lorenzen, M. and Zontone, F., Microfocusing of Hard X-rays with Cylindrically Bent Crystal Monochromators, Journal of Synchrotron Radiation, 5 (1998) 77-81

[Sch03] Schena, G.; Dreossi, D.; Montanari, F.; Olivo, A.; Pani, S., Multiple-energy x-ray radiography and digital subtraction for a particle-composition sensor, Minerals Engineering, 16 (7) (2003) 609-17

[Sol24] Soller, W., A new precision X-ray spectrometer, Physical Review, 24 (1924) 158-67

[Spr08] Spring, K.R.; Davidson, M.W., Introduction to Fluorescence Microscopy, Nikon MicroscopyU. http://www.microscopyu.com/articles/fluorescence/fluorescenceintro.html, Retrieved 2008

[Sto96] Stohr, J., NEXAFS Spectroscopy, Springer-Verlag, Berlin. (1996)

[Str09] Strang, G., Introduction to Linear Algebra, 4th edition, Wellesley-Cambridge Press, Wellesley, MA, (2009) chapter 7.3

[Sun08] Sun, T.; Ding, X.; Liu, Z.; Zhu, G.; Li, Y.; Wei, X.; Chen, D.; Xu, Q.; Liu, Q.; Huang, Y.; Lin, X.; Sun, H., Characterization of a confocal three-dimensional micro X-ray fluorescence facility based on polycapillary X-ray optics and Kirkpatrick-Baez mirrors, Spectrochimica Acta - Part B Atomic Spectroscopy, 63 (1) (2008) 76-80

[Suo88] Suortti, P.; Thomlinson, W., A bent Laue crystal monochromator for angiography at the NSLS, Nuclear Instruments & Methods in Physics Research, Section A (Accelerators, Spectrometers, Detectors and Associated Equipment), A269 (3) (1988) 639-48

[Suo93] Suortti, P.; Thomlinson, W.; Chapman, D.; Gmur, N.; Siddons, D.P.; Schulze, C., A single crystal bent Laue monochromator for coronary angiography, Nuclear Instruments & Methods in Physics Research, Section A (Accelerators, Spectrometers, Detectors and Associated Equipment), 336 (1-2) (1993) 304-9

T

[Tak09] Takeuchi, A.; Terada, Y.; Suzuki, Y.; Uesugi, K.; Aoki, S., Confocal full-field X-ray microscope for novel three-dimensional X-ray imaging, Journal of Synchrotron Radiation, 16 (5) (2009) 616-21

[Tak10] Takeuchi, A.; Terada, Y.; Uesugi, K.; Suzuki, Y., Three-dimensional X-ray fluorescence imaging with confocal full-field X-ray microscope, Nuclear Instruments and Methods in Physics Research, Section A: Accelerators, Spectrometers, Detectors and Associated Equipment, 616 (2-3) (2010) 261-5

[Tho89] Thompson, A.C.; Rubenstein, E.; Zeman, H.D.; Hofstadter, R.; Otis, J.N.; Giacomini, J.C.; Gordon, H.J.; Brown, G.S.; Thomlinson, W.; Kernoff, R.S., Coronary angiography using synchrotron radiation, Review of Scientific Instruments, 60 (7) (1989) 1674-9

[Tho00] Thompson, A.C.; Mills, D.; Naday, S.; Hormes, J.; Gruner, S.; Siddons, P.; Arthur, J.; Wehlitz, R.; Padmore, H., A program in detector development for the US synchrotron radiation community, White Paper on a Workshop, (2000) Oct. 30-31, Washington DC

[Tie06] Tie, Y.; Ma, R.; Ye, M.; Wang, D.; Wang, C., Rapid prototyping fabrication and finite element evaluation of the three-dimensional medical pelvic model, International Journal of Advanced Manufacturing Technology, 28 (3-4) (2006) 302-6

[Tsu06] Tsuji, K.; Matsuda, A.; Nakano, K.; Okhrimovskyy, A., X-ray fluorescence analysis of soft materials using needle-type collimators enabling greater tolerance in analysis depth, Spectrochimica Acta - Part B Atomic Spectroscopy, 61 (4) (2006) 460-4

[Tsu07] Tsuji, K.; Nakano, K.; Ding, X., Development of confocal micro X-ray fluorescence instrument using two X-ray beams, Spectrochimica Acta - Part B Atomic Spectroscopy, 62 (6-7) (2007) 549-53

U

[Ume92] Umetani, K.; Ueda, K.; Takeda, T.; Anno, I.; Itai, Y.; Akisada, M.; Nakajima, T., Two-dimensional real-time imaging system for subtraction angiography using an iodine filter, Review of Scientific Instruments, 63 (1) (1992) 629-31

V

[Vin04] Vincze, L.; Vekemans, B.; Brenker, F.E.; Falkenberg, G.; Rickers, K.; Somogyi, A.; Kersten, M.; Adams, F., Three-dimensional trace element analysis by confocal X-ray microfluorescence imaging. Analytical Chemistry, 76 (22) (2004) 6786-91

W

[Wel04] Welch, L.S.; Rappaport, S.M.; Susi, P., Construction welding exposures to manganese likely to exceed proposed TLV, Journal of Occupational & Environmental Hygiene, 1 (6) (2004) D63-5

[Whi50] White, J.E., X-ray diffraction by elastically deformed crystals, Journal of Applied Physics, 21 (9) (1950) 855-9

[Wol06] Woll, A.R.; Mass, J.; Bisulca, C.; Huang, R.; Bilderback, D.H.; Gruner, S.; Gao, N., Development of confocal X-ray fluorescence (XRF) microscopy at the Cornell high energy synchrotron source, Applied Physics A: Materials Science and Processing, 83 (2) (2006) 235-8

[Wol52] Wolter, H., Grazing-incidence reflecting systems for optical imaging by X-rays, Annalen der Physik, 10 (1-2) (1952) 94-114, Language: German

[Wol52] Wolter, H., Generalized Schwarzschild reflecting system for grazing-incidence X-ray optics, Annalen der Physik, 10 (4-5) (1952) 286-95, Language: German

[Wyr00] Wyrwicz, A.M.; Chen, N.K.; Li, L.; Weiss, C.; Disterhoft, J.F., fMRI of visual system activation in the conscious rabbit, Magnetic Resonance in Medicine, 44 (3) (2000) 474-8

Z

[Zac45] Zachariasen, W.H., Theory of X-ray diffraction in crystals, John Wiley & Sons, New York (1945)

[Zem84] Zeman, H.D.; Hughes, E.B.; Otis, J.N.; Rolfe, J.; Thompson, A.C., Rotating X-ray collimating slit for line-scan dual-energy medical imaging, IEEE Transactions on Nuclear Science, NS-31 (1) (1984) 548-52

[Zem86] Zeman, H.D.; Hughes, E.G.; Otis, J.N.; Brown, G.S.; Thompson, A.C., High-speed rotating-drum X-ray beam choppers for line-scan dual-energy medical imaging, IEEE Transactions on Nuclear Science, NS-33 (1) (1986) 515-18

[Zha08] Zhang, H.; Zhu, Y.; Bewer, B.; Zhang, L.; Korbas, M.; Pickering, I.J.; George, G.N.; Gupta, M.; Chapman, D., Comparison of iodine K-edge subtraction and fluorescence subtraction imaging in an animal system, Nuclear Instruments and Methods in Physics Research, Section A: Accelerators, Spectrometers, Detectors and Associated Equipment, 594 (2) (2008) 283-91

[Zha09] Zhang, H., Imaging dilute contrast materials in small animals using synchrotron light, PhD dissertation, University of Saskatchewan, 2009

[Zho97] Zhong, Z.; Le Duc, G.; Chapman, D.; Thomlinson, W., A tunable Laue/bent-Laue monochromator with fixed second crystal for synchrotron radiation, AIP Conference Proceedings, 417 (1997) 95-100

[Zho97-2] Zhong, Z.; Chapman, D.; Menk, R.; Richardson, J.; Theophanis, S.; Thomlinson, W., Monochromatic energy-subtraction radiography using a rotating anode source and a bent Laue monochromator, Physics in Medicine and Biology, 42 (9) (1997) 1751-62

[Zho99] Zhong, Z.; Chapman, D.; Bunker, B.; Bunker, G.; Fischetti, R.; Segre, C., A bent Laue analyzer for fluorescence EXAFS detection, Journal of Synchrotron Radiation, 6 (3) (1999) 212-4

[Zhu07] Zhu, Y.; Zhang, H.; McCrea, R.; Bewer, B.; Wiebe, S.; Nichol, H.; Ryan, C.; Wysokinski, T.; Chapman, D., Fabrication of a small animal restraint for synchrotron biomedical imaging using a rapid prototyper, Nuclear Instruments and Methods in Physics Research, Section A: Accelerators, Spectrometers, Detectors and Associated Equipment, 582 (1) (2007) 229-32

[Zhu08] Zhu, Y.; Zhang, H.; Bewer, B.; Popescu, B.F.; Nichol, H.; Chapman, D., Field flatteners fabricated with a rapid prototyper for K-edge subtraction imaging of small animals, Nuclear Instruments and Methods in Physics Research, Section A: Accelerators, Spectrometers, Detectors and Associated Equipment, 588 (3) (2008) 442-7

[Zhu10] Zhu, Y.; Bewer, B.; Zhang, H.; Nichol, H.; Thomlinson, B.; Chapman, D., Bent Laue X-ray Fluorescence Imaging of Manganese in Biological Tissues – Preliminary Results, 10th International Conference on Radiation Instrumentation (SRI 2009), Melbourne, Australia, American Institute of Physics Conference Proceedings, 1234 (2010) 457-60

[Zoe08] Zoeger, N.; Streli, C.; Wobrauschek, P.; Jokubonis, C.; Pepponi, G.; Roschger, P.; Hofstaetter, J.; Berzlanovich, A.; Wegrzynek, D.; Chinea-Cano, E.; Markowicz, A.; Simon, R.; Falkenberg, G., Determination of the elemental distribution in human joint bones by SR micro XRF, X-Ray Spectrometry, 37 (1) (2008) 3-11